Measuring fracture properties using digital image and volume correlation: decomposing the *J*-integral for mixed-mode parameters

Matthew Robert Molteno

Dissertation presented for the degree of Doctor of Philosophy
in the Faculty of Engineering at Stellenbosch University

Supervisor: Thorsten Hermann Becker

December 2017

Declaration

By submitting this dissertation electronically, I declare that the entirety of the work contained therein is my own, original work, that I am the sole author thereof (save to the extent explicitly otherwise stated), that reproduction and publication thereof by Stellenbosch University will not infringe any third-party rights and that I have not previously in its entirety or in part submitted it for obtaining any qualification.

Date: December 2017

M.R. Molteno

Abstract

The degradation of material properties over time is one of the core constituents of structural integrity monitoring. For this purpose, the materials' resistance to brittle fracture is the most widely used property in the determination of safe operation and predicting component life. Measuring such properties by conventional methods presents challenges: large numbers of samples are needed, accounting for mixed-mode loading. Non-contact measurements by digital image correlation shows promise in extracting such parameters from *in situ* loaded structures, accounting for their complex geometry and loading.

This thesis aims to develop a framework that allows for the extraction of mixed-mode brittle fracture properties, using three-dimensional (3D) image correlation techniques: multi-camera Digital Image Correlation (stereo-DIC), and Digital Volume Correlation (DVC). The J-integral method was chosen for obtaining the fracture resistance, with the decomposition method used for determining separate J_{I-III} components (opening, sliding and shearing: modes I, II and III), and stress intensity factors (K_{I-III}), as both methods are resilient to crack tip and displacement errors.

The first stage of development is a finite element based method for the removal of experimental displacement artifacts from DIC or DVC results, intended as a pre-processor for the J-integral. Subsequently, a theoretical derivation is provided to link the two volumetric forms: the volume and the path-area integrals. This results in a proposed 'hybrid' integral, which benefits from the resilience to crack-front positional errors of the path-area approach, and resilience to random displacement noise of the volume integral.

Initial testing of the J-integral based decomposition method was on the surface using stereo-DIC and the Arcan fixture to induce mixed-mode loading. The results are verified with mixed-mode fracture toughness values measured from PMMA and compared to literature and ASTM 1820 tests. The typical image correlation errors close to fracture are quantified by a methodology of applying the J-integral to analytical crack tip fields to which displacement errors are added artificially. It was found that the J-integral is most prone to DIC errors under anti-symmetric (mode II/III) loading.

Testing in the volume used X-ray computed tomography to acquire images and DVC for displacement maps. The measurements were verified on two configurations: a SENT polyurethane composite specimen (mode I), and a shear loaded inclined notch in Magnesium alloy-WE43 (mixed-mode). The J-integral was verified against values from finite element fields resulting again in larger errors in mixed-loading. Decomposition of the volume integral requires an approach to separate the anti-symmetric J-integral. Two extensions are proposed: the first using a ratio derived from mode II/III Williams series formulas, and the second using the interaction integral. Both approaches are verified on DVC displacements.

This thesis finds that J based decomposition offers a versatile method to extract K_{I-III} values from non-standard 3D geometries and loadings. However, the pre-processing of fields to minimise errors is essential when mode II-III displacement fields are prominent.

Although it is beyond the scope of this thesis, the hope is that this work will assist in the adoption of full-field measurement techniques as a standard testing practice in structural integrity assessments, and lead to better informed maintenance and inspection schedules.

Opsomming

Die agteruitgaan van material-eienskappe met tyd is een van die kernkomponente van strukturele integriteit monitering. Vir hierdie doel is die materiaal se weerstand teen brosfraktuur die mees algemene gebruikte eienskap vir die bepaling van veilige werking en die voorspel van die komponent se leeftyd. Die meet van sulke eienskappe volgens konvensionele metodes bied uitdagings, bv. groot getalle monsters word benodig en komplekse kragte moet in ag geneem word. Nie-kontakmetings deur digitale-beeldkorrelasie toon belofte om sulke parameters uit *in situ* gelaaide strukture te onttrek, terwyl komplekse kragte en material vorme in ag geneem word.

Hierdie proefskrif beoog om 'n raamwerk te ontwikkel wat die ontginning van gemengde-modus brosfraktuur-eienskappe moontlik maak deur gebruik te maak van driedimensionele (3D) beeldkorrelasietegnieke: Digitale Kamera-Korrelasie (stereo-DKK) en Digitale Volume Korrelasie (DVK). Die J-integrale metode is gekies vir die verkryging van die breukweerstand, met behulp van die ontbindingsmetode vir die bepaling van afsonderlike J_{I-III} komponente (opening, gly en skeer: mode I, II en III) en stresintensiteitsfaktore (K_{I-III}), aangesien beide metodes skerm teen kraakpunt en verplasings foute.

Die eerste fase van ontwikkeling is 'n eindige element gebaseerde metode vir die verwydering van eksperimentele verplasing artefakte van DKK of DVK resultate, wat bedoel is as 'n voorverwerker vir die J-integraal. Vervolgens word 'n teoretiese afleiding verskaf om die twee volumetriese vorms te verbind, naamlik die volume en pad-area integrale. Dit lei tot 'n voorgestelde 'hibriede'-integraal. Hierdie ‘hibriede’-integraal vereis ‘n kompromie tussen die robuustheid van die pad-area-benaderingsfout van die pad-area-benadering en robuustheid van lukrake verplasings geraas van die volume-integraal.

Aanvanklike toetsing van die J-integraal gebaseerde ontbindings metode is op die oppervlak met behulp van stereo-DKK, en die Arcan greep om gemengde-mode laai te veroorsaak. Die resultate word geverifieer met gemengde-mode-fraktuur taaiheid waardes, gemeet vanaf PMMA en baseer op literatuur sowel as die ASTM 1820 toetse. Die tipiese beeldkorrelasie foute naby aan fraktuur word gekwantifiseer deur die toepassing van die J-integraal op analitiese kraakpuntvelde waarby verplasingsfoute kunsmatig bygevoeg word. Daar is bevind dat die J-integraal die meeste geneig is tot DKK foute onder asimmetriese (mode II/III) laai.

Toets in die volume gebruik X-straal-rekenaartomografie om beelde en DVK vir verplasings kartering te bekom. Die metings is geverifieer op twee konfigurasies: 'n SENT saamgestelde-polyuretaan monster (mode I) en 'n skuinsbelaaide spleet in magnesium-allooi, WE43 (gemengde mode). Die J-integraal is geverifieer teen waardes van eindige elementvelde wat weer groter foute in gemengde laai veroorsaak. Ontleding van die volume-integraal vereis 'n benadering om die anti-simmetriese J-integraal te skei. Twee uitbreidings word voorgestel: die eerste met behulp van 'n verhouding wat afgelei word vanaf mode II / III Williams reeks formules, en die tweede maak gebruik van die interaksie integraal. Albei benaderings word geverifieer op DVK-verplasings.

Hierdie proefskrif bevind dat J gebaseerde ontbinding 'n veelsydige metode bied om K_{I-III} waardes uit nie-standaard 3D-geometrieë en ladings te onttrek. Die voorbereiding van velde om foute te beperk, is egter noodsaaklik wanneer die mode II-III verplasingsvelde prominent is.

Alhoewel dit buite die omvang van hierdie proefskrif is, is die hoop dat hierdie werk sal help met die aanvaarding van volwaardige metingstegnieke as 'n standaard toetspraktyk in strukturele integriteit assesserings, en lei tot beter ingeligte onderhouds en inspeksieskedules.

Acknowledgements

My heartfelt acknowledgement goes to Dr Thorsten Becker whose expertise, vision, and leadership were a constant inspiration; and whose kindness and foresight guided this work through diverse terrains. Secondly, I sincerely thank Prof. James Marrow, whose insights, supervision and support significantly contributed to the development of this thesis, and who made me feel very welcome in Oxford.

I would also like to thank my defense committee: Prof. Fabrice Pierron, Prof. Satoru Yoneyama and Prof. Gerhard Venter, for their insightful comments, encouragement, and probing questions.

My deepest gratitude goes to my parents, Martin and Jane for their understanding and support through each of my post-graduate endeavors. Thanks also goes to my brothers: Steve, Robin, and Chris, for keeping me motivated.

Thank you to Marisa Storm for her unwaivering love and support during the doctoral journey. To Dr Robert Pott, thank you for leaving food out for the nocturnal creature that took up residence in your house during the final stages of write-up. To Uri Bram, Mieke du Plessis, Joelle Grogan, Anna Frangou, Teddy Rose (TR) Stegmann, Daan Henselmans, and Lily Prollius; thank you for whisking me away from my thesis when it was most needed.

Thanks are also extended to the research groups I have attended who provided encouragement, and many laughs. In the Stellenbosch group: Richard Huchzermeyer, Nur Dhansay, Sergey Petrov, Lucas Anderson, Devan Atkinson, Melody van Rooyen, Arno Scholtz and Gerrit ter Haar; in the Oxford group: Matthew Jordan, Selim Barhli, Ahmet Cinar, Yelena Vertyagina and Luis Saucedo Mora.

It is also essential to mention the staff who greatly enlivened my time at Stellenbosch University with their dedication and general positivity. In particular, I would like to thank Ms Welma Liebenberg, Prof. Gerhard Venter, Dr Martin Venter and Prof. Thomas Harms.

Importantly, I would like to acknowledge the NRF-Thrip fund for the financial support, as well as the ESKOM EPPEI programme for the bi-yearly meetings, and valuable input from industry.

Table of contents

List of figures

Page

List of tables

Page

List of abbreviations

2D	Two-Dimensional
3D	Three-Dimensional
ASTM	American Society for Testing and Materials
BEM	Boundary Element Method
COD	Crack Opening Displacement
DIC	Digital Image Correlation
DLS	Diamond Light Source synchrotron (United Kingdom)
DVC	Digital Volume Correlation
EPFM	Elastic-Plastic Fracture Mechanics
EPRI	Electric Power Research Institute
ESKOM	Electricity Supply Commission (of South Africa)
FE	Finite Element
FEM	Finite Element Method
FFT	Fast Fourier Transform
IARE	Incremental Artifact Relaxation Energy
LEFM	Linear Elastic Fracture Mechanics
PMMA	Polymethyl Methacrylate
ROI	Region of Interest
RMSE	Root-Mean-Square-Error
SA	South Africa
SF	scale factor
SIF	Stress Intensity Factor
SNR	Signal-to-Noise Ratio
UCT	University of Cape Town
UK	United Kingdom
X-CT	X-ray Computed Tomography

Nomenclature

a	Length of a flaw
Δa	Maximum value of the virtual crack extension on the crack front
c_n	Co-efficient of strain
$f_{M_{ij}}^{(n)}$	Co-efficient of stress
f_i	Nodal forces
$\hat{f}$	Vector of normalized force magnitudes
g_{ij}	Stress function for the virtual fields method
l	Crack front position
n	Order of terms within the Williams series expansion
n_j	Outward unit normal for the J-integral
p-p	2D cross-section of 3D volume
q	Virtual crack front extension
r	Radial distance from the crack tip
r_c	Contour position (rectangular)
r_i	Region of crack influence (rectangular)
r_k	Radius of K-dominance
r_m	Region of mask (rectangular)
s	Crack front position parameter
s^l	Discrete crack front segment
Δs	Crack front segment length
u_{acc}	Image correlation displacement accuracy
u_{crack}	Crack tip displacements
u_{err}	Full-field displacement errors
u_i	Displacement field
$u_{i,j}$	Displacement gradients
$\tilde{u}_i$	Displacements in the global co-ordinate system

u_M	Decompositions for crack tip displacements
u_{prec}	Experimental precision
u_{AS}	Anti-symmetric component of displacement
v	Poisson's Ratio
x_j	Local co-ordinate system
$\tilde{x}_1^l$	Global crack segment co-ordinate system
A	Area integral domain
A_c	Virtual crack extension area
A_M	Mode ($M = I, II, III$) coefficients of the Williams series
C	Correlation coefficient
C_{NCC}	Normalized cross-correlation coefficient
C_{ij}^R	Rotation matrix
C_i^T	Rotation vector
D	Area integral width
E	Young's Modulus
E_{ij}	Cauchy stiffness tensor
E^*	Nodal Young's modulus
E_l	Young's modulus of a single finite element
E_{min}	Young's modulus of void material
E'	Young's modulus for plane strain or stress
F	Reference image
$\bar{F}$	Mean pixel intensity of reference image
F^*	Reference image after deformation
$\mathcal{F}$	Fast Fourier Transform (FFT)
$\check{\mathcal{F}}$	Fast Fourier Transform followed by a complex conjugate operation
$\mathcal{F}^{-1}$	Inverse Fast Fourier Transform
G	Strain energy release rate
J	J-integral value

J_a	Area component of the path-area J-integral
J_p	Path component of the path-area J-integral
J_{pa}	Path-area integral
J_{w-pa}	Weighted path-area integral
J_{vol}	Volume J-integral
$J^{(k)}$	J-integral vector
J_{AS}	Antisymmetric component of J
J_S	Symmetric component of J
J_{SENT}	J for the standard Single-Edge-Notch-Test geometry
J_{hyb}	Hybrid J-integral
J_M	Modal component of J $(M = I, II, III)$
J_{th}	Theoretical value for J from analytical solution
$J = J^{(1)}$	J-integral scalar assuming x_1 direction crack growth $(k = 1)$
J_I	Mode I component of J
J_{II}	Mode II component of J
J_{III}	Mode III component of J
K_I	Mode I stress intensity factor
K_{II}	Mode II stress intensity factor
K_{III}	Mode III stress intensity factor
K_{Ic}	Mode I fracture toughness
K_{IIc}	Mode II fracture toughness
K_{IIIc}	Mode III fracture toughness
K_l^t	Template stiffness matrix
K_J	Stress intensity factor determined by the J-integral approach
K_M	Modal K value
M	Mode
N	Total number of nodes of points in DVC or DIC
P_{ij}	Eshelby's Energy momentum tensor

P'	Reflected position of a point
P*	Displaced position of a point
Q	Virtual crack extension field
QF	Replacement factor for outlier removal
Q_{hyb}	Hybrid virtual crack extension field
R_{AS}	Antisymmetric ratio
S	Surface
S_a, S_b	volume integral end-caps
S_c	volume integral crack faces
S_f	Surface over which a traction is applied
S_u	Constrained surface
T_j	Traction on the surface
U	Elastic stored energy
U_{ext}	External energy
U_{int}	Internal energy
U_n	Potential energy due to random errors
U_o	Portion due to outliers
$\widetilde{U}$	Energy residual due to displacement errors
$\delta\widetilde{U}_{RMSE}$	Root-mean-square-error relaxation energy
V	Volume
W	Strain energy density
X_i	Global co-ordinate system
Y	Crack geometric factor
°C	Degrees Celsius

Greek symbols

γ_i	Rotation about the x_i axis [degrees, °]
δ_{ij}	Kronecker-delta
ε_{ij}	Strain tensor
$\varepsilon_{AS_{ij}}$	Anti-symmetric strain components
$\varepsilon_{M_{ij}}$	Strains for mode $M = I, II, III$
ε_0	Strain at yield
θ	Angle theta [degrees, °]
κ	Bulk modulus
ρ	Density distribution of a material
ρ_l	Density of a single finite element
σ_{ij}	Cauchy stress tensor
$\sigma_{AS_{ij}}$	Anti-symmetric components of the Cauchy stress tensor
σ_{crack}	Crack tip stresses
σ_{ff}	Stress of the field far from the crack tip region
Γ	Contour of the line integral
Γ^+, Γ^-	Contour path coinciding with the upper and lower crack faces
$\Gamma_0,\ \Gamma_1$	Inner and outer boundary contours
∇	First-order gradient of the deformed image
Ω	Domain of outlier removal

1 Background reading

Compared to classical solid mechanics, fracture mechanics is still a relatively new field. As man-made structures have increased in size, it has become increasingly clear that failures could still not be explained or wholly prevented by solid mechanics principles applied to constituent parts. Fracture mechanics principles neglect the larger structure, focusing instead on the notion that failure can be fully characterised by the deformations and loading of the crack tip, regardless of location. Therefore, the fracture mechanics methodology can be conveniently applied to laboratory tests, as well as full-scale structures. The proving grounds for these theories are remembered in the shadow of several catastrophic structural failures in the 1940s and 1950s that mystified the engineering communities of the decade[1] (Wells, 1955).

The modern engineer has a wide array of tools to more fully understand material performance: numerical methods can simulate the deformation of large structures *in silico*, and accurate experimental techniques have become available to directly monitor material deformation across the full-field of the material surface or volume. The latter can be achieved in an accessible and versatile manner through image correlation.

However, there is a significant gap dividing the numerical modelling and experimental techniques used for the task of fracture characterisation. This thesis aims to bridge this gap, utilising image correlation techniques across the full-field of the surface and volume, and feeding into mathematical derivations of the J-integral to characterise fracture. The synthesis of these experimental and numerical approaches can then be directed towards gaining a better understanding of fracture in novel materials and structures.

This has applications in two main spheres. Firstly, conventional fracture mechanics allows for the direct assessment of structural integrity through non-destructive estimation of the crack tip parameters (for example, through quantification of crack tip stress fields, or energy release rate approaches such as the J-integral). Secondly, the techniques are applicable to laboratory tests aiding in the development of new fracture-resistant materials.

Recent trends, described in academic journals such as *Strain*[2], *Fracture*[3], and *Experimental Mechanics*[4], have been to combine full-field optical measurements with established numerical methods to characterise deformations and damage – often referred to as 'photo-mechanics' due to the optical component. Recent developments in this area has been spurred on by advances in digital image correlation, which provide deformation data from the full-field of the material with great versatility, as the images can be acquired from transmission

---

[1] The two famous examples are the Liberty ships, and the Comet aircraft failures. The Liberty ships, used for transport of supplies from the United States to Great Britain during World War II featured an all-welded steel hull as a replacement to the *de facto* riveted panels. The square corners of the hatch doors acted as stress concentrations and initiation sites for cracks. Without riveted joints, cracks could propagate unchecked. In 10 cases failure resulted in clean separation of the ships into two-halves, often in calm waters. The Comet jet aircraft was the world's first commercial passenger jet, considered state-of-the-art at the time. In 1954 several Comets experienced catastrophic hull loss during routine flight within a three-month period. By replicating flight conditions on the remaining grounded planes, Engineers found that mirco-flaws initiated at pop-rivet sites would propagate due to the regular pressurising and depressurising of the cabin. The final failure initiated near the corners of square cabin windows, which acted as stress concentrators.

[2] Strain ISSN, online: 1475-1305

[3] Fracture ISSN, print: 0376-9429; online: 1573-2673

[4] Experimental Mechanics ISSN, print: 0014-4851; online: 1741-2765

electron microscopy, neutron diffraction and X-ray computed tomography. This new branch of methods provides the potential to perform online assessment of structures while inspection of the micro-scale and within the volume can lead to a better understanding of the mechanisms that drive them toward fracture.

This doctoral project grew from two earlier projects: the MSc work of the author on non-destructive testing (Eddy-current detection of fatigue cracks – Molteno, 2012) and the doctoral work of Becker (2012). The vision was formed that the post-detection monitoring and analysis of cracks could be achieved by extracting fracture parameters directly from the fracture site, within a single framework. The approach of Becker *et al.* (2012), achieved this without prior knowledge of the crack tip position using the *J*-integral approach and two-dimensional (2D) measurements. This provided the impetus to extend the framework to more general three-dimensional (3D) geometries, and crack orientations.

The following doctoral work commenced in 2013 at Stellenbosch University, with a two year investigation into fracture parameter extraction from regular (white light) images of the surface using image correlation (work summarised in Molteno and Becker, 2015c. The extensions to the volume were developed at Oxford University during 2015 under the auspices of Prof. James Marrow (Department of Materials Science), and using X-ray imaging facilities: MXIF (Manchester University), Diamond Light Source (DLS), to image the volume, including image data-set contributions from Stellenbosch University and Poitiers (France).

The aim of this thesis is therefore to present a framework for the analysis of the *J*-integral on the surface, and within the volume using image correlation, but also to enable the extraction of fracture parameters.

1.1 Project background

Structural survivability is a growing concern in South Africa (SA), brought to light by the nationwide power shortages and load shedding since 2008 (Bazilian *et al.*, 2012). The fast-rising demand for electrical energy in SA has forced suppliers to exceed the original operational lifetimes of over 70 % of coal-fired power plants (Figure 1.1), which still generate 68 % of the country's electricity. Eskom, the primary power utility in SA, and various government agencies have committed to addressing these shortages through various programmes and incentives. These include large capital investments into coal, gas and various renewables, aiming to add 12 GW of generating capacity by 2020 (Jestin *et al.*, 2014).

This transition period has placed great importance on the reliability of existing stations as they see South Africa into a new era of robust electricity supply and economic growth (Trollip *et al.*, 2014). Therefore, effective structural integrity management has become an important short and long-term national goal. A significant limitation is that quantitative damage or fracture estimates are mainly replicated in laboratory controlled tests (Jestin *et al.*, 2014; Scheepers *et al.*, 2010). Such tests seldom reproduce plant conditions (e.g. high temperatures, cyclic loads, corrosive contact), which are known to aggregate and accelerate damage (Bezuidenhout, 2010). This results in uncertainty in the extracted parameters, over-conservatism in component design, ultimately resulting in errors in life estimates on in-service plant components.

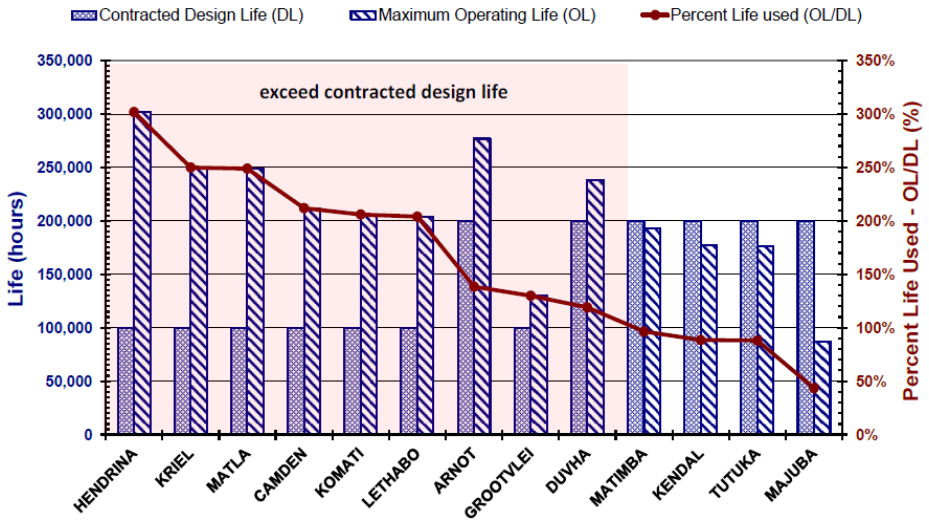

Figure 1.1: Life expenditures of the current coal-fired Eskom power plants (Molokwane, 2014)

To increase expertise in this area, Eskom launched the Eskom Power Plant Engineering Institute (EPPEI) programme in 2012 (Jestin *et al.*, 2014), which included a specialisation in damage characterisation and the prediction of residual component life. Several projects in damage measurement and monitoring are presently underway as part of a collaboration between the Material Engineering centres at the University of Cape Town and Stellenbosch University. Projects at Stellenbosch University have included accelerated creep damage characterisation (van Rooyen, 2016) and the measurement of fracture parameters from small sample tests (Huchzermeyer, 2017). Numerous complementary projects have also been conducted at the University of Cape Town, and can be viewed on the EPPEI Materials Science and Mechanics Specialisation website[5]. These projects have similar aims: to feed into the component service-life management programme currently established at Eskom.

The current Eskom programme seeks to firstly locate damage, and then determine the risk levels so that high-risk components can be elevated to more in-depth evaluation (e.g. detailed modelling of bolted joints to determine joint stiffness and contact stresses). The programme involves non-contact inspection to detect all forms of aberrations (e.g. ultrasonic testing, eddy current testing), followed by manual dimensioning and monitoring of detected damage (e.g. by metallographic replication of the surface microstructure), in order to determine the risk of failure of individual components.

These methods are well established to detect and measure surface and near-surface defects, but are subject to numerous equipment and operator specific limitations when large surface areas must be covered, and objective measurements are required.

1.2 Full-field measurements with image correlation

Optical full-field measurements in the field of experimental mechanics refers to a collection of techniques, which measure deformation over the full surface or volume of the object from

[5] "Eskom EPPEI", University of Cape Town, www.mateng.uct.ac.za/mateng/industry/eskom-eppei (accessed 19 June 2017)

recorded images. Early methods, based on incoherent[6] light, required separate gratings for each deformation state (e.g. moiré (Hareesh and Chiang, 1988)). Various coherent light based methods have since been developed including holographic interferometry (Kreis, 2005), electronic speckle interferometry (Jacquot Pierre, 2008) and moiré interferometry (Post, 1991). Although these methods provide high spatial resolution (two orders of magnitude more independent data-points than DIC), they also require specialised equipment and complex sample preparations.

As a result, white-light based methods have become increasingly popular for experiments in which precision can be traded-off for a simpler experimental setup. The two most well-known white light methods are the grid method, and Digital Image Correlation (DIC) (Grédiac *et al.*, 2016). The grid method is based on the processing of predetermined patterns, which are required to be as regular as possible and therefore some sample preparation is required. Conversely DIC involves the processing of random patterns. Although the pattern quality has been shown to influence accuracy (Bossuyt, 2013; Schreier *et al.*, 2009), the method is generally less prescriptive in terms of sample preparation. For instance, random patterns occur naturally in many materials (e.g. due to grain structure or porosity), and so the amount of sample preparation is often left to the discretion of the experimentalist.

DIC differs from other optical flow-based methods in that it focuses on the high accuracy needed in engineering problems to study strains in stiff structures (typically 50-100 µm/m). This typically leverages assumptions of the materials mechanics, such as continuity and limited volume change[7].

The approach has extensions to multiple cameras, called stereo-DIC; and can be applied within the volume when volumetric images are available (e.g. via X-ray based imaging), called Digital Volume Correlation (DVC). These approaches are termed full-field[8] techniques because they can obtain deformation data from the entire surface or volume within the field of view of each image captured. The use of digital images results in a method that is intuitive (phenomena can often be verified visually by the user) and cost effective while remaining more accurate and objective than manual measurements. The popularity of image correlation is apparent from the large body of literature (see for example the review by Pan *et al.* (2009)) and the growing attention received by these methods in industry (Feng *et al.*, 2015).

1.3 The role of fracture mechanics in damage evaluations

Damage quantification is a broad field requiring precise understanding of both the material and environmental parameters of micro and macro length scales. Although damage originates from the microstructure of the material (from physical mechanisms such as creep and fatigue), it is generally first identified as an aggregated effect on the material surface in relatively late stages of damage evolution.

---

[6] Coherent light is defined as containing electromagnetic waves, which are in phase with a plane normal to the beam direction. Conversely, incoherent light is out-of-phase with the orthogonal plane. Coherent light is commonly produced for practical purposes by a laser, or when studies in the volume require high-energy rays a synchrotron is used.

[7] Contrastingly, another optical technique called Particle Image Velocimetry (PIV) involves loosely connected regions to allow for the random rearrangement of particles in fluid flow.

[8] Also, historically, to discern from point-wise measurements (for example using extensometers and strain gauges), upon which there has been great reliance.

Although significant changes in the design properties may occur during the aging of a material, non-destructive tests tend to be most sensitive to physical defects (e.g. fracture and void growth). As a result, structural integrity assessment is typically an upstream procedure starting from the detection of cracking requiring an estimation of short-term risks, towards an understanding of the underlying damage mechanisms and long-term life predictions.

Short-term risks are often assessed based on Linear Elastic Fracture Mechanics (LEFM) parameters which describe the fracture toughness of the material. The task of non-destructive testing and evaluation is then to estimate the subcritical values for such parameters from components while *in situ*, and compare them to the material limits provided by manufacturers or *ex situ* tests (e.g. using standards such as ASTM (2015)). This requires a method to estimate the strain energy release rate (G); the energy released per unit advancement in crack area.

However, such approaches are typically based on planar deformations and loadings and standard sample geometries, whereas the geometry of plant components are generally diverse and three-dimensional. These effects cause complex 3D loading on the crack tip, which strongly influence crack growth directions (Richard *et al.*, 2005) and the prediction of ultimate failure (Richard *et al.*, 2014). In LEFM these conditions can be delineated as the superposition of three distinct modes of fracture (I, II and III, elaborated in section 2.2.1). Fracture characterisation in the mixed-mode framework requires that G is obtained or separated into its modal components (G_I, G_{II}, and G_{III}, written G_{I-III}), which can be related under LEFM assumptions to equivalent stress intensity factors K_{I-III}. The resulting K_{I-III} factors are the most widely-used fracture parameters in theoretical, numerical and structural integrity analysis (LEFM theory given in section 2.2.3).

The JMAN method by Becker *et al.* (2012) demonstrated that G could be estimated directly from DIC displacement fields using the J-integral without prior knowledge of the crack tip position. This characteristic facilitated the study of micro-crack nucleation and the rising R-curve behaviour in nuclear grade graphite (Becker *et al.*, 2011). JMAN has also been extended to a resourceful approach in which G is computed from neutron diffraction based strain maps, enabling the direct estimation of G without plastic contributions (Barhli *et al.*, 2016). However, the JMAN framework was developed for planar problems, and has therefore been limited to linear regions in surface experiments (Becker and Tait, 2013), although the constitutive methods (J-integral, finite elements) are well established in non-linear materials (Rice and Rosengren, 1968; Kolednik *et al.*, 2014; Yoneyama *et al.*, 2014) and the volume (Shih *et al.*, 1986).

1.4 Summary of aims

This project aims to extend the J-integral framework to 3D, both on the surface and within the volume, that allows for efficient and accurate extraction of mixed-mode fracture parameters (G_{I-III}, K_{I-III}) in the volume. The aim is to move away from a finite element framework, prescribed in the original JMAN approach, to allow for direct application to stereo-DIC (in- and out-of-plane measurements) and DVC data while remaining versatile and accessible for future research on mixed-mode behaviour observed in digital images. As such, the capability to extract mixed-mode stress intensity factors from G estimates is seen as essential: firstly, for providing a quantitative damage assessment tool in the context of national energy security in light of the forecasted energy requirements (Jestin *et al.*, 2014); and secondly, to enable mixed-mode analysis in the volume to study damage mechanisms. These aims are developed further in Chapter 3.

Although it is beyond the scope of this thesis, the hope is that this work will assist in the adoption of full-field measurement techniques as a standard testing practice in structural integrity assessments and lead to better informed maintenance and inspection schedules.

1.5 Details of thesis layout

The chapters of this thesis concern the various stages of the experimental-numerical methodology to extract G and stress intensity factors from stereo-DIC and DVC displacement fields. The intention of this section is to explain the philosophy of the document and to provide suggestions to the reader, who may prefer to read the chapters in a different order.

The results chapters (4-8) have been presented in paper format, as these chapters are either published, in-press or due to be submitted for publication. Therefore, the assistance received from co-authors requires clarification. The convention used in this thesis is to list the contributions in the preamble at the beginning of each chapter. In keeping with this format, each chapter is self-contained. Therefore, this thesis does not contain a single comprehensive literature review, but rather a background reading chapter (Chapter 2) containing broad contextual information on the methods used. The detailed literature concerning each technique can be found in the introduction of each results chapter (4-8).

The techniques introduced in Chapter 2 include: the principles of image correlation and the limitations in terms of spatial resolution close to fracture surfaces, elements of full-field fracture mechanics, the methods to acquire mixed-mode parameters, and some methods to acquire the constitutive properties of materials are presented in brief. This final topic concerns a broad field of inverse problems in experimental mechanics that is not developed elsewhere in this thesis.

Chapter 3 develops the hypothesis of the thesis. Initially the methodology is formulated in terms of the advantages that certain highlighted techniques can achieve with DIC and DVC data (summarised in section 2.4). These are presented in a series of methodology statements. The aim is to focus this thesis on a small number of techniques that can form a complete methodology for practical applications (e.g. with Eskom) at an early stage. The objectives for the development and verification of this methodology are then defined, giving rise to the central hypothesis of the thesis in section 3.3. All following chapters, excluding the final discussion and conclusions (chapters 9 and 10), present the developments of the methodology following the order of the objectives listed in section 3.2.

Chapter 4 introduces a technique for pre-processing displacement fields to locate and remove errors. The techniques in this thesis rely on the capabilities of DIC and DVC in the presence of fracture surfaces, which results in well-known error localisations (discussed in section 2.1) and which are challenging to separate from inherent random errors. This section proposes a framework that minimises such errors in both surface and volume datasets. This chapter is the first results chapter and sets the scene in terms of the limitations of DIC and DVC in fracture problems.

Chapter 5 develops a framework to establish the noise susceptibility of the J-integral. The framework has a theoretical basis that builds on the generic derivation of the J-integral provided in the background reading (section 2.2.5). The following chapters (0, 7 and 8) draw on this framework to determine J from DIC and DVC displacement data and separate J values into separate opening, shearing and tearing (I, II and III) modes to determine stress intensity factors. The procedure in each case (on the surface, within the volume, and in

various discussion sections) always covers the *J*-integral method first, and then the decomposition method.

Chapters 0, 7, and 8 introduce the *J*-integral based decomposition method starting with displacements on the surface and then in the volume. Chapter 0 introduces and verifies the *J*-integral and decomposition method on the surface using DIC data. However, the same brevity could not be achieved in the volume. Instead, the 3D *J*-integral implementation and testing (Chapter 7) is separate to the decomposition method in the volume (Chapter 8).

To assess the combined methodology developed throughout the thesis, a comprehensive discussion is included. The objective is to assess the suitability of the proposed techniques to perform *in situ* measurements from standard DIC and DVC experiments. This section also contains recommendations for future work and highlights complementary aspects of this work to the existing approaches used by Eskom. Chapter 10 contains the thesis conclusions, which highlight the main achievements and novel contributions to the underlying methods used to achieve the objectives (in section 3.2) of this thesis.

2 Background reading

The following sections introduce deformation measurement using digital images, the extraction of fracture parameters, and mechanical properties. The methods proposed in this thesis do not acquire all the properties necessary to achieve fracture parameter estimation, as discussed in the scope section (section 3.4). Therefore, certain topics – too relevant to omit (e.g. 2.2.4, 2.3) – have been included for a more complete picture.

2.1 Image correlation

Digital Image Correlation (DIC) as referred to in the thesis title, typically refers to 2D images. However, the same principles have been established in 3D both on the surface using multi-camera setups (called stereo-DIC), and in the volume using Digital Volume Correlation (DVC). Note that appart from the dimensional extension, the principles of both DIC and DVC are identicle. Therefore, for simplicity of presentation, the following sections assume 2D deformations (i.e. DIC analysis) as a starting point.

2.1.1 Overview of principles

DIC was first established in the early 1980s as a versatile alternative to traditional extensometry (Peters and Ranson, 1982; Sutton *et al.*, 1983; Chu *et al.*, 1985; Sutton *et al.*, 1986). The method enables the processing of digital images captured both before and after material loading in order to obtain the samples' deformations (Figure 2.1a). Within areas of uniform isotropy, displacements can be obtained from arbitrary selections of pixels, or 'subsets', over the field of view of the sample. The resulting displacement vectors are thus able to occupy the 'full-field'[9]. In practice, users may select parameters (e.g. subset size and

[9] The density of displacements is also limited by the principles found in sampling theory such as the Nyquist-Shannon rate and the photo-detector grid spacing.

spacing) that are optimal for a particular experimental setup, which may be limited in terms of image quality, or computational resources.

The image correlation procedure may be further explained with the example of a pre-cracked compact tension specimen, shown in Figure 2.1a. If the specimen surface is parallel to the camera lens, and if imaging non-linearities can be disregarded (e.g. perspective, lens distortion), calibration of 2D images involves only the scaling of pixels using a direct length-to-pixel ratio. This approach is frequently applied at smaller length scales, such as SEM images (Sutton *et al.*, 2007) or in volumetric imaging (Maire and Withers, 2014). However, it is often the case that imaging non-linearities cause spurious displacements that require removal to improve the accuracy of the displacement fields. To achieve this, an object with a precisely known geometry and high contrast features can be used for calibration. In this thesis, this approach is needed to account for perspective effects in multi-camera (stereo) DIC systems, which typically use a stepped calibration plate marked with a dotted or checkerboard pattern (Schreier *et al.*, 2009). Note that with most calibration strategies, the displacement data is mapped to the co-ordinate system of the calibration plate. In fracture mechanics analysis the convention is to align the co-ordinate axes with the x_1 axis ahead of the crack, the x_2 axis perpendicular to the crack plane and (in 3D problems), the x_3 axis perpendicular to the surface, or tangential to the crack front in the volume[10] (Figure 2.1b - top image).

To illustrate the problem of image motion, consider the function $F(x_i)$, a grey-level image with pixel intensity values at positions x_i. Note that the although images only contain information at the pixel positions, it is assumed that inter-pixel positions can be obtained via interpolation. Therefore, $F(x_i)$ is a continuous scalar function that can be mapped using a displacement field u_i, written as $F(x_i + u_i)$. The subscript i is $i = 1,2$ for 2D images (DIC) but extends to $i = 1,2,3$ for 3D (stereo-DIC or DVC). The task of obtaining the deformation field from a subsequent image F^* of the deformed object can then be derived from the optical flow equation,

$$F(x_i) = F^*(x_i + u_i) \tag{2.1}$$

assuming ideal mapping conditions (constancy of brightness, exact interpolation, etc.). One approach is to select a subset of pixels $\{x_i\}$ with local deformation field $\{u_i\}$. Each subset is referenced to its centre at location P in the reference image (Figure 2.1c). The task is then to determine the local displacement, rotation, and deformation parameters to optimally match each subset from P to their corresponding positions in the deformed image F^* at P^*. This is achieved when the optical flow is satisfied locally within each subset $F(\{x_i\} + \{u_i\}) = F^*(\{x_i\})$ (e.g. between F and F^* in Figure 2.1b). Numerous approaches to solve Equation (2.1) have been proposed, including global methods (see section 2.1.3). An efficient and widely used method to achieve the best match is by linearization of (2.1) and iterative updating of the displacement field $\{u_i\}$ via Newton's method (Yates *et al.*, 2010),

[10] In geometries with curved crack fronts, the axis alignment and mapping of kinematics is often specified within the subsequent fracture mechanics technique. Such a strategy is introduced in Chapter 7 to align with an inclined crack.

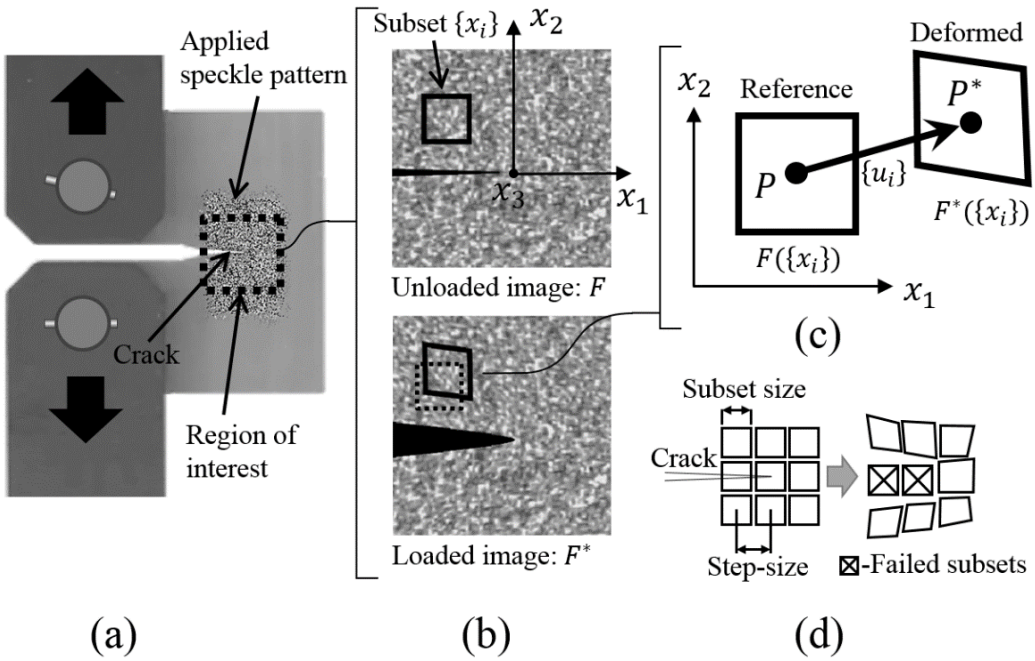

Figure 2.1: (a) Crack sample (CT specimen) loaded in tension, (b) images from before (top) and after (bottom) loading in the crack tip co-ordinate system, used as the reference and deformed configurations respectively on the surface (c) – schematic (d) shows typical subset parameters relative to fracture

$$\{u_i\}^{(n+1)} = \{u_i\}^{(n)} - \left(\frac{F^*(\{x_i\}) - F^{(n)}(\{x_i\})}{\nabla F^*(\{x_i\})}\right) \tag{2.2}$$

where n is the iteration number, ∇ is the first-order gradient of the deformed image, and F is the reference image after the n^{th} deformation $F^{(n)}(\{x_i\}) = F\left(\{x_i\} + \{u_i\}^{(n)}\right)$. The quality of the match can also be determined directly by formulating a correlation criterion, with examples including the sum of square differences, Fourier transform based criteria, and point-wise methods (Jin and Bruck, 2005). A commonly used criterion is the normalized cross-correlation coefficient (C_{NCC}), expressed as,

$$C_{NCC} = \frac{\sum_{ss}[\left(F^* - \bar{F}^*\right)\left(F^{(n)} - \bar{F}^{(n)}\right)]}{\sum_{ss}\{[F^* - \bar{F}^*]^2 \sum_S [F^{(n)} - \bar{F}^{(n)}]^2\}^{\frac{1}{2}}}, \qquad C_{NCC} \in [0,1] \tag{2.3}$$

in which, F^* and $F^{(n)}$ may be optimised globally or over subsets $\{x_i\}$, overbar ($\bar{F}$) indicates a mean pixel intensity, and ss is the domain of the selected subset. When the correlation criterion is defined explicitly (e.g. Equation (2.1)), the DIC method relies on a robust and efficient optimisation algorithm to determine $\{u_i\}$. In the subset based procedure, image matching is repeated on a regular grid resulting in a deformation map of the surface (DIC) or the volume (DVC). In the subset based approach, the user typically optimises the accuracy by adjusting the subset parameters (e.g. the subset size, spacing or overlap shown in Figure 2.1d), to maximise spatial resolution and accuracy, as discussed further in section 2.1.3. A study on stress corrosion cracking mechanisms (loading of a submerged fatigue crack in 3.5 % sodium chloride at 90 °C (Becker *et al.*, 2016)) is shown in Figure 2.2a, to illustrate two limitations of image correlation:

(1) The tracking of features relies on the fidelity and uniqueness of the features across all images captured before and during deformation. Feature fidelity is only considered to be maintained if the contrast patterns of any image can be mapped to match the same feature in all other images of the deformed sample. Such effects are numerous, but are commonly due to damage (e.g. fracture, scratched surface during testing, as shown in Figure 2.2a), foreign particles on the sample or sensor grid, or movement of the sample during image capture.

(2) There is a further requirement for uniqueness of the pattern, often referred to as the correspondence problem. This effect results from repetitive patterns (see Figure 2.2b), such as regular grids of dots, or parallel lines. This results in multiple possible solutions to the pattern matching approach between a reference pattern at position indicated by position P, and a pattern translated and deformed to a new position P^*. This problem can also be linked to low image gradients, as shown in Figure 2.2c.

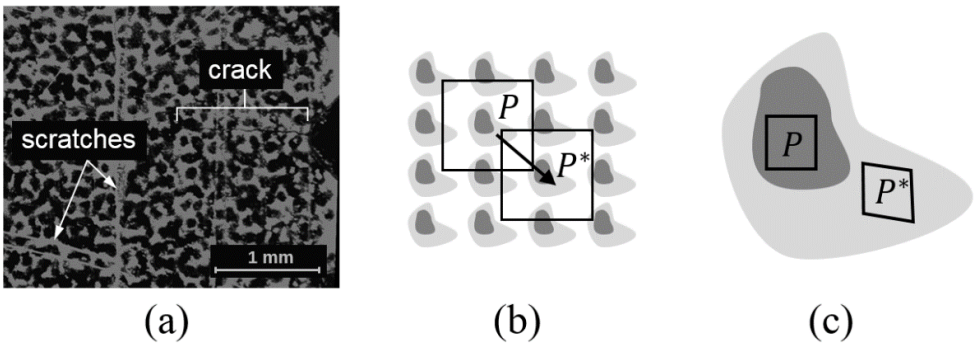

Figure 2.2: Examples of fundamental problems in image matching: (a) loss of pattern fidelity and (b, c) the correspondence problem.
(a) shows an example of stress corrosion cracking in a laser etched sample from (Becker *et al.*, 2016), (b) is a repeating structure and (c) is a textureless deforming structure.

Correspondence errors can be reduced by global optimisers (e.g. genetic algorithms (Jin and Bruck, 2005; Bing and Xie, 2007; Zhao *et al.*, 2012)). However, these approaches are computationally expensive (Pan *et al.*, 2009).

Another approach which achieves greater efficiency and a wider search range is the phase-correlation based approach developed by Chen *et al.* (1993). This performs image matching in the frequency domain, usually calculated by fast Fourier transforms. Due to translation invariance, C_{NCC} correlation values can be determined at each point in $\{x_i\}$ from a single calculation,

$$C_{NCC}(\{x_i\}) = \mathcal{F}^{-1}\frac{\mathcal{F}(F^*(\{x_i\})) \circ \check{\mathcal{F}}(F(\{x_i\}+\{u_i\}))}{\left|\mathcal{F}\left(F^*(\{x_i\})\right) \circ \check{\mathcal{F}}(F(\{x_i\}+\{u_i\})\right|}, C_{NCC} \in [0,1] \qquad (2.4)$$

in which $\circ$ is the entry-wise product[11], $\mathcal{F}$ and $\mathcal{F}^{-1}$ are the forward and inverse discrete Fourier transforms, and $\check{\mathcal{F}}$ is the forward Fourier transform followed by a complex conjugate operation (change of sign of the imaginary part). The division by the complex modulus $|\cdot|$ normalizes the entries in the numerator so that C_{NCC} ranges between $[0,1]$ (zero is no correlation). The displacement is then determined by the location of the peak in $C_{NCC}(\{x_i\})$. With this method, correlation values are only available at pixel locations, and so subpixel accuracy requires interpolation using the neighbourhood of C_{NCC} values, for example the efficient 2×2 method by Foroosh *et al.* (2002). This approach is sensitive to rotation and scaling. However, such parameters can also be determined in a translation invariant manner by first converting the reference and deformed images to log-polar co-ordinates (De Castro and Morandi, 1987; Srinivasa Reddy and Chatterji, 1996). As neither approach solves the entire set of deformation parameters, iterative updating (e.g. switching between log-polar and cartesian) is often used to so that the images may be better aligned by interpolation (as shown by $\{u_i\}$ in Equation (2.4)).

Note that the Fourier transform is also sensitive to non-uniqueness of patterns, particularly if the pattern is periodic (Schreier *et al.*, 2009). These requirements have led to the widespread use of random speckle patterns (e.g. spray paint, or air-brush), when the natural features of the material do not suffice (see example speckle patterns in Figure 2.1 (a) and

[11] Known more formally as the Hadamard product.

(b)), or need to be optimised to improve the accuracy of calculated strains (Bossuyt, 2013). Other aspects of accuracy are related to the image correlation parameters, as discussed in the next section.

2.1.2 Displacement accuracy and spatial resolution

The accuracy and computational efficiency of image correlation is particularly high if image regions exhibit low deformation gradients. This allows the selection of large subsets while maintaining the low order of deformation complexity[12] (usually linear or cubic basis functions are preferred for efficiency). However, a limit is reached when further increases in subset size yield no improvement, or a reduction in accuracy. This occurs when the subset contains deformations that do not belong to the space of shape functions of the subset. Complex deformations are mainly the result of geometric boundaries, damage, complex loading, and various unwanted artifacts (such as the previously discussed pattern errors in Figure 2.2). More formally, the spatial resolution, defined as *the shortest distance between two spatially independent measurements* in (Grédiac and Sur, 2014). Therefore, the spatial resolution is not improved by use of subsets with significant overlaps, but requires a reduction in subset size.

Due to the complexity of deformation, it is challenging to ascertain the true displacement errors from deformation experiments. An effective test for DIC or DVC errors is therefore to rigidly translate the sample (without rotation). It has also been shown that the relationship between subset size (l) and displacement errors is proportional to l^{-1} and $l^{-3/2}$ for DIC (Besnard *et al.*, 2006) and DVC (Leclerc *et al.*, 2011) respectively. However, such relations are difficult to separate from the other parameters linked to the image correlation method (such as interpolation function and length scale). This has been studied by Yaofeng and Pang (2007), and optimised by Li *et al.* (2017).

This dilemma is a pertinent issue in fracture measurements, in which a high accuracy is needed for various approaches to extract fracture parameters (e.g. direct measurements of crack opening displacement, or displacement extrapolation approaches (Lim *et al.*, 1992)). The crack tip fields are discontinuous along the crack faces and asymptotic in gradient as they approach the crack tip, leading to large inaccuracies and failed correlations over the crack region (as shown previously in Figure 2.1d). Reducing the subset size leads to a reduction in accuracy in this region, which is worsened if the nonlinear effects of damage have spread ahead of the crack tip (Pan *et al.*, 2009). Some examples of works which address these issues are the subset-splitting based strategy to enable crack face discontinuities (Poissant and Barthelat, 2010), regularisation to reduce errors in regions of high deformation gradients and continuity (Cofaru *et al.*, 2010; Werlberger *et al.*, 2009), or including analytical crack tip fields in the basis set of the correlation (Besnard *et al.*, 2006; Réthoré, Hild, *et al.*, 2008; Réthoré, Tinnes, *et al.*, 2008). Despite these advancements, such methodologies have yet to become established in commercial image correlation approaches.

2.1.3 Global vs. local approaches to image correlation

The numerous algorithms developed for DIC and DVC are often classified as either local (subset-based), or global in approach. The terms local and global generally refer to whether the displacements are solved in a modular subset-by-subset type approach (local), or within

[12] Complexity may be thought of in these examples as the order of the Taylor expansion needed to accurately fit the underlying displacement field.

a framework which enforces connectivity between neighbouring displacements, usually with the finite element framework (FE-DIC).

Global approaches based on the finite element method can apply h-adaptivity to increase spatial resolution and p-adaptivity when higher order basis functions are required (Wang and Ma, 2014; Wittevrongel *et al.*, 2015), and X-FEM based approaches in fracture cases (Réthoré, Hild, *et al.*, 2008). In local approaches, these improvements are implemented on a per-subset basis, and are therefore programmatically simple (Cofaru *et al.*, 2010; Molteno and Becker, 2014), particularly in handling discontinuities (Poissant and Barthelat, 2010). The accuracy and efficiency of the two methods must be similar because Hild & Roux (2012) reported that global approaches are most accurate, and Wang & Pan (2016) reported the converse to be true. A possible advantage of the global approach is that it allows for direct integration with finite element capabilities. However, it seems that most commercial products[13] and open-source codes[14] are based on the local approach which can be iterative, or phase-correlation based.

2.1.4 Digital volume correlation

DVC is similar to DIC in principle, but less prevalent due to the relative difficulty with which volumetric images are acquired. However, the access to the volume provides a valuable extension to verify mechanics principles with full-field experiments of the volume. As with DIC, DVC involves the acquisition of images with suitable hardware, followed by processing (correlation) of the images to determine the full-field displacement maps.

Digital volumetric imaging with X-rays

Volumetric imaging systems are highly specialised to the desired image characteristics (length scale, resolution, etc), which in turn can significantly affect image correlation. However, the most common forms involve X-rays penetration and measurement. In particular X-ray Computed Tomography, or X-CT is increasingly available due to the versatility of length scales and materials that can be imaged (Maire and Withers, 2014).

X-CT involves the construction of numerous 2D digital radiographs into a 3D image, as illustrated in Figure 2.1. Note that the base units in 3D imaging are voxels, the 3D equivalent to pixels. Digital radiographs are generated by X-rays that travel from the source, penetrate the sample, and are captured on the sensor grid of detectors (also called the scintillator). The variations in X-ray brightness on the detector grid are due to the differences in X-ray absorption in the sample, described by the X-ray absorption co-efficient. This is correlated with variations in the material properties, such as density, or electrical conductivity. Such variations may be visible from the radiographs before reconstruction as shown in Figure 2.3.

[13] e.g. LaVision, www.lavision.de; GOM, www.gom.com (both accessed 19 June 2017)

[14] e.g. www.ncorr.com, www.franck.engin.brown.edu/digital-volume-correlation (both accessed 20 June 2017)

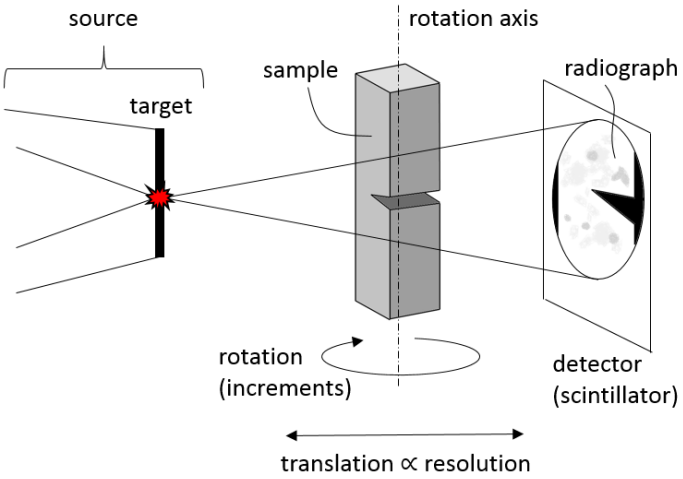

Figure 2.3: Typical laboratory X-CT setup of the source, rotating and translating sample, and detector

The process of computed tomography requires specialised equipment to position the sample so that radiographs can be captured at precise angular increments. The typical laboratory X-CT setup (comprised the X-ray source, translation/rotation stage, and detector) is shown in Figure 2.3. The reconstruction results in a 3D array of voxels at regular grid positions. Note that the voxel positions are defined by the reconstruction algorithm rather than physical grid positions of the sensors on the scintillator. The voxel sizes and positions within the regular grid can also be altered by the relative placement of the sensor, source and sample; wherein movement of the sample close to the target enlarges the image cast on the detector screen.

Deformation measurement

The first 3D image correlation method made use of X-ray radiography (Bay *et al.*, 1999), in which it seems that the term Digital Volume Correlation was first used. Apart from the dimensional extension (x_3 appended to displacement and deformation definitions), DVC is identical to DIC. Similar to the pixel extension to voxels, subsets are extended to subvolumes. Determination of the deformation map between the reference and deformed volumes then proceeds in the same manner by maximising correlation between subsets (see Equation (2.3)). The main differences arise from the more complex processes needed to create high quality 3D images, and the additional computational expense in storing and analysing the data in a timeous manner.

To compute volumetric displacement fields, the same procedure is followed as a DIC experiment. A reference image and a rigid body translation image are captured to ascertain displacement errors, and subsequent images are captured while the sample is under load. This latter aspect also requires specialised equipment, in order to transmit load through the sample while on the X-CT stage, without blocking the X-ray beam. This is usually achieved by a load carrying tube manufactured from material with low X-ray attenuation properties (e.g. PMMA), and a load-cell attachment.

Due to long scan times (typically between 15-45 minutes), and large datasets produced (file sizes between 1-100 GB). The time from experiment to displacement field acquisition that can be expected with DVC is several orders of magnitude greater than DIC. This places importance on the correct estimation of the experimental parameters, of which the following are highlighted:

- A material should be selected that contains natural features which produce suitable contrast patterns for image correlation (i.e. uniqueness).

- Sample and loading rig materials must allow high X-ray penetration.
- The *in situ* loading equipment should not cause large fluctuations in beam energy (e.g. due to parts of the structure exiting the field of view, large density variations, or high aspect ratio components).
- Virtually all testing is limited to the quasi-static regime due to long scan times, these effects may also emerge within a sample if crack propagation occurs during scans.

2.2 Damage and fracture mechanics

The previous sections have explained the processes involved with acquiring displacements from image correlation. This section aims to introduce the topic of fracture: both as a full-field methodology, and in terms of the broader definitions in damage mechanics.

2.2.1 Overview of principles

Damage mechanics is an engineering methodology used to characterise and predict the events leading to fracture – seen as the final stage of damage within the continuum mechanics framework. The progression of damage toward final fracture may be represented by variables that are directly measurable (e.g. porosity or micro-crack density), or inferred from macro-scale measurements (e.g. by estimating constitutive parameters, as elaborated in section 2.3). Damage variables may also be continuous (e.g. material stiffness, or thermal expansion coefficients), or defined at discrete locations such as by fracture parameters (i.e. the stress intensity factors, or energy release rates).

The assumption made in damage studies is that the material is initially in an undamaged or 'pristine' state, and accumulates damage over time due to thermodynamic or environmental forces (e.g. corrosion, loading, irradiation), until the observed damage state is reached. The determination of damage parameters in a particular damage state is often through measurement of the unrecoverable strain energy lost during component operation in severe conditions. Such events are thermodynamically driven from distributed damage toward damage localisations, microscopic crack initiations, and the formation of macroscopic damage such as cracking (Figure 2.4).

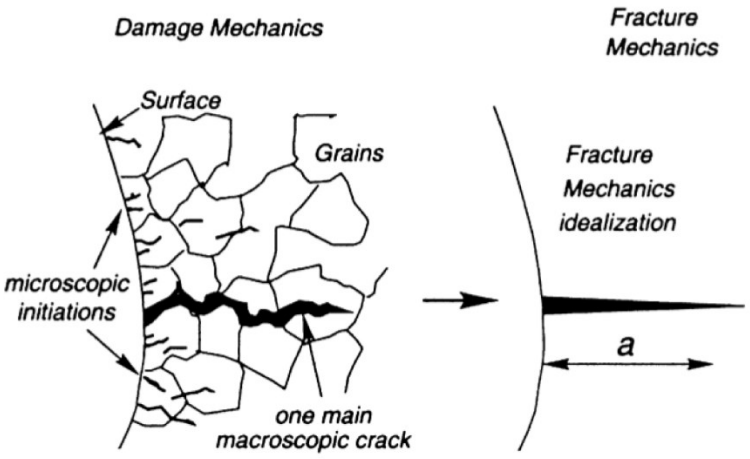

Figure 2.4: The various defect sizes involved in fatigue and the two definitions, from Ref. (Chaboche, 2006)

Although fracture is also described under the damage mechanics framework (e.g. by reduction of local stiffness values to zero), damage mechanics is typically dedicated to diffuse phenomena such as creep or plasticity. As aforementioned, fracture is the basis for most non-destructive detection and structural integrity management programmes for which the main directive is determination of the remaining component life (Scheepers *et al.*, 2010).

The standard approach in LEFM to estimate components life is via the material specific energy release rate from crack extension already introduced as G (section 1.2). This concept finds experimental use as a material specific threshold for fracture, and a theoretical interpretation as the driving force of fracture (Mueller and Maugin, 2002). In the former, material databases for G values in virgin material and various damaged states are widely used to predict and diagnose failures (for example, the British standards for assessing the acceptability of metallic flaws BSI 7910 (2015)). The classical definition for the energy release rate is the change in total strain energy stored in the crack system U per unit of generated crack area A:

$$G = -\frac{dU}{dA} \tag{2.5}$$

Equation (2.5) is the energy criterion for fracture (Griffith, 1921), in which the negative sign accounts for the reduction in energy due to crack growth.

A significant milestone for the application of Equation (2.5) in brittle materials was the discovery by Irwin (1957) that the stress and displacement fields close to a crack tip could be predicted by the stress intensity factor, by which the stress, strain and displacement fields around the crack tip can be directly related to the material fracture resistance. The concept assumes isotropic linear elastic material properties and deformations that are small relative to the crack length and dimensions of the body (otherwise alternative methods apply, e.g. crack opening displacement, or the J-integral). The magnitude of the crack tip stress field for a particular loading could then be defined as,

$$K_I = \lim_{r \to 0} \left(\sigma\sqrt{\pi r}\right) \approx Y\sigma_{ff}\sqrt{\pi a} \tag{2.6}$$

in which σ is the nominal stress perpendicular to the crack plane (i.e. mode I), and r is the radial distance from the crack tip. For structural integrity assessments, the limiting term is approximated by planar conditions near the crack tip, as written in the last term of Equation (2.7). Here, σ_{ff} is the stress of the field far from the crack tip region, and Y is a numerical modifier to account for various crack geometries. This approximation based on the three variables[15] – stress (σ_{ff}), crack length (a), and SIF (K_I) – is the basis for structural integrity evaluations using fracture mechanics.

As with Equation (2.5), this brings the idea of the critical K_I value - termed K_{Ic} - at which the crack propagates. The concept of a critical value for K_I can be applied to each modes of fracture: I, II and III, being the three fundamental loading configurations. The fracture modes can be shown as a result of the analytical crack tip fields resulting from 3D planar deformations derived independently by Irwin (1957) and Williams (1961) and are the: opening mode 'I', in plane sliding mode 'II', and out-of-plane sliding mode, or tearing mode

[15] Also referred to as the 'triangle of integrity'.

'III', as shown in Figure 2.5. The mode (M) is indicated in the subscript of the corresponding stress intensity factors (SIFs) as,

$$K_M = K_{Mc}, \qquad M = I, II, III \tag{2.7}$$

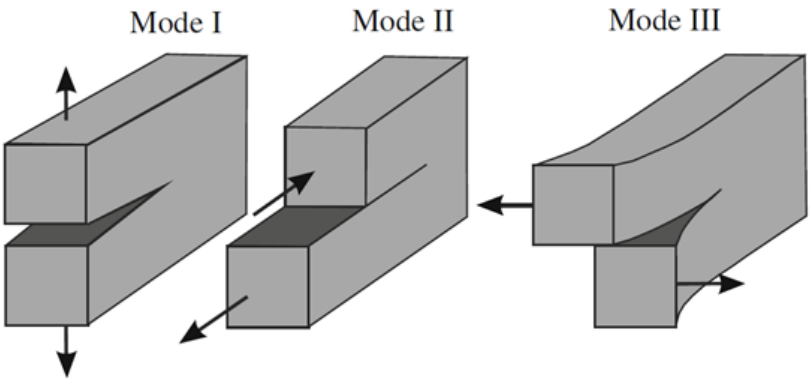

Figure 2.5: Representation of the three fracture modes: opening (mode I), shearing (mode II), and tearing (mode III).
Image from (Kuna, 2013a)

2.2.2 Full-field fracture mechanics

This section directs attention to approaches to extract the aforementioned fracture parameters to predict failure from DIC and DVC displacement data. As discussed in section 2.1.3, the accuracy achievable with image correlation in large contiguous regions is reduced in the presence of high gradient material non-linearities such as plasticity (Rechenmacher, 2006) or fracture (Becker *et al.*, 2012; Sutton *et al.*, 1991). As a result, it is common practice to omit such results – either by masking the images before analysis, or detecting and removing spurious results after correlation (Molteno and Becker, 2015c; Sutton *et al.*, 1992; Chao *et al.*, 1998). Numerous strategies have been proposed that maximise the remaining data with either image (Cinar *et al.*, 2017; Barhli *et al.*, 2017; Barhli *et al.*, 2016).

Typically, the quality of the correlation for each displacement is available directly from the matching algorithm through the correlation coefficient: a value between 0 and 1 – relating to no correlation and perfect correlation respectively[16]. A straightforward approach to remove unreliable data is by thresholding the correlation coefficient to eliminate crack biased data (Helm, 2008). However, due to the non-uniformity of suitable features, and overlapping analysis regions, data may be deleted needlessly. Some previously mentioned approaches propose to improve the robustness of the correlation algorithm to cracking by splitting the subsets (Poissant and Barthelat, 2010), or through the use of numerical frameworks that enable discontinuities such as X-FEM (Réthoré, Hild, *et al.*, 2008), and Peridynamics (Turner, 2014). These effects are compounded by the complex nonlinear deformations due to damage and the resulting nonlinear effects on contrast patterns in the near field (Mostafavi *et al.*, 2013; Mostafavi *et al.*, 2015). Such a region may extend or evolve significantly during the life cycle of a component while in-service (e.g. high thermal and loading profiles).

[16] Some other definitions produce correlation ranges between [-1,1], [0,2].

For these reasons, the emphasis of techniques using DIC and DVC for measurement of G from cracks is generally on the fields remote from the crack front. These, can typically be accurately and efficiently mapped by piecewise and low order deformations. To address this issue, full-field approaches to estimate fracture parameters have been developed as alternatives to approaches that depend on near tip data (e.g. displacement extrapolation method, CTOD measurements).

2.2.3 Computation of energy release rates

Despite the limitations of DIC and DVC in obtaining measurements close to the crack tip (outlined in section 2.1.2), the availability of data in the full-field of the experiment has given rise to several viable approaches to extract SIFs. In analytical form, the SIFs are the coefficients of a series expansion describing the stress and displacement fields surrounding the crack tip (Williams, 1957). The equations can be fitted to experimental data to obtain SIFs, as first shown by McNeil *et al.* (1987). However, a well-known limitation of the field fitting approach is that the singular K_{I-III} displacement fields are only applicable in a singularity dominated region surrounding the crack tip (known as the region of *K*-dominance). Outside of this region other (non-singular or extraneous) fields become dominant (as elaborated in section 2.2.4). Therefore, the applicability to the full-field is limited (Hui and Ruina, 1995). Furthermore, such approaches lose applicability when the nonlinear region ahead of the crack extends beyond the small scale yielding region defined by Irwin (Irwin, 1957), such as ductile plasticity (Réthoré *et al.*, 2005) or quasi-brittle fracture (Becker, 2011).

An alternative approach is the J-integral method. This is an integral of stress, strain and displacement gradients arranged in the tensor format introduced by Eshelby (1975). The integral results in a vector $J^{(k)}$ ($k = 1,2,3$). In elastic fracture, the first term $J^{(1)}$ represents the crack energy release rate *G*. The use of the integral on cracks was first suggested by Rice (1968), with the key result that J values may be calculated on arbitrary contours encircling the crack tip. This property enables statistical averaging of larger areas, and the ability to select data from low order deformation regions far from the crack front. Under the assumption of small scale yielding, SIFs can be related to $J^{(1)}$ with,

$$G = J^{(1)} = J_I + J_{II} + J_{III} \tag{2.8}$$

where,

$$\begin{aligned} J_I &= \frac{(K_I)^2}{E'} \\ J_{II} &= \frac{(K_{II})^2}{E'} \\ J_{III} &= (1+v)\frac{(K_{III})^2}{E} \end{aligned} \tag{2.9}$$

$$E' = \begin{cases} E & \text{for plane stress} \\ \dfrac{E}{1-v^2} & \text{for plane strain,} \end{cases}$$

Note that this work uses the symbol J (rather than G), although under LEFM assumptions they are equivalent. Despite the unique relationship shown by Equation (2.9) between J_M

and K_M $(M = I, II, III)$, Equation (2.8) is underdetermined. One approach to solve Equation (2.8) and thereby obtain SIFs is to compute G_{III} separately using only mode III components in the J-integral, thereby reducing the number of unknowns to two. The next step requires computing the $J^{(2)}$ integral which provides the additional equation needed to decouple K_I and K_{II} (Nikishkov and Atluri, 1987). The problem with this approach is that calculation of $J^{(2)}$ requires crack face integrals in all but a few special cases, pointed out by Herrmann and Herrmann (1981). Some numerical strategies have been proposed by Judt and Ricoeur (2013) to improve the robustness, however, the robustness to experimental errors is unclear. Also, the mode III fields are assumed to be available by some other technique - Judt and Ricoeur (2013) only applied the method to planar problems and Nikishkov and Atluri (1987) used the decomposition method.

Two further approaches are discussed that either directly or implicitly use analytical fields, being the interaction integral approach, and the decomposition method. The interaction integral, introduced by Stern (Stern *et al.*, 1976), uses the Maxwell-Betti reciprocal theorem to decouple the J values into separate SIFs. In this approach, direct use is usually made of the analytical crack tip fields in order to provide physically permissible auxiliary fields (Gosz *et al.*, 1998). Another technique is to separate the crack tip fields into mode I, II and III parts prior to computing J. This can be performed without analytical crack tip fields using the decomposition method proposed by Ishikawa *et al.* (1980). The mode of interest is separated from the other modes by a single symmetry operation - a sum or difference operation on the reflected and non-reflected fields about the crack plane - making the method simpler than the interaction integral to implement. The drawback of the decomposition approach is that fields emanating from other nearby stress sources such as edges or neighbouring cracks can become involved in the symmetry operation resulting in loss of stress equilibrium as discussed by Shivakumar & Raju (1992).

Several authors have already successfully employed the J-integral to extract SIFs from displacement field extracted using DIC or DVC (Becker *et al.*, 2012; Yoneyama *et al.*, 2014; Rannou *et al.*, 2010). In these approaches, the fields required for integration (stresses, strains and displacement gradients tensors) have been computed directly from the experimental displacement data[17] (Yoneyama *et al.*, 2016; Molteno and Becker, 2015c), or calculated within a numerical framework by applying the displacements as boundary conditions (e.g. using FEM (Becker *et al.*, 2012; Rannou *et al.*, 2010)). The J-integral also shows promise in nonlinear experiments as it remains valid under non-linear deformation assumptions as shown in incremental plasticity (Simha *et al.*, 2008) and verified experimentally in elasto-plasticity (Yoneyama *et al.*, 2014).

In brief summary, the J-integral methods introduced above achieve significant computational savings over methods which attempt to model the entire fracture problem by obtaining displacement fields directly from experiments, and only considering the stable region surrounding the crack tip. The method is also extendable to non-linear elastic problems and analysis in the remote fields of the crack.

2.2.4 The field fitting approach

Irwin derived the energy release rate in terms of a single constant that could be used to determine the intensification of the stress field near the crack tip relative to the nominal

[17] As a point of interest, Barhli and co-authors demonstrated a method in which strains extracted directly from neutron diffraction maps were used to calculate J (Barhli *et al.*, 2016)

stress, later termed the stress intensity factor (1957). This approach used an earlier semi-inverse method developed by Westergaard in 1939 to predict stresses ahead of a crack tip (Westergaard, 1939). The same stress distribution was found by Williams, and is usually referred to as the Williams series (Williams, 1957). These derivations express the stress, strain, and displacement fields in terms of the crack tip position, the elastic properties (Young's modulus and Poisson's ratio), and the coefficients of the n terms of the series expansion for modes I, II, and III ($A_{I-III}^{(n)}$),

$$u_1 = \sum_{n=1}^{\infty} \frac{A_I^{(n)}}{2\mu} r^{n/2} \left\{\kappa \cos\frac{n}{2}\theta - \frac{n}{2}\cos\left(\frac{n}{2}-2\right)\theta + \left\{\frac{n}{2}+(-1)^n\right\}\cos\frac{n}{2}\theta\right\}$$

$$-\sum_{n=1}^{\infty} \frac{A_{II}^{(n)}}{2\mu} r^{n/2} \left\{\kappa \sin\frac{n}{2}\theta - \frac{n}{2}\sin\left(\frac{n}{2}-2\right)\theta + \left\{\frac{n}{2}-(-1)^n\right\}\sin\frac{n}{2}\theta\right\} \qquad (2.10)$$

$$u_2 = \sum_{n=1}^{\infty} \frac{A_I^{(n)}}{2\mu} r^{\frac{n}{2}} \left\{\kappa \sin\frac{n}{2}\theta + \frac{n}{2}\sin\left(\frac{n}{2}-2\right)\theta - \left\{\frac{n}{2}+(-1)^n\right\}\sin\frac{n}{2}\theta\right\}$$

$$-\sum_{n=1}^{\infty} \frac{A_{II}^{(n)}}{2\mu} r^{\frac{n}{2}} \left\{-\kappa \cos\frac{n}{2}\theta - \frac{n}{2}\cos\left(\frac{n}{2}-2\right)\theta + \left\{\frac{n}{2}-(-1)^n\right\}\cos\frac{n}{2}\theta\right\} \qquad (2.11)$$

$$u_3 = \sum_{n=1}^{\infty} \frac{A_{III}^{(n)}}{\mu} r^{\frac{n}{2}} \begin{cases} \sin\left(\frac{n}{2}\theta\right) & \text{for } n = 1,3,5,\ldots \\ \cos\left(\frac{n}{2}\theta\right) & \text{for } n = 2,4,6,\ldots \end{cases} \qquad (2.12)$$

with plane stress as $\kappa = \frac{3-v}{1+v}$ and plane strain as $\kappa = 3-4v$, v is Poisson's ratio, μ is the shear modulus, u_1, u_2 and u_3 are the displacement components with respect to r and θ from the crack tip which are the polar co-ordinate positions as indicated by P in Figure 2.6. It is important to note that the equations with the cosine terms are symmetric about the x_1 axis ($P = P'$) and the sine terms are anti-symmetric ($P = -P'$). In fact, these are uniquely related to the $n = 1$ co-efficients $A_M^{(1)}$ ($M = I, II, III$). This is the basis of a method to separate the terms $A_M^{(1)}$ using the decomposition method, discussed further in section 2.2.6.

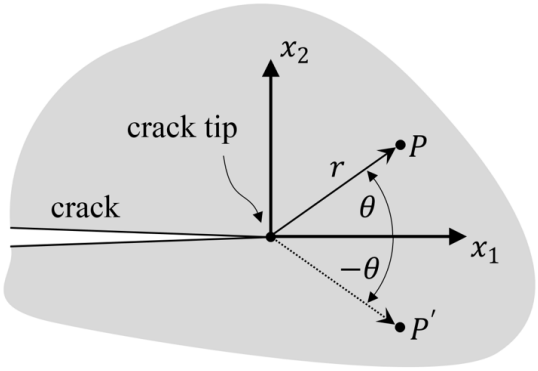

Figure 2.6: Planar crack tip co-ordinate system of point *P*, and reflected point *P'*

Likewise, the stress fields are available using,

$$\sigma_{ij} = \sum_{n=1}^{\infty} A_I^{(n)} f_{I_{ij}}^{(n)}(r,\theta) + \sum_{n=1}^{\infty} A_{II}^{(n)} f_{II_{ij}}^{(n)}(r,\theta) + \sum_{n=1}^{\infty} A_{III}^{(n)} f_{III_{ij}}^{(n)}(r,\theta) \tag{2.13}$$

in which $f_{I-III_{ij}}^{(n)}$ is a polar function described by,

$$f_{I_{11}}^{(n)} = \frac{n}{2}\left[\left(+2+\frac{n}{2}+(-1)^n\right)\cos\left(\left(\frac{n}{2}-1\right)\theta\right) - \left(\frac{n}{2}-1\right)\cos\left(\left(\frac{n}{2}-3\right)\theta\right)\right] \tag{2.14}$$

$$f_{II_{11}}^{(n)} = \frac{n}{2}\left[\left(-2-\frac{n}{2}+(-1)^n\right)\sin\left(\left(\frac{n}{2}-1\right)\theta\right) + \left(\frac{n}{2}-1\right)\sin\left(\left(\frac{n}{2}-3\right)\theta\right)\right] \tag{2.15}$$

$$f_{III_{13}}^{(n)} = r^{\left(\frac{n}{2}-1\right)}\frac{n}{2}\begin{cases}\sin\left(\left(\frac{n}{2}-1\right)\theta\right) \text{ for } n = 1,3,5,\ldots \\ \cos\left(\left(\frac{n}{2}-1\right)\theta\right) \text{ for } n = 2,4,6,\ldots\end{cases} \tag{2.16}$$

$$f_{III_{23}}^{(n)} = r^{\left(\frac{n}{2}-1\right)}\frac{n}{2}\begin{cases}\cos\left(\left(\frac{n}{2}-1\right)\theta\right) \text{ for } n = 1,3,5,\ldots \\ -\sin\left(\left(\frac{n}{2}-1\right)\theta\right) \text{ for } n = 2,4,6,\ldots\end{cases} \tag{2.17}$$

$$f_{I_{22}}^{(n)} = \frac{n}{2}\left[\left(+2 - \frac{n}{2} - (-1)^n\right)\cos\left(\left(\frac{n}{2}-1\right)\theta\right) + \left(\frac{n}{2}-1\right)\cos\left(\left(\frac{n}{2}-3\right)\theta\right)\right] \tag{2.18}$$

$$f_{II_{22}}^{(n)} = \frac{n}{2}\left[\left(-2 + \frac{n}{2} - (-1)^n\right)\sin\left(\left(\frac{n}{2}-1\right)\theta\right) + \left(\frac{n}{2}-1\right)\sin\left(\left(\frac{n}{2}-3\right)\theta\right)\right] \tag{2.19}$$

$$f_{I_{12}}^{(n)} = \frac{n}{2}\left[-\left(\frac{n}{2} + (-1)^n\right)\sin\left(\left(\frac{n}{2}-1\right)\theta\right) + \left(\frac{n}{2}-1\right)\sin\left(\left(\frac{n}{2}-3\right)\theta\right)\right] \tag{2.20}$$

$$f_{II_{12}}^{(n)} = \frac{n}{2}\left[-\left(\frac{n}{2} - (-1)^n\right)\cos\left(\left(\frac{n}{2}-1\right)\theta\right) + \left(\frac{n}{2}-1\right)\cos\left(\left(\frac{n}{2}-3\right)\theta\right)\right] \tag{2.21}$$

Note again, that sine and cosine terms conveniently group according to modes in the same manner as the displacements. The stress intensity factor concept is related to the $n = 1$ terms of the series expansion, as these are the only singular terms in Equation (2.13). Irwin showed that A_{I_1}, A_{II_1} and A_{III_1} relate to the mode I, mode II and III stress intensity factors K_I, K_{II} and K_{III} as,

$$A_I^{(1)} = \frac{K_I}{\sqrt{2\pi}} \;;\; A_{II}^{(1)} = -\frac{K_{II}}{\sqrt{2\pi}};\; A_{III}^{(1)} = \frac{K_{III}}{\sqrt{\pi/2}} \tag{2.22}$$

the higher order terms for each mode M ($A_M^{(2)}, A_M^{(3)} \ldots A_M^{(n)}$) dominate at increasing distances from the crack tip[18] with increasing n. As a result, experiments close the crack tip do not require higher order terms, as demonstrated by McNeill *et al.* with up to $n = 48$, with no noticeable improvement in error. However, these terms can be useful at larger radial distances to accommodate for geometric effects to improve the accuracy of the $n = 1$ terms (Yoneyama *et al.*, 2007). Henninger *et al.* have shown that decreasing values of n ($n < 1$, so-called 'super-singular' terms) can be used to describe limited elasto-plastic deformation in the crack tip region in certain materials (2010). These terms have been ignored in most other works as the energy density is not defined (Kanninen and Popelar, 1986).

Use of the above equations to obtain SIFs involves an optimisation procedure to obtain the best match between the analytical crack tip displacement fields (Equations (2.10) - (2.12)) and the experimental data. The procedure was first applied to DIC data by McNeill *et al.* (McNeill *et al.*, 1987), whose approach was simple. Only mode I was considered, and the approximate crack tip position was assumed to be known in advance. As a result, the SIFs could be determined using linear least-squares. However, misplacement of the fields results

[18] Other than the T-stress, which is related to the $A_I^{(2)}$ (by a factor 4), Kuna (2013).

in errors in the estimated SIFs (Yoneyama *et al.*, 2007). Furthermore, the precise location of the crack tip may be obscured by the spatial resolution of the subsets used in image correlation, and surrounding data may contain errors. Some authors have addressed the 'smeared' errors by excluding them from the analysis (McNeill *et al.*, 1987; Yoneyama *et al.*, 2007). In particular, Yoneyama and various different co-authors have developed methods which address crack tip position uncertainty and mixed-mode I-II loading (Yoneyama *et al.*, 2006; Yoneyama *et al.*, 2007; Yoneyama *et al.*, 2014). Notably, it was found by (Hamam *et al.*, 2007)

An advantage of this approach is that analytical fields may be fitted directly to experimental displacement fields without computing mesh parameters or stresses, and it naturally extends to mixed-mode applications. This approach has been extended to non-homogenous materials[19] (Abanto-Bueno and Lambros, 2002; Méité *et al.*, 2013) and small scale-plasticity with the aforementioned methods of Réthoré and Roux using super-singular displacement field (2011), and Yoneyama *et al.* using elastoplastic displacement fields (2014), known as the HRR fields due to the innovators Hutchinson (1968), Rice, and Rosengren (1968). Acquisition of SIFs from the full range of modes (I-III) SIFs by fitting mixed $K_{I\text{-}III}$ crack tip fields has been implemented by Réthoré *et al.* (2005), and developed into an integrated image correlation approach (I-DIC)[20] by Roux and Hild (2006).

2.2.5 The *J*-integral

The *J*-integral has proven to be an invaluable tool to obtain strain energy release rates in both linear and non-linear fracture mechanics. The method is computationally efficient (Shih *et al.*, 1986), and facilitates the prediction of crack growth initiation in materials that exceed their elastic limits (under conditions such as *K*-dominance and monotonic loading, see (Hutchinson, 1983)). The concept was first introduced by Cherepanov (1967) and Rice (1968) as a 2D line integral with the property that all contours surrounding a notch or crack tip provide the same value for J, i.e. *J* contour-independence. This property is frequently the motivation for use of the *J*-integral due to the tendency for data near the crack tip to be less accurate in experimental and numerical methods. Significant developments in this area include efficient implementations in the finite element (Shih *et al.*, 1986), extended finite element (Rannou *et al.*, 2010), and boundary element frameworks (Rigby and Aliabadi, 1993), and certain mesh independent strategies (Nikishkov *et al.*, 2016; Červenka and Saouma, 1997).

Contour independence is particularly relevant to avoid crack tip errors due to optical measurement with image correlation, as achieved on the material surface (Hild and Roux, 2006a) and within the volume (Rannou *et al.*, 2010). Becker *et al.* (2012) evaluated the *J*-integral directly from DIC results using the finite element framework, in which DIC displacements were used to constrain nodes directly. The method enforces continuity between elements, and provides accuracy through the equivalent domain integral implementation of *J*-integral. Yoneyama *et al.* (2014) showed that elastic-plastic stresses could be calculated at DIC control points by direct inversion of the deformation plasticity equations, and applied this approach using both the line and domain integral forms, and

[19] Using the relation that crack tip stress fields are consistent between homogenous and non-homogenous materials.

[20] Optimisation of the analytical displacement field *K* factors for pixel mapping to match image data directly as opposed to fitting to DIC obtained displacement data.

elasto-plastic HRR (Hutchinson-Rice-Rosengren (Hutchinson, 1968; Rice and Rosengren, 1968)) field fitting methods finding close agreement between these methods.

The general form of the J-integral given in Equation (2.23) can be defined in the crack co-ordinate system (Figure 2.7) as shown by Blackburn (1972),

$$J^k(\mathrm{s}) = \lim_{\Gamma \to 0} \int_{\Gamma} \left(W n_1 - \sigma_{ij} \frac{\partial u_i}{\partial x_k} n_j \right) \mathrm{d}\Gamma, \quad (i,j,k = 1,2,3) \tag{2.23}$$

in which Γ is the contour path in the x_1, x_2 proceeding in the clock-wise direction, n_i is the outward unit normal (Figure 2.7), W is the strain energy density, σ_{ij} is the Cauchy stress tensor and u_i the displacement fields. The above terms are defined in the following section. Note that Equation (2.23) is only truly achieved when approached as the path integral contour size is reduced to zero – Equation (2.23) and Figure 2.7. This is precisely where DIC and DVC data is least reliable, and therefore alternate forms are necessary.

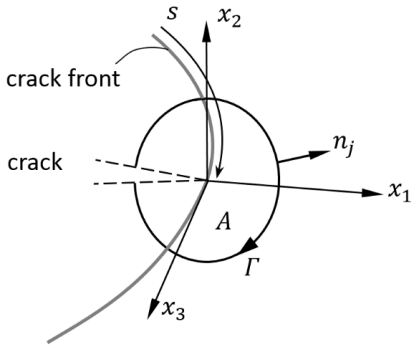

Figure 2.7: J path integral with contour (Γ) looping the crack front, and local co-ordinate system (x_i) at crack front position s

The integral forms presented in the following sections are derived from Equation (2.23), leading to the path-area integral, and the volume integral. It can be found that the 2D use of Equation (2.23) is easily realised by imposing planar (2D) assumptions on (2.23). This approach is also applied in the following sections as it is more concise to derive the general 3D case first (i.e. the volume form), and then reduce each case to the classical 2D forms (i.e. plane stress and plane strain). For reference in the following sections, the integral forms and their original authors are summarised in Table 2.1. Note that the following derivations are the background reading for Chapter 5.

Table 2.1: Summary of J-integral forms and original developers

Dim.	**original integral**	**equivalent domain integral**
2D	line (Rice, 1968)	area (Li et al., 1985)
3D	path-area (Blackburn, 1972)	-
3D	path (Blackburn, 1972)	volume (Shih et al., 1986)

Derivation of the path-area and line integrals

The following derivation of the J-integral develops from Eshelby's energy momentum tensor for elastic homogenous materials (Eshelby, 1975) using Noether's theorem as shown by (Knowles and Sternberg, 1972). For an extension to non-homogenous materials, see the work of Eischen (1987). The strain energy density of a homogenous elastic body can be defined by the function,

$$W = W(\varepsilon_{ij}) = \int_0^{\varepsilon_{ij}} \sigma_{ij} \mathrm{d}\varepsilon_{ij}, \text{ with } \sigma_{ij} = \frac{\partial W}{\varepsilon_{ij}} \ (i,j,k = 1,2,3) \tag{2.24}$$

where σ_{ij} and ε_{ij} are the stress and strain tensors fields in the domain described by a co-ordinate system x_i. The strain tensor is defined with components under infinitesimal strain assumption,

$$\varepsilon_{ij} = \frac{1}{2}(u_{i,j} + u_{j,i}) \tag{2.25}$$

in which the ',' followed by an index denotes a derivative by that index with respect to co-ordinates x_i. The stress components of an isotropic linear elastic material can then be written as

$$\sigma_{ij} = \frac{E}{1+v}\left[\varepsilon_{ij} + \frac{v}{1-2v}\varepsilon_{kk}\delta_{ij}\right] \tag{2.26}$$

Where E and v are the Young's modulus and Poisson's ratio respectively, and δ_{ij} is the Kronecker-delta. As per fracture mechanics convention, the co-ordinate system is chosen at a location on the crack front with x_1 perpendicular to the crack front, x_2 perpendicular to the crack plane, and x_3 tangential to the crack front. Differentiating the strain energy density with respect to x_k gives,

$$\frac{\partial W}{\partial x_k} = \sigma_{ij}\frac{\partial \varepsilon_{ij}}{\partial x_k} \tag{2.27}$$

Substituting the strain definition in Equation (2.25) gives,

$$\frac{\partial W}{\partial x_k} = \frac{1}{2}\sigma_{ij}\left(\frac{\partial u_{i,j}}{\partial x_k} + \frac{\partial u_{j,i}}{\partial x_k}\right) \tag{2.28}$$

As shown by Rice (1968), applying the chain rule gives,

$$\frac{\partial}{\partial x_j}\left(\sigma_{ij}\frac{\partial u_i}{\partial x_k}\right) = \sigma_{ij}\frac{\partial u_{i,j}}{\partial x_k} + \frac{\partial \sigma_{ij}}{\partial x_j}\frac{\partial u_i}{\partial x_k} \tag{2.29}$$

Due to stress equilibrium, the absence of body forces and under static conditions, the second term in Equation (2.29) is zero, therefore,

$$\sigma_{ij}\frac{\partial u_{i,j}}{\partial x_k} = \frac{\partial}{\partial x_j}\left(\sigma_{ij}\frac{\partial u_i}{\partial x_k}\right), \quad \text{and} \quad \sigma_{ji}\frac{\partial u_{j,i}}{\partial x_k} = \frac{\partial}{\partial x_i}\left(\sigma_{ji}\frac{\partial u_j}{\partial x_k}\right) \tag{2.30}$$

Substituting the right-hand-side of Equation (2.30) into (2.28) gives,

$$\frac{\partial W}{\partial x_k} - \frac{\partial}{\partial x_j}\left(\sigma_{ij}\frac{\partial u_i}{\partial x_k}\right) = 0 \tag{2.31}$$

due to the equilibrium of moments ($\sigma_{ij} = \sigma_{ji}$). Rearranging Equation (2.31) reveals it as the divergence of the energy momentum tensor P_{ij}, which is zero in the absence of material discontinuities (Eshelby, 1975),

$$\frac{\partial}{\partial x_j}\left(W\delta_{kj} - \sigma_{ij}\frac{\partial u_i}{\partial x_k}\right) = \frac{\partial P_{kj}}{\partial x_j} = 0 \tag{2.32}$$

where δ_{kj} is the Kronecker delta. Recall that all terms of Equation (2.32) are defined in terms of the crack co-ordinate system shown in Figure 2.8. To represent Equation (2.32) in J-integral form, consider the area A bounded by the contour Γ, on a 2D cross-section of the crack front defined by the plane perpendicular to the crack front (i.e. $x_3 = 0$) at position s as shown in Figure 2.8. Γ_1 and Γ_0 are the inner and outer boundaries with normal n_j, and Γ^+ and Γ^- are the contour segments on the upper and lower crack faces.

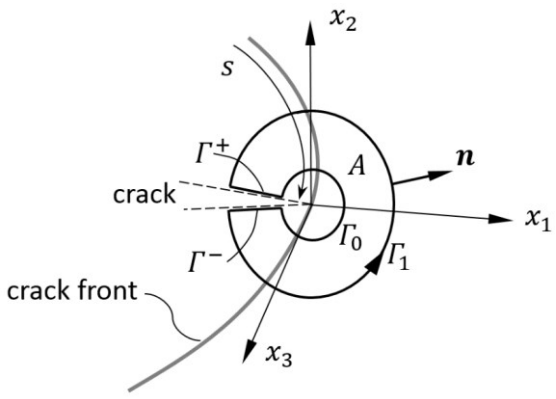

Figure 2.8: J-integral contour Γ, and local crack co-ordinate system x_j

Integrating $\partial P_{kj}/\partial x_j$ in Equation (2.32) within A results in,

$$J^{(k)} = \int_{A(\Gamma_1-\Gamma_0)} \frac{\partial}{\partial x_j}\left(W\delta_{kj} - \sigma_{ij}\frac{\partial u_i}{\partial x_k}\right)\mathrm{dA} \quad (i,j,k = 1,2,3) \tag{2.33}$$

Note at this point that the usual derivation by Rice (1968), is equivalent but this expression is generated by assuming crack advance in the x_1 direction, and energy balance between strain energy and tractions on the boundary. In this derivation, this is implied by the choice of co-ordinate system which is aligned with the x_1 axis in the assumed crack propagation direction, then selecting the $J^{(1)}$ component (shown below, see the step between Equations (2.36) and (2.37)).

The divergence theorem is given for any two fields α and β as,

$$\int_\Gamma (\alpha n_1 - \beta n_2)\mathrm{d}\Gamma = \int_A \left(\frac{\partial \beta}{\partial x_1} - \frac{\partial \alpha}{\partial x_2}\right)\mathrm{dA} \tag{2.34}$$

Since $dx_1 = n_2 d\Gamma$, and $dx_2 = n_1 d\Gamma$. Application of the divergence theorem to Equation (2.33) gives,

$$\int_{\Gamma_1} \left(W n_k - \sigma_{ij} \frac{\partial u_i}{\partial x_k} \right) d\Gamma - \int_A \frac{\partial}{\partial x_3} \left(\sigma_{i3} \frac{\partial u_i}{\partial x_k} \right) dA = 0 \tag{2.35}$$

in which the second term on the left-hand-side results from rearranging the terms, see (Rigby and Aliabadi, 1998; Amestoy *et al.*, 1981; Blackburn, 1972). Noting that $\Gamma = \Gamma_1 + \Gamma_0 + \Gamma^+ + \Gamma^-$ enables reordereing of Equation (2.33) as,

$$\begin{aligned} &\int_{\Gamma+\Gamma^+ +\Gamma^-} \left(W n_k - \sigma_{ij} \frac{\partial u_i}{\partial x_k} \right) d\Gamma - \int_{A(\Gamma)} \frac{\partial}{\partial x_3} \left(\sigma_{i3} \frac{\partial u_i}{\partial x_k} \right) dA \\ &= - \int_{\Gamma_0} \left(W n_k - \sigma_{ij} \frac{\partial u_i}{\partial x_k} \right) d\Gamma - \int_{A(\Gamma_0)} \frac{\partial}{\partial x_3} \left(\sigma_{i3} \frac{\partial u_i}{\partial x_k} \right) dA \end{aligned} \tag{2.36}$$

Then as Γ_0 tends toward the crack front, the area term on the right-hand side tends toward zero, as shown in (Dodds and Read, 1990). Then setting k=1, the crack front J-integral can be defined as,

$$J_{pa}(s) = J_p + J_a$$

$$\int_{\Gamma^*} \left(W \delta_{kj} - \sigma_{ij} \frac{\partial u_i}{\partial x_k} \right) d\Gamma - \int_A \frac{\partial}{\partial x_3} \left(\sigma_{i3} \frac{\partial u_i}{\partial x_k} \right) dA \, , (i,j,k = 1,2,3) \tag{2.37}$$

in which Γ^* is the same as Γ_0 but proceeds in the counter-clockwise direction, and the area A is the entire enclosed area (Figure 2.9a). Equation (2.37) is the path-area integral J_{pa} (sometimes called J_{xl} (Omer and Yosibash, 2005; Giner *et al.*, 2010) or the disk integral (Kuna, 2013b)).

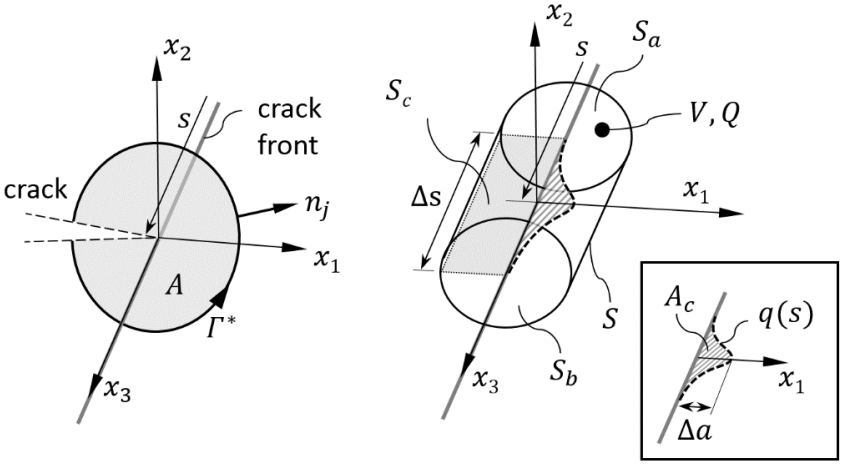

Path-area integral (a)

Volume integral (b)

Figure 2.9: (a) J path integral with contour (Γ) looping the crack front, and local co-ordinate system (x_i), (b) the virtual crack front extension $q(s)$, inset shows the crack extension area A_c, and Δa, the maximum q value on Δs.

Then Rice's classical 2D J-integral (1968) can be easily shown by dropping the second term in Equation (2.37) due to plane strain or plane stress conditions,

$$J = \int_{\Gamma} \left(W n_1 - \sigma_{ij} \frac{\partial u_i}{\partial x_1} \right) \mathrm{d}\Gamma \tag{2.38}$$

Note that the superscript $k = 1$ is implied if omitted, and that Γ proceeds in the counter-clockwise from Γ^* in Equation (2.37). Note also that usually k is subscripted (e.g. J_k), but in this project subscripts are used to denote the mode numbers I-III (i.e. J^k_{I-III}), to be consistent with standard SIF notation (e.g. K_{II}, K_{Ic}, etc).

Equivalent domain integrals: the volume and area integrals

Equations (2.38) and (2.37) can be used to extract J from 2D and 3D problems respectively. However, these forms are not as numerically robust as the equivalent domain integral forms for 2D and 3D (Li *et al.*, 1985). This approach transforms the 2D path integral into the area integral, and the 3D path integral into the volume integral (Table 2.1). Notably, the latter case avoids integration of the second term in Equation (2.37), which involves derivatives of stress close to the crack front (Giner *et al.*, 2010).

A more numerically stable result than the path-area integral can be obtained by assuming a 3D virtual crack extension along a crack front segment Δs, shown in Figure 2.9b. The procedure, introduced in (deLorenzi, 1982; Shih *et al.*, 1986) is briefly described here. The J-integral is based on an infinitesimal virtual crack extension vector Δa_i, $i = 1, 2, 3$. Δa_i is again aligned with the x_1 axis, and therefore is written in scalar form Δa (i.e. with $i = 1$), as shown in the inset of Figure 2.9b. The crack front is assumed to be approximately straight over the distance Δs, otherwise it would be important to continue assuming vector valued crack extensions (Shih *et al.*, 1986). The crack front function $q(s)$ is introduced that is zero outside the arc of interest Δs and defines the virtual crack extension area within Δs as $A_c = \int_{\Delta s} q(s) ds$. Considering the volume V enclosed by end-caps S_a and S_b, outer surface S, and the crack faces S_c, the virtual crack extension field Q is defined as equal to $q(s)$ on the crack front, zero on S_a, S_b and S, and is arbitrary and differentiable within V (Figure 2.9b).

Pre-multiplying Equation (2.23) by Q and applying the divergence theorem gives Equation (2.39): the classical volume integral (J_{vol}) for quasi-static planar straight cracks in isotropic materials (for detailed procedure, see (Shih *et al.*, 1986))

$$J_{vol}(\mathrm{s}) = \frac{1}{A_c} \int_V \left(\sigma_{ij} \frac{\partial u_i}{\partial x_1} - W \delta_{1j} \right) \frac{\partial Q}{\partial x_j} \mathrm{d}V, \quad (i,j = 1,2,3) \tag{2.39}$$

where δ_{1j} is the Kronecker delta (Anderson, 2005), in which Q has the constraints of the conventional crack extension function (deLorenzi, 1982; Shih *et al.*, 1986):

$$Q = \begin{cases} 0 & \text{on } S_a, S_b, S_1 \\ q(s) & \text{on crack front} \end{cases} \tag{2.40}$$

referring to the end-caps (S_a, S_b) and outer surface S_1 shown in Figure 2.9b.

Then the domain integral of (Li *et al.*, 1985), can be shown by noting that gradients of Q, the virtual crack extension in the x_3 direction are zero in plane strain or plane stress conditions, resulting in the classical area integral:

$$J = \int_A \left(\sigma_{ij} \frac{\partial u_i}{\partial x_1} \frac{\partial Q}{\partial x_j} - W \frac{\partial Q}{\partial x_1} \right) dA, \quad (i,j = 1,2) \tag{2.41}$$

in this case, the Q function is a planar cross-section of the 3D case in the plane of constant x_3. The 2D forms are elaborated in Chapter 0, in which the 2D form for Q is also formally presented (Figure 6.2).

The advantage of the volume integral is that the integrand does not contain derivatives of stress (as in the path-area integral, see the J_p term in Equation (2.37). The disadvantages are that the Q function requires accurate placement on the crack front position so that A_c can be determined for a suitable arc-weighted value. It should also be noted that no domain integral form exists for the path-area integral, as shown by Table 2.1. These matters are addressed in Chapter 5.

2.2.6 The decomposition method

J calculated from any of the forms above (e.g. Equations (2.37) or (2.38)) is related to G (Equation (2.5)) in linear or non-linear materials (Anderson, 2005). This is in turn expressed by Equation (2.8) as the summation of separate modal components I-III. The various methods to calculate the separate modal components for J or K have been presented in section 2.2.3, including the interaction integral, the decomposition method, and the direct approach. This section specifically presents the decomposition method.

To illustrate the method, consider the set of kinematic fields required to calculate J, i.e. stresses, strains, and displacements (see Equation (2.38)). If all field quantities associated with two of the three modes can be removed prior to the computation of J (e.g. II and III), then ordinary application of the J-integral calculates the remaining J component (i.e. J_I). This is a direct result of the superposition of the modal J values expressed in Equation (2.8). Ishikawa *et al.* proposed that the separation can be conducted by separation of the symmetric and antisymmetric fields about the crack plane (1980).

The decompositions for crack tip displacements (u_{crack}) are (Shivakumar and Raju, 1992; Huber *et al.*, 1993; Nikishkov and Atluri, 1987),

$$\begin{aligned} u_{crack} &= \sum_{M=I}^{III} u_M = \{u_I\} + \{u_{II}\} + \{u_{III}\} \\ &= \begin{Bmatrix} u_1 \\ u_2 \\ u_3 \end{Bmatrix} = \frac{1}{2} \begin{Bmatrix} u_1 + u_1' \\ u_2 - u_2' \\ u_3 + u_3' \end{Bmatrix} + \frac{1}{2} \begin{Bmatrix} u_1 - u_1' \\ u_2 + u_2' \\ 0 \end{Bmatrix} + \frac{1}{2} \begin{Bmatrix} 0 \\ 0 \\ u_3 - u_3' \end{Bmatrix} \end{aligned} \tag{2.42}$$

and the crack tip stresses (σ_{crack}) (Rigby and Aliabadi, 1998),

$$\sigma_{crack} = \sum_{M=I}^{III} \sigma_M = \{\sigma_I\} + \{\sigma_{II}\} + \{\sigma_{III}\}$$

$$= \frac{1}{2}\begin{Bmatrix} \sigma_{11} + \sigma'_{11} \\ \sigma_{12} - \sigma'_{12} \\ \sigma_{13} + \sigma'_{13} \\ \sigma_{22} + \sigma'_{22} \\ \sigma_{23} - \sigma'_{23} \\ \sigma_{33} + \sigma'_{33} \end{Bmatrix} + \frac{1}{2}\begin{Bmatrix} \sigma_{11} - \sigma'_{11} \\ \sigma_{12} + \sigma'_{12} \\ 0 \\ \sigma_{22} - \sigma'_{22} \\ 0 \\ \sigma_{33} - \sigma'_{33} \end{Bmatrix} + \frac{1}{2}\begin{Bmatrix} 0 \\ 0 \\ \sigma_{13} - \sigma'_{13} \\ 0 \\ \sigma_{23} + \sigma'_{23} \\ 0 \end{Bmatrix} \quad (2.15)$$

in which the notation u'_i or σ'_{ij} denotes a field that has been reflected about the crack plane (e.g. $u'_i = u(x_1, -x_2)_i$), in the local co-ordinate system of the crack front shown in Figure 2.8. In polar co-ordinates, this refers to the reflection of the point P to P' in Figure 2.6. It is important to note that these symmetry operations imply planar fields, as they are derived from their analytical forms: Equations (2.10) - (2.21) which are planar (Huber *et al.*, 1993). The history and implications of the 3D approach are further discussed in Chapter 8, as decomposition of 3D fields yields some interesting attributes.

Assuming that stresses are linear elastic functions of strain, the mode I-III J-integral may be expressed by application of Equations (2.37) or (2.38) to the decomposed displacement field components u_{M_i} ($M = \mathrm{I} - \mathrm{III}$).

$$J_M = \int_\Gamma \left(W_M n_1 - \sigma_{M_{ij}} \frac{\partial u_{M_i}}{\partial x_1} n_j \right) \mathrm{d}\Gamma \quad (i,j = 1,2,3) \quad (2.15)$$

In which the decomposed strain, stress, and strain energy can be obtained for planar problems (2D) using decomposed displacements using Equations (2.25), (2.26) and (2.27). It has been shown that direct separation as proposed here (Equation (2.19)) does not result in contour independent results for J_{II} and J_{III} (Rigby and Aliabadi, 1998; Rigby and Aliabadi, 1993). For this reason, the decomposition method in the volume is more involved than is presented here, and is developed further in Chapter 8 (particularly section 8.2 if the historical perspectives are of interest).

2.3 Extracting material properties from displacements

The previous sections have discussed the development of damage toward fracture, and introduced several full-field methods to measure fracture parameters (e.g. J and K concepts, degradation in E). However, many of the above methods rely on prior knowledge of the material properties, whether for calculation of stresses of initialisation of field fitting methods. For such approaches, the material properties of the virgin (as manufactured) material are may be unreliable in the observed state due to accumulated damage. Direct determination of the material properties at the time of measurement requires so called inverse methods, a broad field concerned with the identification of system parameters from observed results. The techniques span many disciplines, including electromagnetics, acoustics, heat conduction, and even medicine and finance. This thesis uses the linear elastic fracture mechanics framework and therefore this section focuses only on the extraction of elastic parameters. However, creep and plasticity are also key concerns to the motivation for this

project (and Eskom) to which some adjacent projects have been dedicated (Bezuidenhout, 2010; Huchzermeyer, 2017; van Rooyen, 2016).

Approaches discussed thus far to determine the state of a material have been directed toward measuring and understanding the deformed state of a material (e.g. FEM, DIC, DVC), from the boundary constraints in the reference (undeformed) state. This is the so-called 'forward' problem. The reversal of this process to estimate the model parameters from the deformed state is hence referred to as the 'inverse' problem.

Prior to the advent of full-field imaging, solution of the inverse problem required precise models to capture the component geometry due to the limitation of the measurement techniques to sample at discrete locations, e.g. with strain gauges. The small number of measurements results in numerical instability, referred to as ill-posedness, in which multiple permissible solutions are accepted by the algorithm as solutions to the inverse problem. Such experiments required significant foresight from the experimentalist to design problem domains and suitable regularisation procedures to ensure uniqueness of the solutions.

In these ways, full-field measurements have greatly assisted with inverse parameter identification in experimental mechanics by providing direct access to the materials geometry and deformation fields in situ. This is a highly complementary branch of techniques to the work of this thesis despite not being one of the objectives (listed in section 3.2). This section is brief and so the reader is referred to the work of Avril *et al.* (2008) for a more detailed review.

2.3.1 Optimisation based approaches

Solution of the inverse problem can be framed as a balance between externally applied work, e.g. due to boundary forces and displacements; and the stored internal strain energy due to observed deformations and the constitutive parameters. These relations are summarised in Table 2.2.

Table 2.2: Information assumed to be available in the inverse problem

Known	**Unknown**
Geometry	Constitutive parameters, e.g. E, v
Applied external energy, $U_{ext}(f, u)$	Internal energy, $U_{int}(\sigma, \varepsilon)$
Constitutive equations	Dissipated energy

The same efficient numerical solutions for the forward problem (e.g. direct inversion of the finite element stiffness matrix), are not in general possible for the inverse problem, and therefore specialised methods to minimise errors between the experimental measurements and the model are required. This approach is often applied by updating the finite element model to achieve the closest match with the measured displacements by digital image correlation, a procedure known as model updating. A common implementation is finite element method updating (FEM-U) (Ruybalid *et al.*, 2017; Weng *et al.*, 2011; Wang *et al.*, 2011; Jafarkhani and Masri, 2011). Note that the field fitting approach can be defined in a similar manner as the displacement fields are analytical solutions to idealised crack problems, and so similar approaches have been attempted to obtain material properties in linear elastic problems using the Williams series expansion (Huchzermeyer, 2017).

2.3.2 The virtual field method

The virtual fields method is an approach which extracts material parameters based on the principle of virtual work. The 'virtual fields' are user constructed fields which act as displacements on the solid with unknown parameters. The method involves the generation of several simultaneous equations from the weak form of the equilibrium equations to solve for these parameters. The number of virtual fields is therefore related to the number of unique equations required to solve for the material properties. In linear elastic problems the parameters can be solved directly by a matrix inversion, otherwise non-linear solvers are needed (Grédiac *et al.*, 2006).

The method is derived from the principle of virtual work, which is applied to the volume V in Figure 2.10 as,

$$-\int_V g_{ij}(\varepsilon, p^k)\bar{\varepsilon}_{ij}dV + \int_{S_f} T_j\bar{u}_i dS + \int_V f_i\bar{u}_i dV = \int_V \rho a_i\bar{u}_i dV \qquad (2.43)$$

where $g_{ij}(\varepsilon, p_k)$ is a function that returns the stress tensor σ_{ij}, which in turn is a function of the measured strains ε_{ij}, and a set of k material parameters p^k (e.g. Young's modulus and Poisson's ratio in linear elasticity), $\bar{\varepsilon}_{ij}$ is the virtual strain tensor, T_j is the traction on the surface S_f, $\bar{u}_i$ are virtual displacements, f_i are the body forces acting on V, ρ is the material density (mass per unit volume), and a_i is the acceleration (Grédiac *et al.*, 2006). The virtual displacements are conveniently arbitrary, except for the requirements for continuity throughout V, and zero valued within displacement constrained regions S_u (see Figure 2.10). The virtual strains should comply with strain compatibility, and so can be obtained from $\bar{u}_i$ using Equation (2.25) under infinitesimal deformation assumptions.

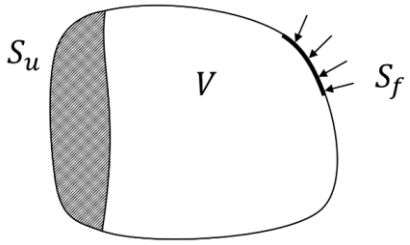

Figure 2.10: Solid shape loaded on boundary S_f and fixed by displacements on boundary S_u

A system of equations can be generated from Equation (2.43) by designing several unique virtual fields, with the prevailing condition that the true strain field is heterogenous in V. In cases in which Equation (2.43) is a linear function of the constitutive parameters, the virtual fields method can be solved directly by generating the same number of equations as unknown parameters, i.e. repeated entries of Equation (2.43) with unique virtual fields. This applies to linear elasticity, and some cases of damage and non-linear elasticity (Pierron and Grédiac, 2012).

The method can be extended to non-linear constitutive equations within g_{ij}, in which case the additional parameters result in a coupled non-linear system of equations, which requires iterative numerical techniques, as shown in Chapter 4 of the book (Pierron and Grédiac, 2012). There has also been some discussion on the choice and optimisation of virtual fields, as this has been shown to affect the methods accuracy, discussed in section 4 of Grédiac *et al.* (Grédiac *et al.*, 2006).

2.4 Summary

This chapter has introduced the concepts of image correlation on the surface using DIC, and the extension to the volume (DVC), derived the J-integral in the 3D forms and simplified 2D forms, presented the decomposition method used to extract mode I – III SIFs from planar problems, and highlighted the process involved with subsequent material parameter extraction.

The first section highlighted the challenges of image correlation on a per-subset basis in which the problems of pattern uniqueness and fidelity were introduced. The main concern arising from this discussion was that fracture leads to a high probability of displacement errors in the crack front and crack face regions if conventional image correlation approaches are used. The effect on fracture parameter extraction techniques which rely on near field data was highlighted (e.g. using COD or displacement extrapolation). The 'local' and 'global' approaches to image correlation were presented and compared. Global methods typically achieve deformation mapping and image matching within the finite element framework, which provides improved results on material boundaries if properly meshed. Both approaches may extend the set of basis functions to improve the mapping of crack tip singularities (e.g. via the X-FEM framework), and discontinuities. DVC (the volumetric extension to DIC) relies on longer scan times, sample aspect ratios as close as possible to unity, and adequate natural features within the imaged material.

The extraction of energy release rates and possibilities to further obtain stress intensity factors (SIFs) is also reviewed. The methods included are field fitting approach and the J-integral. The field fitting involves directly matching the experimental displacements with the analytical displacement fields of mode I, II and III SIFs. Therefore K_I, K_{II} and K_{III} can be obtained, but solutions for the material parameters (E,v) and the crack tip location are required (e.g. by prior knowledge or optimisation).

The J-integral approach involves calculation of the Eshelby tensor. Although stress computation is required, this can be performed remotely from the crack tip to minimise errors. Three methods to obtain SIFs from J are presented: the direct approach, the interaction integral, and the decomposition method. The direct approach requires crack face data, which is undesirable. The interaction integral requires placement of crack tip fields. The decomposition method does not seem to require analytical crack tip fields or crack face data in the classical planar (2D) form.

3 Hypothesis development

The previous sections outlined the context of the project and several methods that can be applied to fracture problems using image correlation data. This section serves as a discussion to focus the methods introduced in Chapter **Error! Reference source not found.**, and detailed in the background reading (Chapter 2). The main aim is to establish the methodology upon which the rest of the thesis is based, therefore a key outcome is in defining the scope. The following discussions mainly focus on selecting techniques (as reviewed in Chapter 2), which function well with the limitations of image correlation in order to acquire fracture parameters.

3.1 Justification for choice of techniques

The main advantage of DIC and DVC when compared to other image matching techniques is versatility and general ease-of-use. However, it was highlighted in section 1.2, and elaborated in section 2.1.2 that image matching is often unreliable in regions of cracking. Improved accuracy may be achievable with other optical methods, such as: the grid method, speckle and holographic interferometry, moiré-fringe methods (Rastogi, 2000), particularly in strain computation. However, these methods require specific materials, light sources or surface preparations (e.g. the grid method requires a periodic pattern applied to the surface). Image correlation can be applied to a versatile range of image types (photography, electron or atomic force microscopy). The only requirements of the material and lighting are that the features are persistent, random and unique (as outlined in section 2.1.2). The method also naturally extends to the volume (DVC), an approach that is assessable using X-ray CT as discussed in section 2.1.4.

> *Methodology statement 1: Deformation measurements from fractured materials shall be obtained utilising digital image correlation methods: DIC on the surface, and DVC in the volume.*

However, such a methodology is likely to cause poor performance in regions of non-linear deformation, mainly localising at the faces and near the crack tip or front (section 2.1.2). Section 2.2 presented two techniques that have become established in full-field fracture experiments despite these effects: the fitting of analytical crack tip fields to experimental data (2.2.4), and the calculation of stress fields and then the J-integral (2.2.5). However, field fitting approaches may be ill-suited to cases where the crack tip region is poorly defined; as in large scale plasticity, crack branching or micro-cracking (e.g. graphite or concrete (Becker *et al.*, 2011)). Furthermore, the field fitting approach would be ill suited to length scales, which either allow larger scale geometric effects to dominate or do not provide sufficient resolution of the field within the K-dominant zone.

The J-integral approach enables estimation of fracture parameters in a length scale independent manner provided that the deformations can be defined by the energy-momentum tensor (Eshelby, 1975). A disadvantage of the J-integral approach is that stresses must be computed. However, the J-integral is contour independent enabling the selection of data in regions of smooth deformations remote from the crack tip, the 'far field', which is likely to be accurate in image correlation.

> *Methodology statement 2: The J-integral will be used to calculate the energy release rate, G.*

However, the use of *J*-based approaches requires an extension of the method to enable the calculation of mixed-mode SIFs. The interaction integral and decomposition method were introduced in section 2.2.3 and discussed in section 2.2.6. Here, it is noted that the interaction integral requires crack tip fields, for which the placement and definition on the surface and in the volume are essentially prone to the same challenges as the field fitting approach. The decomposition method has different requirements, based on the assumptions of symmetry. The first is that the plane of symmetry is required and the second is that the symmetry operation should preserve the validity of the *J*-integral calculation. An example of the second case is if extraneous fields (e.g. due to geometric edges) are included in the decomposed fields. This may cause loss in contour-independence (Rigby and Aliabadi, 1998). However, the main advantage of the decomposition method is that the full crack tip location is not required, only the position of the crack plane is needed for symmetry.

Methodology statement 3: The decomposition method will be used to decouple Stress Intensity Factors for Modes I, II and III.

The final methodology statement concerns the extension of the above methodologies from the surface to the volume. Image correlation, typically only available on the surface with DIC, only serves as a framework for preliminary life estimates and component monitoring. Such estimates are limited by the visible portion of the crack from the surface. Extension of the procedure to the volume through DVC stands to improve understanding of the development of damage below the surface. Therefore, a key aspect of the methodologies is to enable subsurface measurement. For this purpose, the decomposition method – originally intended for planar analysis (Ishikawa *et al.*, 1980) – will require some development to implement in the volume.

Methodology statement 4: Extension of the techniques to estimate J values and the decomposition method from the surface to the volume.

3.2 Aims and objectives

The aim of this research is to develop the objectives of the framework needed to predict failures as outlined in the Chapter **Error! Reference source not found.** (i.e. power-plant materials weakened by cracking). The methodology has been outlined in the previous section, leading to the extraction of stress intensity factors using image correlation. This involves: calculation of strains and stresses from displacement fields, calculation of the *J*-integral, and determination of stress intensity factors.

Although this point is repeated in the thesis scope (section 3.4), it is worth mentioning here that this project does not include the development of the image correlation method, which will be available using commercial software. Also, further structural integrity assessment (e.g. using the acquired stress intensity factors) are considered beyond the scope. The following objectives can be outlined:

Objective 1: Identification and mitigation of displacement errors

This thesis aims to apply image correlation technology to fracture mechanics experiments, resulting in the inevitable question of accuracy and spatial resolution. Such errors are amplified when differentiated to calculate strains, stresses and the subsequent *J*-integral (Methodology statement 1). The aim is therefore to quantify and suppress such errors in crack problems analysed with image correlation. Note that this objective applied to the surface and the volume.

Objective 2: Development of a robust J-integral framework for the surface and the volume

The *J*-integral can be applied on the surface with 2D line or area integral forms (Rice, 1968), and in the volume with 3D path area (Blackburn, 1972) or volume integral forms (Shih *et al.*, 1986). However, the equivalent domain integral forms are typically preferred for the reasons listed at the end of section 2.2.5. This objective seeks to establish a framework to understand the relative numerical robustness of these *J*-integral forms, and thereby develop suitable integral equation forms for use with data in 3D surface and volume experiments.

Objective 3: Verification of the J-integral with experimental full-field displacements derived from image correlation

This objective involves verification of the *J*-integral applied to image correlation data both on the surface and in the volume. This objective will cross-compare implementations on theoretical fields using the Williams series (Williams, 1957), numerical fields using the finite element method, and the obtained displacement fields using image correlation and *in situ* loaded specimens.

Objective 4: Development of the J-integral decomposition method to obtain stress intensity factors

The decomposition method has been tested experimentally, for example by Diekmann *et al*. (1991). However, this objective aims to test the method on image correlation data both on the surface (including out-of-plane motion) and the volume. Such 3D implementations have not been tested before on either DIC or DVC data, and will require special attention to the volume due to the loss of contour independence experienced by the *J*-integral under typical decomposition conditions (see the end of section 2.2.6).

3.3 Central hypothesis

It is well established that mixed-mode SIFs can be used to predict failure in real world applications (section 2.2). Full-field methods show promise for research into predicting crack behaviour through versatility of application afforded by image correlation methods. Thus, a framework is needed that firstly provides SIFs and secondly will enable future research into crack behaviour.

It has been noted in section 1.3 that the use of analytical crack tip fields restricts analysis to linear elastic fields. Therefore, such approaches may limit the versatility of future research.

Hypothesis: The J-integral based decomposition method, a full-field method proposed in this thesis, can be used to determine mixed-mode SIFs from image correlation displacements of the surface and volume. The method for determining SIFs does so without analytical fields and so remains versatile for future research on mixed-mode behaviour observed in digital images.

3.4 Scope

There are numerous challenges involved in the implementation of the proposed framework. This section aims to delimit the project from the overall methodology needed to improve future structural integrity assessments.

3.4.1 Non-destructive testing and evaluation

This project is not concerned with locating or monitoring structures weakened by cracking, nor the limitations of in-service measurements (e.g. topics such as probability of detection). Similarly, although the technique is partially motivated by future applications in non-destructive evaluation, this would often be plant or component specific Therefore this project does not evaluate risk and structural integrity and assumes that the provision of mixed-mode SIFs, in a manner that is tolerant to displacement errors, is sufficient for use in the standard structural integrity assessment programmes currently used by Eskom (BSI, 2015).

3.4.2 Experimental errors from image correlation

The displacement fields in this project are experimentally obtained using DIC and DVC. The errors can be related to imaging artifacts, environmental conditions and pattern quality, among numerous other possible sources. Currently there is no standard approach for the characterisation of errors, although some resources are becoming increasingly used (e.g. the methodology of Bornert *et al.* (2009), or SEM's DIC challenge[21]). In the context of this project, the steps necessary to provide useful characterisation of errors would require on-site experiments. Therefore, experimental errors are collected for each experiment individually and no further attempts are made to delineate the systematic errors. Commercial software was used (DaVis, LaVision) and assumed to be similar to other commercial systems. Similarly, improvements in robustness of the DIC or DVC methods were not investigated in this project.

3.4.3 Linear-elastic deformations

Although there is great interest from Eskom to measure nonlinear fracture parameters caused by advanced levels of damage accumulation, the aim of this project is to establish the framework to calculate fracture parameters. It is envisioned that this framework could be expanded to a study of non-linear systems, as demonstrated in Yoneyama *et al*. (2014). However, it is key that the J-integral remains relatable to mixed-mode SIFs for validation purposes needed to achieve objectives 3 and 4. Therefore all implementations in this project are linear-elastic. In the experimental sections, small-scale yielding is assumed – i.e. that the size of the plastic zone surrounding the crack front is small enough relative to the crack size so that a purely elastic solution may be used to calculate the energy release rate. The method used to calculate fracture parameters is the J-integral, which can be justified in an elastic framework due to:

- Contour independence which enables the selection of contours far from non-linearities at the crack tip;

[21] See: sem.org/dic-challenge (accessed 20 July 2017)

- J is applicable to nonlinear-elasticity, as validated and implemented in various works (Stump and Zywicz, 1993; Kolednik *et al.*, 2014; Begley and Landes, 1972). This characteristic motivated for the selecting of the J-integral technique.

These extensions are useful and relevant in the SA context, but are relegated to possible future work.

Although all deformation fields are assumed to be 3D, the separation of fracture modes into mode I, II and III components rely on plane and anti-plane assumptions. To simplify computations of stress and conversion of the J-integral into SIFs, the materials are assumed to be isotropic throughout, and crack fronts are assumed to be planar and straight fronted in the volume. It is also worth mentioning that deformations due to thermal, dynamic, and gravitational effects are assumed to be negligible.

3.4.4 Nominal loading

The framework is aimed at extracting fracture parameters directly from DIC and DVC displacements, eventually leading to *in situ* analysis. Therefore, sample loading and cross-head displacements, which are typically involved in inverse methods (section 2.3) are not considered in this framework.

3.4.5 Spatial resolution

Numerical approaches to solving crack problems routinely use mesh refinement to improve the accuracy of crack tip fields. However, the enclosed methods are all similarly limited by the displacement accuracy and spatial resolution limitations afforded by regularly sampled digital 2D and 3D images. Although accuracy improvements in crack tip regions have been implemented in some image correlation approaches (see section 2.1.3), these techniques are not yet in general use. Therefore, this thesis does not apply such mesh refinements to experimental or numerical data. Instead, analytical solutions are used when reference stress and displacement data are needed. In the absence of mesh refinement, all field data in used for the determination of fracture parameters in this thesis are determined at evenly spaced material points. Note that the commercial software used in this thesis (DaVis v8.3, LaVision) has the same regular grid convention.

4 Robust removal of displacement artifacts from digital image and volume correlation results

This chapter presents an iterative approach to reducing errors found in full-field displacement measurements. The chapter uses DIC and DVC data from experiments described in other chapters of this thesis, and therefore serves to highlight characteristic error sources from notch and crack problems using image correlation. In doing so, this chapter addresses the first objective of this thesis.

The thesis aims to extract linear fracture parameters (section 3.3), thus the material constitutive laws should be assumed to be linear elastic (section 3.4). In this chapter, these assumptions enable additional efficiency and automation in the numerical implementation using the finite element method. However, it is worth mentioning at the outset that the presented method only uses the numerical framework to compute nodal forces, and so can be extended to non-linear deformation experiments (e.g. plasticity), as discussed in section 3.4.3.

This chapter was presented at the 14th International Conference on Fracture (Molteno *et al.*, 2017), and has been prepared for publication (*Optics and Lasers in Engineering*) with co-authors (in no particular order): McDougall, Marrow and Becker. The contributions of the authors are:

- The author (Matthew Molteno): Conception of the method, designed and performed experiments, implementation of the method, and reporting of the results. All sections are written by the author, with review by the co-authors.
- Mr Duncan McDougall: Technical assistance with the extension of the finite element framework presented by Liu and Tovar (2014), enabling direct use of DIC and DVC displacements as nodal constraints.
- Prof. James Marrow: Provided financial and academic support during the conception and early development of the method at Oxford University.
- Dr Thorsten Becker (project supervisor): Outside of the ordinary supervisory role – identification of the relationship between experimental errors and artifact relaxation energy. This relationship is important because it allows users to predict an *a priori* error-energy criterion to prevent over-smoothing of the original (DIC or DVC acquired) displacement field.

Other noteworthy contributions from non-co-authors:

- Prof. S. Yoneyama: Suggestions for implementation, and comparison of the presented method with their approach (Yoneyama, 2011), which is very similar to our approach but achieves smoothing rather than outlier removal. This is done in a least-squares sense in which the sample geometry is captured by the finite element mesh (see section 9.2).
- Liu and Tovar: Original developers of the open-source finite element framework (Liu and Tovar, 2014). Their code provides an optimised method of assembling and inverting the global stiffness matrix finite element in Matlab.

4.1 Introduction

Optical methods have become established tools to supply full-field displacement data in solid mechanics experiments. For example, full-field measurements can provide verification for existing deformation theories (e.g. with the finite element method (Barranger *et al.*, 2010)), estimate constitutive parameters (Grédiac *et al.*, 2006), or characterise new material behaviour (Marrow *et al.*, 2016).

There are now several techniques at the disposal of the experimentalist to determine accurate full-field measurements. The interferometric-type methods (such as moiré, speckle, holographic) require a coherent light source and so additional sample preparation and equipment is required to take measurements. As a result, non-interferometric methods have become popular as they are relatively simple to implement (natural lighting can be used, and sample preparation is minimal). These include the grid method (Grédiac *et al.*, 2016) and the image correlation method (i.e. DIC and DVC). A notable advantage of image correlation is that the sample surfaces do not require regular patterns of features (in fact, it is essential that they are not, for the reasons given in section 2.1). Therefore, experiments using image correlation can be considerably less prescriptive. Image correlation is now well-established for multi-camera measurement of 3D surfaces (Luo *et al.*, 1993; Malesa *et al.*, 2015) and volumetric imaging systems using DVC (Bay, 2008; Maire and Withers, 2014). This extended functionality is favourable if a single framework is desired for the surface and the volume.

However, due to the dependence of image correlation on random patterns, the strain field can be unreliable in regions of low contrast, particularly near to stress concentrators. A common practice to minimise errors is to increase the area and overlap of the analysis windows used in correlation (i.e. the image subset sizes). The result is that image correlation errors seldom contain distinct outliers, but rather form a smooth surface in which errors can be imperceptibly small. Another source of errors is due to image artifacts, which are particularly persistent in volumetric imaging (e.g. stripe or ring artifacts (Trtik *et al.*, 2009)). These effects become problematic in engineering analysis because small errors in the displacement field results, result in relatively larger errors in the strain fields due to numerical differentiation.

A long-standing solution is the use of local least-squares matching applied to a specified region of the displacement field. The selected basis functions may then be tuned with classical statistical tools such as weighted least-squares or multiple cross-validation to minimise the impact of experimental displacement errors. The displacement gradients may then be calculated from the derivative forms of the optimised basis functions.

The finite element method provides a convenient numerical framework for the implementation of such approaches. The shape functions allow for a user defined geometry by aligning the nodes with specimen edges (Yoneyama, 2011), and further in-depth analysis can be performed within the finite element framework (e.g. contact, or vibrational analysis). However, the least-squares method is inherently sensitive to outliers. Furthermore, these methods do not ensure that the smoothed result also satisfies stress equilibrium – an important requirement for numerous solid mechanics applications (e.g. convergence of the J-integral, or the extraction of material properties using VFM).

Some hybrid finite element approaches have been developed that simultaneously satisfy internal equilibrium while smoothing displacement data, for example using the penalty-method (Sutton *et al.*, 1991), or variational principles (Nishioka *et al.*, 1997; Fujikawa, 2005; Nishioka *et al.*, 2000). In these approaches, the strains are calculated through the strain-displacement relationship after a state of minimum virtual work has been reached. However, these methods are not optimised to

deal with non-normally distributed outliers, which remain part of the energy minimisation until the final state is reached. As previously mentioned, the treatment of such errors is critical in DIC and DVC datasets, as these often arise due, for example, to image artifacts (e.g. inhomogeneity's in the light source, movement of sample during capture), or low feature fidelity of the contrast pattern.

This chapter presents an alternate, robust method for the iterative removal and replacement of displacement outliers from full-field displacement data. The method is finite element based, using internal reaction forces as an error quantifier. Conversely, the improvement to the data is assessed after each iteration by defining the work involved in restoring internal equilibrium, similar to the approach of Nishioka *et al.* (1997). However, unlike previous works, a convergence criterion based on the strain energy related to random errors is defined. This criterion is designed to limit 'over-smoothing' and thereby preserve the true material behaviour within image correlation results. The FE procedure is optimized for efficiency from the use of linear-elastic elements and regular Cartesian grids. This decision is because regular grids are amenable to most DIC and DVC methods which use low order subsets and regular grids for similar computational efficiency reasons.

The method was inspired by Yoneyama *et al.* (2011; 2016), Garcia (2010) and Becker *et al.* (2012), who proposed a finite element based framework for the analysis of surface displacement data obtained using DIC. The approach is not intended as a replacement for existing least-squares or finite element based smoothing methods, but rather as a pre-processor to eliminate outliers.

The chapter is organized as follows: section 4.2 provides the procedure used to identify unreliable data, including an introduction to the density-based finite element framework, and explanation of the iterative procedure. Section 4.3 illustrates the application of the method on a cantilever problem. Section 4.4 presents applications to experimental data from stereo-DIC and DVC, examining the displacement fields around mixed-mode crack and notch tips respectively. The performance of the method on DIC and DVC data is discussed in section 4.5. A summary of the chapter can be found in section 4.6.

4.2 Identification of unreliable data

Consider a typical full-field experiment of a sample captured with 2D or 3D imaging before and after loading (Figure 4.1a). Then the full-field displacement map between the reference and deformed image can be obtained by application of the image correlation method (DIC or DVC). This usually involves subdividing the reference image into groups of pixels called subsets (or subvolumes of voxels in volume images). Then displacements are determined per subset by matching to an optimal location in the deformed image (a), as discussed in section 2.1. To maximise the use of the imaging sensor grid, the available field of view is centred on the feature of interest, e.g. the crack in Figure 4.1 (a) and (b). The displacements determined in the region of interest (ROI) contain errors due to the crack and a moving foreign body, in this example a bug on the camera lens or sample (cartoon in Figure 4.1a). Figure 4.1b shows a neighbourhood of displacements u_i $(i = 1,2,3)$ computed within a predefined mask. The computed nodal force values f_i over domain Ω are shown in Figure 4.1c, which have been calculated through the FE framework presented in section 4.2.1. If equilibrium is met, internal force vectors should be negligible. Non-physical force outliers are a consequence of the displacement outliers.

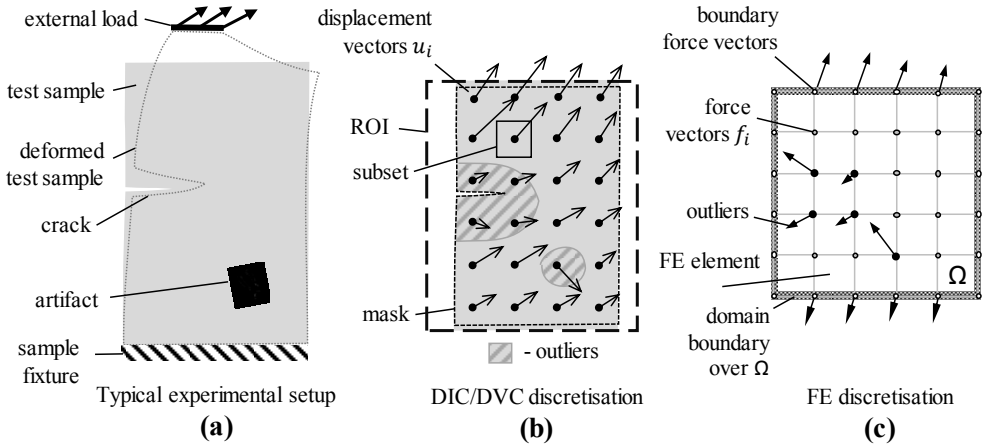

Figure 4.1: The stages of outlier identification: (a) experimental *in situ* loading with artifact, (b) acquisition of full-field displacements using DIC or DVC and definition of the mask (c) FE discretization showing forces at internal nodes and on the boundary of the domain Ω

4.2.1 Finite element framework

Computerized tomography often draws on two main strategies to perform finite element computations: the geometry-based or voxel-based strategies (Lengsfeld *et al.*, 1998). The geometry-based strategy enables arbitrary element shapes that are matched to the geometric edges of the scanned sample. The advantage of mesh based strategies is that users can design the mesh to the precise requirements of a geometry (e.g. crack tip mesh refinement), and is the most common strategy for general use in mechanics (e.g. Figure 4.2a). The voxel-based strategy focuses on enabling a high density of cubic 'brick' elements, usually of a low order to enable efficiency. The mesh is then implicitly applied by setting the stiffness values of elements that represent empty space 'void material' to zero. The advantage of voxel-based strategies is that the mesh can be generated in a highly automated manner, as the shape can be inferred directly from the image mask used for DIC or DVC. The disadvantage is that the efforts to increase efficiency prevent flexible element design (e.g. higher order elements). It is important to remark that the term 'voxel' in the finite element strategy name does not imply image voxel number matches the number of elements (seldom the case as volumetric images may range between 1-100 million voxels). Typically, the mesh is determined after a binning operation to reduce image size (Lengsfeld *et al.*, 1998). The FE framework employed in this chapter is voxel-based, and uses the method developed by Liu and Tovar (2014).

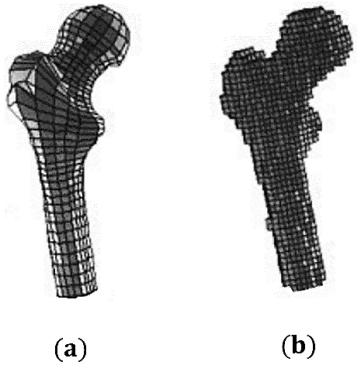

Figure 4.2: Geometry of a human femur generated by (a) geometry-based and (b) voxel-based meshing strategies.
Image from Lengsfeld *et al.* (1998)

The material stiffness distribution is represented by elemental densities ρ_l at each location in the image mask $\rho(x_i)$, in which x_i $(i = 1,2,3)$ is the global co-ordinate system - aligned with the calibration plate in DIC, or by the X-CT scanner or digitizer in DVC. Then the elemental Young's modulus values E_l are defined as:

$$E_l = E_l(\rho_l) = E_{min} + \rho_l(E_0 - E_{min}), \quad \rho_l \in [0,1] \tag{4.1}$$

in which E_0 is the nominal Young's modulus of the material set to unity for this method (see section 2.1.2), and E_{min} the modulus of void material, a value close to zero. The selection of ρ values at any values within the range $(0,1)$ implies softer material at these points in the voxel grid, however in the presented approach only binary values are used.

The element stiffness matrix K_l is constructed with generalized Hooke's law, and linear shape functions for an 8-noded hexagonal element:

$$K_l(\rho_l, v) = E_l(\rho_l)K_l^{\mathrm{t}}(v) \tag{4.2}$$

In which K_l^t is a template stiffness matrix prepared for efficient assembly. It may be noted that the formulation is 3D using brick elements. Therefore, to enable DIC displacements, a single layered sheet of brick elements is used, in which DIC displacements are copied onto the front and back faces, assuming that anti-plane shear is minor.

The elemental stiffness matrices of Equation (4.2) are then assembled into the global stiffness matrix K, using the procedure described by Liu and Tovar (2014). Similarly, known forces f and displacements u are appended in column vectors of the length $3\times N$ in which N is the total number of nodes. This results in an equation for nodal forces f, which can be calculated with varying density:

$$f = K(E_{\min}, \rho(x), v)u \tag{4.3}$$

Subsequently, the global structure is partitioned into displacement and force constrained quantities, denoted by subscripts e (essential or Dirichlet) and n (natural or Neumann) respectively, as shown in Figure 4.3. For clarity on the notation, subscripts e and n indicate sets of nodes indexed in the global array, whereas subscripts i, j, and k continue to refer to vector or matrix indices (1,2,3). Then the assembled structure can be partitioned into:

$$\begin{bmatrix} K_{ee} & K_{en} \\ K_{ne} & K_{nn} \end{bmatrix} \begin{Bmatrix} u_e \\ u_n \end{Bmatrix} = \begin{Bmatrix} f_n \\ f_e \end{Bmatrix} \tag{4.4}$$

and the unknown forces and displacements can be solved using:

$$u_e = [K_{ee}]^{-1}(\{f_n\} - [K_{en}]\{u_n\}) \tag{4.5}$$

$$f_e = [K_{ne}]\{u_e\} + [K_{nn}]\{u_n\} \tag{4.6}$$

To prevent infinite displacements on zero density elements, nodes located in void material ($\rho_l = 0$) are set to zero ($f_n = 0$), and displacements are undetermined at these locations (Figure 4.3). Displacements of elements involved in restraining the external problem are permanently fixed.

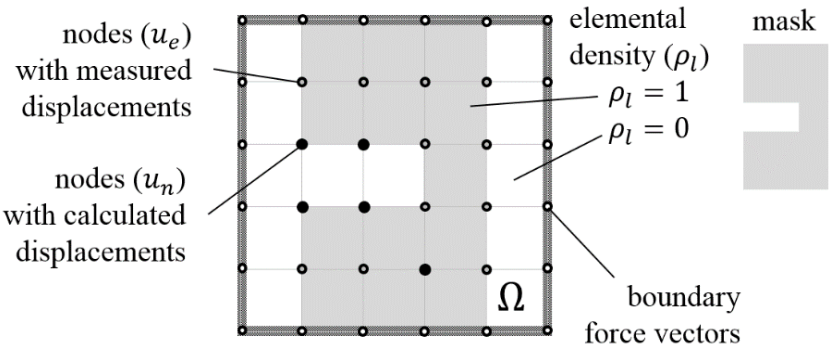

Figure 4.3: Nodal information in ROI of deformation field

Note that the number of outer nodes that are fixed is arbitrary, and can be increased or decreased without reconstructing K. The reliability of data points may then be estimated from the norm of both the displacement and force constrained nodes as:

$$\hat{f} = \frac{|f|}{|f|^{max}}, \quad \hat{f} \in [0,1] \tag{4.7}$$

In which $\hat{f}$ is a vector of normalized force magnitudes, $|f|$ is a vector of force magnitudes where $|\cdot|$ is the 2-norm, and $|f|^{max}$ is the maximum magnitude found in $|f|$, i.e. a normalising scalar.

4.2.2 Iterative procedure for artifact removal

The procedure used to remove outliers repeats the following four steps until convergence:

- Step 1: Select a small percentage (e.g. 1-5 %) of the largest nodal forces $\hat{f}$
- Step 2: Replace the displacements for the selected nodes using FE,
- Step 3: Compute the work-energy released by step 2: $\delta U = \sum \delta f_i \cdot \delta u_i \,/2$,
- Step 4: Terminate the procedure if δU falls below a threshold δU_{exp}, otherwise repeat (from Step 1).

In the above steps, δ indicates a change in either the forces f_i or displacements u_i. The following sections are dedicated to defining a suitable threshold δU_{exp} (Step 4) that terminates the procedure when outliers are removed. This is defined as the energy due to purely random errors (i.e. normally distributed). The hypothesis is therefore that random errors exert significantly smaller forces than non-random errors (outliers), and therefore will be preserved until most outliers have been removed. Constraining the nodes of the FE mesh with DIC or DVC displacements results in nodal forces and resulting energies,

$$U = \frac{1}{2}\sum f_i \cdot u_i \tag{4.8}$$

in which U is elastic energy. Equation (4.8) can be partitioned into two parts, the energy due to applied forces on the boundary U_{ext} and the energy due to internal forces U_{int}. In typical FE problems U_{int} calculated with Equation (4.8) on internal nodes provides a value close to zero due to internal equilibrium, and the boundary forces determine the total potential energy.

As all forces in the proposed framework are derived from displacements through K, the nominal Young's modulus E_0 defined in Equation (4.1) plays no role in the equilibrium, and so is set to unity. Note that this does not necessarily require the material to be homogeneous as stiffness variations can still be defined by $\rho(x_i)$. In experimental fields, a force is exerted on all nodes due to the experimental errors. Therefore, the resulting energy balance can be written,

$$U_{ext} - U_{int} = U_n + U_o + \Delta U = \widetilde{U} \tag{4.9}$$

in which U_n is the potential energy due to random (i.e. normally distributed) errors, U_o is the portion due to outliers, and ΔU accounts for possible changes of energy in the system (e.g. heat dissipated by plastic deformation). Assuming a linear-elastic system in which energy is conserved (i.e. $\Delta U \to 0$), then $\widetilde{U}$ is the energy residual due to displacement errors:

$$U_{ext} - U_{int} = \widetilde{U} \tag{4.10}$$

It is assumed that $\widetilde{U}$ is mostly due to errors at internal nodes. This is necessary because the errors on the boundary are more challenging to detect, as addressed by methods such as that of Yoneyama *et al.* (2012). Under this assumption, the energy relaxation due to a small subset of nodes (i.e. step 2) translating to an equilibrium position in a new state (k) can be written as:

$$\widetilde{U}^{(k)} = U_{ext} - {U_{int}}^{(k)} = \sum f_{ext} \cdot u_{ext} - \sum f_{int}^{(k)} \cdot u_{int}^{(k)} \tag{4.11}$$

in which $(\cdot)$ is the dot product. Then an increment of internal work-based energy is given as,

$$\delta\widetilde{U}^{(k)} = {U_{int}}^{(k)} - {U_{int}}^{(k-1)} = f_{int}^{(k)} \cdot u_{int}^{(k)} - f_{int}^{(k-1)} \cdot u_{int}^{(k-1)} \tag{4.12}$$

The equation above can be interpreted as the Incremental Artifact Relaxation Energy (IARE) calculated between present and previous iterations. Note that the standard deviation and mean are suitable to quantify random and non-random errors separately. When the data contains random errors biased by outliers, the root-mean-square-error (RMSE) is a more suitable measure. The RMSE for internal energy on the domain Ω can be defined as,

$$\delta\widetilde{U}^{(k)}{}_{RMSE} = \sqrt{\frac{\sum_\Omega \delta\widetilde{U}^{(k)^2}}{\sum_\Omega 1}} \tag{4.13}$$

In which the denominator is the same as the total number of nodes. In 'ideal' (linear-elastic, small deformation) cases, it would be sufficient for convergence that $\delta\widetilde{U}^{(k)}{}_{RMSE}$ tends toward zero. However, in real experiments this would always steer the system toward linear-elasticity. It is therefore useful to determine the experimental potential energy due to random errors. If full-field displacement errors (u_{err}) are known (e.g. from rigid body tests), the RMSE due to experimental errors, $\delta\widetilde{U}_{exp}$, can be calculated using,

$$\delta\widetilde{U}_{exp} = \sqrt{\frac{(\{u_{err}\}^{\mathrm{T}}[K]\{u_{err}\})^2}{\sum_{\Omega} 1}} \tag{4.14}$$

in which the units are energy (Joules). Note that both $\delta\widetilde{U}_{exp}$ and $\delta\widetilde{U}^{(k)}{}_{RMSE}$ are independent of the number of points selected if a statistically defensible number of points are used. This leads to the first convergence criteria:

$$C1\colon\ \delta\widetilde{U}^{(k)}{}_{RMSE} \leq \delta\widetilde{U}_{exp} \tag{4.15}$$

$C1$ states that convergence can occur once the energy released on iteration k becomes less than the energy due to random experimental errors, using the statistical relation between the RMS variables[22].

The second criterion determines true outliers from random data. Once determined, such outliers should be omitted from the model in all further iterations to prevent biasing of the results. An outlier is here defined as a data point that consistently releases IARE values larger than the experimental threshold ($\widetilde{U}_{exp}$). The total energy is calculated as the sum of the incremental IAREs as,

$$\widetilde{U}^{(k)} \approx \sum_{i=1}^{k} \delta\widetilde{U}^{(i)} = U_{int} \tag{4.16}$$

Values in $\widetilde{U}^{(k)}$ are orders of magnitude greater than $\widetilde{U}_{exp}$, and so a scale factor (SF) is assumed (typically set to 10).

$$C2\colon \widetilde{U}^{(k)} \leq \widetilde{U}_{exp} \times SF, \qquad SF > 1 \tag{4.17}$$

Finally, the rate of convergence depends on the on the fraction of nodes replaced during each iteration, hence a second factor is introduced (QF).

$$\hat{f} \leq QF, \qquad QF \in [0,1] \tag{4.18}$$

Values of $SF = 10$, $QF = 0.1$ were found to achieve robust performance for most problems, and are the values used in all examples in this chapter. With the criteria defined, the steps 1-4 outlined at the beginning of this section are now elaborated as the algorithm in Table 4.1.

Although the ΔU energy portions of the residual energy are not accounted for with the proposed method, the method allows for such an offset by way of adding the additional energy loss (e.g. from R-curve tests) to ΔU in Equation (4.10). In the next section, the relationships derived to estimate the thresholds $\widetilde{U}^{(k)}$ and $\delta\widetilde{U}^{(k)}{}_{RMSE}$ are investigated on a numerical example.

---

[22] Any RMSE computed variable x_{RMSE} is always greater than the random errors x_{std} due to bias, based on the relation: ${x_{RMSE}}^2 = {x_{bias}}^2 + {x_{std}}^2$

Table 4.1: Algorithm for outlier detection and removal

STEP	DESCRIPTION
1	Initialize iterations $k \rightarrow 0$;
2	Import experimental displacements $u^{(k)}$, positions x;
3	Define material distribution $\rho(x) \in [0,1]$;
4	Initialize $f^{(k)} = 0$, $E_o = 1$, v, K (Liu and Tovar, 2014);
5	Calculate IARE threshold, $\widetilde{U}_{exp}$, Equation (4.14);
6	Initialise SF (=10),
7	**while** (convergence criteria $C1$) **do**
8	Solve for nodal force vector $f_e^{(k)}$, Equation (4.6);
9	Calculate nodal reliability q, Equation (4.7);
10	Compute ARE and IARE: $\widetilde{U}^{(k)}$, $\delta\widetilde{U}^{(k)}{}_{RMSE}$
11	**if** (convergence criteria $C2$ for node i) **do**
12	Replace $u_i^{(k+1)}$ with FE solution, Equation (4.5)
13	**else if** ($\hat{f}$>QF) **do**
14	Replace $u_i^{(k+1)}$ with FE solution, Equation (4.5)
15	**end if**
16	Set $u^{(k+1)} \leftarrow u^{(k)}$; $k \leftarrow k+1$
17	**end while**

4.3 Example: cantilever beam

In this example, two known artifacts (gaussians) are iteratively removed from the displacement field of an end loaded cantilever beam, in the presence of other (random) displacement errors.

The cantilever is dimensioned as shown in Figure 4.4, and loaded with a downward force of $w = 1 \times 10^6$ N distributed along the vertical free end. The implementation of the method on the cantilever example introduces displacement errors which are: gaussians located at α and β, and Gaussian white random noise defined spatially over the domain Ω. The non-random noise at α and β are Gaussian functions (also shown in Figure 4.5b), with a standard deviation of σ = 20 mm and a peak displacement value of $10 \times u_{err}$ in the directions u_i = 1. For purposes of discussion in later sections, the problem is given image correlation properties, based on a DIC accuracy of 0.01 pixels as reported by Zhou and Goodson (2001) and Amiot *et al.* (2013). The resolution is chosen as 0.1 mm/voxel leading to a $u_{err} = 1e$-3 mm measurement accuracy.

The ROI is 60×60 mm centred on the cantilever and a grid-spacing of 2.5 mm resulting in the elements shown in Figure 4.5a. Per these parameters, the experimental energy threshold from Equation (4.13) is $\delta\widetilde{U}_{RMSE} = 1 \times 10^{-6}$ J. The beam has material properties, $E = 10$ GPa, and $v = 0.25$. Except for the end surfaces, the cantilever is surrounded by a single layer of void elements on the boundaries ($\rho = 0$) to allow 3D surface and volume deformations (Figure 4.5a).

To test Equation (4.14), the cross-plot between displacement accuracy and the energy convergence criterion for random errors increased from $0 \rightarrow 1 \times 10^{-3}$ mm/voxel shown in Figure 4.6, binning the results of 1×10^4 tests to achieve trend lines. The mean value (solid) and standard deviation (99 % confidence - dashed) lines are shown. Recall that the Young's modulus in these problems

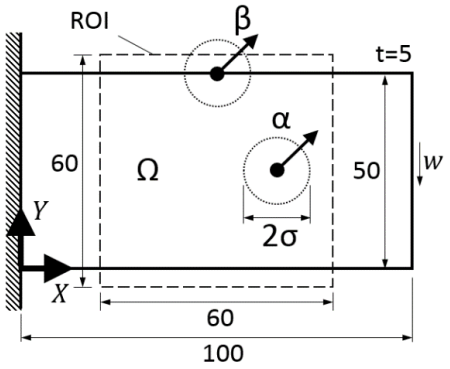

Figure 4.4: Cantilever beam with artifact locations at α, β (gaussian width σ) and random noise over the domain Ω

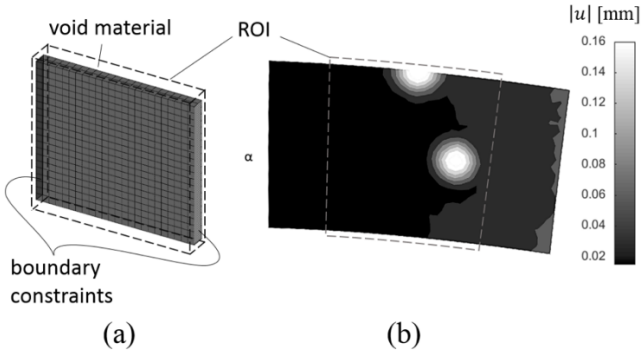

Figure 4.5: (a) Material distribution with boundary constraints, (b) displacement field amplitude contour plot showing noise components α and β, and random noise over the entire ROI Ω Locations and dimensions shown in Figure 4.5.

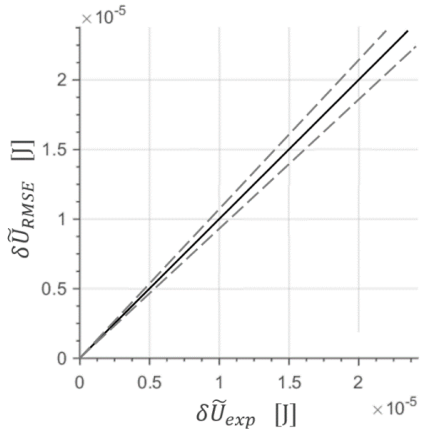

Figure 4.6: Cross-plot of Equation (4.14), with mean (solid) and 99 % confidence (dashed)

is set to unity. However, the effect of Poisson's ratio is unknown, and could not be clearly discerned in these results – appearing to have zero effect. These observations were made by reproducing Figure 4.6 with different Poisson's ratio values between 0.2 and 0.4.

The iterative artifact removal procedure is applied to the ROI until the initial energy state reaches a state of internal equilibrium. The internal energy on this sub-domain is determined from the noise free FE model to be 7.5×10^{-5} J, and with noise and artifacts added, to be 3×10^{-4} J. Figure 4.7a

shows the internal energy computed on each iteration for 100 iterations – a large number to show the effects of over-smoothing. The internal energy is calculated before the data is altered on each iteration (shown in terms of nodal force ($|f|$) and displacement ($|u|$) magnitudes, and so the first data-point in Figure 4.7a matches the internal energy computed at iteration zero exactly.

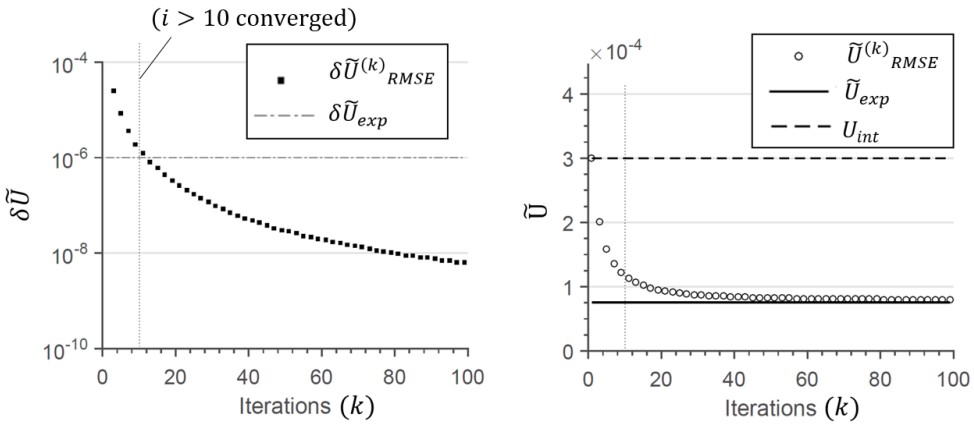

Figure 4.7: (a) Internal energy during iterations *k* between (b) the systems transition from initial to final energy

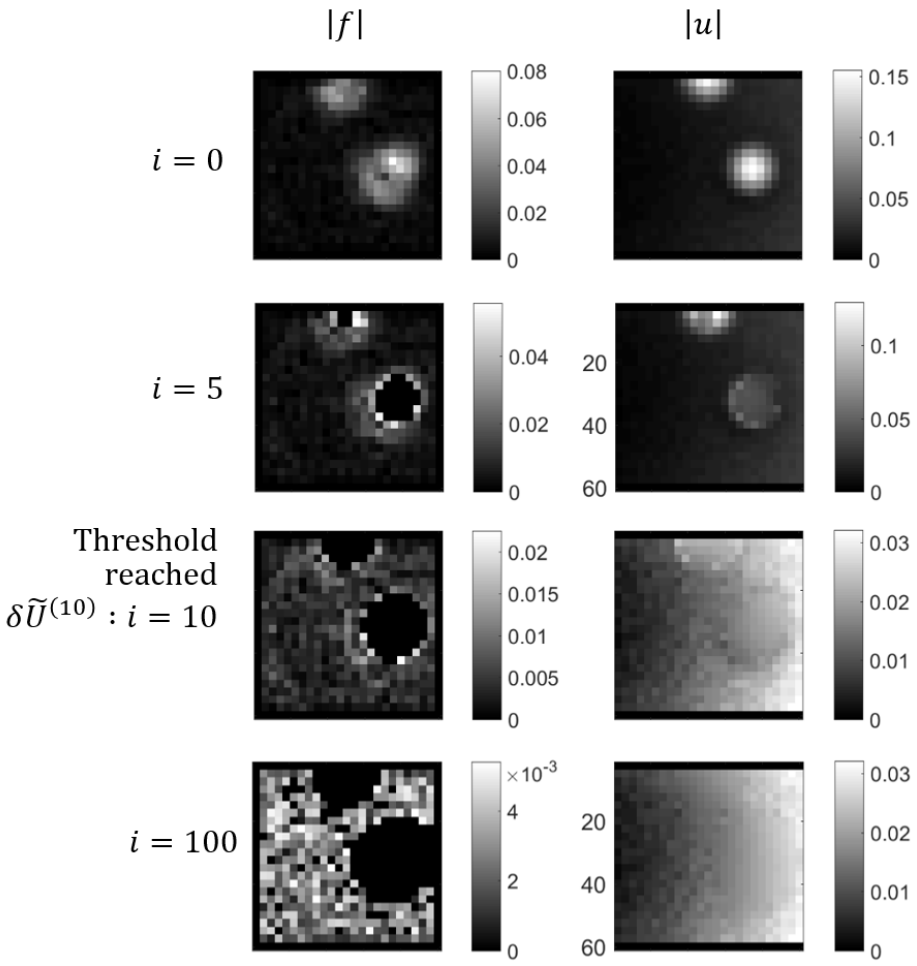

Figure 4.8: (a) artifact removal from region of interest of the cantilever showing magnitudes of force $|f|$ and displacement $|u|$, threshold at iteration $i = 10$

4.4 Applications to experimental results

4.4.1 Application to DIC data

In this section, the artifacts from a region of interest surrounding a crack are studied. Large subsets and small grid spacing (i.e. large subset overlap) is used. The commercial DIC code used that does not map crack tip fields or discontinuities, and therefore displacement and errors are likely to occur close to the crack faces and tip. A symmetrically loaded crack (mode I) allows low stresses in the crack faces. To introduce asymmetry, the crack is inclined by 30° using the Arcan and Banks-Sills methodology (Molteno and Becker, 2015c; Banks-Sills and Arcan, 1986). This uses specimens that are the bowtie shaped (Figure 4.9a), which were laser-cut from 12 mm PMMA sheet (transparent thermoplastic), and is assumed to be linear-elastic. DIC displacement fields were obtained with a LaVision stereo DIC system, and DaVis v8.3 software, using subsets of 60×60 pixels, a stepsize of 5 pixels. Figure 4.9b shows the 16×16 mm ROI, including 2.3 mm of pre-notch, and a 5 mm length of sharp crack (induced with a screw-driven sharp blade), with the crack tip centred at ⟨0,0⟩ as indicated by the cross-hair. The red overlay shows the stereo reconstruction error, a feature of the DaVis software, and is used to qualitatively indicate regions influenced by possible errors.

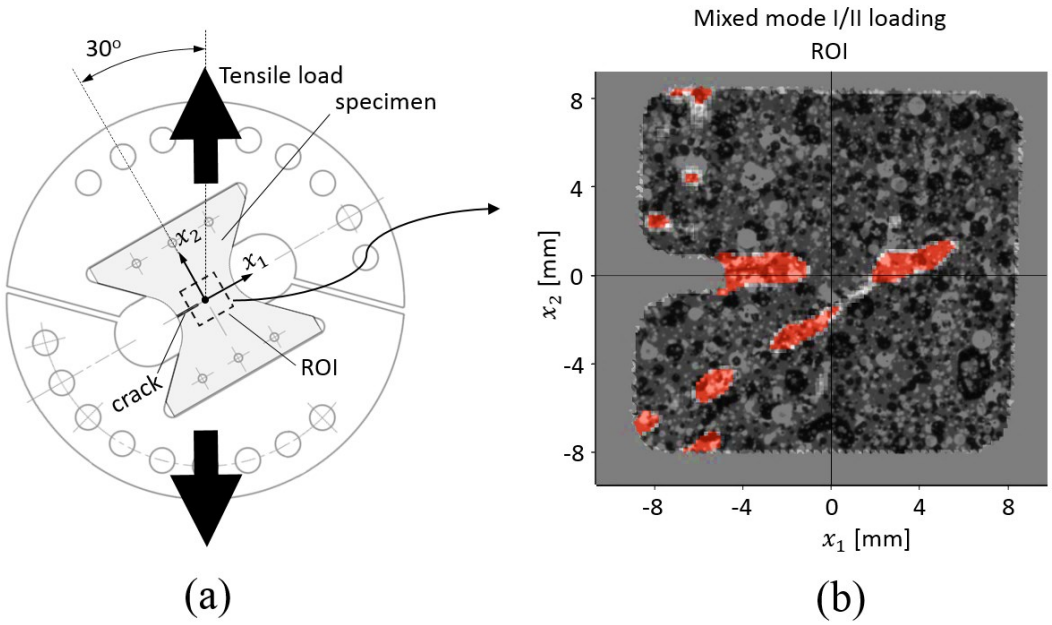

Figure 4.9: (a) Arcan fixture and specimen inclined by 30° loaded vertically, (b) corresponding region of interest (ROI) showing speckle pattern and unreliable regions (red overlay)

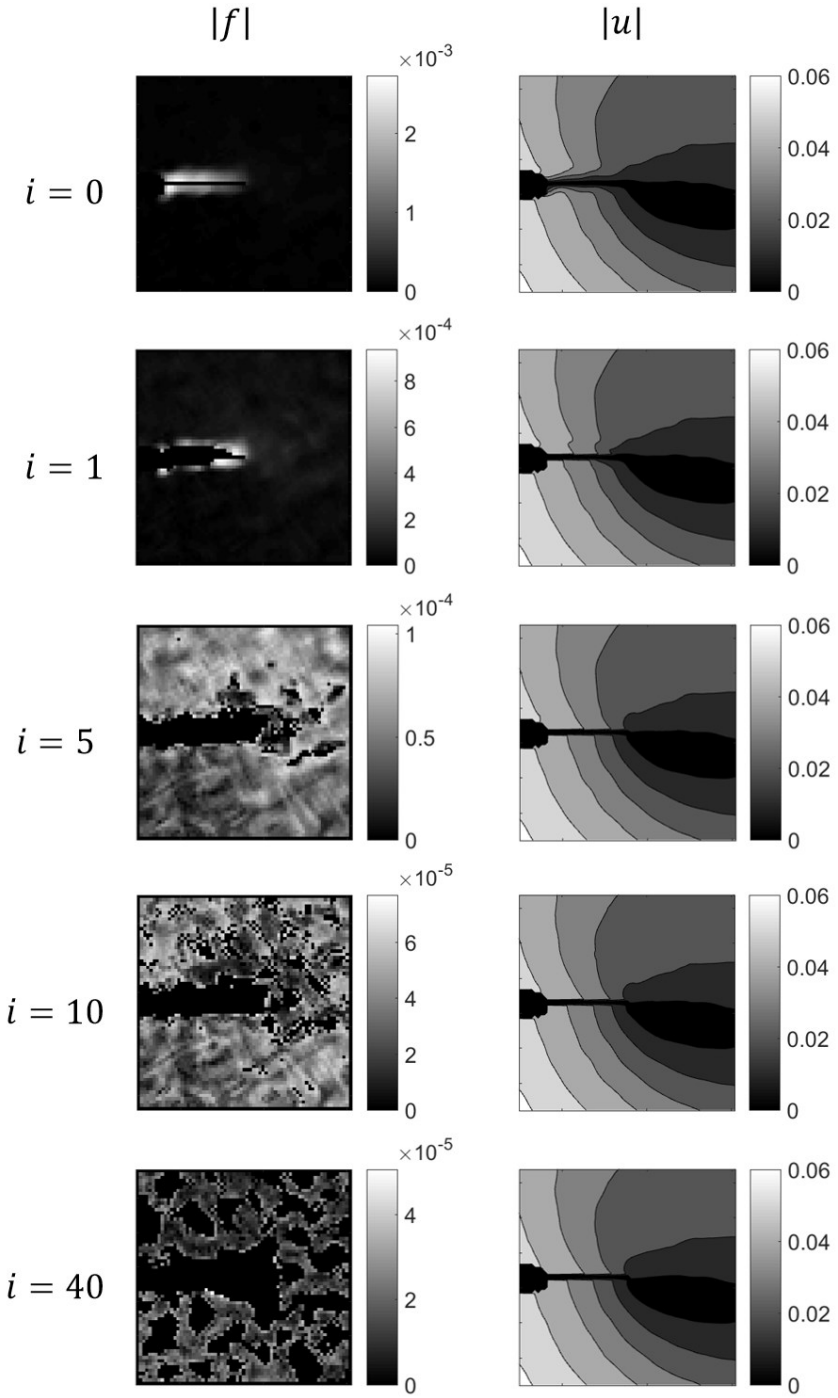

Figure 4.10: Artifact removal from region of interest of the Arcan specimen (ROI, Figure 4.9) showing magnitudes of force $|f|$ and displacement $|u|$, predicted to converge at iteration 10 Note: colour bar axis is rescaled in each iteration.

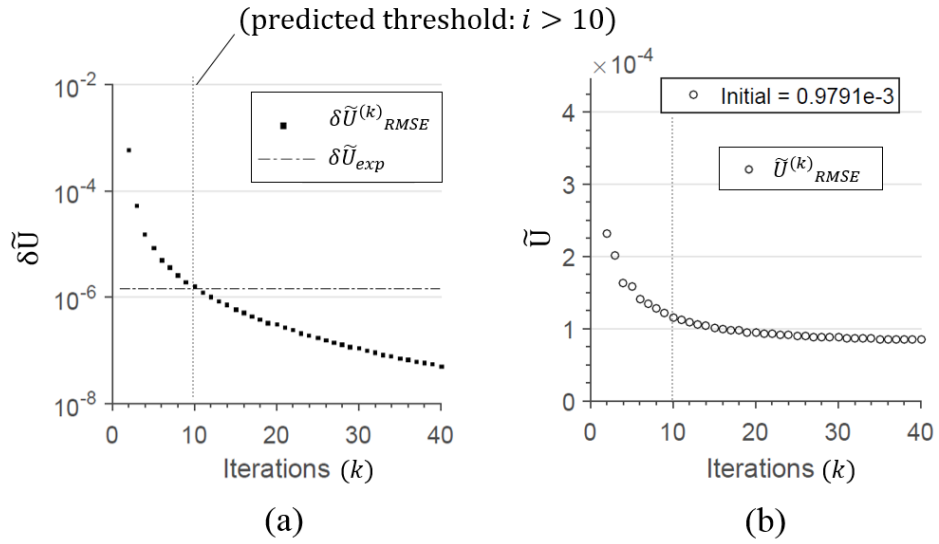

Figure 4.11: (a) Incremental quantities from DIC measurements of the ROI of the inclined crack, (b) Energy increments between initial and final states,

4.4.2 Application to DVC data

This section demonstrates application of the method to DVC data obtained from Magnesium WE43 specimens with mixed mode notch. Volume imaging was obtained from mixed-mode samples at the Stellenbosch University CT Scanner facility, using a glass fibre shear loading rig shown in Figure 4.12a.

The Specimen is Magnesium WE43 (E = 44 GPa, v = 0.35, ρ = 1840 kg / m3) which is well suited to XCT and DVC characterization due to its low attenuation and small percentage of high attenuating precipitates (4wt % Yt, 3wt % Nd), (Mostafavi *et al.*, 2015). The DVC analysis was performed with DaVis v8.3 volume correlation software using a phase-correlation based (FFT) approach with a subset size of 160 voxels, and a step size of 80 voxels. The specimen geometry is shown in Figure 4.12b. The scans were performed with a General Electric Phoenix VTomeX L240 microCT scanner to a voxel resolution of 10 µm, and an experimental accuracy of 7e-3 mm, this corresponds to a $\delta\tilde{U}^{(k)}_{RMSE}$ of 3.6e-5. As can be seen in Figure 4.13, a greater number of iterations was needed before convergence could be achieved at 28 iterations.

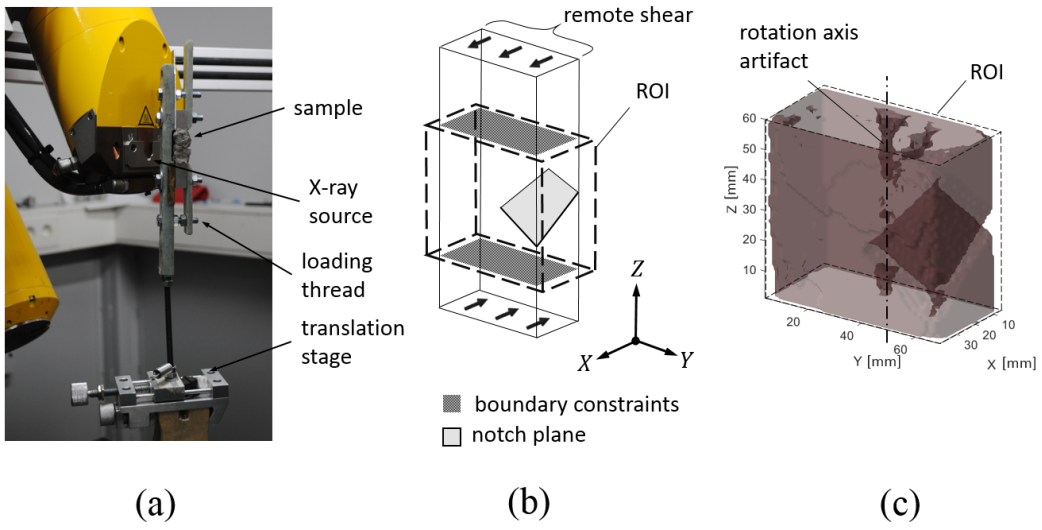

Figure 4.12: The X-ray facilities with specimen in place and translation stage shown (a), specimen geometry (b), rendering of the specimen surface using correlation coefficient

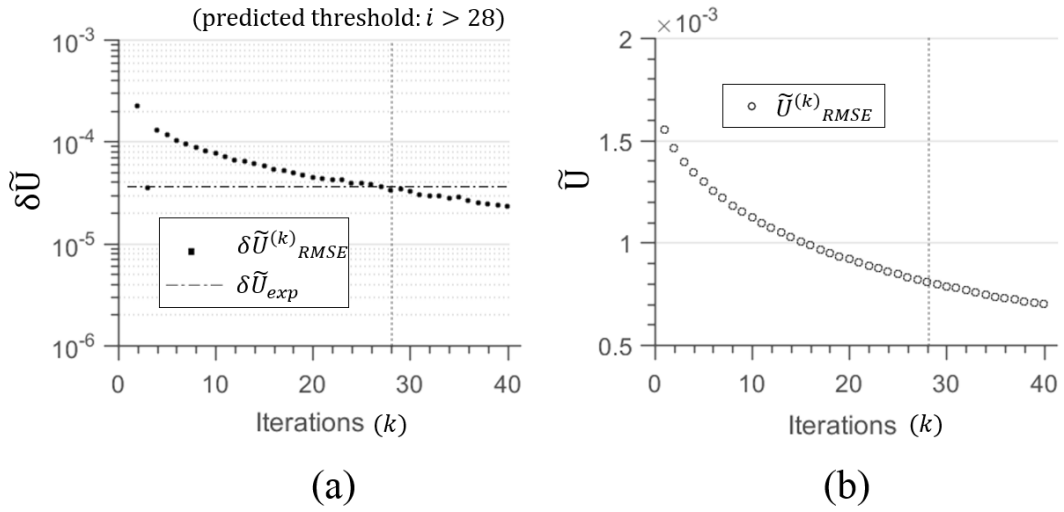

Figure 4.13: (a) Energy increments between initial and final states (top), together with incremental quantities (bottom) from region of interest of the inclined crack DIC measurements

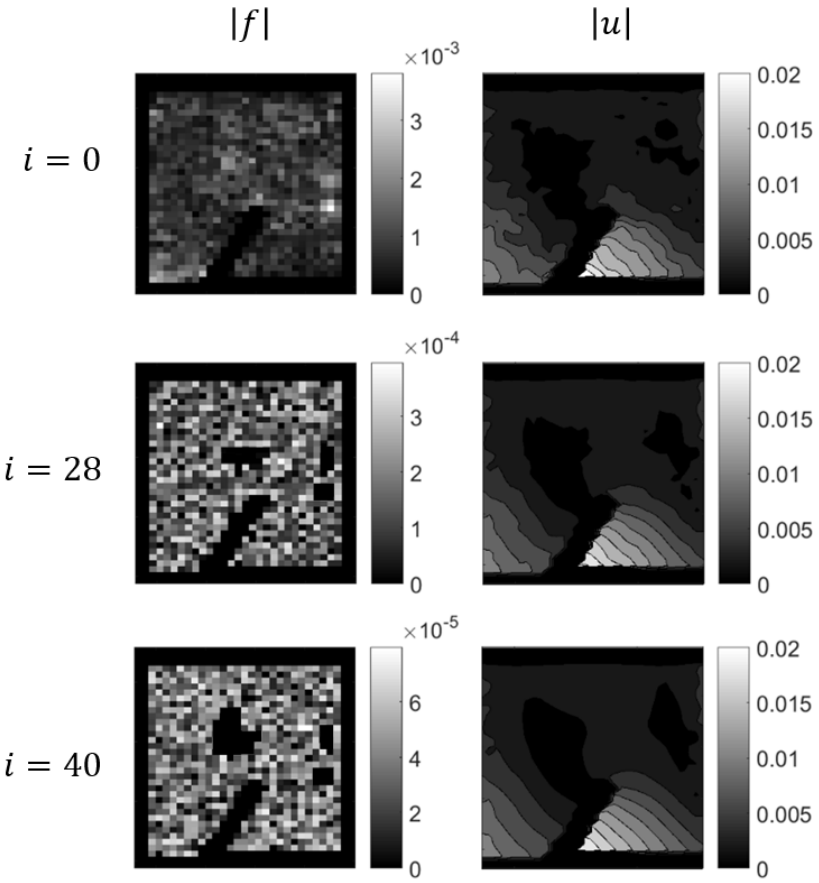

Figure 4.14: Artifact removal from region of interest of the Magnesium specimen (ROI, Figure 4.12b) showing magnitudes of force $|f|$ and displacement $|u|$,
Note: axes are rescaled in each iteration, predicted to converge at iteration 28

4.5 Discussion

The aim of this chapter was to provide a robust method to address DIC and DVC results. The method proposed the removal of outliers detected by the nodal forces, which are replaced with the FE solution using neighbouring unfiltered data as boundary conditions. The effectiveness of the method in separating random noise from outliers is tested in an idealised cantilever example. It was shown through this example (and tested experimentally) that classical random noise related to DIC or DVC accuracy is quantifiable to a relative artefact energy parameter which underpins the convergence criteria of the approach.

Experimentally, the method was found to be effective in the elimination of typical DIC and DVC artifacts. It is unclear to what extent the use of low order elements is effective in the refining of the fields close to the crack front. This has not been investigated further as the J-integral approach using DIC data does not require the crack front data to be accurate (Becker *et al.*, 2012). The volume experiment uses a notch which can be well-represented by the voxel-based method. Note that the left-hand-side figures in Figure 4.14 reveal the removal of the rotation artifacts indicated in Figure 4.12c.

4.6 Summary

Displacement measurement uncertainties, which are often exacerbated when differentiated to obtain strain data, are typically filtered using median or least-squares based approaches. However, these methods do not necessarily remove outliers due to the limitations of local and global based DIC and DVC in terms of spatial resolution. The proposed method provides an efficient and automated framework to detect and replace outliers in full-field displacement data based on the finite element method.

The method constrains FE node points with the experimentally obtained displacement data from DIC or DVC. The resulting nodal reaction forces are then used as a proxy for error in the displacement data. The approach then also uses the FE method to replace outliers with the linear-elastic solution based on the outlier's neighbours. A criterion was developed to terminate the process of outlier identification and replacement at a user-specified displacement accuracy. This criterion is also intended to prevent underlying non-linearities from being affected by the linear-elastic assumption.

The method is demonstrated on two mixed-mode experiments which exhibit outliers: a DIC displacement field from an Arcan specimen, and DVC displacements from a shear loaded bar (both cracks inclined 30°, materials: PMMA and Mg WE43 respectively). Results show that the proposed criteria achieve the predicted experimental noise floor for both experiments.

The method provides a post-experiment filter to iteratively remove outliers until the experimental error distribution is reached. The method is particularly suitable for use with the J-integral as it focuses on the restoration of internal equilibrium, an essential requirement for contour independence.

5 Linking the path-area and volume integral approaches: a hybrid *J*-integral formulation

The aim of the previous chapter was to provide a tool to eliminate outliers in full-field displacement measurements from DIC and DVC and hence in *J*-integral calculations. This chapter follows on from this by developing a volumetric form that is optimally robust to image correlation errors. This chapter therefore continues from section 2.2.5, in which both the surface and volume *J*-integral forms were presented. It may be recalled that either the path-area or volume integral forms may be used to calculated *J* values on the crack front in the volume, however, neither approach can provide a robustness to errors in both crack front position and displacement noise.

This chapter aims to develop a *J*-integral form with improved robustness to both forms of error. The outcome is a *J*-integral form that is a hybrid between the volume and path-area integral. The hybrid form establishes a link between these two famous integrals and demonstrates a trade-off in terms of robustness to both crack front position and random displacement errors.

Presented at the 14th International Conference on Fracture (Molteno and Becker, 2017), this chapter has been prepared for publication in *Strain* (Wiley) with co-authors Marrow and Becker (in no particular order).

The authors contributions are:

- Prof. James Marrow: Provided financial and academic support during the early development of the method at Oxford University.
- Dr Thorsten Becker (project supervisor): Supervisory role.

Other noteworthy contributions from non-co-authors:

- Dr Nicholas Hale: Aided with the mathematical terminology.

5.1 Introduction

The various classical J-integral forms have been introduced in section 2.2.5, showing a variety of methods available for J calculation on the surface or within the volume. However, application of the J-integral to DIC or DVC data is susceptible to the following typical errors:

(1) displacement errors distributed evenly throughout the field and,

(2) localised errors due to high strain gradients near the crack tip, leading to displacement artifacts, and uncertainty in the crack front position.

The previous chapter focused on error type (1) by eliminating the non-random errors from the integration region before J is calculated. This is beneficial because random errors have a significantly smaller effect in methods which involve integration (due to cancellation of positive and negative errors). The previous chapter also demonstrates the removal of crack tip artifacts, i.e. type (2). However, the method assumed a prior knowledge of the crack tip position. Determination of crack tip position is typically done by visual inspection on the surface. However, mechanical effects such as crack closure, and the resolution limitations of the imaging system, tend to introduce uncertainty in any crack tip position estimate (Maire and Withers, 2014). Some approaches achieve improved accuracy and objectivity by fitting displacement fields with analytical crack tip fields (Yoneyama *et al.*, 2006; Huchzermeyer, 2017), or the automatic discontinuity detection technique using phase congruency (Cinar *et al.*, 2017). However, these approaches are still limited by the spatial resolution that can be provided by image correlation near to the crack front.

These reasons have motivated for the use of the J-integral in the Hypothesis (section 3.1), due to the ability to select far field data, lessening the dependence on crack front data. This also increases the statistical averaging of errors addressing (1) (Becker *et al.*, 2011; Becker *et al.*, 2012). In DVC data, the volumetric J-integral forms are required, in which integration of the crack front data is unavoidable (see section 2.2.5). However, two J-integral forms exist that are uniquely robust to either (1) or (2): the path-area integral and the volume integral.

The path-area integral (Equation (2.37)) enables the extraction of point-wise J-values at the location where the contour plane crosses the crack front. A notable advantage of the path-area integral is that the location of the crossing does not affect the J value – assuming that other numerical factors (e.g. computing of displacement gradients across the crack discontinuity) contribute a constant error. The drawback is that the numerical computation is highly sensitive to displacement errors of type (1), usually attributed to the differentiation of stresses in the J_p term. As a result, the path-area integral is typically avoided in discretised methods, such as FEM. The method is mostly applied in the Boundary Element Method (BEM) in which the displacement gradients are represented accurately in integral form[23] (Aliabadi, 1997; Sollero and Aliabadi, 1992).

Generally, the more suitable approach for noisy data is the volume integral (Equation (2.39)). The stability of this form derives from the use of a larger integration volume, facilitated through a derivation using the virtual crack extension field, Q, and its derivatives (see Equation (2.40)). The differentiation does not necessarily generate errors, as Q can be specified to possess analytical derivatives. However, misplacement of the crack tip location results in errors in computing the weighting term $1/A_c$ in Equation (2.39). As a result, errors in crack front position can cause

[23] Derived from the Somigliana identity in post-processing of the BEM results.

uncertainties in J-estimates of several percent in DVC data (Rannou *et al.*, 2010). In this study, a procedure using shape functions enriched with crack tip fields was used to locate the crack front.

The background on both the path-area and volume integral forms has been provided in section 2.2.4. However, in this section the link between them was not established. Such a link could not be found in literature, possibly due to the unique way each method has been derived (Blackburn, 1972; Shih *et al.*, 1986; Rigby and Aliabadi, 1993). For example, although the path integral has been transformed into equivalent domain integrals on the surface and the volume, no such attempt has been applied to the path-area integral (see the summary of integral forms in Table 2.1). This could provide similar improvements to robustness, as experienced by the other original integral forms. The aim of this chapter is to establish such a link between the volume and path-area integrals, and attempt to reconcile the properties of the two integrals – robustness to random displacement errors, and robustness to positional uncertainty – in a single integral form.

To achieve this, the plan of this chapter is as follows: the first two sections focus on linking the path-area integral and the volume integral. This is achieved in two stages. Firstly, an equivalent domain integral form of the path-area integral is derived, here named the surface-volume integral; secondly, the surface-volume form is used to establish a hybrid form based on both the path-area and volume integral forms. This last form provides the link between volume and path-area integrals. The final section tests the derived approaches against FE generated fields with superimposed errors of types (1) and (2). The results are summarised in the final section (final results summarised in Figure 5.6).

5.2 Derivation of a volumetric form of the path-area integral

The numerical instability of the path-area integral mainly arises from the area J_a term (Equation (2.37)), which contains x_3 derivatives of stress (the last term of Equation (2.37)). Therefore, the objective of this section is to transfer this partial derivative from the stress term to a more stable (user defined) function using the divergence theorem.

Setting Equation (2.23) equal to Equation (2.37) and multiplying by $q(s)$ gives Equation (5.1). The contour from Equation (2.37) is given the subscript ε (Γ_ε) to separate it from Γ on the right-hand-side which does not tend to zero on the crack front. Note that Equation (2.37) does not include crack face terms by assuming that crack face tractions are zero (Rigby and Aliabadi, 1998). As $q(s)$ is constant everywhere in the x_1, x_2 plane for a particular s value, it can be moved inside the integration:

$$\lim_{\Gamma_\varepsilon \to 0} \int_{\Gamma_\varepsilon} \left(W n_1 - \sigma_{ij} \frac{\partial u_i}{\partial x_1} n_j \right) q(s) d\Gamma$$

$$= \int_{\Gamma} \left(W n_1 - \sigma_{ij} \frac{\partial u_i}{\partial x_1} n_j \right) q(s) \mathrm{d}\Gamma \qquad (5.1)$$

$$- \int_A \frac{\partial}{\partial x_3} \left(\sigma_{i3} \frac{\partial u_i}{\partial x_1} \right) q(s) dA, \quad (i,j = 1,2,3)$$

The weighted average of J values across the line segment Δs using $q(s)$ as a weighting function (inset of Figure 5.1) is denoted $\tilde{J}_{\Delta s}$ and is approximately equal to global energy release rate as follows:

$$-\frac{\delta\pi}{A_c} \cong \tilde{J}_{\Delta s} = \frac{\int_{\Delta s} J(s)q(s)ds}{\int_{\Delta s} q(s)ds} \tag{5.2}$$

in which $\delta\pi$ is the reduction in energy of the global system and A_c is the crack extension area shown in Figure 2.9b. Note that if $q(s) = 1$ then $\tilde{J}_{\Delta s}$ is the statistical mean of the point-wise $J(s)$ values over the length of Δs. Integrating across Δs:

$$\int_{\Delta s}\left[\lim_{\Gamma_\varepsilon \to 0}\int_{\Gamma_\varepsilon}\left(Wn_1 - \sigma_{ij}\frac{\partial u_i}{\partial x_1}n_j\right)d\Gamma\right]q\mathrm{d}s$$

$$= \int_{\Delta s}\int_{\Gamma}\left(Wn_1 - \sigma_{ij}\frac{\partial u_i}{\partial x_1}n_j\right)q\,d\Gamma\,ds \tag{5.3}$$

$$-\int_{\Delta s}\int_{A}\frac{\partial}{\partial x_3}\left(\sigma_{i3}\frac{\partial u_i}{\partial x_1}\right)q\,dA ds, \quad (i,j = 1,2,3)$$

Referring to the original volume integral definition in volume V of Figure 2.9b - partitioned into an outer volume V_1, and an inner volume V_0, sharing the surface S_0, and enclosed by end-caps S_{a1}, S_{b1}, S_{a0}, S_{b0}, the crack faces S_c, and the outer surface S_1 as shown in Figure 5.4.

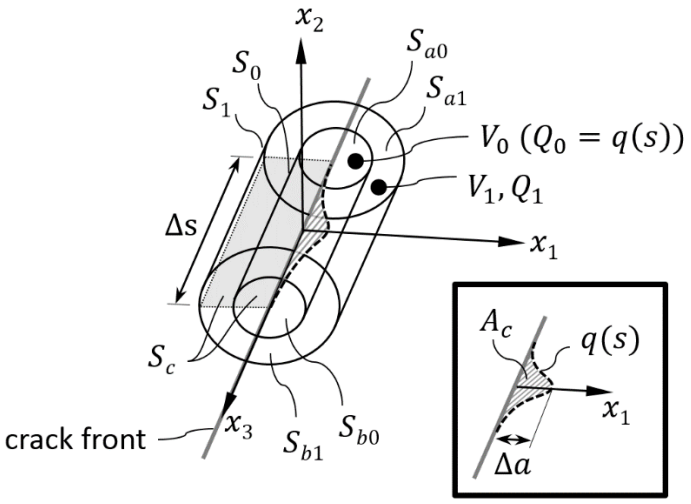

Figure 5.1: Surfaces (S) defining the surface-volume integral and the volume integral over crack front segment Δs. Surfaces with subscripts 0 and 1 define volumes V_0 and V_1 respectively, S_a and S_b are the end-caps and S_c includes the upper and lower crack faces for V_0 and V_1.

Subsequently, the differentials can be simplified to volume ($\mathrm{d}A\mathrm{d}s = \mathrm{d}V$), and surface ($\mathrm{d}\Gamma\mathrm{d}s = \mathrm{d}S$) elements respectively. Note that n_j is now the outward pointing normal to dS in x_1, x_2 plane on S_0 and S_1. Therefore, the first integral on the right-hand-side of Equation (5.3) becomes an integral over surface S_1 and the second integral becomes a volume integral throughout V_1. The result is that the integral on the left-hand-side of Equation (5.3) becomes a tube (S_0), that (in the limit) converges on the crack front over Δs. Rewriting Equation (5.3) with new integral definitions gives,

$$\lim_{S_0 \to 0} \iint_{S_0} \left(W n_1 - \sigma_{ij} \frac{\partial u_i}{\partial x_1} n_j \right) q \mathrm{d}S$$

$$= \iint_{S_1} \left(W n_1 - \sigma_{ij} \frac{\partial u_i}{\partial x_1} n_j \right) q \mathrm{d}S \tag{5.4}$$

$$- \iiint_{V_1} \frac{\partial}{\partial x_3} \left(\sigma_{i3} \frac{\partial u_i}{\partial x_1} \right) q \mathrm{d}V, \quad (i,j = 1,2,3)$$

Now carrying out the limit $S_0 \to 0$, converts the left-hand-side of Equation (5.4) to a line integral across Δs. This represents the weighted average as defined by Equation (5.2), for the path-area integral along crack front segment Δs ($\tilde{J}_{\Delta s}$).

Asserting that the crack front is straight on Δs, then $\mathrm{d}s = \mathrm{d}x_3$. Then, applying the divergence theorem to the last term gives,

$$\int_{\Delta s} J(s) q(s) ds = \tilde{J}_{\Delta s}(s) \int_{\Delta s} q dx_3$$

$$= \iint_{S_1} \left(W n_1 - \sigma_{ij} \frac{\partial u_i}{\partial x_1} n_j \right) q \, dS \tag{5.5}$$

$$+ \iiint_{V} \left(\sigma_{i3} \frac{\partial u_i}{\partial x_1} \right) \frac{\partial q}{\partial x_3} dV - \left[\left(\sigma_{i3} \frac{\partial u_i}{\partial x_1} \right) q(s) \right]_{S_{a1}}^{S_{b1}}, \quad (i,j = 1,2,3)$$

The simplification of the integral operators in Equation (5.5) reveals the weighted path-area integral (J_{w-pa}),

$$J_{w-pa}(\mathrm{s}) = \frac{1}{A_c} \int_{S_1} \left(W n_1 - \sigma_{ij} \frac{\partial u_i}{\partial x_1} n_j \right) \mathrm{d}S$$

$$- \frac{1}{A_c} \int_{V} \frac{\partial}{\partial x_3} \left(\sigma_{i3} \frac{\partial u_i}{\partial x_1} \right) \mathrm{d}V, \qquad (i,j = 1,2,3) \tag{5.6}$$

Note that the divergence theorem acts on a scalar partial derivative, and so reduces to integration by parts. Setting $q = 0$ at the ends of Δs (S_{a1} and S_{b1}), the third term on the right-hand-side is zero. Usually q is also set to zero on S_1 to manipulate the integral to a volume integral. However, this derivation requires that q has a constant value (i.e. zero gradient) in directions perpendicular to the crack front. In implementations on straight cracks, this requires that the value for q on S_1 is equal to q on the crack front. It is worth mentioning that a similar derivation using arbitrarily valued q on S_1 can be derived with the same steps, however, this results in a classical volume integral with an extra surface integral and so was not pursued further.

The final step is to divide by the crack extension integral on the left-hand-side ($\int_{\Delta s} q_k(x_3)dx_3 = A_c$). The resulting J-integral in Equation (5.7) includes a surface integral and a volume integral and so is called the surface-volume integral with the symbol J_{s-vol},

$$J_{s-vol} = \frac{1}{A_c}\int_{S_1}\left(Wn_1 - \sigma_{ij}\frac{\partial u_i}{\partial x_1}n_j\right)qdS + \frac{1}{A_c}\int_V\left(\sigma_{i3}\frac{\partial u_i}{\partial x_1}\right)\frac{\partial q}{\partial x_3}dV, \quad (i,j = 1,2,3) \tag{5.7}$$

Equation (5.7) can be used to extract arc-weighted J-integral values from straight crack fronts with planar crack faces in 3D. It is more numerically stable than the path-area integral (as tested later), because the partial derivative in the last term has moved to the q function.

The first term on the right-hand-side of Equation (5.7) can be recognised as the classical volume integral (Equation (2.39)) but with a Q function that is equal to the crack front extension function q, and therefore only changes in the x_3 direction. The second term is an additional surface integral that emerges when the Q function is non-zero on a volume boundary. Some further insight into the reason for the second term can be gained by reverse derivation from the volume integral formula using the crack front extension q in place of the Q function. This is shown in the Appendix.

5.3 A hybrid path-area - volume integral

The aim of this section is to provide a link between the path-area and volume integral. To achieve this the integration volume is partitioned into two parts: an inner volume (V_0) with a Q-function equal to the virtual crack front extension (called Q_0), and an outer volume V_1 with the classical volume integral Q-function (called Q_1), as shown in Figure 5.1. At the end of this section, the two integration volumes are combined to show that the surface-volume integral is only a special case of the volume integral.

Applying the surface-volume integral in Equation (5.7) on the inner volume V_0 gives:

$$J_{s-vol_0} = \frac{1}{A_c}\int_{S_0}\left(Wn_1 - \sigma_{ij}\frac{\partial u_i}{\partial x_1}n_j\right)Q_0(x_3)\mathrm{d}S + \frac{1}{A_c}\int_{V_0}\left(\sigma_{i3}\frac{\partial u_i}{\partial x_1}\right)\frac{\partial Q_0(x_3)}{\partial x_3}\mathrm{d}V, \quad (i,j = 1,2,3) \tag{5.8}$$

The outer volume V_1 is then assigned a Q-function Q_1, that is zero on S_1, S_{a1}, S_{b1} and equal to $q(s)$ on S_0, and is C^1 continuous with Q_0 on S_0. Applying the divergence theorem to Equation (2.37) now results in an additional surface integral on S_0 (using the procedure in the Appendix).

$$J_{vol_1} = \frac{1}{A_c}\int_{V_1}\left(\sigma_{ij}\frac{\partial u_i}{\partial x_1}n_j - Wn_1\right)\frac{Q_1}{\partial x_1}dV \tag{5.9}$$

$$-\frac{1}{A_c}\int_{S_0}\left(Wn_1-\sigma_{ij}\frac{\partial u_i}{\partial x_1}n_j\right)Q_1(x_3)dS,\quad (i,j=1,2,3)$$

Adding Equations (5.8) and (5.9), the surface integrals cancel, leaving volume integrals within V_0 and the tube surrounding V_0 (i.e. V_1). This is the last integral form developed in this chapter, and is termed the hybrid integral because it contains a path-area form in V_0 (which has been modified to eliminate derivatives of stress from the crack front), and a classical volume integral form in V_1. The resulting hybrid integral J_{hyb} is given as:

$$J_{hyb}=J_{s-vol_0}+J_{vol_1}$$

$$J_{hyb}=\frac{1}{A_c}\int_{V_0}\left(\sigma_{i3}\frac{\partial u_i}{\partial x_1}\right)\frac{\partial Q_0(x_3)}{\partial x_3}dV \tag{5.10}$$

$$+\frac{1}{A_c}\int_{V_1}\left(\sigma_{ij}\frac{\partial u_i}{\partial x_1}n_j-Wn_1\right)\frac{\partial Q_1}{\partial x_i}dV,\quad (i,j=1,2,3)$$

A hybrid Q-function Q_{hyb} created from the union of Q_0 and Q_1 ($Q_{hyb}=Q_0+Q_1$) is differentiable throughout $V=V_0+V_1$, zero on its outer surfaces (S_{a1}, S_{b1}, S_{a0}, S_{b0} and S_1), and equal to q on the crack front. Therefore Q_{hyb} also meets the requirements of the virtual crack extension function used in the classical volume integral (Shih *et al.*, 1986), and so can be written as;

$$J_{hyb}=\frac{1}{A_c}\int_{V_1}\left(\sigma_{ij}\frac{\partial u_i}{\partial x_1}n_j-Wn_1\right)\frac{\partial Q_{hyb}}{\partial x_i}\mathrm{d}V,\quad (i,j=1,2,3) \tag{5.11}$$

in which Q_{hyb} is the same as the classical virtual crack extension function defined in Equation (2.40), but with the additional constraint on the gradients perpendicular to the crack front,

$$\frac{\partial Q_{hyb}}{\partial x_i}=0\ \text{ in } V_0,\qquad (i=1,2) \tag{5.12}$$

This can be verified very concisely by applying Q_{hyb} in the classical volume integral (Equation (2.39)) and writing the result as a sum of the parts of Q_{hyb} belonging to V_0 and V_1 respectively. Therefore Equation (5.10) is a convenient link between the path-area and volume integral through the derivation above, as can be illustrated by reducing V_1 to zero. It is worth noting that we could have gone another route from Equation (5.8), in which J_{s-vol} is applied to the outer tube V_1 and the volume integral to the inner volume V_0, but this would introduce an extra surface integral which does not provide further insight without any apparent advantage.

5.4 Review of developments

The previous derivations have produced several intermediate integral forms between the classical path-area and volume integrals (Equations (2.37) and (2.39)), these being the: arc-weighted-path-

area ($J_{w\text{-}pa}$, Equation (5.6)), surface-volume integral ($J_{s\text{-}vol}$, Equation (5.7)), and the tube-volume integral (the hybrid form: J_{hyb}, Equation (5.10)). The developed J forms – which have been derived from the path-area form – are expected to be invariant to crack front position errors, and so may be advantageous in DIC and DVC experiments. This can be illustrated by observing the gradients of Q in the in-plane (a-c) and out of plane (d) directions shown in Figure 5.2. The sensitivity of these integrals is related to Q (the second column) due to the calculation of A_c. Therefore, the path-area derived forms (a-b) are unaffected because Q does not vary close to the crack front. The path-area integral also has this property, but does not have a volumetric Q function and so is not shown.

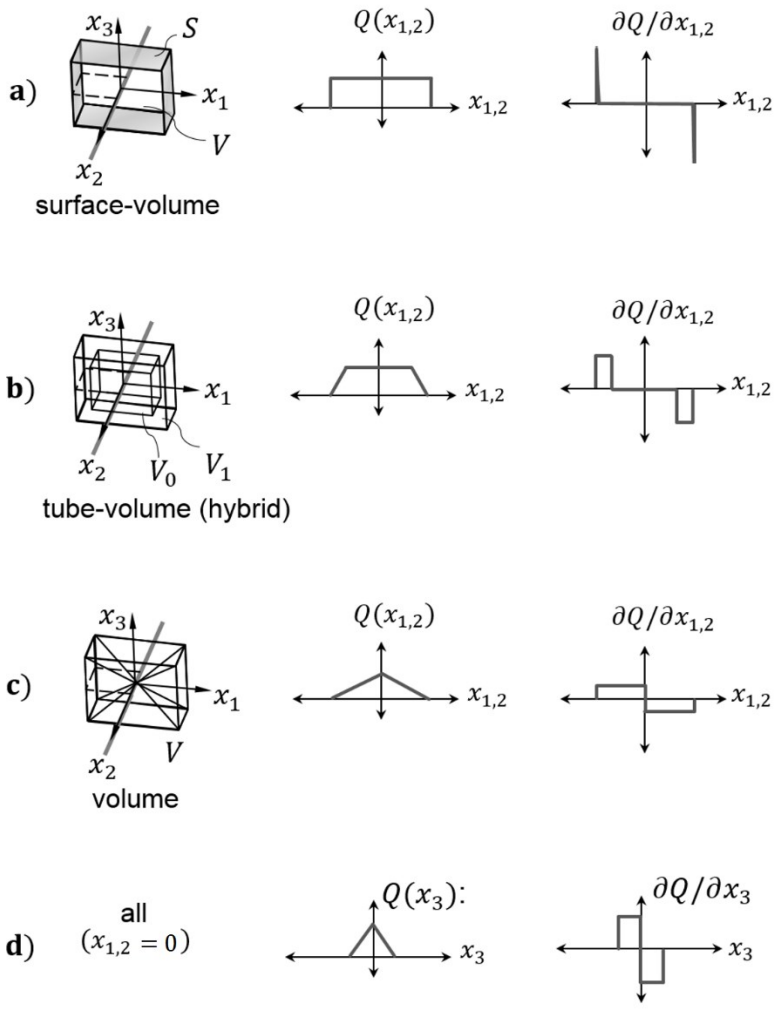

Figure 5.2: Illustration of the surface-volume integral ($J_{s\text{-}vol}$), the tube-volume integral (J_{hyb}), and the classical volume integral (J_{vol}), with Q functions and derivatives shown

However, the advantage of the volume integral is robustness to errors. This can be seen in the $\partial Q/\partial x_{1,2}$ column, as the volume integral is weighted over a larger field of view (Figure 5.2c). These aspects of numerical performance (crack front position uncertainty, random displacement noise), are tested in the next section.

5.5 Example on numerical fields

An example problem of a rectangular single edged block modelled using Abaqus finite element software (v. 6.13) is presented. The block ($20 \times 20 \times 40$) is loaded by displacements of $\pm< 0.5;\ 0.5;\ 0.5 >$ on the top and bottom surfaces ($X_2 = \pm 20$) respectively, to obtain asymmetric J values along the crack front from the applied mixed-mode loading. Note that the procedure to

place an integration volume at a location on the crack front is presented in Chapter 7. In this section the integration volume is translated along the crack front (i.e. accurately over the crack front) with random noise added to the displacement fields, and then translated randomly transverse to the crack front to determine sensitivity to crack front positional errors (random noise not present). The implementation of the volume integral is described in detail in Chapter 7 - specifically the positioning of the integration volume for each J calculation is explained in Figure 7.10, and Table 7.1c.

Linear-elastic kinematic fields and J values were obtained from Abaqus, using a Young's modulus and Poisson's ratio of E = 100 GPa, ν = 0.3. The usual crack treatment procedure of quarter point elements and mesh refinement were not applied in this case, as some ill-conditioning is tolerated by the J-integral (Kuna, 2013b). Instead, a 'banded' refinement was used which allowed simple implementation in Matlab by means of a regular grid, Figure 5.3b.

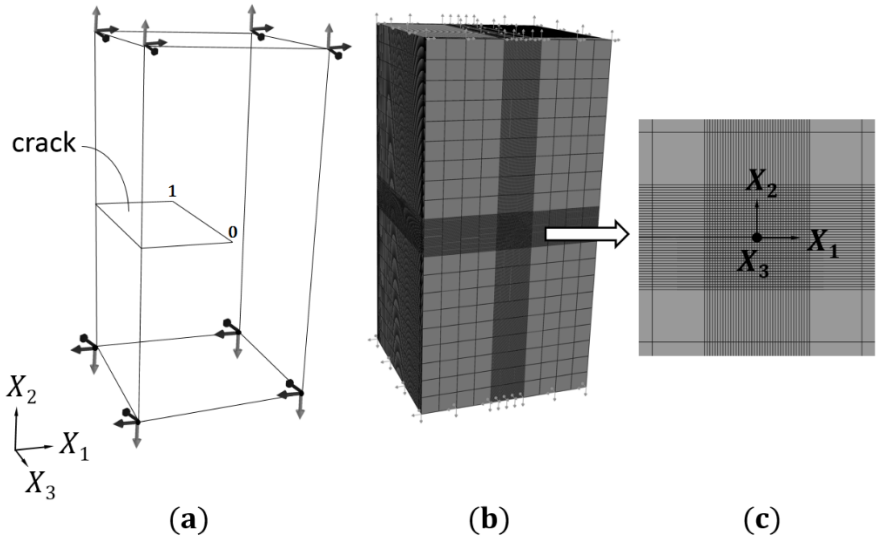

Figure 5.3: FEM mesh showing (a) boundary conditions and crack front (0→1), (b) surface mesh, and (c) banded crack region

Displacement, stress and strain fields were exported for computation of the path-area, surface-volume, tube-volume and classical volume integrals using Matlab ver. 2015b, with a crack front length $\Delta s = 1$ (5 % of the crack front). A linear Q-function as defined in (Shih *et al.*, 1986) was used in the volume integral, from which the same crack front extension q was used to generate $\tilde{Q}$ and the hybrid $Q_{hyb} = Q_1 + \tilde{Q}_0$. The ratio of the volumes occupied by the outer Q_1 and inner $\tilde{Q}_0$ in Q_{hyb} was 50 %. To compare results from the various volume integrals to the original (point-wise) path-area integral, average values of the path-area integral (Equation (2.37)) over crack segment Δs were used. The Abaqus computed J values from the 6th contour (element distances from the crack front) were used as the benchmark result. The results show close agreement (within 1 %) between the path-area, surface-volume, tube-volume and volume integrals, as compared with Abaqus results (Figure 5.4a).

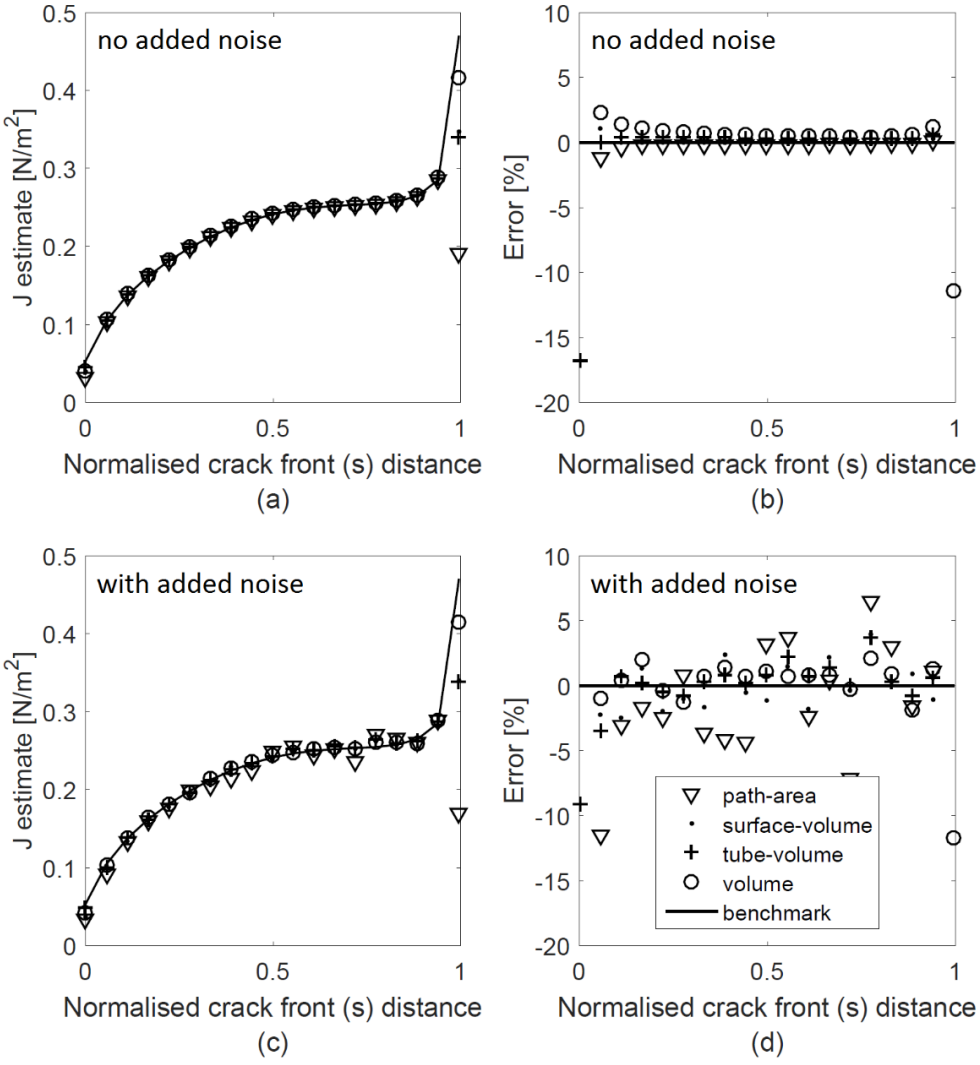

Figure 5.4: (a) *J* results obtained from finite element obtained kinematic fields, (b) showing only the error from a, (c) *J*-values obtained after introducing noise, (d) showing only the error from c

Random displacement noise

To assess robustness to displacement errors, random white noise was added to the FE displacement fields with a signal-to-noise ratio of 51 dB on the displacement fields (0.01 % based on the FE model units). This value was estimated from experimental digital volume correlation displacement fields obtained from loaded Magnesium alloy (WE43) specimens and X-ray computed tomography imaging (T. J. Marrow *et al.*, 2014). Figure 5.4c shows the estimated *J* values computed from kinematic fields with errors deviating from the envelope (compare with Figure 5.4a). To highlight the errors, the axes are rescaled in Figure 5.4d using the Abaqus results as a benchmark. Note that although the volume integral contains a greater bias in the results in Figure 5.4b, it is the most rhobust to random noise as shown in Figure 5.4d. Note that these errors, together with the positional errors shown in the next section, are summarised in Figure 5.6.

Crack front position uncertainty

The intention of this section is to understand the nature and scale of the error in *J* estimates from each integral form, resulting from misalignment of the integration volume (Figure 7.10). This is defined as translation from the crack front in Euclidean distance, and does not include rotation, which is tested separately in Chapter 7. The resulting translations were normalised with respect to

the width of the integration volume as defined in Figure 7.2, and averaged from $1e4$ computations for each point in the range shown.

The results in Figure 5.5 confirm that the surface-volume, tube-volume (hybrid form), and path-area integral forms are invariant to such positional errors. Also, confirming the relative sensitivity of the volume integral, which is exponential in nature. This can be expected, as the error in J should be proportional to $1/A_c$ – the co-efficient in Equation (2.39). These results, assuming a positional error is in the order of the width of the integration region (i.e. 1 %), are added to the final results in Figure 5.6.

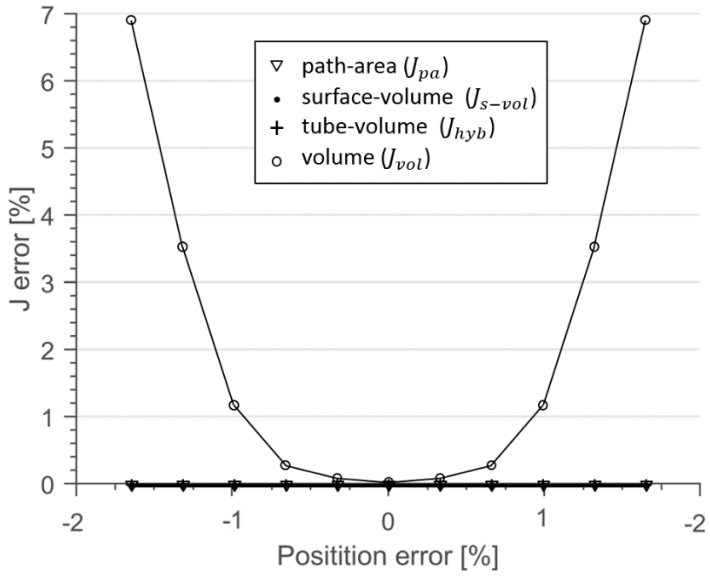

Figure 5.5: J-integral errors due to positional errors

Figure 5.6 shows that the volume integral exhibits the highest noise resilience, and the path-area integral is most vulnerable to noise, as expected. Furthermore, a marked improvement is achieved from the transformation of the path-area integral to the surface-volume integral form, and the hybrid 'tube-volume' integral form achieves slight further improvements (less than 1 %). It is clear that the volume form outperforms the others in robustness to random errors. However, considering the total error, including the displacement uncertainty, the $1/A_c$ errors become prominent in the volume form.

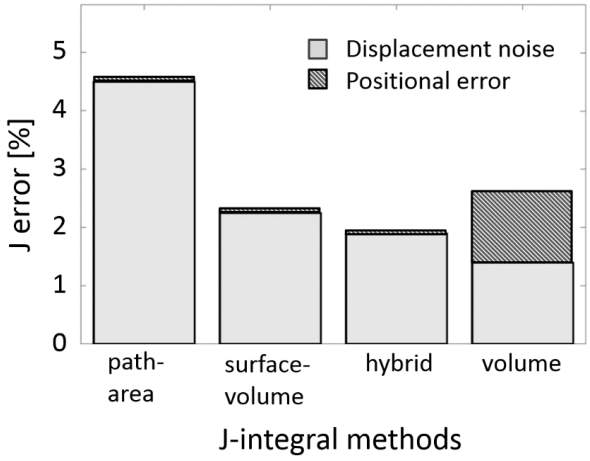

Figure 5.6: Comparison of J-integral total errors from displacement noise and positional errors

5.6 Discussion

The main objective of this chapter was to provide a theoretical explanation for the mechanisms of noise resilience between the path-area and the volume integral forms. As a secondary goal, the equivalent domain integral form of the path-area integral was developed.

It was shown that to achieve this, a virtual crack extension field is needed in which the Q-function is equal to the crack extension along the crack front. This interpretation has a possible advantage over the volume integral in terms of the simplicity of the Q function, and provides an improvement in noise resilience compared to the path-area integral by a factor 2. Although not shown in this chapter, a more concise derivation of the surface-volume integral is also possible by following the procedure of (Shih *et al.*, 1986). This is presented separately in the Appendix. To illustrate the consistency between surface-volume and volume integrals, a hybrid form is derived in which the surface-volume integral is applied to an inner volume and the classical volume integral to the outer volume. In this case, the result is equal to the classical volume integral in which the region of the Q function enclosing the crack front is equal to the virtual crack front extension. The hybrid form provides a link between the classical path-area integral and the volume integral equations.

A numerical example has been provided which confirms the improved noise resilience of the volume integral over the path-area integral as quoted in literature (Kuna, 2013b; Shih *et al.*, 1986). The main difference between J_{s-vol} and the path-area integral is that out-of-plane (x_3) derivatives of stress that appear in the path-area integral are no longer present, leading to a significant improvement in noise resilience. The reduced noise resilience of the hybrid tube-volume integral versus the classical volume integral, confirms the result that the volume integral is best if only noise resilience is required.

The authors note that the accuracy improvements of J_{s-vol} may be more apparent in cases where out-of-plane deformation errors are more significant, as in large-scale plasticity for example. On this point, the usefulness on plastic problems has not been investigated, but would require more careful consideration of the mesh design and the selection of crack tip elements. Out-of-plane errors in experimental volume displacement fields may lead to significant errors in damage and fracture estimates based on the surface based J-integrals (Molteno and Becker, 2013). Further work is required to determine the usefulness of the surface-volume integral in these cases.

5.7 Summary

This chapter studied the numerical errors in the path-area and volume integral forms due to: random errors, and crack tip position errors. This was achieved in the following steps.

- The equivalent domain integral method was applied to the path-area integral to derive a surface-volume integral (J_{s-vol}) form. This achieves the elimination of the stress derivatives in the integrand of the path-area integral.
- A hybrid between the path-area and volume integrals was developed providing a link between the classical volume and path-area integral forms.
- Numerical experiments using finite element data and synthetic errors were conducted to test the various integral forms for resilience against both random errors and crack tip position errors.

- The various path-area derived forms are all resilient to crack tip position errors, but not necessarily to random errors. Conversely, the classical volume integral is most robust to random errors.
- Accounting for positional errors, the hybrid form of the J-integral was determined to be the most robust to both forms of errors.

6 Mode I-III decomposition of the J-integral from DIC displacement data

This chapter presents the implementation of the decomposition method on DIC displacement fields to obtain J-integral results and respective SIFs. The main aim of this work is to validate the use of the decomposition method applied directly to DIC displacement fields using the classical J-integral approach. The method is tested in three stages: analytically, experimentally on separate modes I, II and III, and on a mixed-mode experiment. The chapter therefore concerns the third objective of this thesis (section 1.5.3).

This chapter was published in *Strain* (Wiley) (Molteno and Becker, 2015c). The error assessment strategy based on analytical fields was presented at CFRAC (Molteno and Becker, 2015a), and the experimental work was presented at BSSM (Molteno and Becker, 2015b). The contributions of the authors are:

- The author (Matthew Molteno): Implementation of the method and completion of all tests and results.
- Dr Thorsten Becker (project supervisor): Outside of the ordinary supervisory role – assistance in the conception and theory required for mode III implementation of the J-integral, which is not typically applied with DIC data (as $K_{III} = 0$ under the typical plane stress assumptions on the surface).

Other noteworthy contributions from non-co-authors:

- Mr Johan Conradie: Assistance with the measurement of fracture toughness values for the sample material (PMMA) according to ASTM standards (ASTM International, 2015).
- Dr Mahmoud Mostafavi: Details of Arcan testing and numerical implementation of the J-integral in planar form.

Note that the publication (Molteno and Becker, 2015c) has been provided verbatim, apart from formatting. Therefore, some repetition may exist.

6.1 Introduction

The capability to accurately predict failure alleviates numerous risks and costs related to over conservative designs and catastrophic failures. As such, the management and understanding of cracking is a fast-growing specialisation in industry and research[24]. Usually the first approach is to measure the strain energy release rate of a crack system under loading and compare this to the materials fracture toughness. However, measuring fracture toughness' via modelling approaches is often complex, and fracture toughness values measured in lab conditions are not always applicable to components that have accumulated damage over long periods or extreme conditions. In these cases, *in situ* fracture measurement may form an important part of the damage modelling framework (section 1.1). Furthermore, numerous failures in engineering structures occur under complex loading (e.g. pressure vessels, pipe lines, aerospace). In these cases, it is necessary to decompose the strain energy release rates into Mode I, II and III components.

Optical methods may be used to obtain displacement measurements from the full-field of a fractured geometry. This enables the measurement of fracture properties from non-standard parts and mixed Mode I-III loading *in situ* (McNeill *et al.*, 1987; Réthoré *et al.*, 2005). For this purpose the Digital Image Correlation (DIC) method is frequently favoured (Sutton *et al.*, 1983). DIC resolves displacement fields from sequences of digital images taken of a solid structure during loading. This is achieved by comparing the texture displacements of the deformed images to a reference image, usually of the unloaded structure. Other advantages are that digital images are intuitive, and may be reprocessed with different parameters until an optimal displacement field is obtained. DIC is also extendable to 3D volumes when X-ray imaging is available (Marrow *et al.*, 2014).

In brittle materials, Mode I-III strain energy release rates may be directly converted to stress intensity factors (SIFs), denoted $K_{I\text{-}III}$. SIFs have been extensively studied such that analytical solutions are available which directly relate SIFs to crack tip displacement fields (Williams, 1957). In this way, SIFs may be determined by fitting analytical fields to experimental or model data, as first outlined by McNeill *et al.* (1987). An advantage is that analytical fields may be fitted directly to experimental displacement fields without computing stresses. This approach has been extended to non-homogenous materials[25] (Abanto-Bueno and Lambros, 2002; Méité *et al.*, 2013), higher order terms, and small scale plasticity (Réthoré, Roux, *et al.*, 2011). Separate Mode I-III SIFs can be obtained by fitting mixed $K_{I\text{-}III}$ crack tip fields with the methods of Réthoré *et al.* (2005), or using the integrated approach (I-DIC)[26] of Roux and Hild (Roux and Hild, 2006).

However, field fitting approaches may be ill-suited to cases where the crack tip region is poorly defined; as in large scale plasticity, crack branching, or micro-cracking (e.g. graphite or concrete) (Becker *et al.*, 2011). Furthermore, displacement fields in regions near the crack tip are a challenge to measure using DIC methods. This is because DIC usually assumes a small set of deformation parameters for efficiency purposes. As a result sharp discontinuities, and crack tip singularities tend to be inconsistent with the assumed deformations within a subset (region of analysis) causing poor correlation in crack regions (Poissant and Barthelat, 2010).

---

[24] Linked to recent pressures for sustainable power generation in South Africa, and plans for expansion to sustain future economic growth (Winkler, 2007), as discussed in the introduction.

[25] Using the relation that crack tip stress fields are consistent between homogenous and non-homogenous materials.

[26] Optimisation of the analytical displacement field K factors for pixel mapping to match image data directly as opposed to fitting to DIC obtained displacement data.

Of particular interest is the J-integral approach. This enables the computation of the scalar J value through a single integration of crack tip fields surrounding a crack tip. The J-integral is applicable to both elastic (Rice, 1968) and plastic (Hutchinson, 1968; Rice and Rosengren, 1968) materials, where J values may be converted directly to SIFs in the elastic case. A disadvantage of the J-integral approach is that stresses and strains are required. However, the integral is contour independent enabling the user to select data in regions far from the crack tip – where the material model is simpler, and DIC measurements are less likely to fail. Becker et al. (2012) evaluated the J-integral directly from DIC results using efficient finite element method (FEM) elements, in which nodal displacements were constrained with DIC obtained displacements. FEM enforced continuity and the area integral were shown to improve the accuracy. Yoneyama et al. (2014) showed that elastic-plastic stresses could be calculated at DIC control points by direct inversion of the deformation plasticity equations, and applied this approach to J line integral, area integral, and elastic-plastic HRR (Hutchinson-Rice-Rosengren) field fitting methods with close agreement.

Unlike field fitting approaches, specialised methods are needed to separate J into Mode I-III components (denoted $J_{I\text{-}III}$). An early approach by Budiansky and Rice used the J^2 integral – derived normal to the crack plane – together with J^1 to solve for $J_{I\text{-}III}$ values (Budiansky and Rice, 1973). However, it was shown by Herrmann and Herrmann that contour dependence in this case relies on special in-plane conditions ($\sigma_{11} = \sigma_{22}$) (1981). The interaction integral[27] approach developed by Stern et al. (Stern *et al.*, 1976) and Yau et al. (1980) extracts SIFs from mixed-mode problems by the addition of an auxiliary stress state to the integrand of the J-integral. Réthoré et al. applied the interaction integral to DIC data for static mixed-mode problems (2005), and Kim and Paulino extended the method to non-homogenous materials (2005), but found that material in-homogeneities were cause for error.

The decomposition method, originally proposed by Ishikawa et al. (Ishikawa *et al.*, 1980), requires no specialised J-integral formulation. The kinematic fields are decomposed into Mode I, II and III components before J integration so that only the corresponding Mode I-III part of J is calculated. Field separation is simplified owing to the distinct symmetric and anti-symmetric properties of Mode I-III fields about the crack plane, and so can be achieved by the sum and difference of reflected and original field components. Hence the only additional requirement is a prior knowledge of the crack plane. Originally the method was applied to mixed-mode problems through integration with the method of virtual crack extension (Ishikawa, 1980). Subsequently Nikishkov and Atluri proposed an extension to 3D cracks using mapping parameters to map curved crack fronts to straight fronts needed for symmetry (1987) . Červenka and Saouma showed that comparable accuracy could be achieved with interpolation applied to asymmetrical meshes (1997). In 1998, Rigby and Aliabadi showed that the anti-symmetric σ_{33} component was incorrectly decomposed in various earlier works (1998).

The proposed method presents the methodology and considerations for determining separate Mode I-III strain energy release rates and SIFs from DIC obtained displacement data using the decomposition method. The original methodology separates all kinematic fields based on symmetry characteristics. Here it is shown that stresses may be computed from the decomposed displacement fields and evaluated separately using the classical J-integral approach. Therefore, the method does not require knowledge of the crack tip position (only the crack plane), and both the line and area integral formulations are applicable.

The first section of this paper is a presentation of the theoretical framework. This section outlines the J line and area integral equations applicable to 3D DIC displacement data, and presents the

[27] Also referred to as the M-integral

method for displacement field decomposition. The following section presents calculations on analytical crack tip fields to study the sensitivity of the method to DIC errors (synthetically generated). The final part contains experimental mixed-mode results from PMMA Arcan specimens to demonstrate the capability of the method to separate SIF values from pure Mode I-III and mixed-mode experiments.

6.2 Theoretical framework

6.2.1 The classical *J*-integral

The *J*-integral, developed by Rice (1968), characterises the energy available for crack propagation in the direction of the assumed crack plane. Consider the 2D planar solid containing a straight crack, and arbitrary counter-clockwise contour shown in Figure 6.1.

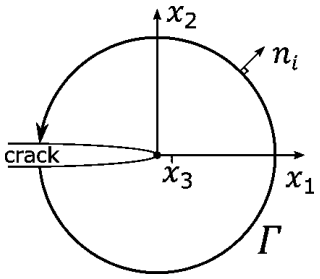

Figure 6.1: *J* line integral, contour path (Γ), and local (crack tip) co-ordinate system (x_i)

The contour is defined in terms of local Cartesian co-ordinates x_i, with x_1 oriented in the crack direction, x_2 perpendicular to the crack plane, and x_3 perpendicular to the page. Initially only in-plane components (x_{1-2}) will be considered. Assuming zero body forces, a straight crack front perpendicular to the material surface, traction free crack faces, a contour free of singularities (Γ), and crack extension in the x_1 direction (Rice, 1968); the following simplified definition of the *J*-integral applies (Budiansky and Rice, 1973):

$$J^k = \int_\Gamma \left(W n_k - \sigma_{ij} \frac{\partial u_i}{\partial x_k} n_j \right) d\Gamma \quad (i,j,k = 1,2) \tag{6.1}$$

where, W is strain energy density, n_i are the displacement vector components of the outward unit normal and σ_{ij} is the Cauchy stress tensor. Note that $\sigma_{ij} n_j$ represents the traction acting on the boundary Γ. Usually k is subscripted (e.g. J_k), but in this paper subscripts are used to denote the mode numbers I-III (i.e. J^k_{I-III}), to be consistent with standard SIF notation (e.g. K_{II}, K_{Ic}, etc).

6.2.2 Mode decomposition of *J*

If $k = 1$ in Equation (6.1), then J^1 (usually simply written as *J*) is the total energy released per unit crack extension for linear or non-linear materials (Anderson, 2005). This is equal to the sum of the independent *J* values obtained from fracture Modes I-III:

$$J^1 = J_I + J_{II} + J_{III} \tag{6.2}$$

Equation (6.2) is an underdetermined system, however; if for example, Mode II and III displacement fields are removed prior to the computation of J^1, then the unmodified procedure for the computation of J^1 gives J_I directly. Similarly, J_{II} and J_{III} may be obtained. Due to distinct symmetry characteristics, crack tip displacement fields (u_{crack}) may be decomposed directly into Mode I-III components in the same manner that any function may be separated into symmetric and anti-symmetric parts (Ishikawa *et al.*, 1980):

$$u_{crack} = \sum_{M=I}^{III} u_M = \{u_I\} + \{u_{II}\} + \{u_{III}\} = \frac{1}{2}\begin{Bmatrix} u_1 + u_1' \\ u_2 - u_2' \\ 0 \end{Bmatrix} + \frac{1}{2}\begin{Bmatrix} u_1 - u_1' \\ u_2 + u_2' \\ 0 \end{Bmatrix} + \frac{1}{2}\begin{Bmatrix} 0 \\ 0 \\ u_3 - \end{Bmatrix} \tag{6.3}$$

where, the notation u_i' represents a displacement field that has been reflected about the crack plane ($u_i' = u(x_1, -x_2)_i$), in the local co-ordinate system of the crack front (Figure 6.1). Assuming that stresses are linear-elastic functions of strain, the Mode I-III J-integral may be expressed by application of Equation (6.1), with $k = 1$, to the decomposed displacement field components u_{M_i} ($M = \mathrm{I} - \mathrm{II}$).

$$J_M^1 = \int_\Gamma \left(W_M n_1 - \sigma_{M_{ij}} \frac{\partial u_{M_i}}{\partial x_1} n_j \right) ds \quad (i,j = 1,2) \tag{6.4}$$

where,

$$W_M = \frac{1}{2}\left(\sigma_{M_{11}}\varepsilon_{M_{11}} + \sigma_{M_{22}}\varepsilon_{M_{22}} + 2\sigma_{M_{12}}\varepsilon_{M_{12}}\right) \tag{6.5}$$

$$\varepsilon_{M_{ij}} = \frac{1}{2}\left(\frac{\partial u_{M_i}}{\partial x_j} + \frac{\partial u_{M_i}}{\partial x_j}\right) \qquad (i,j = 1,2) \tag{6.6}$$

$$\sigma_{M_{ij}} = E_{ij}\varepsilon_{M_{ij}} \quad (i,j = 1,2) \tag{6.7}$$

Since all DIC measurements are surface measurements, E_{ij} is the second order stiffness tensor for plane stress. Mode III anti-plane shear loading requires that in-plane tractions are zero. Therefore considering stresses and strains as functions of displacement differentiated in the x_3 direction ($\varepsilon_{III_{i3}} = \partial u_{III_i}/\partial x_3$), Equation (6.4) reduces to (Nikishkov and Atluri, 1987):

$$J_{III}^1 = \int_\Gamma \left(W_{III} n_1 - \sigma_{III_{3j}} \frac{\partial u_{III_3}}{\partial x_1} n_j \right) ds \quad (j = 1,2) \tag{6.8}$$

where,

$$W_{III} = \sigma_{III_{3j}} \varepsilon_{III_{3j}} \quad (j = 1,2) \tag{6.9}$$

$$\varepsilon_{III_{3j}} = \frac{\partial u_{III_3}}{\partial x_j} \quad (j = 1,2) \tag{6.10}$$

$$\sigma_{III_{3j}} = 2\mu \varepsilon_{III_{3j}} \quad (j = 1,2) \tag{6.11}$$

and μ is the shear modulus.

6.2.3 The area integral

The area integral, also known as the Equivalent Domain Integral (EDI) formulated by Shih (1986), and Li (1985) *et al*., is equivalent to the line integral – but incorporates a larger field area for a single J calculation, and is therefore well suited to full-field data (Becker *et al.*, 2012).

Applying the divergence theorem to Equation (6.1) on the closed boundary Γ_0, Γ_1, Γ^+, Γ^- (Figure 6.2), under the same assumptions as before (but also assuming that no discontinuities exist within the area A (Shih *et al.*, 1986)), gives:

$$J^1 = \int_A \left(\sigma_{ij} \frac{\partial u_i}{\partial x_1} \frac{\partial Q}{\partial x_j} - W \frac{\partial Q}{\partial x_1} \right) dA \quad (i,j = 1,2) \tag{6.12}$$

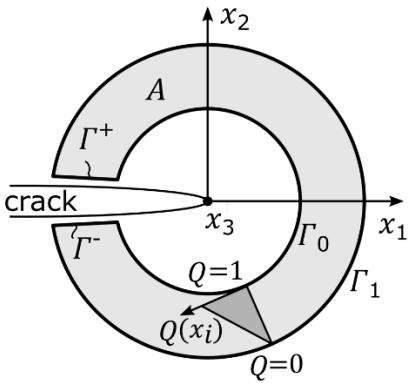

Figure 6.2: J area integral, contour path (Γ_0, Γ_1, Γ^+, Γ^-), crack tip local co-ordinates and Q function schematic

In this case the integration is of the area A surrounding the crack tip (Figure 6.2). Note that Γ^+ and Γ^- are assumed to coincide with the crack faces, where tractions are zero. Hence crack face integral terms do not appear in Equation (6.12) (Anderson, 2005). The function $Q(x_i)$ is a weighting function which may be interpreted as the displacement of A with a virtual increase in crack length. It has been shown by Shih et al. (1986) that if Q is sufficiently smooth, the shape of the function has little effect on value of J. All implementations in this paper use a linear function between zero and one.

$$Q = \begin{cases} 0 & \text{on } \Gamma_0 \\ 1 & \text{on } \Gamma_1 \end{cases} \tag{6.13}$$

Again, strain and stresses are derived from decomposed displacement data u_{M_i} (Equation (6.3)), to compute the EDI energy release rates:

$$J_M^1 = \int_A \left(\sigma_{M_{ij}} \frac{\partial u_{M_i}}{\partial x_1} \frac{\partial Q}{\partial x_j} - W_M \frac{\partial Q}{\partial x_1} \right) dA \quad (i,j,M = 1,2) \tag{6.14}$$

while anti-plane shear (Mode III) components, give:

$$J_{III}^1 = \int_A \left(\sigma_{III\,3j} \frac{\partial u_{III\,3}}{\partial x_1} \frac{\partial Q}{\partial x_j} - W_{III} \frac{\partial Q}{\partial x_1} \right) dA \quad (i,j = 1,2) \tag{6.15}$$

6.3 Validation using analytical fields

The acquisition of accurate DIC displacement fields is greatly affected by the presence of cracks (Becker *et al.*, 2012). These sources of experimental error are explored using analytical crack tip fields to represent DIC displacement fields. Analytical crack tip fields provide access to displacement fields with exactly known SIF values. Therefore J_{I-III}^1 values calculated on analytical displacement fields may be compared with the known K_{I-III} values using Equation (6.16). This is the basis for the methodology developed in the following sections to test the sensitivity of the proposed method to synthetic DIC errors.

$$\begin{aligned} J_M^1 &= G_M = (K_M)^2/E' \quad (M = I - II) \\ J_{III} &= G_{III} = (K_{III})^2(1+\nu)/E \\ E' &= \begin{cases} E & \text{for plane stress} \\ \dfrac{E}{1-\nu^2} & \text{for plane strain,} \end{cases} \end{aligned} \tag{6.16}$$

6.3.1 Implementation on analytical fields

Separate Mode I, II, and III displacement fields were generated from K_{I-III} values using Williams' series crack tip displacement fields (Williams, 1957), using Equations (2.10) - (2.12). In every case with $K_{I-III} = 1$ MPa.m$^{1/2}$, so that similar field amplitudes could be obtained. A local co-ordinate system is defined with (r, θ), the radius from the crack tip, and angle from the positive x_1 axis, as explained in section 2.2.4. Mixed-mode analytical displacement fields ($u_{crack} = \sum_{i=1}^{3} u_i$) were then generated using Equation (6.3).

The length scale and material properties of PMMA Arcan specimens were used for comparable results to the experimental section. Note that DIC data is typically evenly spaced. Therefore, rectangular co-ordinates were mapped to polar co-ordinates so that displacements could be defined in a regular grid with the area 40 × 40 mm (Figure 6.3). The density of data points was also derived from the experimental setup: namely, a subset step size of 20 pixels and a camera resolution of

5MP – although only 50 % of the field of view covered the region of interest[28]. Pixel distances were 7.93×10^{-3} mm/pixel, such that the resulting analytical dataset was 120 × 120 data points, with a spacing of 0.65 mm between data points. The array was centred at the origin (Figure 6.3), such that the crack length, $a = 20$ mm, was half the field of view, with the crack tip a $(0, 0)$. The material properties used were E = 3 GPa, and v = 0.36 for Young's modulus and Poisson's ratio respectively.

6.3.2 J-integral implementation

The analytical displacement field (u_{crack}) was decomposed into mode I-III components using Equation (6.3) about the horizontal ($x_2 = 0$) crack axis (symmetry line - Figure 6.3), resulting in 9 displacement components (u_{M_i}). Strain fields were calculated using central differences, except at the borders of the region and at the crack faces where second order skew finite differences were used. Subsequent stress calculation assumed linear-elasticity, Equation (6.7) & (6.11). Line (Equations (6.4), (6.8)) and area J-integrals (Equations (6.14), (6.15)) were evaluated on rectangular contours selected with reference to the contour position (r_c) as defined in Figure 6.3. Subsequently Equation (6.16) was used to obtain K_{I-III} values. Note that r_c is located at the centre of width (D) of the area integral. A fixed area size of $D = 2$ mm (equivalent to approximately 3 adjacent data points) and a plateau shaped Q function (Shih *et al.*, 1986) were used for all area integral computations. Note that due to the width of the area integral, results could only be computed between $1 < r_c < 19$ mm. It is necessary to define a region of crack influence (r_i) to study the effects of failed DIC subsets over the crack. A rectangular mask of length $a + r_i$, and width $2r_i$ was used, as shown in Figure 6.3. In this region displacements were set to zero.

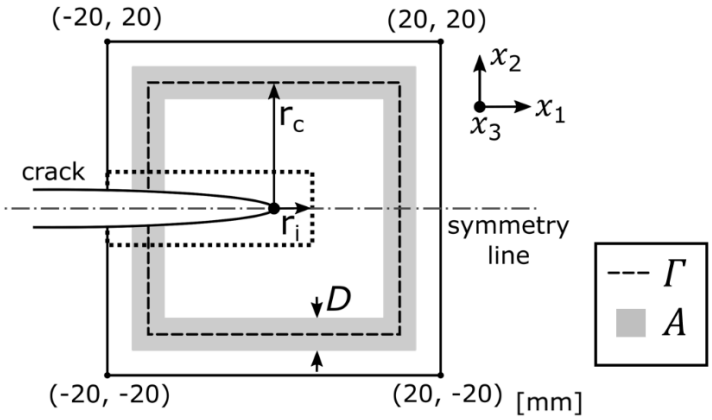

Figure 6.3: Schematic of data range and contour selection (Γ, or A) for analytical field data, showing: contour position (r_c), region of crack influence (r_i), and area integral width (D).

Figure 6.4 shows the line and area integral $K_{I\text{-}III}$ values obtained from noise free analytical displacement fields at various contour positions (r_c). The results are contour independent (constant value), except where errors occur close to the crack tip ($r_c \approx 0$). These are due to low order differentiation used in a high displacement gradient region. These results are considered a validation of combined decomposition method - J-integral approach. It is worth stating that the lower order ($r^{-3/2}, r^{-5/2}$, …), higher order, and T-stress terms of the Williams' series were neglected. This was because their inclusion did not affect these results as shown by Hui and Ruina (1995), and using the first order Williams series simplifies the conversion of $J_{I\text{-}III}$ values into $K_{I\text{-}III}$

[28] Regions of the Arcan fixture were also captured to measure relative specimen and fixture movement.

values. It is further noted that rigid body translation and rotation were not included. Rigid body translation should have no effect on J estimates as all displacement terms appearing in the J formulation are differentiated. However, rotation has a linearly proportional effect on DIC displacements resulting in a spurious strain offset when using a central differencing scheme to calculate strains. These effects were not investigated as these may be removed post DIC analysis. DIC accuracy under rigid body motion has been the subject of extensive study (Amiot *et al.*, 2013).

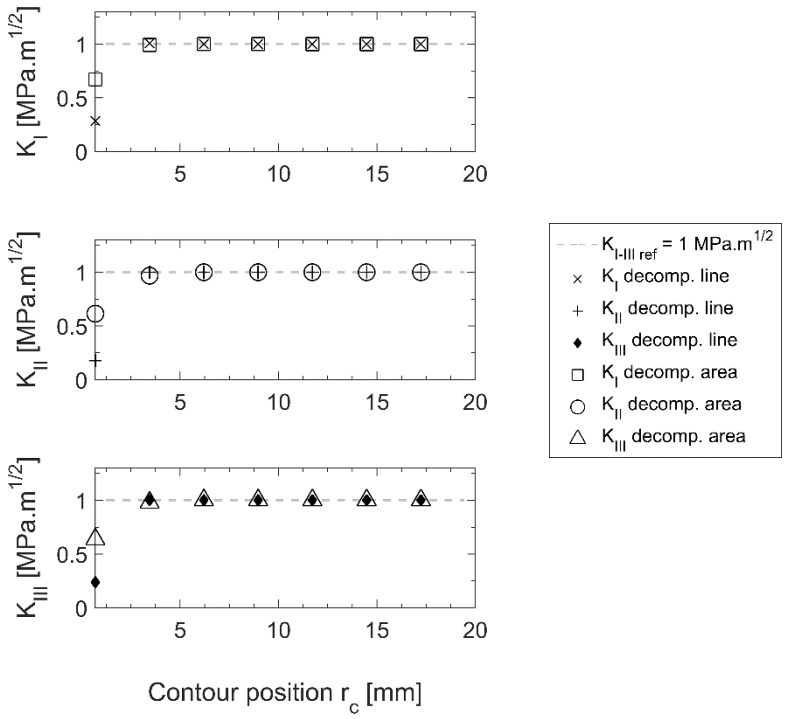

Figure 6.4: J-integral results from mixed-mode I-III displacement fields as a function of contour distance from the crack tip (r_c)

6.3.3 Error analysis procedure

The effects of synthetic DIC errors on J-integral results was investigated by adding artificial displacement errors u_n to the analytical crack tip fields (u_{crack}) before evaluation of the J-integral, and converting the resulting $J_{I\text{-}III}$ values into equivalent $K_{I\text{-}III}$ results. Subsequently, errors were measured relative to the SIFs used to generate the analytical displacement fields. The contour at r_c = 10 mm was used as the reference value for error analysis in order to be away from high gradient region errors. The procedure is summarised below:

Table 6.1: Algorithm for field generation

STEP	DETAILS
1	Select known K^*_{I-III} (= 1 MPa.m$^{1/2}$), and material properties (E = 3 GPa, and υ = 0.36)
2	Generate mix-mode crack tip fields: u_{crack}, Table 1.
3	Compute reference $K_{I\text{-}III}$ values; $K_{I\text{-}III\ ref}$
4	Add synthetic displacement errors, u_n; $u_{test} = u_{crack} + u_n$;

Table 6.2: Algorithm for error analysis

STEP	DETAILS
1	Decompose fields into mode I-III components; Equation (6.3)
2	Compute linear-elastic strain, and stress fields
3	Calculate $J_{I\text{-}III}$; Equations (6.4), (6.8), (6.14), (6.15).
4	Convert $J_{I\text{-}III}$ to equivalent $K_{I\text{-}III}$ estimates; Equation (6.16).
5	Compute $K_{I\text{-}III}$ % errors;$\lvert K_{I\text{-}III\ ref} - K_{I\text{-}III} \rvert / K_{I\text{-}III\ ref}$ (at r_c = 10 mm)

6.3.4 Study of synthetic DIC measurement errors

DIC is a multistage process and therefore the errors are cumulative and complex (Amiot et al., 2013), however, three key error sources are selected:

- Random displacement noise (seen as the inherent DIC accuracy),
- Rigid body misalignment of the symmetry line (translation and rotation of the crack plane)
- Localised displacement errors close to crack interfaces (crack masking defined by r_i)

The typical upper limit of DIC measurement accuracy is approximately 0.01 pixel (in-plane), 0.02 pixel (out-of-plane), and 0.003 degree rotational uncertainty (Zhou and Goodson, 2001; Amiot *et al.*, 2013). However, according to the La Vision product-manual (DaVis 8.2), measurements with a subset size of 85 × 85 pixels should be 0.027 pixel errors in-plane, 0.053 pixels (×2) out-of-plane. In the forthcoming sections, it is assumed that these accuracies may be related to physical measurements using the length scale (7.93×10^{-3} mm/pixel). This gives displacement errors of 0.2 µm in-plane, 0.4 µm out-of-plane.

Random displacement noise

To investigate the effects of noise on the accuracy of J estimates, Gaussian white noise was added to mode I, II, and III displacement fields. In addition, the classical J-integral approach was applied to each field component so that reference $K_{I\text{-}III}$ values could be obtained. These were compared to results obtained using the decomposition method. Although no field separation is performed in this approach, this shows the effect of decomposition on noise mitigation and provides a

comparison to the standard J-integral approach. In both cases, line and area results were also compared (Figure 6.5 a and b).

The random noise was incremented linearly from zero to a maximum of 6 % pixel displacement, averaging the results from 1×10^4 $K_{I\text{-}III}$ estimates, where percentage error was calculated relative to the noise free result (Figure 6.4). Figure 6.5a shows that the line integral is approximately three times less accurate relative to the area integral (b). This improved robustness has also been noted by Tracy *et al.* (2015), and Becker *et al.* (2012). Therefore, for simplicity, all further J values presented in this paper are derived using the area integral approach.

Recall that in-plane DIC accuracy (0.027 pixels) applies to $K_{I\text{-}II}$ errors, and out-of-plane accuracy (0.053 pixel) applies to K_{III} errors. Although the K_{III} errors appear lower, at these measures there is little difference between $K_{I\text{-}III}$, with $K_I = K_{II} = 1$ % accurate, and $K_{III} = 1.4$ % accurate. This is an improvement on the classical J-integral results for $K_{I\text{-}III}$ by 25 %.

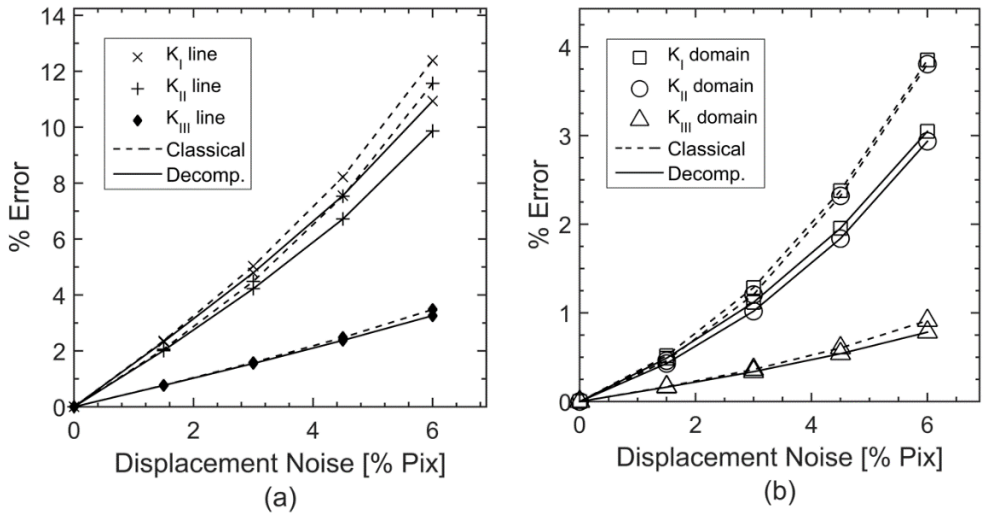

Figure 6.5: $K_{I\text{-}III}$ errors due to % displacement noise from line (a) and area (b) integral methods, with SIFs obtained from pure mode I-III fields (i.e. without decomposition) shown by dashed lines

Rigid body misalignment

The intention of this section is to understand the nature and scale of the error in $K_{I\text{-}III}$ estimates resulting from misalignment of the crack plane. This includes rotation (Figure 6.6a) and off-axis translation in the x_2 direction (b). Note that decomposition is fundamentally immune to translations in the x_1 direction as this is the axis of symmetry. Within the DIC error regime (<0.4 µm), purely random off-axis displacement errors were estimated to be less than 0.1 % total error, mostly in $K_{I\text{-}II}$ components. This was considered negligible. In this paper, no alignment method is prescribed. The design of a robust alignment methodology could be challenging, either due to crack branching, inconsistencies between externally visible cracks and the internal crack path, or changes in surface texture unrelated to cracking. The approach taken in this paper was manual alignment; which was assumed to be within 2 degrees of the crack plane, and 2 mm off-axis translation. Reading from Figure 6.6, this would lead to $K_{I\text{-}III}$ estimates to within 3 % of the target values. The most notable characteristic is that $K_{I\text{-}II}$ errors are consistently several times greater than K_{III}.

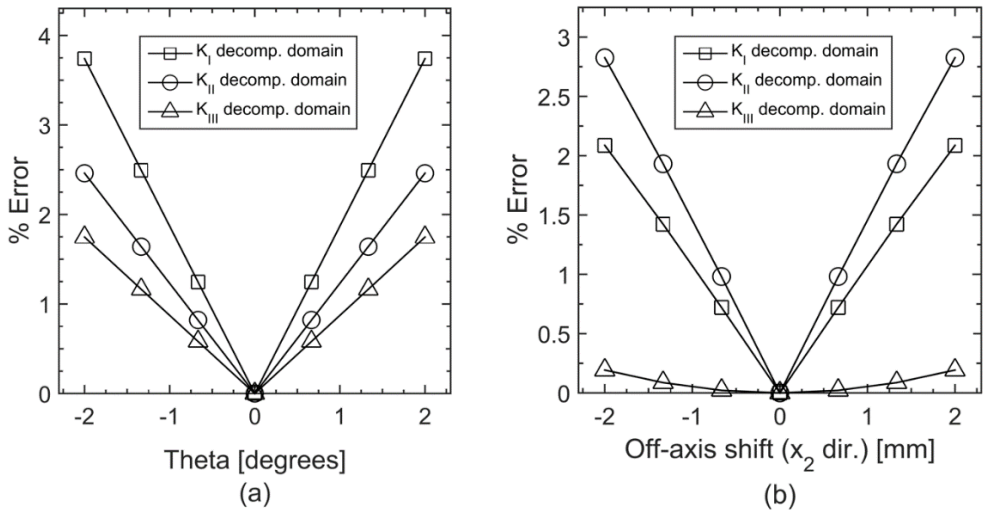

Figure 6.6: *K* estimate % error related to rigid body rotation (a) and off-axis translation in the x_2 direction (b)

Localised displacement errors close to crack interfaces

Figure 6.3 shows the mask region (defined by r_i) used to study the effects of poor DIC results close to cracking on the decomposition of $K_{I\text{-}III}$ factors (i.e. rectangular and localised to the theoretical crack). Assuming a subset size of 85×85 pixels, and a remote crack opening displacement of 1.5 mm from experimental data, a typical masked region of r_i = 3 mm (5 displacement data points) would be sufficient to mask the crack path and adjacent subsets. For this mask size, Figure 6.7 a shows $K_{I\text{-}III}$ values computed from contour positions $r_c > 3$ mm. Data is not available in the masked region – indicated by the vertical dotted line.

Accuracy is lowest close to the crack tip (and masked area), it however improves at larger r_c values. This stabilisation is caused in part by the statistical averaging effect of larger contours. The reduction in accuracy of estimates due to increasing mask size is also shown (Figure 6.7b), at a fixed contour distance ($r_c = 10$ mm).

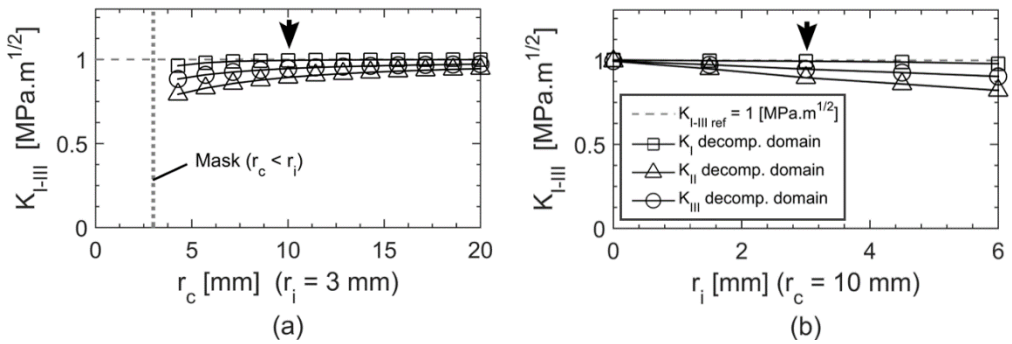

Figure 6.7: $K_{I\text{-}III}$ estimate errors at various contour positions (r_c) and a fixed mask width ($r_i = 3$ mm) (a), and variable mask width with fixed contour position (b). Arrows indicate corresponding data points between (a) and (b). Vertical dotted line in (a) indicates the extent of masking (3 mm)

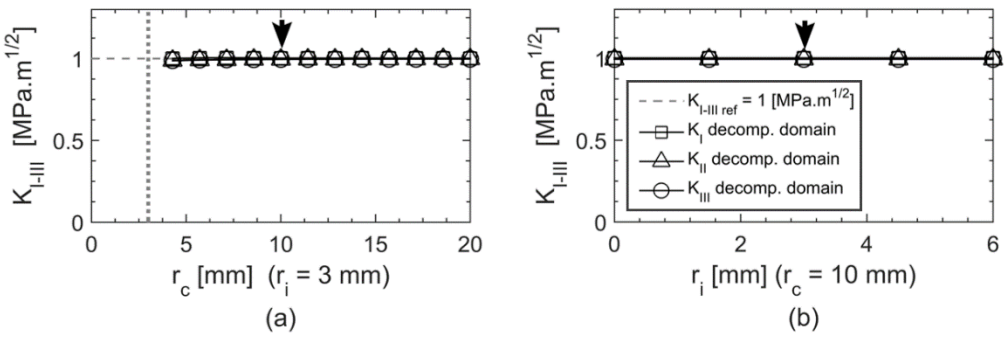

Figure 6.8: $K_{I\text{-}III}$ estimate errors using polynomial interpolation to replace masked data: at various contour positions (r_c) and a fixed mask width (r_i = 3 mm) (a), and variable mask width with fixed contour position (b)

The differences in the accuracy of $K_{I\text{-}III}$ results at different mask widths (Figure 6.7b) may be explained by the differences in strain energy density in the masked regions for each mode. For example, mode I loading results in the lowest strain energy density in this region. Correspondingly, K_I is relatively unaffected by masking. Hereafter it is important to address the missing data close to the crack faces, particularly for reliable K_{II} and K_{III} estimates. A solution proposed for this paper is the replacement of masked data using the iterative least-squares polynomial fitting method developed by Garcia (2010) and Wang et al. (2012)[29]. $K_{I\text{-}III}$ values obtained from masked fields restored by interpolation are shown in Figure 6.8. Although very good accuracy is achieved here, this approach may be limited to low gradient regions (far from the crack tip) and smaller masked areas. This would be due to the inherent inability of polynomial functions to represent crack tip fields.

As yet, the effects of noise on this approach have not been shown. It is expected that poor interpolation would result if the region of crack influence extends beyond the masked area. Therefore, masking should be conservative if the interpolation approach is used as outlined in this paper. These effects were not investigated as the intention of this work is to present the underlying methodology. However, several DIC variants have been developed which improve the resolution close to the crack faces, for example the subset splitting approach (Poissant and Barthelat, 2010), or DIC incorporating extended finite elements (Réthoré, Hild, *et al.*, 2008).

6.4 Experimental implementation

In this section, the decomposition method (with interpolation to fill in missing crack data) is used to measure mode I, II and III SIFs from Arcan specimens (1986). Fracture toughness values ($K_{Ic\text{-}IIIc}$) were used as a primary experimental validation. Therefore $K_{I\text{-}III}$ estimates were obtained from DIC displacement fields measured close to failure in pure mode I, II and III loading configurations. An additional test was performed under mixed-mode loading to demonstrate that separate $K_{I\text{-}III}$ values may be decomposed from mixed-mode tests.

[29] Matlab code is available at: www.mathworks.com/matlabcentral/fileexchange/27994-inpaint-over-missing-data-in-1-d--2-d--3-d--n-d-arrays?focused=3800843&tab=function (accessed 12 July 2017)

6.4.1 Material and specimens

PMMA[30] may be considered as a homogenous and isotropic material which exhibits linear-elastic brittle fracture at room temperature. Clear cast single edge crack PMMA specimens were laser-cut from 6 mm and 12 mm thick sheets into the Arcan geometry shown (Figure 6.10a). The Arcan specimen and fixture design was based on the guidelines of Banks-Sills and Arcan (1986). Sharp pre-cracks were induced from the tip of a starter notch (15 mm) to a total length of 20 mm. Crack tips were located laterally within 2 mm^2 of the centre of each specimen. Material properties were determined from ASTM D638 uniaxial tensile tests: Young's modulus, $E = 3$ GPa, Poisson's ratio, $v = 0.36$. The mode I fracture toughness value for PMMA was determined at K_{Ic} = 1.7 MPa.$m^{1/2}$ (average of three ASTM E1820 Compact Tension (CT) specimen tests, with W = 50 mm and B = 12 mm).

6.4.2 Fixture

The Arcan fixture is comprised of two halves able to rotate through different loading angles in 15° increments (Figure 6.9b). Pure mode I, II and mixed mode I-II loading could be achieved by setting the fixture between 0 and 90 degrees. mode III (anti-plane shear) loading was induced by bolting the specimen against back plates of different thicknesses. This resulted in deflection of 3 or 4.5 mm between the fixture halves (constant during testing). The rig was constrained against lateral and rotational movement by additional pins connecting the fixture halves to the clevis.

6.4.3 Pure mode I, II and II results

The Arcan fixture was axially loaded with a cross-head speed of 0.25 mm/min in an MTS tensile tester. Digital images were captured during loading at a frequency of 1 Hz with a LaVision DIC system (5MP CCD cameras); and loads were measured with a 30 kN load cell. DIC analysis was carried out with DaVis v8.2 software, and parameters for analysis were: subset size = 85 × 85 pixels, and step-size = 20 pixels. The correlation algorithm used was least-squares matching with B-spline-6 interpolation and a 50 % valid pixel per subset requirement[31]. Less than the full field of view was used for all tests (approximately 50 %) so that the images of rotated cracks would not be cropped. The resulting region analysed with DIC and available for J-integral analysis was the area of the specimen located between the fixture halves, 8 mm from the clamps and 3 mm from the crack tip to ensure even stress distributions through the thickness of the specimen (Figure 6.9c). Therefore J-integral contours were selected from $3 < r_c < 12$ mm, as shown in Figure 6.9d. The J-integral was evaluated on strains calculated using Equations (6.5)-(6.7) in modes I and II, and (6.9)-(6.11) for mode III using finite differences within Matlab v.2014a, in which all J calculations were also computed.

The maximum $J_{I\text{-}III}$ -integral (and equivalent $K_{I\text{-}III}$ estimates) were not always a result of the final image captured before fast fracture. Therefore, every image leading up to fracture was analysed, and the largest SIF was taken to be the estimated $K_{Ic\text{-}IIIc}$ for each test. It was likely that the final $K_{I\text{-}III}$ value underestimates the fracture toughness due to the time taken between image captures. The change in $K_{I\text{-}II}$ values between image captures was measured to be equal and constant during testing at $\Delta K_{I\text{-}II}$ = 0.01 MPa.$m^{1/2}$ (K_{III} is constant).

[30] Also known by names: Perspex or Plexiglass.

[31] Values outside this range cause the correlation of the subset to fail.

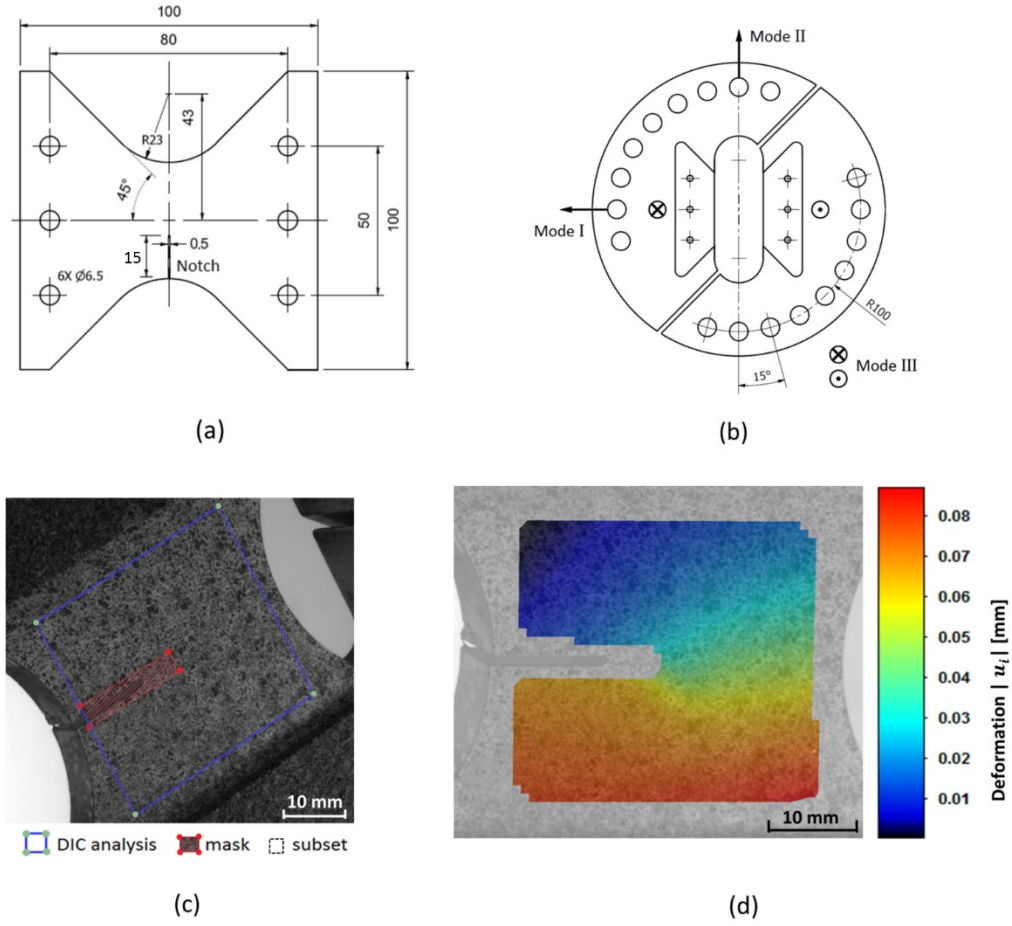

Figure 6.9: Arcan specimen geometry (a), schematic of Arcan fixture showing mode I-III loading directions (b), mounted specimen inclined 30° showing DIC analysed regions (c), and mixed-mode displacement field resulting from DIC analysis (shown on corrected image) (d).

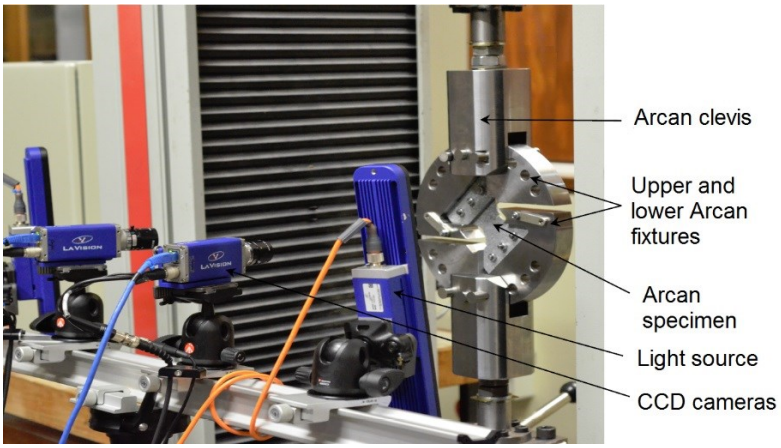

Figure 6.10: Typical Arcan test setup in 45° mixed-mode loading

$K_{I\text{-}II}$ results converged closely to the expected fracture toughness values as shown in Figure 6.11. The fracture toughness $K_{Ic} = 1.7$ MPa.m$^{1/2}$, was used to calculate K_{IIc} fracture toughness from published K_M/K_{Mc} results, which showed close agreement. Note that the K_{IIIc} was never reached as shear loading remained constant during K_{III} tests (a limitation of the rig design). Further it was found that 6 mm thick specimens underwent significant bending which caused loss of contour independence. Improved K_{II} results were obtained from a 12 mm thick specimen. Giner *et al.*

(2010) have shown that the apparent stress intensity factor measured on the surface of a plate decreases with increasing thickness. This factor was found experimentally to be approximately 7 %, and so the expected fracture toughness was adjusted accordingly (K_{IIc} = 1.35 → 1.27 MPa.m$^{1/2}$). $K_{Ic\text{-}IIIc}$ results obtained from these tests and comparable results from the literature are summarised in ASTM 1893.

Theoretically, pure mode I, II, and III loading should result in zero results for the other modes. However, K_{II} and K_{III} estimates contain a relatively large noise contribution from the other modes (compared to K_I). There is presumably an in-plane bending effect in both mode II and III. In mode II, this may also be because K_{II} displacements are on average smaller, effecting the signal-to-noise ratio. The cause of residual $K_{I\text{-}II}$ components in K_{III} measurements is unknown (Figure 6.11c), but could be related to the reduced accuracy of out-of-plane measurements using DIC, or due to bending stresses induced by the s-shaped deflection of the specimen.

Table 6.3: Comparison of fracture toughness values

Method	Specimen	K_{Ic}	K_{IIc}	K_{IIIc}	Source
Decomposition	Arcan	1.68	1.25	-	-
K_{Ic} tests (×3 tests)	CT	1.70	-	-	ASTM 1820
From (K_M/K_{Mc})	Various	1.73	1.27	3.56	*, **
Analytical solution	Arcan	-	1.36	-	**

* (Davenport and Smith, 1993) ** (Banks-Sills and Arcan, 1986)

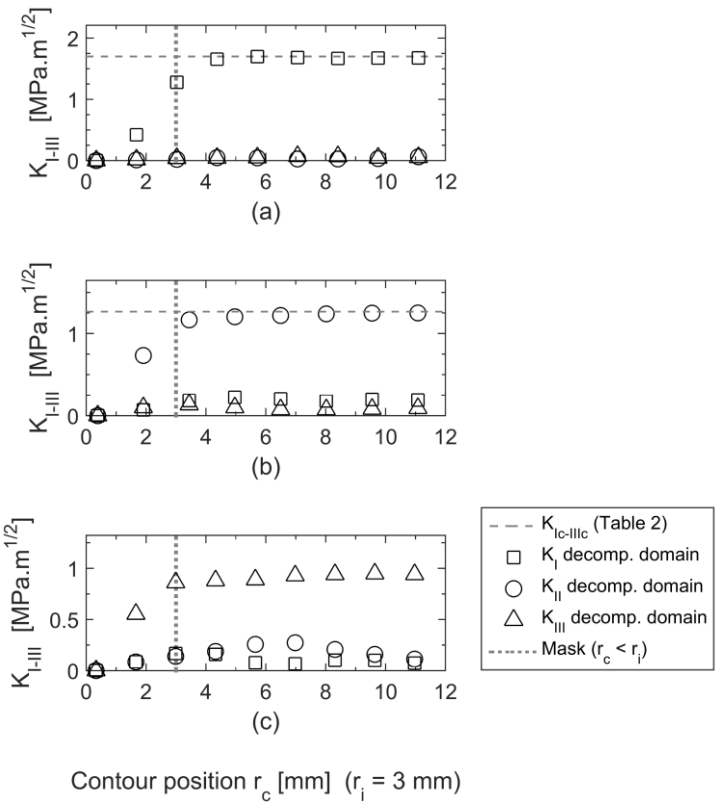

Figure 6.11: $K_{I\text{-}III}$ estimates for pure mode I, II and III loading (a-c)
Note: mode III loading is applied by x_3 deflection = 3 mm

6.4.4 Mixed loading results

A mixed mode I-III test was performed at a loading angle of 30° and a constant out-of-plane deflection of 3 mm. Results are shown in Figure 6.12, normalised to the fracture toughness values determined above (Table 6.3). The surface strains induced by mode III were measured at zero axial load and subtracted from all further strain fields to eliminate offsets to the mode I-II results. Reference mode I SIFs ($K_{I\,ref}$) for corresponding loads were calculated using the analytical solution to the SENT (Single Edge Notched Specimen Tensile) specimen geometry. This provided comparable mode I-II SIFs with the formulas: $K_{I\,eq} = K_{I\,ref}\cos^2\beta$, and $K_{II\,eq} = K_{I\,ref}\cos\beta\sin\beta$, where β is the angle of inclination (30°) (Anderson, 2005).

Figure 6.12 shows the expected linearly increasing K_I and K_{II} values. It is also shown that increasing $K_{I\text{-}II}$ loading does not affect the mode III estimate which remained constant during testing. Despite the differences between the SENT and Arcan geometries, this comparison confirms that the obtained values are within the expected regime. This final result mainly shows that $K_{I\text{-}III}$ values may be detected distinctly in mixed-mode tests using this method.

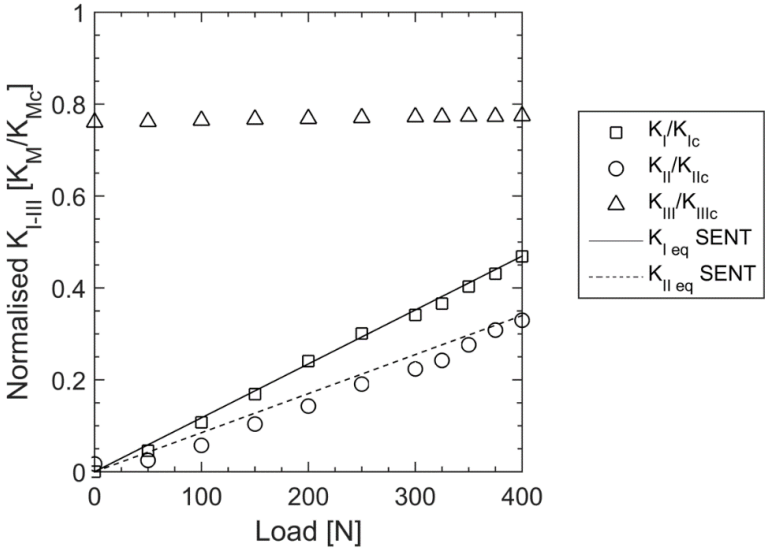

Figure 6.12: $K_{I\text{-}III}$ estimates normalised to $K_{Ic\text{-}IIIc}$, compared to analytical SENT solutions inclined at 30° ($K_{I\text{-}II\,eq}$ SENT)

6.5 Conclusions

- A procedure for the computation of mode I, II and III SIFs using the decomposition method and the J-integral is presented. The method is versatile as both the line and area integral forms may be applied, as demonstrated. The method was verified on 'ideal' (Williams' series) crack tip fields.
- A methodology for characterising synthetic DIC errors on analytical displacement fields was developed. This showed that the area integral combined with the decomposition method achieves the highest accuracy in the presence of noise, and that masked data may be replaced by interpolation to improve the accuracy of mode II and III K estimates.
- The decomposition method was verified experimentally in pure mode I, II and III configurations, and in mixed-loading. Results were compared to fracture toughness values measured from CT specimens, and analytical solutions obtained from literature with good agreement.

6.6 Summary

The aim of this chapter was to verify the decomposition method on the surface, for obtaining mode I, II and III stress intensity factors. This was achieved using analytical crack tip fields, and experimental tests using PMMA, using fracture toughness values from literature and ASTM tests. Therefore, this chapter addresses Objective 3 (section 3.2).

The J-integral was initially verified in modes I, II and III using the line and equivalent area integral to determine the sensitivity to random displacement errors, and errors in the assumed crack tip position (i.e. the same error types as explored theoretically in Chapter 5). A similar result was found here, that the area integral (an equivalent domain integral form) is more than twice as accurate as the original line integral. Note that the same tests will be performed experimentally with DVC data in Chapter 7.

The key finding was that decomposition for the general mixed-mode case yields a lower accuracy than pure mode I cases. This was attributed to the lower strain energy found in the crack face regions in mode I, and therefore a lower dependence on crack face data for the J-integral.

The methodology of this section is carried forward to the following two chapters in which the J-integral is applied to the volume. Due to the increased complexity of the volume integral, verification (Chapter 7) and decomposition (Chapter 8) of the J-integral form two separate chapters.

7 Evaluation of the hybrid volume J-integral on DVC displacement data

The previous section addressed objective 3 by verifying the J-integral on the surface using stereo DIC. This involved implementation of the line and area integral forms introduced in section 2.2.5. The volumetric forms of the J-integral (also in section 2.2.5), have been developed into a hybrid form J_{hyb}, which provides a trade-off between resilience to random displacement noise, and uncertainty in the crack front location (Chapter 5).

This chapter details the implementation of the proposed hybrid J-integral form in the volume; using X-ray computed tomography to acquire images and DVC to obtain displacement maps. Note that the decomposition method in the volume is presented separately in Chapter 8. Apart from excluding the decomposition method from this chapter, the approach used here is similar to the surface (Chapter 0), in the continued use of analytical crack tip fields perturbed with synthetic image correlation errors to determine errors, and subsequent comparison with experimental datasets to verify results. In place of fracture toughness values, which are challenging to control along a 3D crack front, results are compared with those generated from finite element fields.

Section 7.4.2 was presented at the 11th British Society of Strain Measurement Conference (Molteno *et al.*, 2016), and the chapter has been prepared for publication in *Strain* (Wiley) with co-authors: Valle, Hedan, Germaneau, Marrow and Becker (in no particular order).

The contributions of the authors are:

- The author (Matthew Molteno): Completed all implementations and writing apart from the contributions below.
- Prof. Valéry Valle: Co-ordinator for polyurethane dataset (SENT specimen) used for verification of mode I measurements in section 7.4.1.
- Prof. Stephen Hedan, Prof. Arnaud Germaneau: Affiliated with Prof. Valle.
- Prof. James Marrow and Dr Thorsten Becker: Assistance with experimental design at Manchester (Prof. Marrow), and later at Stellenbosch (Dr Becker).

7.1 Introduction

Image correlation techniques to obtain displacement maps have become ubiquitous in experimental mechanics. Such methods benefit from the versatility of digital imaging, which can be obtained on the surface using white light imaging (e.g. mounted 2D cameras), and in the volume using penetrating light (e.g. X-ray based imaging). The most widespread use of image correlation is for the mapping of displacements on the surface, i.e. Digital Image Correlation (DIC), mainly due to relative simplicity of set-up compared to interferometric moiré methods (Hareesh and Chiang, 1988; Kreis, 2005; Jacquot Pierre, 2008; Post, 1991).

Recent growth in the availability and resolution of X-ray Computed Tomography (e.g. fan, cone, or parallel beam) has led to significant growth in the development and use of the volumetric counterpart, Digital Volume Correlation (DVC) (Maire and Withers, 2014), detailed in section 2.1.4. Both approaches operate by matching images captured of various sample deformations – usually from an undeformed state to subsequent loading stages which deform the sample and images. This is achieved by maximising the correlation coefficient in a block-wise fashion in which subsets of pixels (also called image patches, windows) which are regarded individually (or globally in using a FE framework), for further details, see section 2.1.3.

Therefore, apart from the dimensional extension, DVC and DIC are similar in principle. However, despite the similarities, DVC seldom achieves the accuracies that are typical of DIC, even in ideal conditions (DVC ~ 0.05 voxels, DIC ~ 0.01 pixels in-plane ~0.02 pixels out-of-plane (Bay *et al.*, 1999)). This effect is amplified significantly in experimental applications due to the reliance of DVC on naturally occurring features in the material volume - seldom a limitation on the surface which permits manual application (and optimization (Bornert *et al.*, 2009)) of a speckle pattern. As a result, the accuracy that can be achieved from DVC experiments is largely material dependent (Bay, 2008). As a result, material selection is a key factor determining the accuracy achievable by DVC.

Despite these limitations, DVC displacement fields (as with DIC) are accompanied by the source images which, with assistance from volume rendering software such as FEI Avizo[32], often provide visual evidence for complex phenomena observed in displacement fields. Thus, DVC from X-CT images provides an established non-destructive framework to study diverse materials, used in rheological studies on polymers (McDonald *et al.*, 2011), wood (Forsberg *et al.*, 2008), granular materials (Mostafavi *et al.*, 2013; Rechenmacher, 2006) and geomaterials (Tagliaferri *et al.*, 2011). The dissemination of new applications and techniques will doubtless continue with the recent availability of commercial software (e.g. LaVision[33]), open-source codes (Bar-Kochba *et al.*, 2015), and introductory papers (Yoneyama, 2016; Bay *et al.*, 1999).

The use of X-CT based DVC provides a promising fracture mechanics framework to extract parameters from the crack front. Such parameters are generally provided in a global 'average' sense (e.g. using nominal stress intensity factors) (Réthoré, Limodin, *et al.*, 2011; Maire and Withers, 2014; Réthoré, Tinnes, *et al.*, 2008; ASTM International, 2015). However, crack front extensions enable inspection of the fracture mechanics that may aggregate to equal or exceed the global estimates, and provide key information in structural integrity assessments. Such mechanisms may be uncovered with metrics such as the crack tip opening displacement (CTOD), stress intensity factors (SIFs - K), the energy release rate (G) or the J-integral.

[32] www.vsg3d.com (accessed 17 May 2017)

[33] www.lavision.de (accessed 19 June 2017)

As previously discussed (sections 2.2.4 and 6.1), SIFs are readily extractable from linear-elastic displacement fields by directly matching analytical crack tip fields (e.g. Williams' series expansion (1957)) to experimental data. When the crack geometry is precisely known then the fit can be determined by linear least-squares McNeill *et al.* (1987), otherwise automated approaches are needed to determine the crack tip position, as shown by Roux and Hild (2006). Some extensions to non-linear cases have been established on the surface (e.g. non-homogenous materials (Abanto-Bueno and Lambros, 2002; Méité *et al.*, 2013), plasticity (Réthoré, Roux, *et al.*, 2011)), and the method has been used in the volume on DVC data by Rannou *et al.* (2010), with the methodology of Réthoré *et al.* (2005). However, as argued in section 6.1, the displacement field expressions containing SIFs are only applicable to an annular region surrounding the crack tip (K dominant zone) (Hui and Ruina, 1995). Depending on the length scale of the experiment, this may place undue reliance on unreliable data near the crack faces in DIC and DVC experiments (Poissant and Barthelat, 2010; Rabczuk, 2012). Although specialised DIC or DVC methods show promise in improving the results near fracture features (Poissant and Barthelat, 2010; Rannou *et al.*, 2010), such approaches (and subsequent field fits) may be vulnerable to poorly defined crack tip positions as may be the case with micro-cracking (e.g. graphite or concrete (Becker *et al.*, 2011)).

The J-integral, introduced by Rice (1968), is an alternative method for estimating the energy release rate which requires the integration of the stresses, strains and displacement gradients surrounding the crack front segment of interest. Here it is important to establish the difference between 2D, as would be applied on the surface (Chapter 0) or in planar volumes; and 3D approaches, applicable to cracks in 3D stress fields and the volumes. Under 2D assumptions, the J-integral is path independent, a property that extends to some cases of material non-linearity[34] (Hutchinson, 1968; Rice and Rosengren, 1968; Kolednik *et al.*, 2014), assuming continued validity of the Eshelby tensor (Kolednik *et al.*, 2014), e.g. nonlinear-elastic approximations for plasticity (Rice and Rosengren, 1968). Therefore although the contours close to the crack front are generally found to be least accurate (Shih and Needleman, 1984; Yoneyama *et al.*, 2014; Molteno and Becker, 2015c), the J-integral enables the selection of remote paths from the crack tip, which typically are more accurate in DVC results. However, 3D J-integrals require integration of the entire volume enclosed by an outer path or surface. Therefore, although the outer surface of the volume is arbitrary, integration of the crack front region is enforced.

As previously reviewed and developed in Chapter 5, estimates of the J-integral in the volume can be performed with the path-area (Blackburn, 1972; Giner *et al.*, 2010) or volume integral forms (deLorenzi, 1982; Li *et al.*, 1985; Shih *et al.*, 1986). Chapter 5 also developed the hybrid volume integral approach as a form which combines resilience to crack tip positional errors, and random errors. The aim of this chapter is to establish the hybrid volume integral methodology on DVC data to extract J values from 3D crack fronts. As with the classical volume integral (Shih *et al.*, 1986), the hybrid integral does not escape integration of the crack front region, but minimises the contribution from in-plane components when large integration volumes are used (relative to the width of the crack front segment). These errors are studied using synthetic displacement errors, extending the procedure outlined in Chapter 0 to the volume. The rest of this chapter applies the hybrid volume integral to experimental case studies for experimental verification. Note that Chapter 5 used the nominal fracture toughness of pre-cracked PMMA to validate the surface integral. This approach was not replicated in this chapter due to the variations in J along a 3D crack front that would cause irregular crack growth; this would prove challenging to control experimentally. Instead, experimental results are obtained at sub-critical loads and validation is

[34] This is provided that the integration region can be defined in terms of Eshelby's energy balance tensor (Eshelby *et al.*, 2006).

performed against simulations using finite element software Abaqus (which uses the volume integral as detailed in (Shih *et al.*, 1986; Dassault Systèmes Simulia *et al.*, 2013)).

The layout of this chapter is as follows. Section 6.2 is the theoretical framework to review the J-integral equations applicable to 3D volume displacement data. Section 6.3 presents calculations on analytical crack tip fields to study the sensitivity of the method to DVC errors. The final part contains experimental results from two materials. The first is a polyurethane matrix with high attenuation copper particles (3 % volume fraction) containing a V-notch close to the standard SENT specimen configuration[35]. The second material is Magnesium alloy WE43 with high attenuation rare earth metal precipitates (4wt % Yt, 3wt % Nd) and an inclined round notch. The first material has optimised contrast patterns and low energy on the crack faces, which is reversed in the second material (natural pattern, inclined crack). These are so selected to facilitate the study of the previously discussed challenges involved in DVC data and the volume integral.

7.2 Three-dimensional framework

The 3D J-integral is defined conventionally in the local co-ordinate system $x_i(\mathrm{s})$ along an arbitrary crack front with x_1 in the crack plane and perpendicular to the crack front, x_2 normal to the crack plane, and x_3 tangential to the crack front in Figure 2.7. To obtain J-integral estimates from 3D crack fronts, a volumetric form is needed of the various types presented in Chapter 5. Typically the volume integral is chosen due to resilience to errors (Kuna, 2013b), or otherwise the path-area may be used (Blackburn, 1972; Giner *et al.*, 2010). Here, the hybrid volume integral developed in Chapter 5 is used as it has proven to provide a trade-off in resilience to both crack front positional and random displacement field errors. Consider the integration volume V at point s along the 3D crack front $l(s)$, which is assumed to be straight along segment Δs in Figure 7.1.

As with all previous numerical implementations in this thesis, a regular grid is assumed and so V is a cuboid. As prescribed in section 5.3, V is partitioned into inner and outer volumes, V_0 and V_1, by the partitioning surface S_0. The outer surface is relabelled S_1.

Then the volume integral can be expressed in hybrid form as,

$$\begin{aligned} J_{hyb}(\mathrm{s}) &= \frac{1}{A_c}\int_V \left(\sigma_{ij}\frac{\partial u_i}{\partial x_1} - W\delta_{1j}\right)\frac{\partial Q_{hyb}}{\partial x_j}\,dV \\ &= \frac{1}{A_c}\int_V P_{1j}\frac{\partial Q_{hyb}}{\partial x_j}\,dV\,, \qquad (i,j=1,2,3) \end{aligned} \tag{7.1}$$

[35] This data is in collaboration with University Poitiers, France, contact person: valery.valle@univ-poitiers.fr, +33 5 49 49 65 45

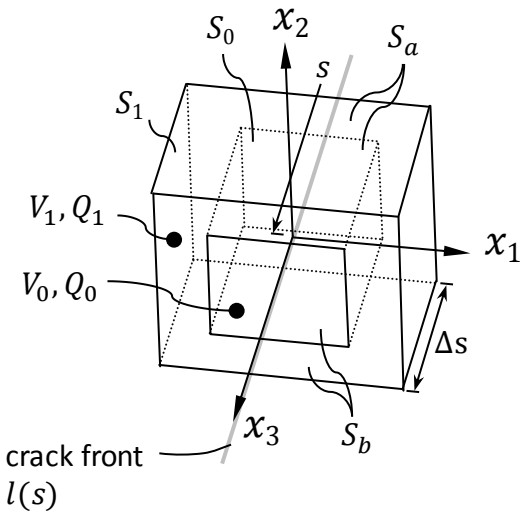

Figure 7.1: Hybrid integral V at s and crack front segment Δs on the 3D linear crack front $l(s)$, with inner and outer surfaces (respectively, S_0 and S_1), volumes (V_0 and V_1), and virtual crack extension fields (Q_0 and Q_1)

where δ_{1j} is the Kronecker delta, A_c is the virtual crack extension area over the crack front increment Δs, given by $A_c = \int_{\Delta s} q(s) ds$, and Q_{hyb} is the hybrid virtual crack extension function introduced in Chapter 5. The left term in the integrand which is Eshelby's 'energy-momentum' tensor can be abbreviated as P_{1j}. Q_{hyb} has the constraints of the conventional crack extension function in Equation (2.40), but with the additional constraint on the gradients perpendicular to the crack front being zero (Equation (5.12)). The strain fields (ε_{ij}) may be evaluated under the infinitesimal strain assumption using Equation (2.25). Assuming linear elastic stresses (σ_{ij}), and isotropic material, and small strains (ε_{ij}), then stress, strain and strain energy (W) can be calculated with Equations (2.24) - (2.26).

7.3 Verification on analytical fields

Displacements determined by DIC and DVC in the crack tip region are highly prone to errors, as shown experimentally in Chapter 5 and Chapter 0. In particular, these have been linked in Chapter 0 to errors in estimation of the domain integral. Such errors have been previously discussed by Rannou *et al.* (2010), as having an even larger effect on the accuracy of the volume integral. In this section, these sources of experimental error are studied using the methodology developed in section 6.3.3., i.e. analytical crack tip fields and superimposed synthetic DVC errors. Linear elastic crack tip displacement fields may be linked to equivalent J values using the relation to SIFs in Equation (6.16).

7.3.1 Implementation on analytical fields

Mixed crack tip displacement fields (u_{crack}) were generated from K_{I-III} values using Williams' series crack tip displacement fields (Williams, 1957), shown in Equations (2.10)-(2.12). A local co-ordinate system is defined in polar co-ordinates using (r, θ, x_3), being the radius from the crack tip, and angle from the positive x_1 axis, and position along the crack front. As in section 5.3.3, the θ range is between $-\pi < \theta < \pi$, with the crack surfaces at $\theta = \pm\pi$. μ is the shear modulus, $\kappa = (3 - v)/(1 + v)$ in plane stress (or $3 - 4v$ in plane strain), and v is Poisson's ratio. Data provided by DVC is regularly spaced in all co-ordinate directions. Therefore, rectangular co-ordinates in three-dimensions were mapped to polar co-ordinates so that displacements could be defined in a

regular grid using Equations (2.10)-(2.12) with the area $L \times L \times \Delta s$ in the local co-ordinate system (with the origin at the centre of V), as shown by Figure 7.2a. The addition of the x_3 dimension in Equations (2.10)-(2.12) is achieved by applying the plane strain assumption to generate a 2D field on the mid-plane ($x_3 = 0$, Figure 7.2a, shown in Figure 7.2b), which is then replicating on all other planes on Δs. Contours are calculated as indicated on the cross-section of V shown by Figure 7.2b.

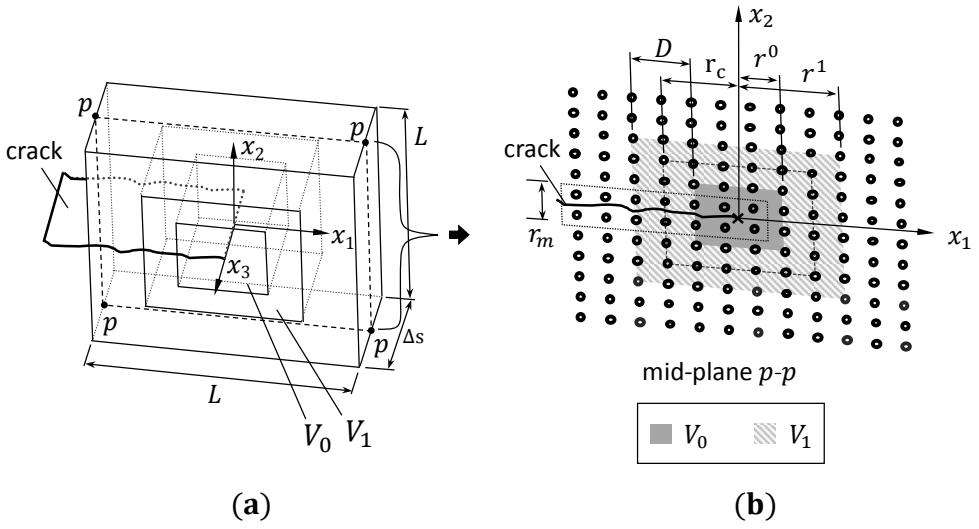

Figure 7.2: (a) Hybrid integral integration volume (V) and (b) cross-section (p-p) showing contour position r_c centred between the minimum and maximum contour positions, r^0 and r^1, with outer volume width D

The hybrid integral contour position (V_1) was evaluated on rectangular contours selected with respect to the contour position (r_c) as defined in Figure 7.2b. This notation and implementation is consistent with the notation used for the 2D J-integral forms presented in section 6.3.2 (see Figure 6.3). However, the phrase 'contour' is loosely used here as V_1 and V_0 are both integrated (whereas only the area A or line Γ are integrated in Figure 6.3). Note that the area integral in Chapter 0 is identical to the mid-plane of the hybrid volume integral (Figure 6.3b) due to the structure of Q_{hyb} shown in Figure 5.2. In the work of Rannou *et al.* (2010), a ramping function is used to prevent area integrals resulting when the integration volume intersects with a free surface (see Figure 23 of that reference). It is worth mentioning that the hybrid volume integral, and area integrals developed here do not have this difficulty. However, this is not tested in this thesis.

7.3.2 Study of synthetic errors in three-dimensional data

This section contains the analysis of synthetic DVC errors to analytical crack tip fields using the procedure detailed in 6.3.3. The aim is to profile typical DVC errors using synthetic datasets to quantify the errors in experimental datasets (as done in Chapter 0). Setting $K_{I-III} = 1$ MPa.m$^{1/2}$, an equivalent theoretical J value (J_{th}) can be determined using Equation (6.16). This was assuming plane strain, and a Young's modulus and Poisson's ratio of 100 GPa, and 0.35; resulting in J_{th} =31.5 MJm^{-2}. Then displacement fields associated with J_{th} can be generated using Equations (2.10)-(2.12), and the procedure in Table 6.1. The calculated J values are normalised to the theoretical value (J/J_{th}), as shown in Figure 7.3. Note that E in Equation (6.16) is cancelled out by this normalisation, enabling comparisons to new experiments with different Young's modulus values, assuming variations in v are not significant.

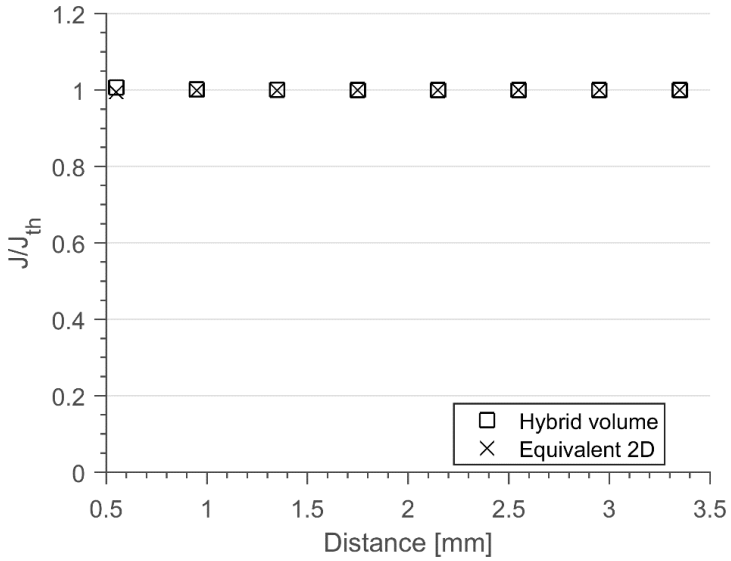

Figure 7.3: Hybrid volume integral compared with domain integral and true *J*-integral values

Random displacement errors

To investigate the effects of noise on the accuracy of *J* estimates, Gaussian (zero mean) white noise was added to the analytical displacement fields, from which stress, strain and displacement gradients were computed. The random noise was incremented linearly from zero to a maximum of 8 % of a pixel displacement, and the error was recorded as the RMS percentage difference from the noise free result. The RMS from each data point is the result of 1×10^4 *J* calculations (Figure 7.4). The results are shown in Figure 7.4, indicating an approximately linear response to random displacement errors of all *J* values.

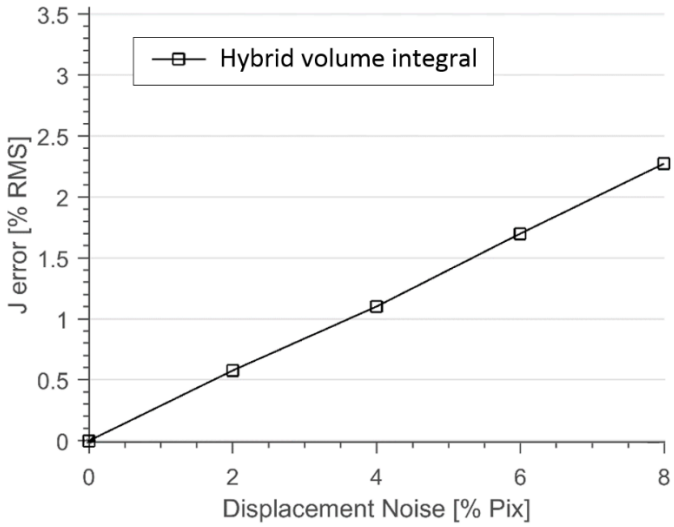

Figure 7.4: Percentage error in *J* values from random displacement noise

Sample misalignment errors

In DVC experiments, sample movement may be caused by the X-CT method used to acquire images. For example, the stop-start approach to improving image sharpness in tomographic reconstructions may jolt samples if not firmly fixed to the rotation stage (Figure 1.4). Similarly, positioning of the *J*-integral on the 3D crack front is liable to errors if the crack front is too elusive to detect accurately (e.g. by crack closure (Rannou *et al.*, 2010)). In this section, misalignments in the positioning of the *J*-integral local co-ordinate system in the reference configuration are studied.

Note that misalignments in the deformed configuration can be removed with rigid body motion correction[36].

For the purposes of investigation, it is assumed that rotational alignment (e.g. by visual inspection) can be maintained to within an angle of 6°. The errors due to rotation of the local co-ordinate axes x_1, x_2, and x_3 by angles γ_1, γ_2, and γ_3 respectively ($\pm 6°$) is shown Figure 7.5, showing only a slight effect. The total errors amount to less than 1 % (assuming errors are additive), with the major contribution from rotation about the crack plane normal. As the hybrid volume integral is shown to be robust to the tested rotational errors, the approach taken in this paper was manual alignment; which was assumed to be within 2° of the crack plane. This test included results from contour distances of $r_c = 50$ %, and $r_c = 75$ %, to demonstrate how these effects are altered by setting different contour distances.

Crack interface errors

This section investigates the errors due to masking of the crack tip region. It was already found in the previous chapter that mode I data was significantly more robust to errors than the asymmetric modes, also shown in this investigation. Figure 7.2 shows the mask region as indicated by r_m, used to study the effects of the deletion of erroneous data localised around cracking in DVC results. This is approximated by a rectangular volume shown in cross-section on the crack schematic in Figure 7.2. r_m is incremented by a single material point per iteration such that $r_m = 5$ %, with an ROI grid of 40×40.

Figure 7.6 shows the results of masking mode I fields by setting $K_I = 1$ MPam$^{1/2}$, $K_{II-III} = 0$. This shows a distinct robustness to masking noticed from the surface J-integral (Figure 5.7). Labels in Figure 7.6 are omitted for clarity and due to the closeness of the line plots. Note that corresponding to the increase in r_m, the plots start from the vertical axis.

Repeating the test with fully mixed mode data $K_{I-III} = 1$ MPa$\sqrt{\text{m}}$ shows a significant increase in susceptibility to crack face errors in Figure 7.6. Again, referring to the 2D data in Figure 6.7, mixed mode data does not achieve similar robustness to masking. The presence of mode II and III displacements results in a 10 % error in J estimates at the mid contour (i.e. a normalised distance of 0.5).

The results of Figure 7.6 and Figure 7.7 are summarised, selecting contours at r_m= 50 % in Figure 7.8. These results show that the hybrid volume integral obtains similar errors to the equivalent 2D integral. However, as stated previously in the conclusions of Chapter 3, the hybrid volume integral is flat topped in the crack front region. Figure 7.8 also shows results from the classical volume integral. The improvement in accuracy of the hybrid volume integral form may be due to the 'flatness' (see Figure 5.2) which appears to improve the robustness to crack face errors in general, particularly in mixed mode cases.

[36] Note that all the terms in the J-integral are derived from displacement derivatives, making J calculations immune to rigid body translations. However, rigid body rotations may have some effect if first order approximations for stresses and strains are used.

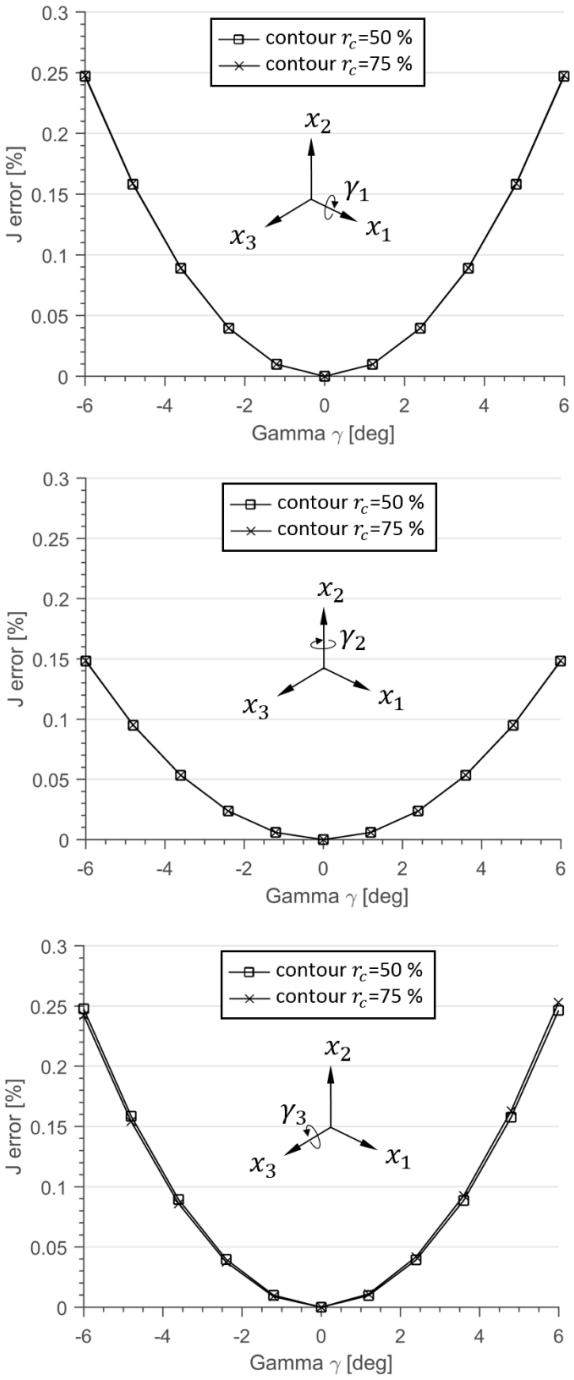

Figure 7.5: J % error due to rotation about axes x_i (γ_i).

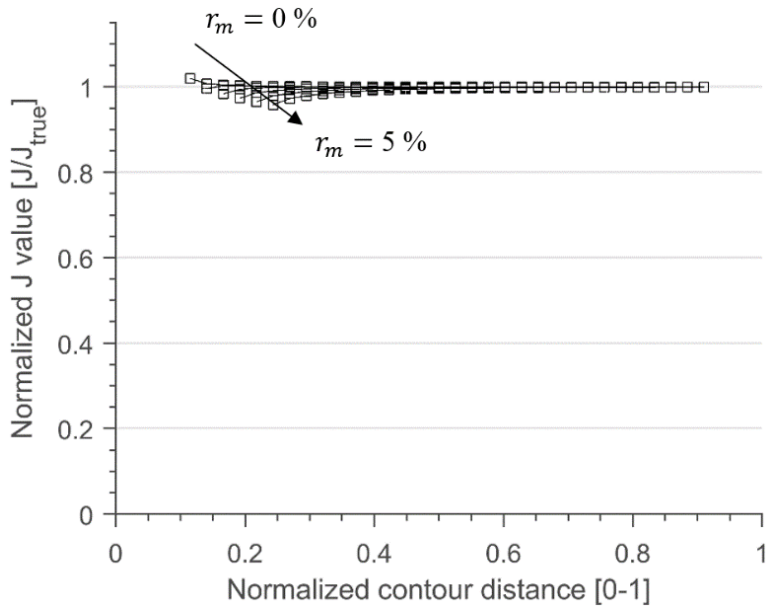

Figure 7.6: Normalised *J* values determined from mixed mode data (K_I = 1 MPa.m$^{1/2}$, K_{II} = K_{II} = 0), direction of increasing mask size indicated

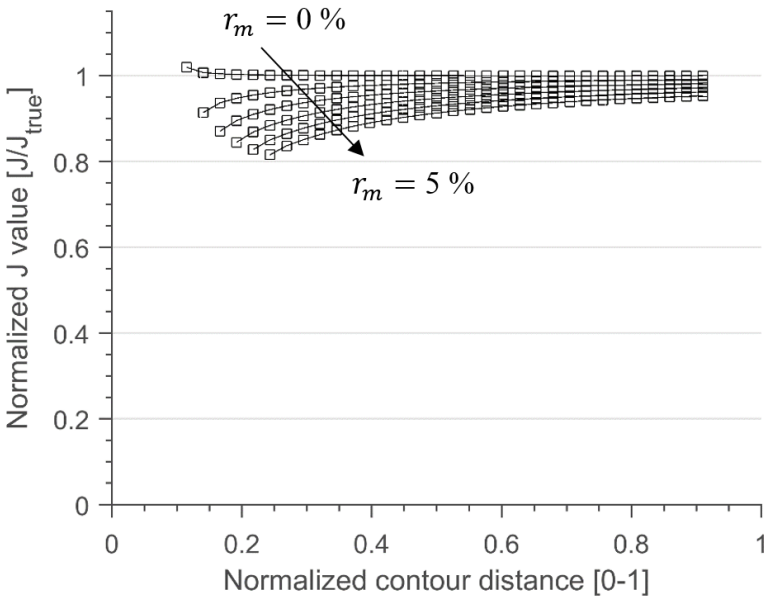

Figure 7.7: Normalised *J* values determined from mixed mode data ($K_{I\text{-}III}$ = 1 MPa.m$^{1/2}$), direction of increasing mask size indicated

To address these errors, it is shown that linear extrapolation can once again restore contour independence to mixed mode results in contours larger than r_m= 50 % (Figure 7.9). However, it is shown that by interpolation of the crack face data, convergence in the mixed mode case can be reinstated. Figure 7.9 shows that analytical fields can be restored to less than 5 % error within several contours of the mask front.

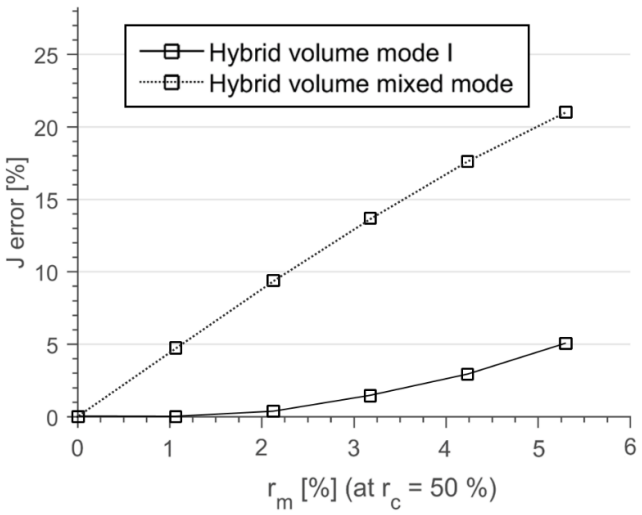

Figure 7.8: Comparison of *J* results from the volume, hybrid volume, and equivalent 2D integral at fixed contour position (r_c = 50 %), for increasing mask r_m

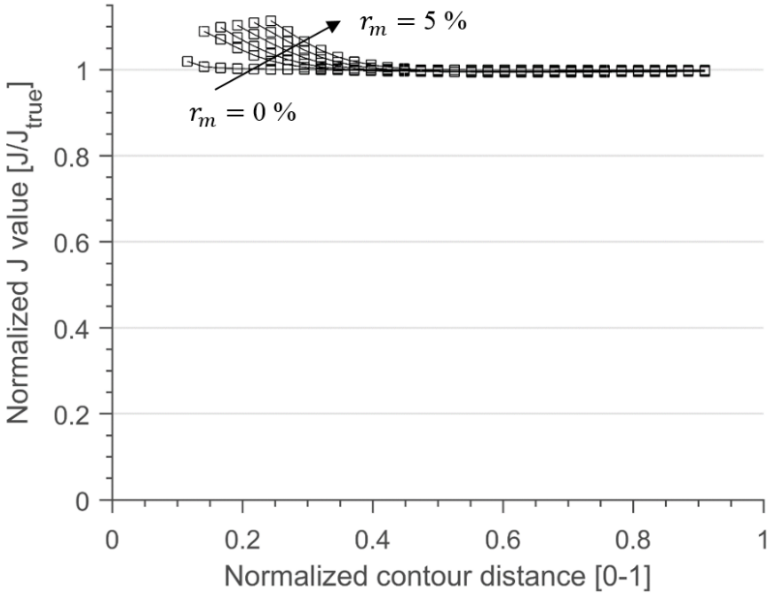

Figure 7.9: Normalised *J* values determined from mixed mode data ($K_{I\text{-}III}$ = 1 MPa.m$^{1/2}$), replaced by linearly interpolated crack face data, direction of increasing mask size indicated

7.4 Verification on DVC obtained displacement fields

In Chapter 0, the *J*-integral was computed directly from DIC fields because the co-ordinate system was automatically aligned with the calibration plate, which in turn was located manually at the crack tip position. However, a mapping procedure is required in global data to map the integration volume to the relevant location on the crack front where *J* is to be calculated. Additionally, in this approach, the integration volume is kept consistent, allowing the procedure to remain identical for each *J* computation. A limitation of the approach developed here is that it only permits *J* integral calculations on crack fronts that are locally straight, and planar. Non-planar crack front geometries require a curvilinear implementation, such as the original work of Fernlund et al. (Fernlund *et al.*, 1994), or the *F*-integral by Eriksson (Eriksson, 2002).

Consider the crack front represented in the global co-ordinate system X_i, as shown in Figure 7.10. In the following procedure, the global displacement field obtained by DVC, denoted $\tilde{u}_i$ is interpolated to a region of interest (ROI), which is exactly the volume previously used for analytical fields in Figure 7.2, i.e. a regular grid of points centred about the crack front. The ROI also possesses co-ordinates and positions in the global system (see global position), centred at a position on the global crack front. The global data is interpolated using the global material positions ($\tilde{x}_i^l$), then mapped with the rotation tensor C_{ij}^R (directional cosines) and the translation vector C_i^T to the local co-ordinate system of the ROI (x_i) using,

$$u_i = C_{ij}^R \tilde{u}_j + C_i^T \quad (i,j = 1,2,3) \tag{7.2}$$

The crack front positions are reliant on a prior procedure to segment the crack geometry from the images or displacement fields. In this approach, the crack is specified as a curve comprised of L piece-wise linear segments (l) between P_1 and P_2 – the positions where the crack front meets the material surface. Each line segment (l) is defined by end-points s^l and s^{l+1}, and contains the centre position c^l about which each J evaluation takes place. Assuming a planar crack geometry, the local crack front orientation $\tilde{x}_i^l$ can be determined in global co-ordinates X_i, using the q-vector (q^l), and the normal to the crack plane (n^c): $\tilde{x}_1^l = q^l$, $\tilde{x}_2^l = n^c$, $\tilde{x}_3^l = n^c \times q^l$ the normal to the crack plane and line segment l. Subsequently, the procedure for evaluation of the local J-integral along the 3D crack front as follows:

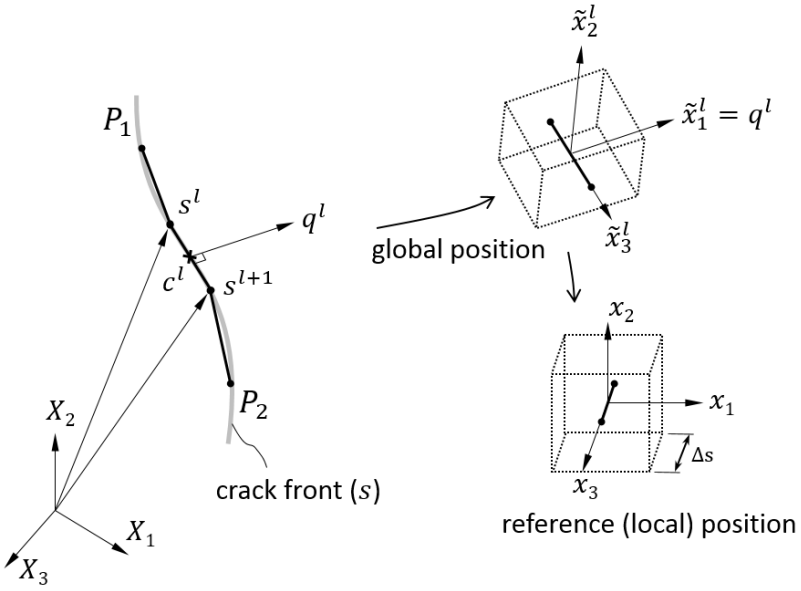

Figure 7.10: Crack front described by discrete points on the crack front s^l, global crack segment co-ordinate system $x^l i$, and local co-ordinate system x^l

Table 7.1: Algorithm to determine J values along 3D crack fronts

STEP	DETAILS
A: PRE-PROCESSING OF DISPLACEMENT FIELDS	
1	Removal of rigid body rotation and translation
2	Cropping and orienting displacement fields
3	Artifact removal (e.g. from crack faces)
B: CRACK SEGMENTATION	
4	Specify crack front positions on the surface[37], P_1 and P_2
5	Segment crack geometry, crack plane (S_c), with normal n_i^c
6	Extract crack front (s) in the direction P_1 to P_2
7	Discretize s into l lines segments Δs, and points s^l
C: J-INTEGRAL EVALUATION	
8	Define and store reference ROI position (Figure 7.10)
9	**for** (segment l between P_1 to P_2) **do**
10	Compute chord centres c^l from s^l, s^{l+1}
11	Determine unit q-vector q^l: perpendicular to l and normal n^c,
12	Define local co-ordinates $\tilde{x}_i^l$: $\tilde{x}_1^l = q^l$, $\tilde{x}_2^l = n^c$, $\tilde{x}_3^l = n^c \times q^l$
13	Map reference position grid crack front centre c^l,
14	Interpolate global displacements $\tilde{u}_i$, to ROI in global position,
15	Transform $\tilde{u}_i$ to local (crack front) co-ordinates (x_i),
16	Compute fields (stress, strain, etc.), Equations (2.24) - (2.26)
17	Construct Eshelby tensor P_{j1}, Equation (7.1)
18	**for** (contour r_c between r^0 and r^1) **do**
19	Generate Q_{hyb}, $\frac{\partial Q_{hyb}}{\partial x_i}$, Equations (2.40) and (5.12)
20	Compute $J_{hyb}(c^l)$
21	**end for**
22	**end for**

[37] e.g. by direct inspection of specimen or reconstructed images.

The following sections contain two experimental case studies to investigate the accuracy of the *J*-integral methodology in the volume, firstly under mode I loading, and secondly due to mixed loading. The errors in each case are studied based on the previous investigations in section 6.3.3.

7.4.1 Mode I loading: SENT specimen

The aim of this section is to verify the *J* hybrid volume integral method on a standard fracture test, in this case the single edge notch tensile (SENT) specimen. Displacement fields are obtained experimentally from DVC and X-ray Computed-micro-Tomography (XμCT). *J*-values computed from the crack front of the SENT specimen can therefore be easily verified with analytical solutions for the geometry (SENT). The pointwise values are also compared with finite element results using Abaqus' in-built volume integral post-processor. The data used in this section was provided by Prof. Valéry Valle[38], UFR - Faculty of Science, Université de Poitiers, Poitiers, France. Further details regarding the material and testing parameters were provided mainly via email correspondence with Prof. Valle.

Experiment and material

The selection of materials with sufficient natural image contrast within the volume is a significant limitation in DVC analysis. In the following study, a material has been designed with an optimised 'artificial' contrast pattern, using the method published in the work of Barranger *et al.* (2010). The required high contrast pattern is achieved by a suspension of high attenuation particles in a low attenuation matrix. It is suitable if the matrix material is of a low enough Young's modulus (relative to the fracture toughness) to allow high SNR deformation maps without risk of material damage (which is hard to quantify, and therefore undesirable for validation studies). The matrix material selected was polyurethane which has a nominal Young's modulus of less than 100 MPa, and low X-ray attenuation (less than 20 %, at 200 keV, using the specimen dimensions in Figure 7.11a). Copper particles were used as the high attenuating pattern material, which could be mixed evenly with the polyurethane while still a resin. Figure 7.11a shows the X-CT region of interest, which is a central region with dimensions 16 × 50 × 14.5 mm, within the larger dog-bone shaped specimen. In this experiment, a sharp V-notch is used as a proxy for a crack. The V-notch has a width of 0.3 mm, notch angle of 16.7° and is situated in the specimen as shown in Figure 7.11.a – dimensions shown on inset. The notch front is planar with the curvature close to the cutter blade radius of 80 mm. The depth of the crack measured at P_1 and P_2 was determined by averaged measurements from the specimen (manually) and from tomographs to be 5 mm (Figure 7.11.b).

XμCT tomographic images were captured before and after loading with a tensile force 292 N in the X_3 direction. The X-ray projections for the reference and deformed configurations were reconstructed with back-projection (Feldkamp *et al.*, 1984), with a final resolution of 14.7 μm/voxel. DVC was performed between the reference and deformed images with a subset size of 120 × 120 × 120, and step-size of 8 voxels (or 117.6 μm). The DVC method is an in-house method of the UFR - Faculty of Science, University of Poitiers. The exact details of the DVC algorithm could not be disclosed as the method is unpublished.

[38] valery.valle@univ-poitiers.fr, +33 5 49 49 65 45

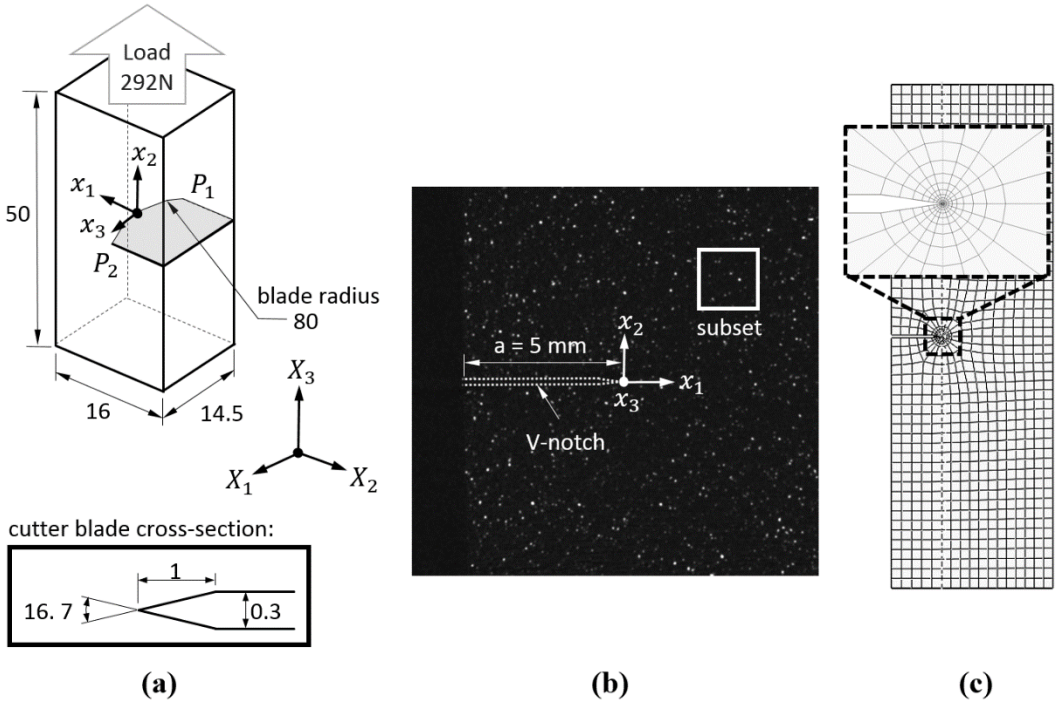

Figure 7.11: (a) Specimen and notch dimensions in global co-ordinate system, (b) X-ray tomograph of V-notch showing copper particles (light dots) and subset size (120^3 voxels), (c) FEM model with crack tip shown expanded.

The material properties were provided by l'Université de Poitiers in the form of tensile test data from un-notched specimens of the same geometry and casting process. The Young's modulus and Poisson's ratio were determined from the experimental stress strain curves from the un-notched geometry to be $E = 96.4$ MPa and $\nu = 0.428$. The specimen geometry with slight crack front curvature was modelled as linear elastic in Abaqus and in the J-integral calculations based on nominal strain values being within 10 % of a linear fit to the stress strain curve. At the notch V-tip, a limited region of high strain is likely to produce nonlinearity's, which have not been accounted for. The Abaqus FE model used quadratic elements with quarter point elements along the curved crack front, an initial radial element width of 0.3 mm at the notch mouth, converging to 0.01 mm (after 10 rings of elements) at the crack front, as shown in the magnified window in Figure 7.11c. For evaluation of the J-integral, a subvolume was used, limited to the 6×6 mm around the crack front. Evaluation of the J-integral followed the algorithms in Table 7.1 (a-c), with problem specific details outlined below.

J-integral methodology

The DVC results from the internal crack front were imported into Matlab for pre-processing (Table 7.1a), crack segmentation (Table 7.1b) and J-integral evaluation (Table 7.1c). After cropping the edges to a remaining volume size of $12 \times 12 \times 12$ mm, the rigid body rotation was removed using the Euler angle extraction methodology of Shoemake (Shoemake, 1994). The DVC analysis for the specimen used an in-house code of the Faculty of Science, Université de Poitiers, which does not make the correlation coefficient values available. However, the crack geometry was provided as inferred from the shape of the cutter blade and the raw images (Table 7.1b). To improve the estimate, a best-fitting plane was determined by least-squares and the crack front shape was regularised to closest approximate circle of radius 80 mm (i.e. matching the cutter blade radius). Artifacts caused by the crack faces and subsets near to the crack tip singularity were minimised with the outlier removal procedure of Chapter 4, in which only the 1 mm region above, below and ahead of the crack faces were processed for artifact removal, and therefore the crack geometry was

the only required input for the material distribution (a requirement of the artifact removal procedure detailed in section 4.2.1).

Then the procedure in Table 7.1c was used to determine J values at increments along the crack front for each crack front segment. The segments and associated global regions of interest are shown on a specimen cross-section (in the crack plane shown in Figure 7.11a) in Figure 7.12. Each computation was interpolated to a regular grid positioned centrally over the crack front segment l, with the crack oriented in the x_1 direction. Once centrally located, errors caused by interpolation and crack face artifacts were masked and interpolated by 0.4 mm ($r_m = 5$ %). Then displacements interpolated to the grid points could be transformed to the local co-ordinate system using standard co-ordinate transformations. Once in the local co-ordinate system, the stresses, strains, and displacement gradients and J integrand including the hybrid Q field (Q_{hyb}) were generated in as demonstrated in section 7.3.1. Figure 7.12 also shows the J integration volumes extending from P_1 to P_2, accounting for the slight curvature (radius 80 mm).

The results from the evaluations in Figure 7.12 (J_{hyb}) are shown in Figure 7.13 extracted at a contour distance fixed at 50 % of the ROI (1.5 mm) and normalised to the total crack front length (P_1 - P_2), on the interval [0.1-0.9]. The plane strain analytical geometric estimate for the SENT specimen was calculated using formulas from Tada et al. (Tada *et al.*, 2000). These values were checked against several other formulas (e.g. Gross (Gross and Srawley, 1964)) with small variation (approx. 0.5 %). Then using Equation (6.16) to convert $K_{I_{SENT}}$ to an equivalent plane strain J_{SENT} value. J_{hyb} estimates and the Abaqus estimates - J_{vol} are normalised to J_{SENT}, as shown in Figure 7.12.

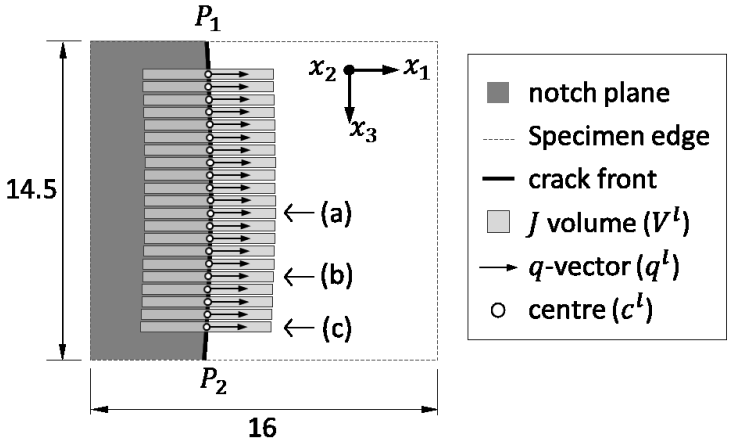

Figure 7.12: Crack front increments showing regions of interest

Other than the approximate agreement between the analytical, Abaqus, and calculated J estimates, one immediately notices the significant deviations at 35 % of the crack front, the source of this error was not apparent from displacement fields or tomographs, and therefore perhaps illustrates the sensitivity of the formulation to errors in the high strain region. It is also notable that J_{hyb} achieves a constant and slight under estimate, with values raised close to the specimen edges, and lowered in the centre. This may be due to the linear elastic assumption which does not account for strain energy history, and therefore results in an error due to the nonlinear strains caused near the notch tip. Verification of this should implement a hyper-elastic material model, but this was not part of the scope of this thesis (section 3.4).

The experimental errors are usually achieved with experimental rigid body motion tests, but this test was not available in the Poitiers dataset. The random error was therefore inferred from a user selected region remote from the notch or specimen edges (experiencing uniform errors and strains).

The random errors were calculated using the standard deviation in this region after the strain effects were approximately removed using subtraction of planar fits. This provided estimates for the error of 5.4 % voxel (random error). This corresponds to a 1.5 % error in J due to random displacement errors. Considering the slight curvature - approximately 4° over the specimen widths arc-length - provides a negligible contribution to the error (less than 0.5%). For the given value of the extrapolation (5 %), contributes a further 1 %. Therefore, the total error that can be accounted for in analytical results amounts to approximately 3 %, which is close to the standard deviation of the J_{hyb} (3.5 %) if it is calculated without the outlier at 35 % of the crack front.

The contours for data points labelled (a), (b) and (c) are shown in Figure 7.14; in which (a) starts at the mid-plane toward (c), the value closest to the specimen edge. These values were selected by rounding to the nearest $s = 1/2$, $s = 2/3$ and $s = 4/5$ on the crack front. Although not shown, the convergence was approximately symmetric – i.e. similar if (a), (b) and (c) were selected on the opposite side of the specimen. Poorest convergence can be found closer to the edge of the specimen suggesting that the rising edges that appear in Figure 7.13 are not an indication that some error source is reducing toward the specimen surface, but rather as an increase in error.

7.4.2 Mixed mode experiment: inclined crack under shear loading

Two prominent error sources related specifically to volume integrals and DVC data have been identified in the previous sections. The first is that DVC accuracy is limited by the natural pattern of the sample material. The second is that volumetric J-integral forms usually require integration of data close to the crack front. Previous sections have also shown that the volumetric J forms are particularly sensitive to mixed mode data, with especially large errors incurred by masking of erroneous data without an appropriate replacement procedure (e.g. extrapolation).

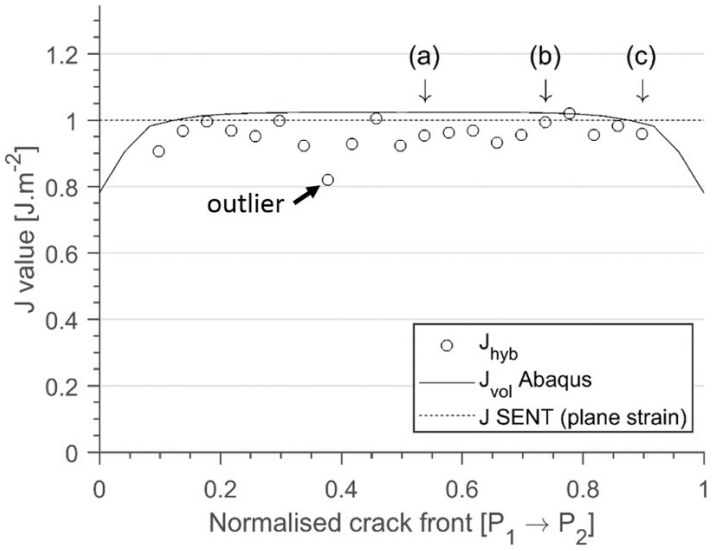

Figure 7.13: J hybrid volume integral estimates, including the volume integral estimates (Abaqus) and the SENT analytical estimate in plane strain

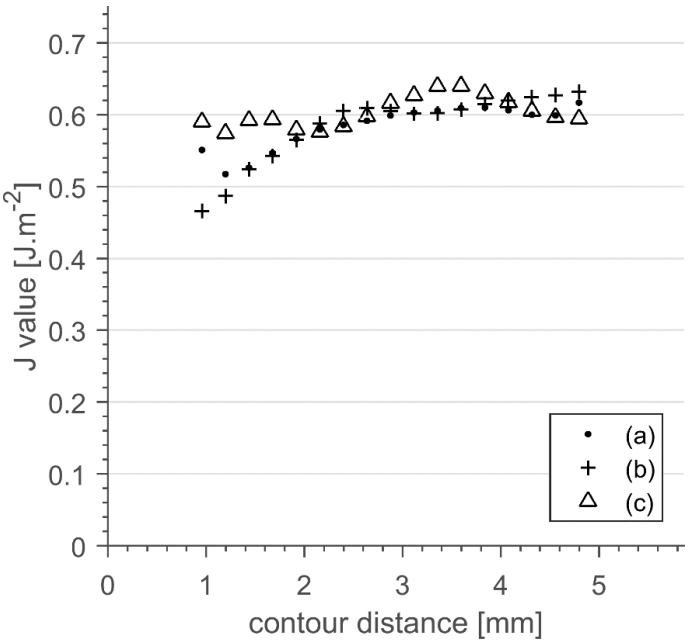

Figure 7.14: Convergence plots for *J*-integrals evaluated at positions nearest to (1/2), (2/3) and (4/5) of the crack front. Note: (a), (b), and (c) refer to labels in Figures and 6.16.

The previous section tested a configuration which minimised both error sources (i.e. high material feature contrast, nominally mode I deformations) for purposes of methodology validation. Therefore, to test the robustness of the method, a material with natural contrast pattern is studied under mixed mode loading in this section. The material is Magnesium alloy (WE43) which has high commercial value due to good castability, high strength, high creep resistance, high corrosion resistance and high flame (ignition) resistance. Hence it is widely used for structural components in aircraft for weight savings, and for orthopaedic implants due to its biocompatibility (Klocke *et al.*, 2011). This experiment studies the capabilities of the developed methodology to extract mixed mode values using the glass-fibre shear loading rig that was introduced in section 5.2. (Figure 5.10), involving an inclined notch.

Experiment and material

Magnesium alloy WE43 produces contrast patterns in X-CT reconstructions due to the attenuation variations between the Magnesium bulk material and rare earth precipitates (4wt% Yt, 3wt% Nd) at the grain boundaries. These are shown in the magnified image of the surface in Figure 7.15a, and more brightly in the X-CT reconstructed image (a central slice) in Figure 7.15b. The brightening effects close to the edges should not be mistaken for variations in precipitate density. Rather, this is due to beam-hardening, common (and persistent in this case[39]) X-CT image artifact (section 2.3.2).

The elastic properties of Mg WE43 were provided by the manufacturer as Young's modulus of 44 GPa and a Poisson's ratio of 0.35. The notch was machined using wire-Electrode Discharge Machining (wire-EDM) to minimize residual stresses and work hardening that would result from mechanical notch cutting methods. The notch was machined at an angle of 30° to each of the global axes X_i. The extremities of the sample (not shown) are flanged in the standard dog-bone shape to

[39] Built in methods for removing beam hardening effects are available in Nikon software, but the could not be fully removed in this experiment.

ensure homogenous fields remote from the notch. For further details on the loading and imaging methodology see section 4.2.

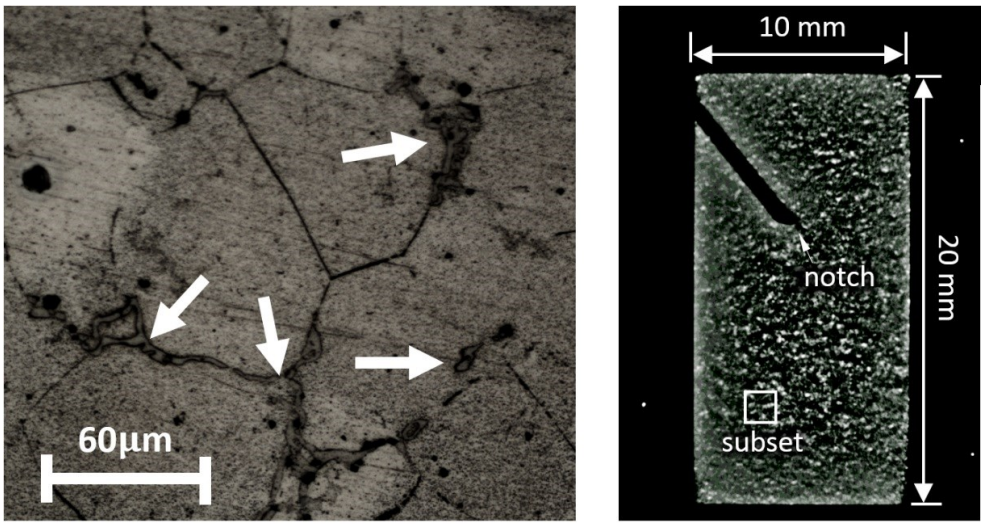

Figure 7.15: (a) Grain boundaries revealing precipitates in WE43 alloy Magnesium using aqueous saturated picric acid with HCL and a wetting agent, (b) X-CT scan of sample showing subset size and notch.
Note: the notch width apparent in (b) is 50 % greater than the true notch width (0.3 mm) due to the acute angle (30°) between the notch and cross-section planes.

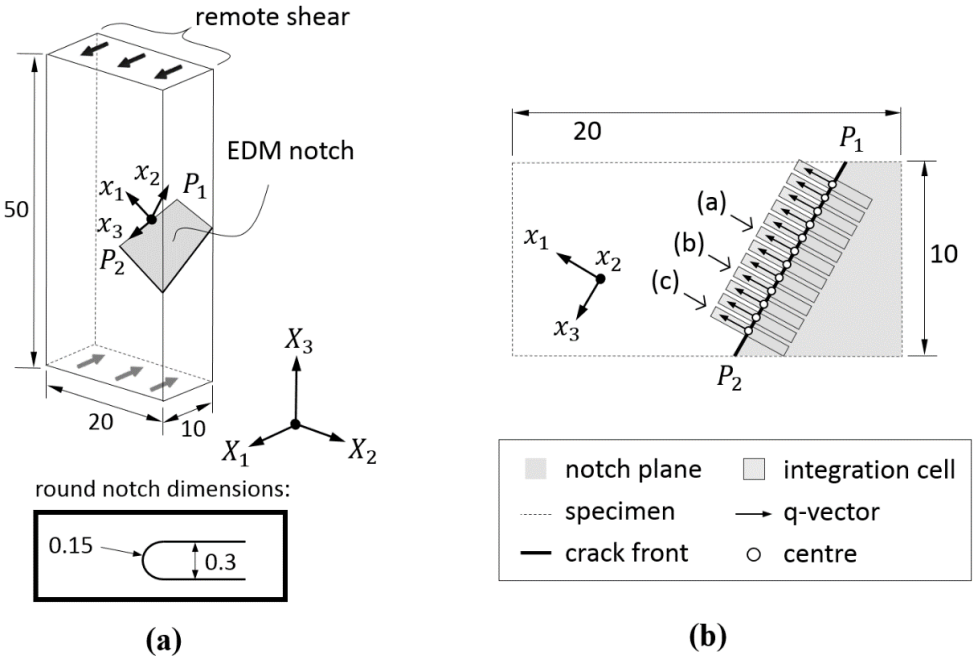

Figure 7.16: (a) Inclined notch dimensions, (b) *J*-integral evaluations

As with the previous case study, Figure 7.16b. shows the notch and integration volumes used for the evaluation of the *J*-integral in Figure 7.17. Note that the integration volumes marked (a), (b), and (c) in Figure 7.16b start at the mid-plane and proceed toward (c), the value closest to the specimen edge using values closest to (1/2), (2/3) , and (4/5) of the crack front (contours are shown in Figure 7.18). The approach was verified with a finite element solution to obtain reference values as shown in Figure 7.17, to which the values were normalised. The most apparent error is the effect

of rising J values close to 0.2 on the crack front. It is estimated that this is a result of beam hardening as this end of the specimen has the longest crack.

An error was calculated as the standard deviation from the finite element results as approximately 5 % (excluding the rising error from fractions of $s = 0.2 - 0.35$ on the crack front). The experimental noise was determined from rigid body displacements of the scans, with displacements determined with the same parameters, giving a resulting value of 6 % displacement noise. However, it should be noted that the Magnesium was significantly affected by outliers near the crack face due to the beam hardening effects, and possible other nonlinear effects due to tomography of conductive material (Mostafavi *et al.*, 2015). Referring to Figure 7.4 this corresponds to an error of approximately 1.75 %, which is a significant under estimation, particularly between $s = 0.2$ and $s = 0.35$. Due to the relatively small contributions from rotation errors (which were minimal during testing), the remaining error source may be due to masking (r_m= 5 %). As shown in Figure 7.9, once the mask faces have been replaced, the effects are minimal in the remote region from the crack tip, but create a characteristic deviation close to the crack front, which is prominent in the falling values between 0.5-1 mm in Figure 7.18.

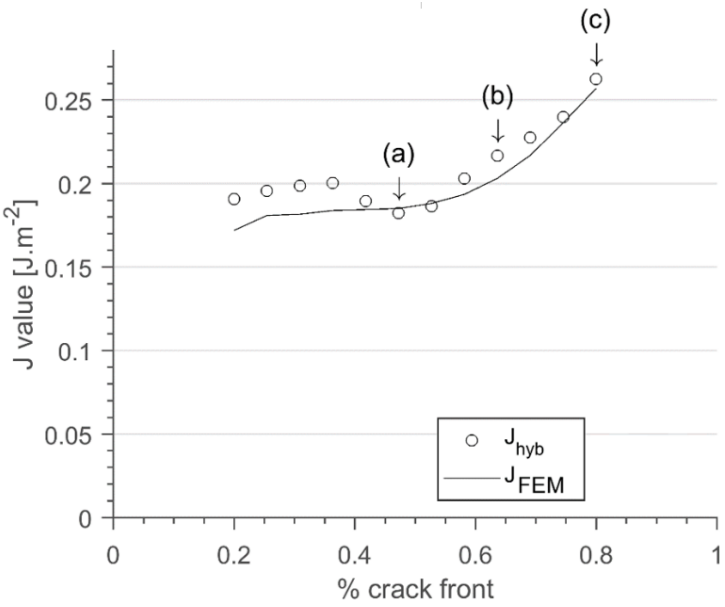

Figure 7.17: Normalised J hybrid volume integral estimates, including the volume integral estimates (in-house FEM) and the SENT analytical estimate in plane strain

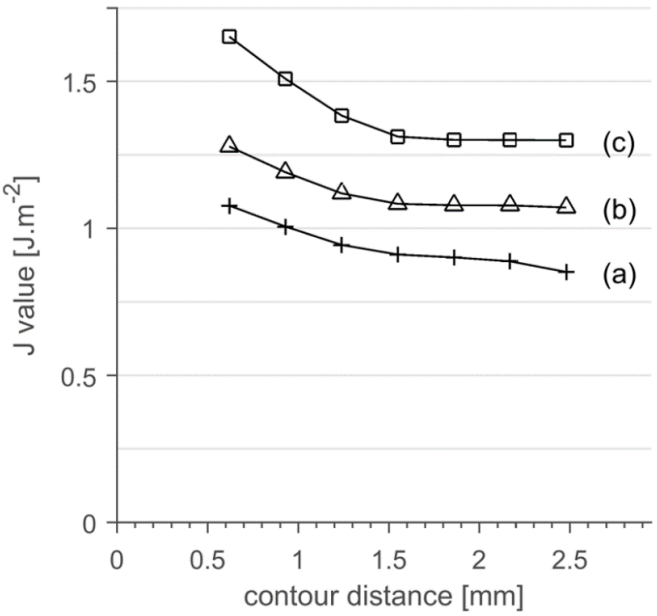

Figure 7.18: J values along the crack fronts at position annotated in 7.18-19

7.5 Conclusions

The aim of this chapter was to verify the hybrid integral on DVC data, and identify sources of error. The analytical fields perturbation approach introduced in Chapter 0 was applied in 3D in this chapter.

The error analysis revealed that the volume method is an order of magnitude more sensitive to errors, than the area integral used in the previous chapter. This was shown to be mainly due to the errors in the crack tip region, as evidenced by omitting these errors and retesting. Errors due to rotational misalignments were too slight to be of experimental concern - provided that manual alignment can be achieved within $\pm 6°$ on each rotation axis (the limit of the range tested). Translational errors are also of little concern as the hybrid form has been shown to be resilient to misplacement of the integration volume provided that the crack front remains within the inner volume (V_0). Hence rigid body positional errors amount to less than 1 % if such errors can be assumed to be additive. As previously demonstrated on the surface, masking provides an effective and simple tool to eliminate crack face errors, but is only applicable to mode I data. Errors compounded in the volume to approximately 10 % under mixed mode loading.

Experimental results from two case studies were analysed to verify the methodology in mode I and mixed mode cases. The mode I case used a polyurethane resin matrix with suspended copper particles and a V-notch crack in the SENT configuration. The J values showed agreement to analytical and finite element (Abaqus volume integral) solutions to within 5 %, which was within the error bounds determined analytically. The mixed mode problem used a Magnesium WE43 alloy with an inclined single edge rounded notch under shear and bending loads. The results were compared to the analytical solution for the SENT geometry, and Abaqus results. In both cases, the profile J values could be determined to within 5 % of the finite element solutions, aside from outliers due to beam-hardening.

7.6 Summary

The volume integral was verified in the hybrid form developed in Chapter 5. This chapter has quantified the errors in terms of the analytical method developed in Chapter 0 for the generation of synthetic fields and errors (Table 6.1) and error quantification (Table 6.2), but applied to the total J instead of decomposed values.

The resilience to random displacement errors, rotational errors about all three-axes, and errors due to masking, were tested. It was found that rotational errors amounted to less than 1 %, and masking errors are minimal if the masked data (0 – 5 % of the ROI) can be extrapolated with the linear elastic finite element solution.

Two case studies were implemented to verify the mode I, and mixed-mode (I-III) cases. The results achieved error amplitudes within 5 % agreement to finite element estimates. The challenge in the mixed mode test was in sustaining convergence while approaching the surface. Comparing the tests shows that the J-integral is most prone to DVC errors under anti-symmetric (mode II-III) loading, consistent with the surface implementation (Chapter 0).

Testing in the volume used X-ray computed tomography to acquire images and DVC for displacement maps. The measurements were verified on two configurations: a SENT polyurethane composite specimen (mode I), and a shear loaded inclined notch in Magnesium alloy-WE43 (mixed-mode). The J-integral was verified against values from finite element fields, showing similar sensitivity to mixed-loading.

Further decomposition of the volume integral is required to obtain SIFs. However, the existing approaches do not allow for contour independent extraction of the anti-symmetric modes from the J-integral. The next chapter discusses the limitations of the existing approaches, and proposes two extensions to improve the contour independence of extracted SIFs.

8 Application of the decomposition method to the volume integral and DVC data

This chapter investigates the extraction of SIFs from displacements in the volume using the *J*-integral and the decomposition method. Chapter 5 developed the hybrid volume integral form which was tested experimentally in Chapter 7. This chapter concentrates only on the decomposition of the volume integral. Therefore, Chapters 7 and 8 combined, achieve for the volume what was achieved on the surface in Chapter 0. Previous DVC datasets introduced in Chapters 4 and 7 assist with the analytical, numerical and experimental verifications.

This chapter was presented at the 11th British Society of Strain Measurement Conference (Molteno *et al.*, 2016), and has been prepared for publication in the *International Journal of Solids and Structures* with co-authors: Marrow and Becker. The contributions of the authors are:

- The author (Matthew Molteno): Developed the method.
- Prof. James Marrow, Dr Thorsten Becker: Standard supervisory roles.

Other noteworthy contributions from non-co-authors:

- Prof. Meinhard Kuna and Prof. Bhushan Lal Karihaloo: Both gave assistance in some detail on the history of the method (section 8.2), and the mode III component of displacements (section 8.4.1) via telephone conversations and email.

8.1 Introduction

It is important to consider that the decomposition method was originally developed for implementation on planar problems (Ishikawa *et al.*, 1980; Ishikawa, 1980). Since its inception, it was has been successfully on propagating elasto-dynamic (Nishioka and Atluri, 1984), elastic-plastic (Diekmann *et al.*, 1991) cracks, to decompose K_I and K_{II}. The standard approach allows direct extraction of K_{I-III} factors from planar experimental data as published by the author (Molteno and Becker, 2015c).

A property of the decomposition method is that separation of the fields (which uses symmetry operations) is theoretically unaffected by crack tip uncertainty in the plane of symmetry (the x_1 direction in all approaches in this thesis), as this is also the symmetry plane about which crack tip fields are reflected. The experimental advantages of this feature are apparent when crack tip positions are too fine or complex to precisely determine experimentally (e.g. due to micro-cracking or due to small COD values in hard materials). This has the possible advantage over alternatives such as field fitting approaches (Huchzermeyer, 2017; Roux *et al.*, 2009), and the interaction integral which both require placement of analytical fields at the crack tip position. It should be mentioned that the errors incurred by the interaction integral by DVC errors have not been quantified. However, the errors due to crack tip position uncertainty appear to have a strong effect on the accuracy of J in the volume (Rannou *et al.*, 2010).

As shown in Chapter 0, the decomposition method can be used as a pre-processing stage to the J-integral, allowing for the convenient application of different J-integral forms interchangeably. However, the sensitivity of the J-integral to errors has been shown to be significantly affected by the choice of J formulation in Chapters 5 and 0. The intention of this chapter is to review the decomposition method in the volume to consolidate the literature, and test the applicability to the methodology developed in Chapter 7. The presently available approaches, mainly the method by Rigby and Aliabadi (Rigby and Aliabadi, 1998), stipulate the use of a specialised J-formulation which is implemented within the BEM environment. Two extensions to the method are proposed which allow for use of the method with DVC data in a similar manner to Chapter 0, i.e. enabling the extraction of mode I, II and III SIFs using the classical J integral formulations. The approach is demonstrated using the hybrid J-integral form developed in Chapter 6 on numerical and experimental data.

The layout of this paper is as follows: section 8.2 contains the historical perspectives on the decomposition method. section 8.3 contains the theoretical framework presenting the J-integral and decomposition method formulations. Section 8.4 contains the experimental implementation on finite element displacement fields. This methodology is used to determine the experimental sensitivity to noise and crack face masking. Section 8.5 presents the experimental validation using Magnesium alloy – WE43 with an inclined straight notch.

8.2 Decomposition in the volume: historical perspectives

The decomposition method is derived from the observation that the singular stress terms of Williams series expansion can be directly separated based on their unique symmetry (see Equation (2.13)). For 2D planar fields (i.e. only modes I and II), the mode I stresses are symmetric, and mode II stresses are anti-symmetric about the crack plane. Subsequent developments to 3D are reviewed below. The order is chronological, except in cases where methods have been amended by later works.

To the best knowledge of the author, the first application of the decomposition method to obtain mode I-III SIFs from the 3D crack front was by Nikishkov and Atluri (1987) who used the classical

volume integral form within the finite element framework presented at this time in (deLorenzi, 1982; Shih *et al.*, 1986). In the following decade, the same numerical approach was presented by Shivakumar and Raju (1992) who tested different virtual crack extension fields, and by Červenka and Saouma (1997) who tested the method on arbitrary (i.e. not necessarily symmetric) finite element grids (Červenka and Saouma, 1997). In the preceding works, the J-formulation for mode III contained principle stress in the x_3 direction, which was missing from the decomposed terms appearing in the work by Rigby and Aliabadi (Rigby and Aliabadi, 1998), and was more recently addressed through a direct formulation of the mode III Eshelby tensor by Eriksson (2007).

In 1993, Rigby and Aliabadi (1993) and Huber *et al.* (1993) showed that in general, only mode I can be decomposed from 3D fields. Consequently, the J integral may only be separated into symmetric part J_S (mode I), and an anti-symmetric J_{AS} (modes II and III) parts[40]. Rigby and Aliabadi (1993) proposed direct separation of J_{AS} using a ratio derived from the COD measurements, and an alternate path-area integral form. Huber *et al.* (1993) demonstrated by the substitution of analytical fields from (Williams, 1957) into the decomposed J-integral equations, that contour dependence is lost in the far field when higher order terms are present, but correct J values result close to the crack front due to K-dominance.

It should be noted that there is disagreement between these two methods. Rigby and Aliabadi (1993) derive a decomposition method (and accompanying path-area integral) from stresses which results in a decomposition of displacement gradients, whereas Huber *et al.* (1993) apply the method directly to the displacement and stress components. Although the stress components are decomposed identically, the displacement gradients do not equate because Rigby and Aliabadi specify gradient rules which are dependent on the mode of decomposition (1998). No such rules are discussed by Huber *et al.* (1993). These works were published within a few months of each-other.

An important development was the revision of the approach by Rigby and Aliabadi originally presented in 1993 in (1998). In this later work, an error in the σ_{33} term[41] in mode II was reallocated to mode III. This amendment applies to the earlier works (Huber *et al.*, 1993; Shivakumar and Raju, 1992; Rigby and Aliabadi, 1993; Nikishkov and Atluri, 1987; Chen and Atluri, 1989), and provided a revised form of the path-area integral in the works (Rigby and Aliabadi, 1993; Huber *et al.*, 1993). Certain of these works showed that the effect was a particular loss of contour independence between modes II and III, mainly in estimation of K_{III} (Rigby and Aliabadi, 1993) – most clear in Figure 7 of that reference.

The method presented by Rigby and Aliabadi is a path-area integral form which requires differentiation of stresses near the crack tip and relies on a single slice transverse to the crack front. The formulation is particularly suited to BEM analysis in which calculations of the interior displacement gradients and stresses are derived from the Somigliana identity, as discussed in (Rigby and Aliabadi, 1993; Aliabadi, 1997). The advantage of the approach is that accurate displacements and stresses can be obtained near the crack front, which is necessary for the J-integral form proposed by Rigby and Aliabadi (1998). As with J calculation, FEM approaches generally defer to the volume integral (Shivakumar and Raju, 1992; Nikishkov and Atluri, 1987; Červenka and Saouma, 1997). It is worth mentioning that a recent work by Nikishkov *et al.* (2016) uses a different definition for J_{III} from other decomposition approaches in order to apply the direct approach. His definition includes σ_{33}, ε_{33} and u_3 in the mode III J integral in agreement with his and other co-authors earlier work (Nikishkov and Atluri, 1987). Their results seem to show

[40] The reference to symmetric or anti-symmetric refers to stress and strain components only. The same grouping does not occur in other field quantities (e.g. displacements, displacement gradients, or strain energy).

[41] See Equation 50 in (Rigby and Aliabadi, 1998).

improvements in accuracy but requires a numerical solver and data close to the crack front (see further details of this method by Nikishkov and Atluri in section 2.2.3). This is not possible with DVC data, and it is not clear if the J_{III} definition is correct because the σ_{33} term tends to zero close to the crack front (Equation (2.13)). However, there is no volume integral developed from the approach of Rigby and Aliabadi (Rigby and Aliabadi, 1998). It is unclear if such an approach requires modification from the classical form as the previous works have not reconciled with the definition presented in (Rigby and Aliabadi, 1998).

8.3 The decomposition of DVC displacements

Decomposition of crack tip fields and evaluation of the 3D J-integral occurs in the local co-ordinate system $x_i(\mathrm{s})$ along an arbitrary crack front shown in Chapter 7, in which the implementation of the hybrid volume integral is given (Equation (7.1)). J determined by the above equations is equal to the sum of the independent J values obtained from fracture modes I, II and III:

$$\begin{aligned} J^1 &= J_S + J_{AS} \\ &= J_I + \{J_{II} + J_{III}\} \\ &= \frac{(K_I)^2}{E'} + \left\{\frac{(K_{II})^2}{E'} + \frac{(1+v)(K_{III})^2}{E}\right\} \end{aligned} \tag{8.1}$$

in which E, v are the elastic Young's modulus and Poisson's ratio, and E' depends on the stress state (Equation (6.16)). Recall that the J-integral calculated on experimental fields after the removal of all but the mode of interest (M), naturally computes J_M – the modal component of the field (section 2.2.5). The decomposition method proposed by Ishikawa allows for the separation of modes based on symmetry about the crack plane (Ishikawa *et al.*, 1980; Nikishkov and Atluri, 1987). For 3D problems, the displacement components can only be considered in symmetric and anti-symmetric parts (Equation (8.2)); where the symmetric part is purely mode I and the antisymmetric part is contains both mode II and III deformations.

$$\begin{aligned} u_{crack} &= \sum_{M=S,AS} u_M = u_S + u_{AS} \\ &= \frac{1}{2}\begin{Bmatrix} u_1 + u_1' \\ u_2 - u_2' \\ u_3 + u_3' \end{Bmatrix} + \frac{1}{2}\begin{Bmatrix} u_1 - u_1' \\ u_2 + u_2' \\ u_3 - u_3' \end{Bmatrix} \end{aligned} \tag{8.2}$$

Here, the notation u_i' represents a displacement field that has been reflected about the crack plane ($u_i' = u(x_1, -x_2)_i$), in the local co-ordinate system of the crack front as shown in Figure 7.1. Equation (8.2) can be used to obtain the symmetric and antisymmetric J-integral components (J_{vol_S} and $J_{vol_{AS}}$) using the volume integral definition (Equation (2.39)), applied to the symmetric and anti-symmetric modes ($M = S, AS$).

$$J_{vol_M}(\mathrm{s}) = \frac{1}{A_c}\int_V \left(\sigma_{M_{ij}}\frac{\partial u_{M_i}}{\partial x_1}n_j - W_M n_1\right)\frac{\partial Q}{\partial x_i}\mathrm{d}V \qquad (i,j = 1,2,3; M = S, AS) \tag{8.3}$$

with elastic stresses, strains and strain energy derived from decomposed displacement data u_{M_i} with,

$$\varepsilon_{M_{ij}} = \frac{1}{2}\left(\frac{\partial u_{M_i}}{\partial x_j} + \frac{\partial u_{M_j}}{\partial x_i}\right) \tag{8.4}$$

$$\sigma_{M_{ij}} = E_{ij}\varepsilon_{M_{ij}} \tag{8.5}$$

$$W_M = \int_0^{\varepsilon_{M_{ij}}} \sigma_{M_{ij}} d\varepsilon_{M_{ij}} \tag{8.6}$$

The displacement gradients for Equations 7.7-9 are described as,

$$\frac{\partial u_i}{\partial x_j} = \sum_{M=I}^{III}\frac{\partial^M u_i}{\partial x_j} = \frac{\partial^I u_i}{\partial x_j} + \frac{\partial^{II} u_i}{\partial x_j} + \frac{\partial^{III} u_i}{\partial x_j}$$

$$= \frac{\partial}{\partial x_j}\frac{1}{2}\begin{Bmatrix} u_1 + u_1' \\ u_2 - u_2' \\ u_3 + u_3' \end{Bmatrix} + \frac{\partial}{\partial x_j}\frac{1}{2}\begin{Bmatrix} u_1 - u_1' \\ u_2 + u_2' \\ 0 \end{Bmatrix} + \frac{\partial}{\partial x_j}\frac{1}{2}\begin{Bmatrix} 0 \\ 0 \\ u_3 - u_3' \end{Bmatrix}, (j = 1,2) \tag{8.7}$$

$$\frac{\partial u_i}{\partial x_3} = \frac{\partial}{\partial x_3}\frac{1}{2}\begin{Bmatrix} u_1 + u_1' \\ u_2 - u_2' \\ u_3 + u_3' \end{Bmatrix} + \frac{\partial}{\partial x_3}\frac{1}{2}\begin{Bmatrix} u_1 - u_1' \\ u_2 + u_2' \\ 0 \end{Bmatrix} + \frac{\partial}{\partial x_3}\frac{1}{2}\begin{Bmatrix} 0 \\ 0 \\ u_3 - u_3' \end{Bmatrix}$$

in which the gradient (∂x_3) is separated from in-plane gradients by the derivation in (Rigby and Aliabadi, 1998). Note that the mode I components have full entries (for $i = 1,2,3$), whereas the anti-symmetric entries are shared between modes II and III. When only symmetric and antisymmetric displacement gradients are desired, summation of the anti-symmetric terms yields a compact form using traditional gradients to differentiate Equation (8.2). This can be applied directly to DVC displacement data, but will only provide J_I and J_{AS} $(= J_{II} + J_{III})$. The full decomposition of displacements has been presented as well as partial decomposition into J_I and J_{AS}. The following section applies these two methods to numerical data.

8.4 Application to finite element data

In Chapter 0, the Williams series was used as an analytical crack tip field to verify the J-integral in modes I – III. The advantage of this analytical approach is that J calculations can be computed arbitrarily close to the crack front, and so crack tip errors in image correlation based displacement

fields can be highlighted. However, the Williams series does not generate coupling between modes II and III series expansions. For this section, a finite element based approach is needed – reutilizing the problem from Chapter 5. As presented in section 5.5, the example finite element model is of a rectangular single edged block (20×20×40) simulated using Abaqus software (ver. 6.13). The model uses banded mesh refinement (see Figure 5.3c). The following experiments operate on the mid-plane of this problem applying the decomposition method outlined in the previous section, and two proposed modifications.

The results are shown for K_I, K_{II}, and K_{III} extracted using Equation (8.7) and are shown in Figure 8.1. Reference values are shown using the same marker as generated by the Abaqus interaction integral (Dassault Systèmes Simulia *et al.*, 2013). The converged values from the final contour (contour 12) were used to mark the reference levels (black lines in Figure 8.1).

The results show that contour independence occurs in mode I after 3 rings of elements, whereas modes II and III exhibit different deviations. It is worth mentioning that reports in literature mainly indicate errors in mode III (Rigby and Aliabadi, 1993; Rigby and Aliabadi, 1998; Nikishkov and Atluri, 1987), whereas there is no marked difference in these results. The errors are within 2-7%, which are close to the range observed in Figure 7 of (Rigby and Aliabadi, 1993), and Figure 12a in (Shivakumar and Raju, 1992).

Instead of decomposing into three separate parts, the second test decomposes the results into symmetric (mode I) and antisymmetric (mode II and III), this time using Equation (8.2), results in only two contour plots, mode I remains unchanged, but modes II and III combine to form the AS part. This numerical verification supports the assertion that the J_{AS} component is contour independent (Rigby and Aliabadi, 1998).

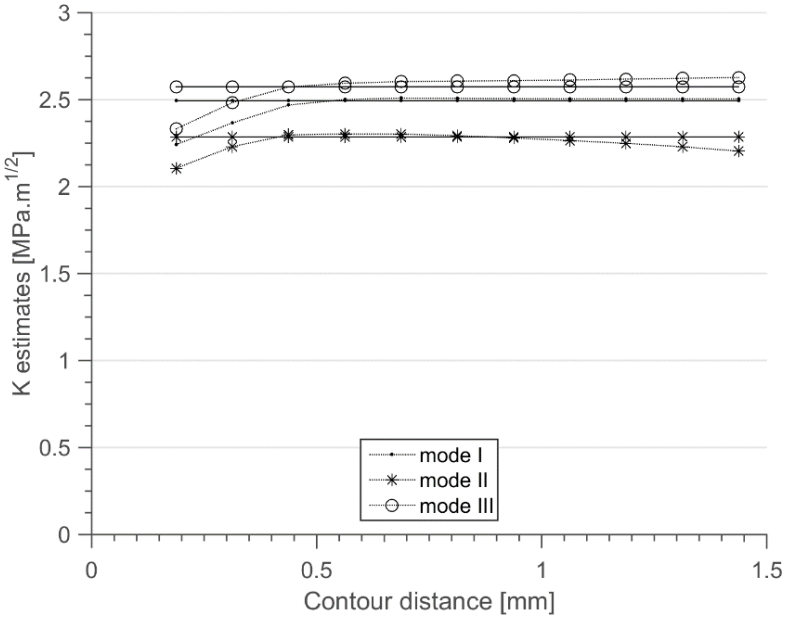

Figure 8.1: K values estimated from the mid-plane of finite element results, decomposition into mode I, II and III components.

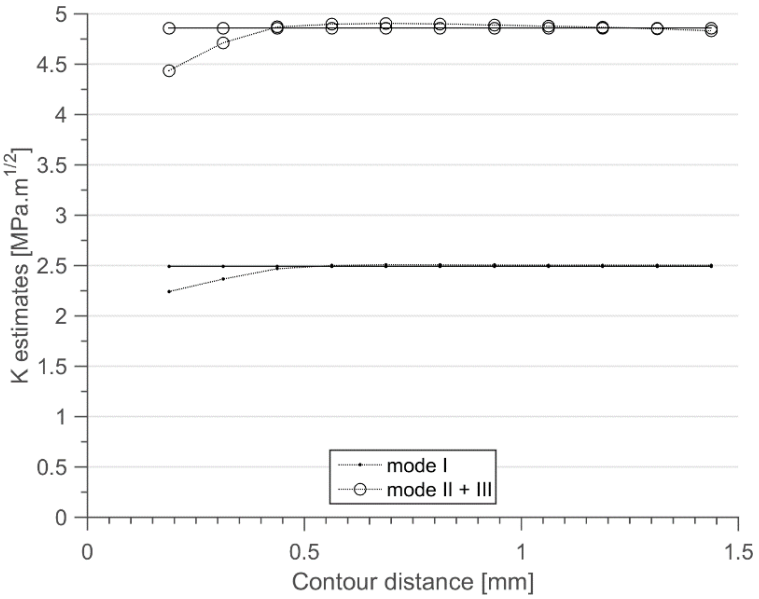

Figure 8.2: Decomposition into symmetric (mode I) and anti-symmetric (modes II and III) components

8.4.1 Discussion

The apparent loss of contour independence between modes II and III is investigated by direct inspection of the analytical fields, focusing on the displacement components. The analytical solutions were implemented in Matlab using the definition provided by Kuna (2013a), and verified against the definitions given by Williams (Williams, 1957), Xiao and Karihaloo (Xiao and Karihaloo, 2007), Huchzermeyer (Huchzermeyer, 2017), and Anderson (Anderson, 2005).

The displacement fields are displayed in Figure 8.3, with normalised amplitudes, showing the first $n = 1{:}\,4$ terms for illustrative purposes. For example, the symmetric displacement fields show that the in-plane components (u_1 and u_2) are unique from the anti-plane (u_3). Note that zero-valued crack tip fields are shown by blocks shaded with uniform grey.

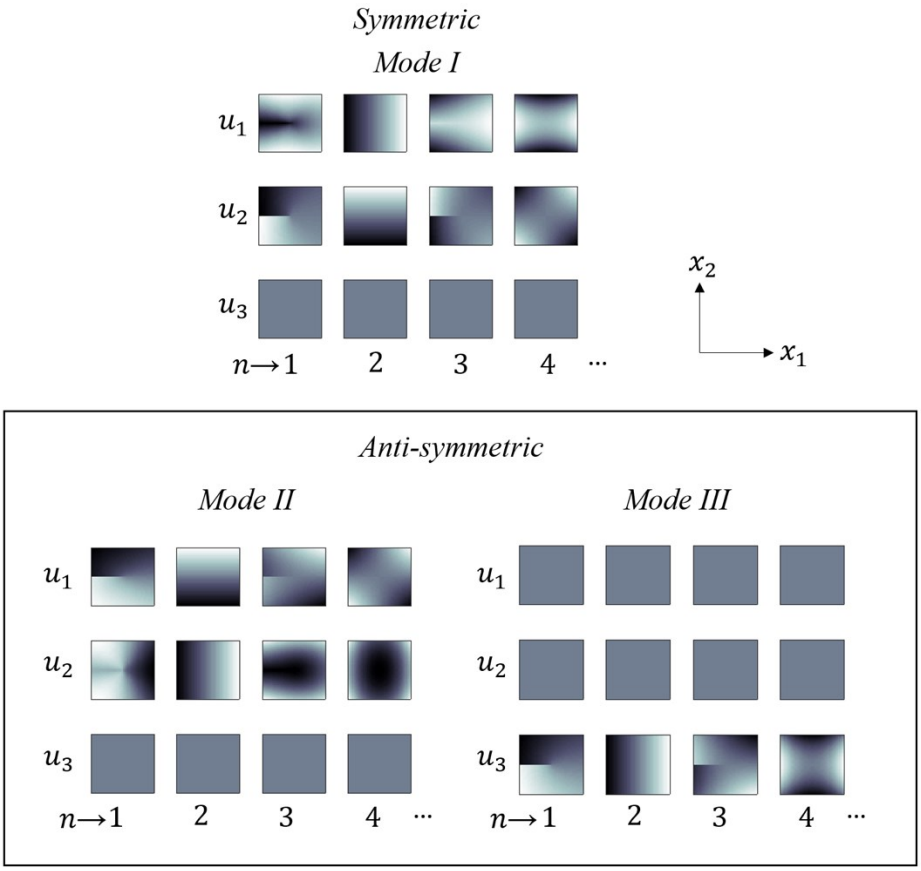

Figure 8.3: Analytical displacement fields including higher order terms

Figure 8.3 also shows that modes I and II are uniquely symmetric and antisymmetric and may be separated directly using Equation (8.2). However, the components of the mode III u_3 displacements are alternate between symmetric and anti-symmetric, expressed as (Kuna, 2013a);

$$u_3^{(n)}(r,\theta) = (1+v)\frac{c_n}{E} r^{\left(\frac{n}{2}\right)} \tilde{H}_3^{(n)}(\theta) \tag{8.8}$$

in which $\tilde{H}_3^{(n)}$ is an angular function with symmetric and anti-symmetric terms,

$$\tilde{H}_3^{(n)} = \begin{cases} \sin\left(\frac{n}{2}\theta\right) for\ n = 1,3 \\ \cos\left(\frac{n}{2}\theta\right) for\ n = 2,4 \end{cases} \tag{8.9}$$

Equation (8.9) contains symmetric and anti-symmetric components. The application of Equation (8.2) preserves the symmetric terms in mode I and the anti-symmetric terms in modes II and III, however, it is unclear how mode II and mode III are affected individually, i.e. if Equation (8.6) is applied.

In some approaches, the u_{S_3} components are neglected because they are non-singular (Hui and Ruina, 1995; Molteno and Becker, 2015c). More commonly they are placed in mode I as shown in Equation (8.6) (Huber *et al.*, 1993; Nikishkov and Atluri, 1987; Shivakumar and Raju, 1992). Although these terms are non-singular, omission of these terms will lead to loss of stress equilibrium when the symmetric part is suppressed in either modes II or modes III. Rigby and Aliabadi provide this reasoning directly through manipulation of the stress terms in the Eshelby

tensor (Rigby and Aliabadi, 1998). In their work, it is shown that the usual commutative property of partial derivatives[42] used to derive strain does not apply between modes II and III,

$$\frac{\partial}{\partial x_3}\left(\frac{\partial u_i^M}{\partial x_1}\right) \neq \frac{\partial}{\partial x_1}\left(\frac{\partial u_i^M}{\partial x_3}\right), \qquad M = II, III. \tag{8.10}$$

Applying the divergence theorem to Equation (7.1) on the closed boundary S assuming that no discontinuities exist within the domain enclosed by Q (V) (Shih *et al.*, 1986), gives (as shown on page 565 of (Anderson, 2005)):

$$J^1 = \int_V \left(\sigma_{ij}\frac{\partial u_i}{\partial x_1} - W\delta_{1i}\right)\frac{\partial Q}{\partial x_j}dA + \int \frac{\partial}{\partial x_j}\left(\sigma_{ij}\frac{\partial u_i}{\partial x_1} - W\delta_{1i}\right)Q\,dV, \tag{8.11}$$

Following the procedure of Rice (1968), the requirement for contour independence is met if the following equalities hold.

$$\frac{\partial W}{\partial x_1} = \frac{\partial W}{\partial \varepsilon_{ij}}\frac{\partial \varepsilon_{ij}}{\partial x_1} = \sigma_j \frac{\partial \varepsilon_{ij}}{\partial x_1} = \sigma_{ij}\frac{1}{2}\left(u_{i,j,1} + u_{j,i,1}\right), \tag{8.12}$$

If the stress fields are in equilibrium, the far right-hand-side of (8.12) simplifies to:

$$\sigma_{ij}\frac{\partial}{\partial x_j}\left(\frac{\partial u_i}{\partial x}\right) = \frac{\partial}{\partial x_j}\left(\sigma_{ij}\frac{\partial u_i}{\partial x}\right) \quad \left(\text{if}\ \frac{\partial \sigma_{ij}}{\partial x_j} = 0\right), \tag{8.13}$$

However, direct application of the decomposition method does not allow for stress equilibrium in the far field of the crack for the case of M = II or III, as shown in (Rigby and Aliabadi, 1998). This identity is usually required to eliminate the second term in Equation (8.11) which contains derivatives of stress and strain energy (i.e. then becoming the classical volume integral form). This evidence is supported by the numerical study and results in Figure 8.1 and Figure 8.2. Further work is needed to determine the full form of the mixed mode volume integral.

8.4.2 Proposed extensions

The works of (Huber *et al.*, 1993; Rigby and Aliabadi, 1993) show that J can be decomposed into contour independent symmetric and anti-symmetric parts. It was proposed by Rigby and Aliabadi to determine a ratio between J_{II} and J_{III} (Rigby and Aliabadi, 1993) (see Equation 54 of this reference), This ratio is defined here as,

$$R_{AS} = \frac{J_{II}}{J_{III}}, \qquad R_{AS} \in [0,1] \tag{8.14}$$

Therefore, from Equation (8.1),

$$J_{AS} = J_{II} + J_{III} = J_{II} + J_{II}/R_{AS} = J_{III}R_{AS} + J_{III}, \qquad R_{AS} \in [0,1] \tag{8.15}$$

[42] See Clairaut's or Schwarz's theorem.

Hence J_{II} and J_{III} can be calculated using,

$$J_I = J_S, \qquad J_{II} = \frac{J_{AS}}{1 + 1/R_{AS}}, \quad J_{III} = \frac{J_{AS}}{1 + R_{AS}} \tag{8.16}$$

Once determined, R_{AS} allows the use of Equation (8.1) and (8.2) to determine the mode I-III SIFs using the decomposition into only the symmetric and anti-symmetric parts. Such an approach is simple, requiring only the standard J-integral procedure and Equation (8.16) to firstly calculate J_I. Two such approaches to obtain R_{AS} are proposed in the remainder of section 8.4.2.

Note that a mode II/III ratio based approach has also been proposed by Sollero and Aliabadi (Sollero and Aliabadi, 1992) and Rigby and Aliabadi (Rigby and Aliabadi, 1993). However, these methods derive the anti-symmetric ratio (R_{AS}) from crack face displacements, which are of poor quality with DVC data. The following sections present two alternatives to calculate the anti-symmetric mode ratio, R_{AS}. The first proposed method follows a similar approach but instead considers the stress field ahead of the crack front as this region in DVC is less unaffected by the fracture faces – this method is hence called the stress ratio method. The second method proposes determination of the ratio with the help of the interaction integral approach.

Stress ratio method

This method finds the ratio based on the stress fields ahead of the crack front. The stress intensity factors for mode II and III are fundamentally defined in terms of the stresses σ_{12} and σ_{23} in the limit of the crack front,

$$K_{II} = \lim_{r \to 0} \sigma_{12} \sqrt{2\pi r} \tag{8.17}$$

$$K_{III} = \lim_{r \to 0} \sigma_{23} \sqrt{2\pi r} \tag{8.18}$$

This relation is extended into the nearby surrounding K-dominant region with the asymptotic stress fields by Williams (1957),

$$\sigma_{12} = \frac{K_I}{\sqrt{2\pi r}} \cos\left(\frac{\theta}{2}\right)\left[1 + \sin\left(\frac{\theta}{2}\right)\cos\left(\frac{3\theta}{2}\right) - \sin\left(\frac{\theta}{2}\right)\sin\left(\frac{3\theta}{2}\right)\right] \tag{8.19}$$

$$\sigma_{23} = \frac{K_{III}}{\sqrt{2\pi r}} \cos\left(\frac{\theta}{2}\right) \tag{8.20}$$

Selecting the plane ahead of the crack axis ($\theta = 0$, see Figure 2.6) sets the sine terms in 7.17 to zero. Then, dividing Equations (8.19) by (8.20) gives,

$$\frac{\sigma_{12}}{\sigma_{23}} = \frac{K_{II}}{K_{III}} \tag{8.21}$$

This ratio is only exact in the absence of higher order or super-singular crack tip field terms. It is possible to remove the symmetric part of J using the decomposition method using Equation (8.2), leaving,

$$J_{AS} = J_{II} + J_{III} = \frac{(K_{II})^2}{E'} + (1+v)\frac{(K_{III})^2}{E} \tag{8.22}$$

Substituting Equation (8.22) into Equation (8.21) gives,

$$\frac{J_{II}}{J_{III}} = \frac{E}{(1+v)E'}\left(\frac{\sigma_{12}}{\sigma_{23}}\right)^2 \tag{8.23}$$

Writing in full gives (see Equation (8.16)),

$$\text{where,} \qquad R_{AS} = \frac{J_{II}}{J_{III}} = \begin{cases} (1-v)\left(\frac{\sigma_{12}}{\sigma_{23}}\right)^2 & \text{for plane stress,} \\ (1+v)\left(\frac{\sigma_{12}}{\sigma_{23}}\right)^2 & \text{for plane strain.} \end{cases}$$

The result is a plane of values ahead of the crack front which estimate the R_{AS} value. In planar crack problems R_{AS} is constant, however in 3D problems, R_{AS} deviates from its true value the further the measurements are from the K-dominant zone. In the present analysis, stable R_{AS} values require averaging the results in the $\theta = 0$ plane in a K-dominant region to obtain a robust estimate.

Antisymmetric interaction integral method

This method is similar to direct application of the interaction integral on the anti-symmetric field decomposed using Equation (8.7). However, the difference in the presented method is that the separation is based on a ratio between mode II and mode III auxiliary fields, and therefore is shown to be robust to crack front position.

The interaction integral, developed by Stern et al. (Stern *et al.*, 1976), and Yau et al. (Yau *et al.*, 1980), determines K_I, K_{II}, K_{III} as a result of the Maxwell-Betti reciprocity theorem within the J-integral framework. In this case, only K_{II}, K_{III} are considered but the framework can be extended to extract each mode and the T-stress (Walters *et al.*, 2005). The method requires two load cases, the first is the original crack data (load case (1)), and the second is a load case in which the SIFs are known (2). Load case (2) is most readily generated by the K_{I-III} terms of the Williams expansion. The only specific requirement is that the auxiliary fields are positioned at the crack tip position identified in load case (1) to be physically permissible. The superimposed fields for load cases (1) and (2) required are the same as those needed for the J-integral,

$$\begin{aligned} u_{AS_{i,k}} &= u_{AS_{i,k}}^{(1)} + u_{S_{i,k}}^{(2)}, \quad (i = 1,2,3; k = 1) \\ \varepsilon_{AS_{ij}} &= \varepsilon_{AS_{ij}}^{(1)} + \varepsilon_{AS_{ij}}^{(2)}, \qquad (i,j = 1,2,3) \\ \sigma_{AS_{ij}} &= \sigma_{AS_{ij}}^{(1)} + \sigma_{AS_{ij}}^{(2)}, \qquad (i,j = 1,2,3) \end{aligned} \tag{8.24}$$

Substitution into the classical J-volume integral Equation (7.1). and grouping terms results in four parts,

$$J_{vol}(\mathrm{s}) = \frac{1}{A_c}\int_V \left(P_{AS_{1j}}^{(1)} + P_{AS_{1j}}^{(2)} + P_{AS_{1j}}^{(1,2)} + P_{AS_{1j}}^{(2,1)}\right)\frac{\partial Q}{\partial x_j}\mathrm{d}V \tag{8.25}$$

Here, grouping refers to terms containing one or both of load cases (1) and (2) in Equation (8.24). Of particular interest are the terms,

$$P_{AS_{1j}}^{(1,2)} = \sigma_{AS_{ij}}^{(1)} u_{AS_{i,1}}^{(2)} - \frac{1}{2}\sigma_{AS_{ij}}^{(1)}\varepsilon_{AS_{ij}}^{(2)}, \quad (j = 1,2,3) \tag{8.26}$$

$$P_{AS_{1j}}^{(2,1)} = \sigma_{AS_{ij}}^{(2)} u_{AS_{i,1}}^{(1)} - \frac{1}{2}\sigma_{AS_{ij}}^{(2)}\varepsilon_{AS_{ij}}^{(1)}, \quad (j = 1,2,3) \tag{8.27}$$

which contain coupled (1) and (2) terms. The interaction integral procedure provides direct evaluation of individual elastic J values with the relation (Walters *et al.*, 2005; Kuna, 2013b).

$$J_M = \frac{E^*}{4A_c}\left\{\int_V \left(P_{M_{1j}}^{(1,2)} + P_{M_{1j}}^{(2,1)}\right)\frac{\partial Q}{\partial x_j}\mathrm{d}V\right\}^2, (j = 1,2,3) \tag{8.28}$$

In which the relation between J_M and K_M in Equation (8.1) has been used, and E^* relates to E' in Equation 7.4 with,

$$E^* = \begin{cases} E' & \text{for } M = I, II, \\ E/(1+v) & \text{for } M = III, \end{cases} \tag{8.29}$$

Note that Equation (8.28) requires the auxiliary fields (2) to be generated from pure mode I, II or III fields. For example, calculating J_{II} requires auxiliary fields with $K_{II} = 1.0, K_I = K_{III} = 0$. Then the anti-symmetric J ratio can be determined with Equation (8.28) using $M = II, III$ and Equation (8.2) (Walters *et al.*, 2005).

Figure 8.4 shows results of the anti-symmetric modes II and III correctly portioned using the stress ratio and interaction integral based methods presented above.

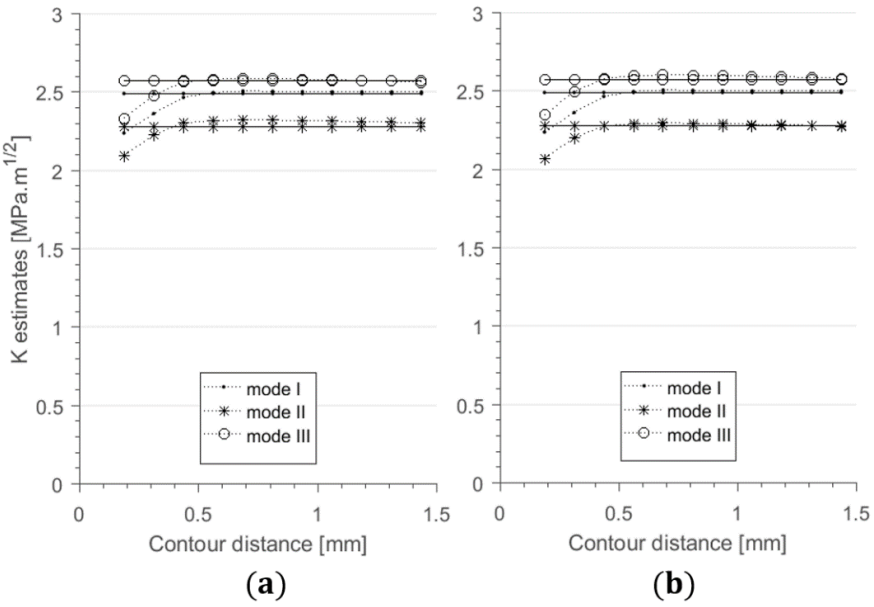

Figure 8.4: Decomposition of J_{AS} by obtaining R_{AS} using (a) the stress ratio and (b) the interaction integral method - mode I results (K_I) remaining unchanged.

8.5 Application to experimental data

Whereas Chapter 7 was concerned with application of the J-integral along the mixed-mode crack front. This chapter is concerned with contour independence within the volume. This section considers a larger lateral slice transverse to the crack front on the mid-plane (as indicated in Figure 6.18b – position (a)), inhibiting motion along the crack front. The experimental setup and DVC parameters for analysis are presented in section 6.4.2.

The crack front positions were analysed in Figure 6.19 and an expected accuracy of 5 % was estimated. As can be seen from the results below, the accuracy to within approximately this factor is apparent in the contour results. Notably, the results consistently exceed the expected K_{I-III}.

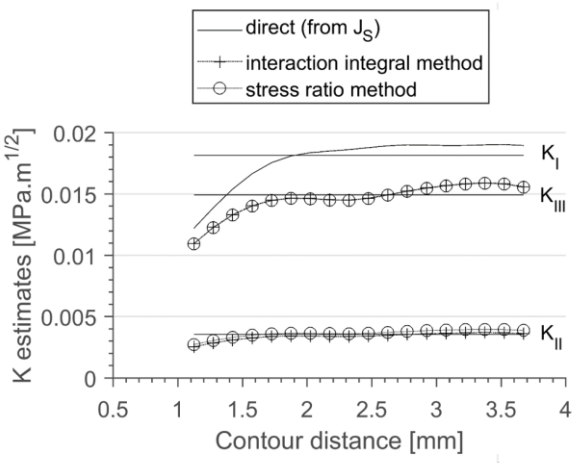

Figure 8.5: Contour plots for the interaction integral method (+) and the stress ratio method (o).

8.6 Conclusions

The decomposition method in the volume has been reviewed, historically, theoretically, numerically on finite element data, and experimentally on DVC data. The historical perspectives showed that many of the early works on the decomposition method in the volume were implemented prior to changes presented by Rigby and Aliabadi (Rigby and Aliabadi, 1998). The amendments included reallocation of a $\sigma_{AS_{33}}$ term to mode II, and a revised J-integral equation which is of the path-area integral form. These are highly relevant to this work as the path-area form has previously been determined to be particularly inaccurate on DVC data due to crack face errors.

A numerical study performed on finite element fields generated in Chapter 5 showed the expected result that the anti-symmetric combined modes are convergent, while separated modes II and III are not. These findings were confirmed by direct application of the decomposition method using the volume integral developed in Chapter 7.

Causes for the loss of contour independence were discussed by inspection of analytical crack tip fields. This showed that the antisymmetric terms are suppressed in an alternating series. The discussion also develops the approach originally used by Rice to prove path-independence to demonstrate that, if a valid form of the volume integral exists, it would involve derivatives of stress that otherwise disappear if only symmetric and anti-symmetric decomposition is used. As this fell outside the scope of this thesis, a different avenue was examined in which the J_{AS} was split into the mode II and III parts as a proposed post-processing stage. Two different methods were developed to achieve this – both methods determine a ratio of J_{II}/J_{III} to split J_{AS}. The first method employed the analytical definitions for mode II and mode III stresses to solve for the ratio in the stress field ahead of the crack front. The second method used the interaction integral approach to solve for the ratio directly.

These methods have been applied to the experimental mixed mode experiment presented in Chapter 7. The results are difficult to discern, suggesting that either approach is equivalent.

8.7 Summary

The decomposition method has been implemented on the surface in Chapter 0, and reviewed and implemented in the volume in the present work using DVC displacements. Direct application of the revised decomposition method using decomposed displacement gradients method prescribed by Rigby and Aliabadi (1998) results in contour dependence in the anti-symmetric modes II and III. A derivation was followed showing that – similar to the new path-area integral form derived by Rigby and Aliabadi (1998) – a volume integral form is needed.

Two alternative approaches were developed, which enable the separation of J_{AS} based on a ratio between modes II and III, derived on analytical formulas, and the interaction integral. This form was successfully tested on DVC data, showing approximate convergence in all three results.

The decomposition method has been tested experimentally, for example by (Diekmann *et al.*, 1991). However, this objective aims to test the method on image correlation data both on the surface (including out-of-plane motion) and the volume. Such 3D implementations have not been tested before on either DIC or DVC data, and will require special attention to the volume due to the loss of contour independence experienced by the J-integral under typical decomposition conditions (see the end of section 2.2.6).

9 Discussion

Throughout this thesis, each chapter has been written as a self-contained section; having an introduction, the main subject matter, relevant discussions and a concluding summary. This chapter maintains a similar format, yet aims to develop the discussions of the previous chapters in the context of the objectives set out in section 3.2 and *in situ* structural measurements. The intention is to link the three main aspects of this thesis; the replacement of unreliable experimental displacements, the required J-integral methodologies for surface and volume evaluations, and the decomposition of mixed-mode parameters. The limitations of the proposed methodology are illustrated by laboratory and Synchrotron X-ray imaging results, acquired for this chapter.

It is also a goal of this chapter to discuss the capabilities of these techniques in the broader context of *in situ* structural evaluation and monitoring, which are proposed in terms of future work and recommendations for Eskom in the final sections.

9.1 Introduction

The work in this thesis was motivated by the considerable attention that DIC and DVC methods have gained in recent years for monitoring material behaviour, and the growing potential of these methods for *in situ* structural integrity assessments. For this purpose, the LEFM framework and mixed-mode stress intensity factors were motivated in section 1.3, as the most imminently realisable by full-field methods, and the most widely-used in industry.

The early work achieving this involved direct parameter fitting to displacement fields acquired using DIC. These measurements use the linear relation between stress intensity factors and analytical crack tip fields (McNeill *et al.*, 1987). This approach has been used for the matching of experimental displacements and crack tip positions, both in LEFM (Réthoré *et al.*, 2005) and EPFM (Yoneyama *et al.*, 2014).

A subsequent approach was introduced named JMAN, developed prior to this thesis by Becker *et al.* (2012). It enabled direct measurement of the J-integral on DIC data through the finite element framework. The approach enabled measurements of crack growth without the requirement for crack length. This methodology was combined with the double torsion experiment which allows for stable crack growth in brittle materials (Becker *et al.*, 2011). The experiment is also well suited to optical surface measurements due to the high aspect ratios of double torsion specimens (a large frontal area available for surface imaging).

This thesis has focused on the experimental implementation and limitations of the J-integral and decomposition into mode I, II and III parts. The findings are highly applicable to methodologies such as JMAN as the decomposition method provides the only means known to the author to theoretically preserve crack length insensitivity in the decomposed SIFs (discussed in Chapters 0 and 8). The JMAN approach has already been used to identify discrepancies between the analytical crack length, K_I, and J estimated using JMAN. This framework therefore has excellent applicability to the double torsion testing methodology, as the contributions from the separate modes of fracture may also be obtained in a crack front independent manner.

9.2 Minimisation of displacement errors

A frequent motivation for the J-integral technique is that the displacement accuracy, geometry and material properties can be accurately estimated in the regions remote from the fracture. Such laboratory experiments frequently assume that the elastic limits of the remote field are not

exceeded to enable successful application of the *J*-integral and study the developing damage mechanisms (Huchzermeyer, 2017). However, outliers are known to concentrate at material boundaries, and particularly close to the crack front.

Despite the development of advanced techniques to obtain improved displacements close to discontinuities (Poissant and Barthelat, 2010; Wang and Ma, 2014; Hild and Roux, 2006b; Helm, 2008; Fujikawa, 2005), and methods to subsequently smooth displacements such as the method of (Yoneyama, 2011), are seldom sufficient to address the problems involved in modern imaging techniques, in which the artifacts are still a problem. The example provided here is an experiment conducted using the Diamond Light Source (DLS) synchrotron facility (Harwell, UK) available through the collaboration with Oxford during this doctoral work. The results are intended to demonstrate the imaging capabilities possible in the volume of the chosen sample geometry.

Figure 9.1a shows the double torsion loading rig used for the experiment. As can be seen in the reconstruction of the central slice in Figure 9.1b, the features could not be fully resolved due to strong nonlinear (NL) crescent ring and vertical stripe artifacts. Note that slices further from the central slice contain significantly higher levels of random image noise, yet the nonlinear artifacts maintain a high clarity in these regions. The result is that the stripe and ring artifacts dominate the correlation throughout most of the image volume. As is the case with many standard geometries, the crack path traverses the centre of the specimen. As this is also the centre or rotation of the sample, it is common practice to offset the specimen so that the centre of rotation and the crack path are not co-linear. However, this offset is limited if the flanking regions surrounding the fracture are needed for calculation of the *J*-integral.

Such artifacts are usually removed as a matter of course using stripe and ring artifact removal routines. The in-house artifact removal method implemented at DLS – a combined wavelet-Fourier filtering tool (Trtik *et al.*, 2009) – is shown in Figure 9.1c. Note that Figure 9.1 (b) and (c) are of the same image volume, and the same central slice.

As shown in Figure 9.1c, the in-house routine does not fully remove such artifacts, leaving low frequency ‘ripples’ throughout the images. DVC computations using the treated images (Figure 9.1c) were also corrupted by such artifacts, with errors concentrating at the specimen borders and centre of rotation. Although edge preservation on displacement fields is possible by traditional outlier removal methods (e.g. median filtering), such methods are unsuccessful when outliers are subtle and distributed as in (Figure 9.1c). In this case, the sparsity of the natural texture relative to the artifact density also poses a challenge.

An approach is presented in this thesis which addresses displacement artifacts using an energy based criterion to separate random errors from outliers. Such non-normally distributed errors, particularly in high stress regions, have been identified as a significant cause for error in *J* estimations in the volume in Chapter 7. The presented approach enables the suppression (or complete removal in linear elastic cases) of non-random errors from the integration region before *J* is calculated. Such an approach is beneficial if the subsequent method employs numerical integration, as this enables cancellation of positive and negative errors.

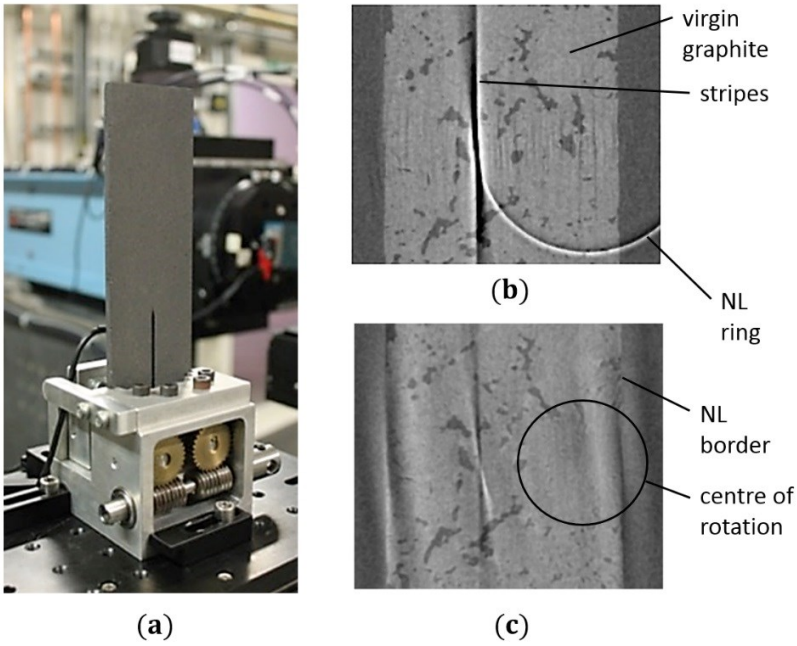

Figure 9.1: Crack propagation in double-torsion loaded polygranular graphite; (a) loading rig and sample; (b) extracted image containing ring artifacts; (c) removal of artifact, and non-linearities on the ring and border (NL)

Note that a prior knowledge of the random displacement error is needed, which may be a limitation if beam time is limited (e.g. for rigid body tests). In such cases, the theories developed by Besnard *et al.* for DIC (2006) and Leclerc *et al.* for DVC (2011) to predict displacement errors from subset parameters may be useful.

As the intended use is with the *J*-integral approach, application of the technique to material non-linearities may be of great relevance to future use of the method. Such non-linearities may be quantified in terms of their effects on the underlying displacement data in terms of the following experimental conditions:

Linear elastic deformations

In this material state, the finite element framework employed by the artifact removal tool is linear elastic, which will yield the most accurate results. However, it is worth considering the case of excessive iterations without termination, from which two effects will emerge. Firstly, incorrect assumption of the material distribution (e.g. due to incorrect masking of the image in DIC) would favour outlier removal in regions related to the true sample position in the reference configuration. Secondly, an effect will be introduced by displacement errors on the boundary as these nodes are not modified in any way by the methodology of Chapter 4. Hence the methodology relies on the statistical dominance of data within the boundary and on the selection of boundaries in regions in which outliers are minimal.

Distributed damage

Distributed damage is here assumed to be low gradient (e.g. plastic and thermal effects on Young's modulus). This would result in a correspondingly low gradient offset in the $|f|$ values. These results in turn would lead to a bias toward the removal of artifacts in damaged regions.

These effects have been minimised throughout the thesis to enable the use of the LEFM framework for verification. Nonetheless, distributed damage frequently emerges in Eskom power plant conditions and is a primary cause for crack initiation, for example due to creep, or variation in microstructure due to thermal cycles. These effects have been observed in austenitic stainless steel

(type 304L) Arcan samples (mode I). Although not formally reported in this thesis, it is worth mentioning that artifact removal was initially successful, localising around speckle-pattern damage (due to flaking under large strains). Subsequent iterations concentrated on the removal of nodes at the boundary between elasticity and plasticity, indicating that attention to this region would provide a significant improvement in applications to non-linear deformations. The robustness of the method to distributed damage in the early iterations is attributed to the sparseness of the removed data relative to unaltered neighbours.

Localised damage

In the context of this thesis, such damage is concentrated at the crack tip and front. Depending on the extent of the damage, this is likely to be strongly affected by smoothing in the initial and final iterations. However, the extent of such effects is challenging to quantify using the DIC and DVC approaches which are inaccurate in such regions.

Discussion

The problem of selecting suitable boundary nodes is limited by the requirement for rectangular elements on a regular grid. This was part of the motivation for the isoparametric element based approach implemented on DIC data by Yoneyama (2011), in which element shapes are flexible. For the problem of displacement errors in the boundary nodes, Yoneyama and Arikawa have proposed a least-squares solution imposed through the finite element mesh (Yoneyama and Arikawa, 2012). However, such extensions are traded for increased numerical cost, method complexity. Such extensions are beyond the scope of this thesis, which specifies that image correlation is used directly in regular grid format (section 3.4.5). However, such advantages may also be gained by concentrating on the crack tip region, as done on DIC and DVC data in section 4.4.1 and 4.4.2. In the former, 2D assumptions can be made in which case the crack tip region can be omitted. As can be seen in Figure 6.11, only the J estimates near the notch tip were affected. A similar effect is seen in DVC analysis mixed-mode DVC results in Figure 7.18. However, these effects are likely to be more severe in the volume integral due to persistent use of crack front data, and so slower convergence is likely. Study of the loss of convergence due to smoothing was not conducted, but is needed before the outlier removal method can be prescribed for general use on crack problems.

9.3 Evaluation of the J-integral

The classical forms for the line, area, path-area and volume integrals have been implemented in Chapters 0 and 7. In both the surface (line and area) and volume (path-area and volume) implementations, it is well established in literature that the conversion to the respective equivalent domain integral forms are, in general, preferable in the presence of displacement errors (Kuna, 2013b). This result is also tested in sections 5.5 and 6.3 using the original 2D line integrals and 3D path-area integrals (Rice, 1968; Blackburn, 1972). Hence further discussion focuses on the domain integral forms of the J-integral.

The path-area and volume integrals were derived by (Blackburn, 1972), and Shih (Shih *et al.*, 1986) using different approaches. The present use of these approaches seems to be on lines of convenience of the path-area integrals simplicity, versus the characteristic robustness provided by the volume integral.

In Chapter 5, the link between the classical path-area and volume integrals is provided, via a new surface-volume integral. It was shown that the surface-volume integral requires a further step, expanding the surface component into a volume form, to further improve robustness. The result is

shown to be identical to the result which would be obtained by setting the gradient of the virtual crack extension function in the region near the crack front to zero (see Equation (5.12), relating to Figure 5.1). Although a similar integral manipulation was performed by (Moës *et al.*, 2002), and the reduction of the gradients of the virtual crack extension field to minimise errors is not new (Réthoré, Roux, *et al.*, 2008), a method relating the path-area and volume integrals to each other (and the intermediate forms: the weighted path-area, and surface-volume integrals) could not be found in the present literature. Furthermore, there are two interesting implications which arise from this derivation:

Firstly, it can be shown that the area integral employed in Chapter 0 can be identically computed by a central cross-section of the hybrid volume integral approach. If the surface of the material is flat and perpendicular to the crack front, then the gradient of the virtual crack extension is also zero on the surface. However, it is uncertain from the current results to what extent 3D fields are measured by the J-integral on the surface during 3D deformation. There is some indication that there is negligible contribution from mode I loading (Giner *et al.*, 2010), but great contributions may develop in mixed mode conditions, especially close to the crack front (Nakamura and Parks, 1989). However, it seems implausible that this reasoning would not also apply to the far field if sufficient out-of-plane motion occurred.

Note that on straight crack fronts in which Q is aligned with x_1 in the local co-ordinate system, $Q_{1,j} = 0$ has the effect of setting the usual J integrand (the Eshelby tensor) to zero, or more accurately, suppressing the Eshelby tensor P_{kj} from calculation of J^k minimising terms in $P_{kj}Q_{k,j}$ at material locations that exhibit experimental (Roux *et al.*, 2009) or numerical (Moës *et al.*, 2002) errors. These references demonstrate the versatility of this approach, in particular, Roux et al. find an arbitrary function shape that does not resemble crack tip fields at all through their minimisation routine (Roux *et al.*, 2009).

It would be beneficial to determine the suitable $Q_{k,j}$ to minimise or eliminate P_{kj} terms close to the crack front, such as is naturally achieved on the surface. On this note, it is apparent that this is not always the case. It has been found in Chapter 5 that non-zero mode III SIFs can be measured on the surface. However, these results exhibited the poorest contour independence, perhaps due to loss of conformity to the definition of the global Q function. As shown in Figure 8.2, the initially 2D function may be misaligned with the surface, in which case the out-of-plane stresses are no longer zero. Evidently some shear stresses will be present.

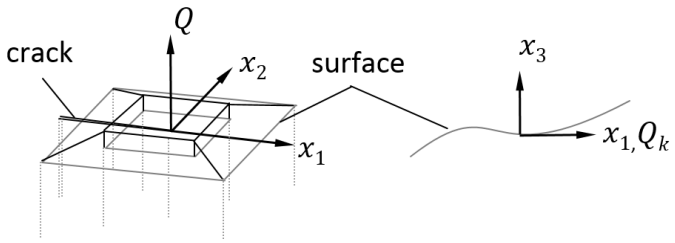

Figure 9.2: Q function amplitude on the material surface (left), with possible out of plane deformations shown (right)

9.4 Decomposition from displacement fields

The motivation for the development of the decomposition method was to achieve separation of mode I-III SIFs with a reduced reliance on analytical crack tip fields in order to improve the robustness of results. In Chapter 0, it was shown that decomposition could take place on displacements directly, enabling further calculation using the classical area integral. Due to

numerous changes to the volumetric equivalent in recent decades, a review of the methods has been conducted in section 8.2, and the technique within the volume has also been tested on DVC data.

Comparison between analytical and experimental fields revealed that mode I J measurements (J_I) are robust to masking on the surface. It was also confirmed that mode I components are directly accessible through the symmetric portion of the displacement field; both on the surface and within the volume. Therefore, mode I can be obtained without the need for analytical crack tip fields, which is usually a requirement for the interaction integral or field fitting approaches. Nor is prior knowledge of crack length or crack front position explicitly needed other than for placement of the symmetry plane. It has also been shown that the decomposition operation has an inherent noise reduction effect on data when compared to non-decomposed results with the same J-integral (Figure 6.5). Therefore, mode I data in the form of J_I, and K_I values is always available from the direct decomposition of displacement fields, from stereo-DIC and DVC data. Similar consistency is not shown by mode II-III results, which are more susceptible to errors and are not contour-independent in the volume.

A primary concern in the treatment of DIC and DVC data is with regard to the crack face displacements. The relative sensitivities of modes I-III have been tested in Chapter 0 in which it was shown that the relative sensitivity of K estimates to masking was related to the strain energy field of the masked region (section 6.4) – a consistently low value for mode I in which the crack faces and flanking regions contain minimal strain energy relative to modes II and III. This highlights the importance of masking accuracy to ensure the quality of crack face data in mixed mode problems. A suitable methodology to achieve accurate replacement of crack face data was developed in Chapter 4, in which unreliable results are replaced with linear elastic solutions. The use of strain energy as an indicator of J and K accuracy is only qualitative, since J estimates are susceptible to various parameters (e.g. selection of large contours on the surface, or modification of the Q function in the volume).

It is important to consider that J_{III} is theoretically zero under assumptions of plane-stress and stress equilibrium on the surface (Equation 3.4). However, the methodology presented enables non-zero K_{III} values through the anti-plane shear definition for J_{III}, as shown in Figure 6.11 and Figure 6.12. As J_{III} is resolved by discrete numerical operations, the presence of non-zero results may represent the mode III loading on the segment of the crack front adjacent to the free surface. This may result in non-zero values due to an artificial thickness caused by numerical discretization.

It is worth mentioning that contour independence in mode III generally improved in thicker specimens (testing 3 mm - 12 mm thicknesses). The reason may be due to geometric non-linearities being possible at lower loads. The contour distance to thickness ratio (r_c/t – see Figure 6.3) for the surface method is therefore assumed to be of limited range to adhere to the anti-plane assumptions, Equation (6.9) - (6.11), which can be tested using convergence plots (Figure 6.11). These find values of r_c to be in the range [0.3, 3] using 6 mm thick specimens. Nakamura and Parks suggest that the region within 3 % of the specimen thickness is dominated by 3D effects, a result also shown with the VCC method (Diekmann *et al.*, 1991). It has however, also been discussed that the alignment with the surface may be an important factor in the convergence of J-values (section 8.2.4).

9.5 Future work

The decomposition method has been developed to enable extraction of SIFs without analytical displacement fields. This result is however susceptible to neighbouring stress raisers such as specimen edges and multi-crack systems. Such field quantities can be represented by higher order field terms. A notable extension to the current approach would enable a hybrid approach in which the non-singular displacement field terms (which dominate remotely from the crack tip), can be used to eliminate non-crack tip field terms prior to the decomposition operation.

As previously discussed, the integrand of the J-integral is primarily influenced by the gradient of the virtual crack extension function. Although many methods have been developed based on nuances of the Q field - e.g. accounting for crack curvature, (Moës et al., 2002) - it is as yet unknown if crack tip fields can be eliminated entirely through the enabling of the suitable minimisation of the product between the Eshelby tensor in the crack growth direction (P_{1j}), and the ($\partial Q/\partial x_j$), in Equation (7.1).

9.6 Recommendations for Eskom

This section summarises the relevant findings of this work for practical applications toward the national development of structural integrity management systems. In particular, the aim is to (1) contribute to the research methods at Eskom and (2) propose new in-line monitoring methodologies for use in the present Eskom framework. In these two areas, the discussion focuses on reducing the number of samples and tests required to determine fracture properties (addressing 1), and improving the robustness of measurements (addressing 2).

In terms of integrating the work developed in this dissertation with Eskom research approaches (1), it is worth mentioning that several previous studies have developed modifications to standard sample geometries, optimising them for full-field analysis with DIC. Examples include the accelerated creep tests developed by van Rooyen (2016), and the modified ASTM E399 half C(T) fracture tests proposed by Huchzermeyer (2017). The main conclusion from these works is that full-field measurements – alongside methodologies such as the virtual fields method, computational plasticity, and LEFM – facilitate the extraction of multiple material, fracture, and damage properties from individual tests, thereby reducing the numbers of samples needed. Although fracture and creep mechanisms are common, it is essential for future use of these methods, that additional emerging damage mechanisms can be correctly identified for further study (e.g. stress corrosion cracking, hydrogen embrittlement).

The methods developed in Chapters 0-8 may be employed to determine total energy dissipation rates from such structures. In purely linear elastic, or creep based models, the linear and non-linear J-framework can be used to provide adequate measurements of J directly. The global energy based approach allows for simplified models to be applied to large contours which enclose new damage of unknown origin and can therefore assist in the discovery of newly developing damage mechanisms. Similar approaches in the volume require consideration of the entire enclosed region of the crack front, and therefore may be sensitive to experimental tests in which the damage mechanisms are unknown. However, it is worth noting that true contour independence is resulted to the hybrid integral under plane strain conditions, i.e. $P_{13} = 0$, Equation (7.1).

The second application to Eskom is for the in-line monitoring of surface fractures (see (2) above). As described in section 1.1, NDT is used for the detection of flaws, and direct surface measurements are used to monitor strain history (e.g. capacitive strain gauges). This task can be performed with greater versatility by DIC if the accuracy can be ensured over long periods (depending on the crack growth rate of the material). This may be challenging due to unforeseen

effects, such as lighting variations, deterioration of surface features, or the robustness of imaging setup. Again, the material non-linearities arising from non-linearities may be accounted for in the J-integral framework under hyper-elasticity assumptions, or modification to the C^*-integral for fractures amid creep deformations (Landes and Begley, 1976). However, non-damage related errors can be removed by the methodology of Chapter 4, which provides the error estimate *a priori*. Such error estimates are also provided for J measurements on the surface using the perturbation approach (section 6.3.3). Therefore, the presented methodology can make excellent use of a future study to investigate the typical image correlation errors in Eskom materials and structures. In particular, DIC measurements are dependent on plant activities and the pattern persistence on surfaces subjected to the plant environment. A similar study for DVC, however, should focus on characterising the natural contrast patterns within various damaged and undamaged power-plant materials.

On a final note, as with fracture features, conventional X-ray imaging systems are unable to provide data near the surface of materials. The presented framework provides fracture parameters for the crack front in the volume and the crack tip on the surface. Therefore, the development to enable both DIC and DVC measurements would be advantageous as a new laboratory measurement system using the enclosed methods. Such tools can be used to extrapolate from the (monitored) damage on the surface, to identify the possible development of subsurface damage.

10 Conclusions

The work was divided between four objectives which included the development of a methodology to minimise experimental errors. The J-integral was extended to the volume leading to the development of a hybrid J-integral, a form that is robust to typical experimental errors from image correlation. The hybrid form was verified on DVC data using analytical crack tip fields to quantify errors. Then the decomposition method was developed and tested both on the surface and within the volume. In the latter case an existing approach to decompose the volume integral did not exist, and so two extensions to the existing method were proposed. Key conclusions and some further recommendations are summarised below:

- Chapter 4 developed a method which enables the robust detection and removal of outliers from DIC and DVC results. The effectiveness of the method in separating random noise from outliers was tested in an idealised cantilever example. A benefit of the method is that classical random noise related to DIC or DVC accuracy is quantifiable to a relative artefact energy parameter, which underpins the convergence criteria of the enclosed technique. Experimentally, the method was found to be particularly effective in elimination of crack face artifacts, as shown in studies on DIC and DVC data.
- The theoretical development has shown a new link between the path-area and volume integrals, and reveals two new integral forms. It was shown that the surface-volume and classical volume integral equations can be combined, providing a link between the surface-volume integral, the hybrid form, and the classical volume integral. The requirement is that the virtual crack extension field is constant over a region surrounding the crack front. Tests on numerical data confirmed a significant improvement in noise resilience over the path-area integral form, and an improvement in positioning of the integral volume.
- A procedure for the computation of mode I, II and III SIFs using the decomposition method and the J-integral is presented. The method is versatile as both the line and domain integral forms may be applied, as demonstrated. The method was verified on Williams' series crack tip fields. The decomposition method was verified experimentally in pure mode I, II and III configurations, and in mixed-loading. Results were compared to fracture toughness values measured from CT specimens, and were also compared to analytical solutions obtained from literature with good agreement.
- The hybrid form was verified on DVC data, and the sources of error were identified. The analytical fields perturbation approach introduced in Chapter 5 was applied in 3D in this chapter. The error analysis revealed that the volume method was mainly due to errors in the crack tip region, as evidenced by omitting these errors and retesting. Errors compounded in the volume to approximately 10 % under mixed mode loading.
- The decomposition method in the volume was reviewed and tested on numerical data, showing loss of contour independence in the anti-symmetric modes as discussed in literature. Using a proof, and considering analytical crack tip fields, it was postulated that an equivalent volume integral would require derivatives of stress in the integrand. Such a form would not be suitable for experimental data and so two alternatives to the classical decomposition method in the volume were proposed. The proposed methods determine a ratio of J_{II}/J_{III} to split J_{AS} into mode II and mode III parts. The first method uses a ratio determined analytically from crack tip stress fields, and the second method used an antisymmetric form of the interaction integral method to solve for the ratio directly.

References

Abanto-Bueno, J., Lambros, J. (2002) Investigation of crack growth in functionally graded materials using digital image correlation. *Engineering Fracture Mechanics*. **69**(14–16), 1695–1711.

Aliabadi, M.H. (1997) Boundary Element Formulations in Fracture Mechanics. *Applied Mechanics Reviews*. **50**(2), 83.

Amestoy, M., Bui, H.D., Labbens, R. (1981) On the definition of local path independant integrals in three-dimensionnal crack problem. *Mechanics Research Communications*. **8**(4), 231–236.

Amiot, F., Bornert, M., Doumalin, P., Dupré, J.C., Fazzini, M., Orteu, J.J., Poilâne, C., Robert, L., Rotinat, R., Toussaint, E., Wattrisse, B., Wienin, J.S. (2013) Assessment of digital image correlation measurement accuracy in the ultimate error regime: Main results of a collaborative benchmark. *Strain*. **49**(6), 483–496.

Anderson, T. (2005) *Fracture Mechanics: Fundamentals and Applications*. 3rd ed. B. Raton, ed. CRC Press LLC.

ASTM International (2015) *E1820: Standard Test Method for Measurement of Fracture Toughness*.

Banks-Sills, L., Arcan, M. (1986) A compact Mode II fracture specimen. *ASTM special technical publication*. (905), 347–363.

Bar-Kochba, E., Toyjanova, J., Andrews, E., Kim, K.S., Franck, C. (2015) A fast iterative digital volume correlation algorithm for large deformations. *Experimental Mechanics*. **55**(1), 261–274.

Barhli, S.M., Mostafavi, M., Cinar, A.F., Hollis, D., Marrow, T.J. (2017) J-Integral calculation by finite element processing of measured full-field surface displacements. *Experimental Mechanics*, 1–13.

Barhli, S.M., Saucedo-Mora, L., Simpson, C., Mostafavi, M., Withers, P.J., Marrow, T.J. (2016) Obtaining the J-integral by diffraction-based crack-field strain mapping. *Procedia Structural Integrity*. **2**, 2519–2526.

Barranger, Y., Doumalin, P., Dupré, J.C., Germaneau, A., Hédan, S., Valle, V. (2010) X-ray computed tomography coupled to Digital Volume Correlation applied to a stationary crack case. *EPJ Web of Conferences*. **6**(June), 42015.

Bay, B.K. (2008) Methods and applications of digital volume correlation. *The Journal of Strain Analysis for Engineering Design*. **43**(8), 745–760.

Bay, B.K., Smith, T.S., Fyhrie, D.P., Saad, M. (1999) Digital volume correlation: Three-dimensional strain mapping using X-ray tomography. *Experimental Mechanics*. **39**(3), 217–226.

Bazilian, M., Nussbaumer, P., Rogner, H.H., Brew-Hammond, A., Foster, V., Pachauri, S., Williams, E., Howells, M., Niyongabo, P., Musaba, L., Gallachóir, B.Ó., Radka, M., Kammen, D.M. (2012) Energy access scenarios to 2030 for the power sector in sub-Saharan Africa. *Utilities Policy*. **20**(1), 1–16.

Becker, T.H. (2011) *Understanding and Modelling Damage and Fracture in Nuclear Grade Graphite*. University of Cape Town.

Becker, T.H., Marrow, T.J., Tait, R.B. (2011) Damage, crack growth and fracture characteristics of nuclear grade graphite using the Double Torsion technique. *Journal of Nuclear Materials*. **414**, 32–43.

Becker, T.H., Mostafavi, M., Tait, R.B., Marrow, T.J. (2012) An approach to calculate the J -integral by digital image correlation displacement field measurement. *Fatigue & Fracture of Engineering Materials & Structures*. **35**(10), 971–984.

Becker, T.H., Naicker, L., Barhli, S.M., Marrow, T.J. (2016) Stress corrosion cracking investigation of FV520B stainless using digital image correlation and the J-integral. In *Conference Proceedings of the 11th British Soceity of Strain Measurement*.

Becker, T.H., Tait, R.B. (2013) Fracture and slow crack characteristics of nuclear grade graphite using the double torsion beam technique. *ICF12, Ottawa 2009*, 1–10.

Begley, J.A., Landes, J.D. (1972) The J-integral as a fracture criterion. *ASTM STP 514*, 1–20.

Besnard, G., Hild, F., Roux, S. (2006) 'Finite-Element' displacement fields analysis from digital images: application to Portevin-le Chatelier bands. *Experimental Mechanics*. **46**(6), 789–803.

Bezuidenhout, M.E. (2010) Integrity and Lifing of Defect Free Components in Eskom Power Plant. In *HIDA-5*.

Bing, P., Xie, H.M. (2007) Digital image correlation method with differential evolution. *Electronic Publishing*. **18**(1), 100.

Blackburn, W.S. (1972) Path independent integrals to predict onset of crack instability in an elastic plastic material. *International Journal of Fracture Mechanics*. **8**(3), 343–346.

Bornert, M., Brémand, F., Doumalin, P., Dupré, J.C., Fazzini, M., Grédiac, M., Hild, F., Mistou, S., Molimard, J., Orteu, J.J., Robert, L., Surrel, Y., Vacher, P., Wattrisse, B. (2009) Assessment of digital image correlation measurement errors: methodology and results. *Experimental Mechanics*. **49**(3), 353–370.

Bossuyt, S. (2013) Optimized patterns for digital image correlation. In *Conference Proceedings of the Society for Experimental Mechanics Series*. Springer, New York, NY, pp. 239–248.

BSI (2015) *BS 7910: Guide to methods for assessing the acceptability of flaws in metallic structures*. London.

Budiansky, B., Rice, J.R. (1973) Conservation Laws and Energy-Release Rates. *Journal of Applied Mechanics*. **40**, 201.

De Castro, E., Morandi, C. (1987) Registration of translated and rotated images using finite fourier transforms. *IEEE transactions on pattern analysis and machine intelligence*. **9**(5), 700–703.

Červenka, J., Saouma, V.E. (1997) Numerical evaluation of 3-D SIF for arbitrary finite element meshes. *Engineering Fracture Mechanics*. **57**(5), 541–563.

Chaboche, J. (2006) Damage Mechanics. In *Comprehensive Structural Integrity*. Elsevier, pp. 214–281.

Chao, Y.J., Luo, P.F., Kalthoff, J.F. (1998) An experimental study of the deformation fields around a propagating crack tip. *Experimental Mechanics*. **38**(2), 79–85.

Chen, D.J., Tan, Y.S., Don, H.S., Chiang, F.P., Chen D. J. Tan Y. S. ,Don H. S., C.F.P. (1993) Digital speckle-displacement measurement using a complex spectrum method. *Applied Optics*. **32**(11), 1839.

Chen, K.L., Atluri, S.N. (1989) Comparison of different methods of evaluation of weight functions for 2-D mixed-mode fracture analysis. . **34**(4), 935–956.

Cherepnov, H.G.P. (1967) Crack propagation in Continuous Media. *Journal of Applied Mathematics and Mechanics*. **31**(3), 10.

Chu, T.C., Ranson, W.F., Sutton, M.A. (1985) Applications of digital-image-correlation techniques to experimental mechanics. *Experimental Mechanics*. **25**(3), 232–244.

Cinar, A.F., Barhli, S.M., Hollis, D., Flansbjer, M., Tomlinson, R.A., Marrow, T.J., Mostafavi, M. (2017) An autonomous surface discontinuity detection and quantification method by digital image correlation and phase congruency. *Optics and Lasers in Engineering*. **96**(May), 94–106.

Cofaru, C., Philips, W., Van Paepegem, W. (2010) Improved Newton-Raphson digital image correlation method for full-field displacement and strain calculation. *Applied optics*. **49**(33), 6472–6484.

Dassault Systèmes Simulia, Fallis, A.., Techniques, D. (2013) ABAQUS documentation. *Abaqus 6.12*. **53**(9), 1689–1699.

Davenport, J.C.W., Smith, D.J. (1993) A Study of Superimposed Fracture Modes I, II AND III on PMMA. *Fatigue & Fracture of Engineering Materials and Structures*. **16**(10), 1125–1133.

deLorenzi, H.G. (1982) On the energy release rate and the J-integral for 3-D crack configurations. *International Journal of Fracture*. **19**(3), 183–193.

Diekmann, P., Buchholz, F.G., Grebner, H., Richard, H.A. (1991) J-Integral Calculations in Mixed-Mode Elastic-Plastic Crack Problems. In *ESIS -EGF9*. London, pp. 35–44.

Dodds, R.H., Read, D.T. (1990) Experimental and numerical studies of the J-integral for a surface flaw. *International Journal of Fracture*. **43**(1), 47–67.

Eischen, J.W. (1987) Fracture of nonhomogeneous materials. *International Journal of Fracture*. **34**(1), 3–22.

Eriksson, K. (2002) A domain independent integral expression for the crack extension force of a curved crack in three dimensions. *Journal of the Mechanics and Physics of Solids*. **50**(2), 381–403.

Eriksson, K. (2007) Decomposition of Eshelby's energy momentum tensor and application to path and domain independent integrals for the crack extension force of a plane circular crack in Mode III loading. *International Journal of Fracture*. **144**(4), 215–225.

Eshelby, J.D. (1975) The elastic energy-momentum tensor. *Journal of Elasticity*. **5**(3), 321–335.

Eshelby, J.D., Douglas, J., Markenscoff, X., Gupta, A. (2006) *Collected Works of J. D. Eshelby: The Mechanics of Defects and Inhomogeneities*. Springer.

Feldkamp, L.A., Davis, L.C., Kress, J.W. (1984) Practical cone-beam algorithm. *Journal of the Optical Society of America A*. **1**(6), 612.

Feng, D., Feng, M.Q., Ozer, E., Fukuda, Y. (2015) A vision-based sensor for noncontact structural displacement measurement. *Sensors (Switzerland)*. **15**(7), 16557–16575.

Fernlund, G., McCammond, D., Spelt, J.K. (1994) Curvilinear formulation of the 3-D J integral: application to delamination cracking of curved laminates. *Composite Structures*. **28**(2), 123–130.

Foroosh, H., Zerubia, J.B., Berthod, M. (2002) Extension of phase correlation to subpixel registration. *IEEE Transactions on Image Processing*. **11**(3), 188–199.

Forsberg, F., Mooser, R., Arnold, M., Hack, E., Wyss, P. (2008) 3D micro-scale deformations of wood in bending: Synchrotron radiation μCT data analyzed with digital volume correlation. *Journal of Structural Biology*. **164**(3), 255–262.

Fujikawa, M. (2005) Modified intelligent hybrid technique reducing experimental error over the entire target area. *Experimental Mechanics*. **45**(6), 541–549.

Garcia, D. (2010) Robust smoothing of gridded data in one and higher dimensions with missing values. *Computational statistics & data analysis*. **54**(4), 1167–1178.

Giner, E., Fernández-Zúñiga, D., Fernández-Sáez, J., Fernández-Canteli, A. (2010) On the Jx1-integral and the out-of-plane constraint in a 3D elastic cracked plate loaded in tension. *International Journal of Solids and Structures*. **47**(7–8), 934–946.

Gosz, M., Dolbow, J., Moran, B. (1998) Domain integral formulation for stress intensity factor computation along curved three-dimensional interface cracks. *International Journal of Solids and Structures*. **35**(15), 1763–1783.

Grédiac, M., Pierron, F., Avril, S., Toussaint, E. (2006) The virtual fields method for extracting constitutive parameters from full-field measurements: A review. *Strain*. **42**(4), 233–253.

Grédiac, M., Sur, F. (2014) Effect of sensor noise on the resolution and spatial resolution of displacement and strain maps estimated with the grid method. *Strain*. **50**(1), 1–27.

Grédiac, M., Sur, F., Blaysat, B. (2016) The grid method for in-plane displacement and strain measurement: a review and analysis. *Strain*. **52**(3), 205–243.

Griffith, A.A. (1921) The phenomena of rupture and flow in solids. *Philosophical Transactions of the Royal Society A: Mathematical, Physical and Engineering Sciences*. **221**(582–593), 163–198.

Gross, B., Srawley, J.E. (1964) Stress-intensity factors for Single-Edge-Notch specimens in bending or combined bending and tension by boundary collacation of a stress function. *NASA Technical note*. **TN D-2603**(January 1965), 1–17.

Hamam, R., Hild, F., Roux, S. (2007) Stress intensity factor gauging by digital image correlation: Application in cyclic fatigue. *Strain*. **43**(3), 181–192.

Hareesh, T.V., Chiang, F.P. (1988) Integrated experimental-finite element approach for studying elasto-plastic crack-tip fields. *Engineering Fracture Mechanics*. **31**(3), 451–461.

Helm, J.D. (2008) Digital image correlation for specimens with multiple growing cracks. *Experimental Mechanics*. **48**(6), 753–762.

Henninger, C., Roux, S., Hild, F. (2010) Enriched kinematic fields of cracked structures. *International Journal of Solids and Structures*. **47**(24), 3305–3316.

Herrmann, G.A., Herrmann, G. (1981) On energy-release rates for a plane crack. *Journal of Applied Mechanics*. **48**(September), 525.

Hild, F., Roux, S. (2012) Comparison of local and global approaches to digital image correlation. *Exp. Mech.*. **52**(9), 1503–1519.

Hild, F., Roux, S. (2006a) Digital Image Correlation: from displacement measurement to identification of elastic properties - a review. *Strain*. **42**(2), 69–80.

Hild, F., Roux, S. (2006b) Measuring stress intensity factors with a camera: Integrated digital image correlation (I-DIC). *Comptes Rendus Mécanique*. **334**(1), 8–12.

Huber, O., Nickel, J., Kuhn, G. (1993) On the decomposition of the J-integral for 3D crack problems. *International Journal of Fracture*. **64**(4), 339–348.

Huchzermeyer, R.L. (2017) *Measuring mechanical properties using digital image correlation: Extracting tensile and fracture properties from a single sample*. Stellenbosch University.

Hui, C.Y., Ruina, A. (1995) Why K? High order singularities and small scale yielding. *International Journal of Fracture*. **72**(2), 97–120.

Hutchinson, J.W. (1983) Fundamentals of the phenomenological theory of nonlinear fracture mechanics. *Journal of Applied Mechanics*. **50**(4b), 1042–1051.

Hutchinson, J.W. (1968) Plastic stress and strain fields at a crack tip. *Journal of the Mechanics and Physics of Solids*. **16**(5), 337–342.

Irwin, G.R. (1957) Analysis of stresses and strains near the end of a crack traversing a plate. *Journal of Applied Mechanics*. **24**(September), 361–364.

Ishikawa, H. (1980) A finite element analysis of stress intensity factors for combined tensile and shear loading by only a virtual crack extension. *International Journal of Fracture*. **16**(5), 243–246.

Ishikawa, H., Kitagawa, H., Okamura, H. (1980) J-Integral of mixed mode crack and its application. In *3rd International Conference on Mechanical Behaviour of Materials*. Pergamon Press: Oxford, pp. 447–455.

Jacquot Pierre (2008) Speckle interferometry: a review of the principal methods in use for experimental mechanics applications. *Strain*. **44**(1), 57–69.

Jafarkhani, R., Masri, S.F. (2011) Finite element model updating using evolutionary strategy for damage detection. *Computer-Aided Civil and Infrastructure Engineering*. **26**(3), 207–224.

Jestin, L., Fawkes, M., Maccoll, B., Koko, M. (2014) *Eskom Power Plant Engineering Institute (EPPEI) - 5 years research strategic plan*.

Jin, H., Bruck, H. a. (2005) Pointwise digital image correlation using genetic algorithms. *Experimental Techniques*. **29**(February), 36–39.

Judt, P.O., Ricoeur, A. (2013) Accurate loading analyses of curved cracks under mixed-mode conditions applying the J-integral. *International Journal of Fracture*. **182**(1), 53–66.

Kanninen, M.F., Popelar, C.H. (1986) Advanced Fracture Mechanics. *Journal of Engineering Materials and Technology*. **108**(2), 199.

Kim, J., Paulino, G. (2005) Consistent formulations of the interaction integral method for fracture of functionally graded materials. *Journal of Applied Mechanics*. **72**(May).

Klocke, F., Schwade, M., Klink, A., Kopp, A. (2011) EDM machining capabilities of magnesium (Mg) alloy WE43 for medical applications. *Procedia Engineering*. **19**, 190–195.

Knowles, J.K., Sternberg, E. (1972) On a class of conservation laws in linearized and finite elastostatics. *Archive for Rational Mechanics and Analysis*. **44**(3), 187–211.

Kolednik, O., Schöngrundner, R., Fischer, F.D. (2014) A new view on J-integrals in elastic–plastic materials. *International Journal of Fracture*. **187**(1), 77–107.

Kreis, T. (2005) Handbook of Holographic Interferometry. *Applied Optics*. **26**, 542.

Kuna, M. (2013a) Basics of Fracture Mechanics. In *Finite Elements in Fracture Mechanics*. Springer Netherlands, pp. 21–151.

Kuna, M. (2013b) Numerical calculation of generalized energy balance integrals. In *Finite Elements in Fracture Mechanics*. Springer Netherlands, pp. 263–304.

Landes, J.D., Begley, J.A. (1976) A fracture mechanics approach to creep crack growth. In *Mechanics of Crack Growth*. 100 Barr Harbor Drive, PO Box C700, West Conshohocken, PA 19428-2959: ASTM International, pp. 128–148.

Leclerc, H., Périé, J.N., Roux, S., Hild, F. (2011) Voxel-Scale Digital Volume Correlation. *Experimental Mechanics*. **51**(4), 479–490.

Lengsfeld, M., Schmitt, J., Alter, P., Kaminsky, J., Leppek, R. (1998) Comparison of geometry-based and CT voxel-based finite element modelling and experimental validation. *Medical Engineering and Physics*. **20**(7), 515–522.

Li, B.J., Wang, Q., Duan, D.P., Chen, J.A. (2017) Modified digital image correlation for balancing the influence of subset size choice. *Optical Engineering*. **56**(5), 54–104.

Li, F.Z., Shih, C.F., Needleman, A. (1985) A comparison of methods for calculating energy release rates. *Engineering Fracture Mechanics*. **21**, 405–421.

Lim, I.L., Johnston, I.W., Choi, S.K. (1992) Comparison between various displacement-based stress intensity factor computation techniques. *International Journal of Fracture*. **58**(3), 193–210.

Liu, K., Tovar, A. (2014) An efficient 3D topology optimization code written in Matlab. *Structural and Multidisciplinary Optimization*. **50**(6), 1175–1196.

Luo, P.F., Chao, Y.J., Sutton, M.A., Peters, W.H. (1993) Accurate measurement of three-dimensional deformations in deformable and rigid bodies using computer vision. *Experimental Mechanics*. **33**(2), 123–132.

Maire, E., Withers, P.J. (2014) Quantitative X-ray tomography. *International Materials Reviews*. **59**(1), 1–43.

Malesa, M., Kujawińska, M., Malowany, K., Lusa, T. (2015) Application of Multi-camera DIC System for Measurements of Industrial Structures. *Procedia Engineering*. **114**, 453–460.

Marrow, T.J., Liu, D., Barhli, S.M., Saucedo Mora, L., Vertyagina, Y., Collins, D.M., Reinhard, C., Kabra, S., Flewitt, P.E.J., Smith, D.J. (2016) In situ measurement of the strains within a mechanically loaded polygranular graphite. *Carbon*. **96**, 285–302.

Marrow, T.J., Mostafavi, M., Hashimoto, T., Thompson, G.E. (2014) A quantitative three-dimensional in situ study of a short fatigue crack in a magnesium alloy. *International Journal of Fatigue*. **66**, 183–193.

Marrow, T.J., Reinhard, C., Vertyagina, Y., Saucedo-Mora, L., Collins, D., Mostafavi, M. (2014) 3D studies of damage by combined x-ray tomography and digital volume correlation. *Procedia Materials Science*. **3**(July), 1554–1559.

McDonald, S.A., Dedreuil-Monet, G., Yao, Y.T., Alderson, A., Withers, P.J. (2011) In situ 3D X-ray microtomography study comparing auxetic and non-auxetic polymeric foams under tension. *Physica Status Solidi (B) Basic Research*. **248**(1), 45–51.

McNeill, S.R., Peters, W.H., Sutton, M. a. (1987) Estimation of stress intensity factor by digital image correlation. *Engineering Fracture Mechanics*. **28**(1), 101–112.

Méité, M., Dubois, F., Pop, O., Absi, J. (2013) Mixed mode fracture properties characterization for wood by digital images correlation and finite element method coupling. *Engineering Fracture Mechanics*. **105**, 86–100.

Moës, N., Gravouil, A., Belytschko, T. (2002) Non-planar 3D crack growth by the extended finite element and level sets-Part I: Mechanical model. *International Journal for Numerical Methods in Engineering*. **53**(11), 2549–2568.

Molokwane, T.J. (2014) *Weldability Limits for X20 Steel [PowerPoint slides]*. Cape Town.

Molteno, M.R., Becker, T.H. (2013) Formulation of a digital image correlation algorithm for fracture mechanics applications. In *South African Institution of Mechanical Engineering*. Cape Town, pp. 2–3.

Molteno, M.R., Becker, T.H. (2014) Implementation of the extreme learning machine for sub-pixel interpolation for digital image correlation. In *16th International Conference on Experimental Mechanics (ICEM-16)*. Cambridge, p. 56.

Molteno, M.R., Becker, T.H. (2015a) Mode I-III decomposition of the J-integral from digital image correlation displacement data. In *4th International Conference of Fracture and Failure of Materials and Structures*. Paris, France, pp. 33–34.

Molteno, M.R., Becker, T.H. (2015b) Mode I-III decomposition of the J-integral to calculate the stress intensity factors from digital image correlation displacement data. In *10th International Conference on Advances in Experimental Mechanics*. Edinburgh.

Molteno, M.R., Becker, T.H. (2015c) Mode I-III decomposition of the J -integral from DIC displacement data. *Strain*. **51**(6), 492–503.

Molteno, M.R., Becker, T.H. (2017) The equivalent volume integral with improved resilience to errors in crack front position. In *14th International Conference on Fracture*. Rhodes, Greece.

Molteno, M.R., Duncan, M., Marrow, T.J., Becker, T.H. (2017) Detection and elimination of spurious results from digital image and volume correlation data. In *14th International Conference on Fracture*. Rhodes, Greece: ICF.

Molteno, M.R., Marrow, T.J., Becker, T.H. (2016) Experimental validation of the decomposition method on digital volume correlation displacement data. In *Conference Proceedings of the 11th British Soceity of Strain Measurement*. Exeter, UK.

Molteno, M.R., Tait, R.B., Wilkinson, A., Becker, T.H. (2012) Eddy current detection of fatigue cracks in drill pipes. *University of Cape Town*.

Mostafavi, M., Collins, D.M., Cai, B., Bradley, R., Atwood, R.C., Reinhard, C., Jiang, X., Galano, M., Lee, P.D., Marrow, T.J. (2015) Yield behavior beneath hardness indentations in ductile metals, measured by three-dimensional computed X-ray tomography and digital volume correlation. *Acta Materialia*. **82**, 468–482.

Mostafavi, M., McDonald, S.A., Mummery, P.M., Marrow, T.J. (2013) Observation and quantification of three-dimensional crack propagation in poly-granular graphite. *Engineering Fracture Mechanics*. **110**, 410–420.

Mueller, R., Maugin, G.A. (2002) On material forces and finite element discretizations. *Computational Mechanics*. **29**(1), 52–60.

Nakamura, T., Parks, D.M. (1989) Antisymmetrical 3-D stress field near the crack front of a thin elastic plate. *International Journal of Solids and Structures*. **25**(12), 1411–1426.

Nikishkov, G.P., Atluri, S.N. (1987) Calculation of fracture mechanics parameters for an arbitrary three-dimensional crack, by the 'equivalent domain integral' method. *International Journal for Numerical Methods in Engineering*. **24**(9), 1801–1821.

Nikishkov, G.P., Vershinin, A. V., Nikishkov, Y.G. (2016) Mesh-independent equivalent domain integral method for J-integral evaluation. *Advances in Engineering Software*. **100**, 308–318.

Nishioka, T., Atluri, S.N. (1984) On the computation of mixed-mode for a dynamically propagating crack, using path-independent integrals. *Engineering Fracture Mechanics*. **20**(2), 193–208.

Nishioka, T., Ikekita, H., Tamai, K. (1997) A variational principle for minimizing experimental measurement errors and its application to a hybrid experimental-numerical method. *Computational Mechanics*. **20**(1–2), 101–108.

Nishioka, T., Kurio, K., Nakabayashi, H. (2000) An intelligent hybrid method to automatically detect and eliminate experimental measurement errors for linear elastic deformation fields. *Experimental Mechanics*. **40**(2), 170–179.

Omer, N., Yosibash, Z. (2005) On the path independency of the point-wise J integral in three-dimensions. *International Journal of Fracture*. **136**(1–4), 1–36.

Pan, B., Qian, K., Xie, H., Asundi, A. (2009) Two-dimensional digital image correlation for in-plane displacement and strain measurement: a review. *Measurement Science and Technology*. **20**(6), 62001.

Peters, W., Ranson, W. (1982) Digital imaging techniques in experimental stress analysis. *Optical Engineering*. **21**(3), 427–431.

Pierron, F., Grédiac, M. (2012) *The virtual fields method: extracting constitutive mechanical parameters from full-field deformation measurements*. New York: Springer.

Poissant, J., Barthelat, F. (2010) A novel 'subset splitting' procedure for digital image correlation on discontinuous displacement fields. *Experimental mechanics*. **50**(3), 353–364.

Post, D. (1991) Moiré interferometry: advances and applications. *Experimental Mechanics*. **31**(3), 276–280.

Rabczuk, T. (2012) Computational methods for fracture in brittle and quasi-brittle solids: state-of-the-art review and future perspectives. *ISRN Applied Mathematics*. **2013**(1), 23–61.

Rannou, J., Limodin, N., Réthoré, J., Gravouil, A., Ludwig, W., Baïetto-Dubourg, M.C., Buffière, J.Y., Combescure, A., Hild, F., Roux, S. (2010) Three dimensional experimental and numerical multiscale analysis of a fatigue crack. *Computer Methods in Applied Mechanics and Engineering*. **199**(21–22), 1307–1325.

Rastogi (2000) *Photomechanics*. Berlin, Heidelberg: Springer Berlin Heidelberg.

Rechenmacher, A.L. (2006) Grain-scale processes governing shear band initiation and evolution in sands. *Journal of the Mechanics and Physics of Solids*. **54**(1), 22–45.

Réthoré, J., Gravouil, A., Morestin, F., Combescure, A. (2005) Estimation of mixed-mode stress intensity factors using digital image correlation and an interaction integral. *International Journal of Fracture*. **132**(1), 65–79.

Réthoré, J., Hild, F., Roux, S. (2008) Extended digital image correlation with crack shape optimization. *International Journal for Numerical Methods in Engineering*. **73**(2), 248–272.

Réthoré, J., Limodin, N., Buffière, J.Y., Hild, F., Ludwig, W., Roux, S. (2011) Digital volume correlation analyses of synchrotron tomographic images. *Journal of Strain Analysis for Engineering Design*. **46**(7), 683–695.

Réthoré, J., Roux, S., Hild, F. (2008) Noise-robust stress intensity factor determination from kinematic field measurements. *Engineering Fracture Mechanics*. **75**(13), 3763–3781.

Réthoré, J., Roux, S., Hild, F. (2011) Optimal and noise-robust extraction of fracture mechanics parameters from kinematic measurements. *Engineering Fracture Mechanics*. **78**(9), 1827–1845.

Réthoré, J., Tinnes, J.P., Roux, S., Buffière, J.Y., Hild, F. (2008) Extended three-dimensional digital image correlation (X3D-DIC). *Comptes Rendus - Mecanique*. **336**(8), 643–649.

Rice, J.R. (1968) A path independent integral and the approximate analysis of strain concentration by notches and cracks. *Journal of Applied Mechanics*. **35**(2), 379–386.

Rice, J.R., Rosengren, G.F. (1968) Plane strain deformation near a crack tip in a power-law hardening material. *Journal of the Mechanics and Physics of Solids*. **16**, 1–12.

Richard, H.A., Fulland, M., Sander, M. (2005) Theoretical crack path prediction. *Fatigue and Fracture of Engineering Materials and Structures*. **28**(1–2), 3–12.

Richard, H.A., Schramm, B., Schirmeisen, N.H. (2014) Cracks on mixed-mode loading - theories, experiments, simulations. *International Journal of Fatigue*. **62**, 93–103.

Rigby, R.H., Aliabadi, M.H. (1998) Decomposition of the mixed-mode J-integral—revisited. *International Journal of Solids and Structures*. **35**(17), 2073–2099.

Rigby, R.H., Aliabadi, M.H. (1993) Mixed-mode J-integral method for analysis of 3D fracture problems using BEM. *Engineering Analysis with Boundary Elements*. **11**, 239–256.

van Rooyen, M. (2016) *Thermal Power Plant Steel Creep Deformation Measurement Using Stereo Digital Image Correlation*. Stellenbosch University.

Roux, S., Hild, F. (2006) Stress intensity factor measurements from digital image correlation: post-processing and integrated approaches. *International Journal of Fracture*. **140**(1–4), 141–157.

Roux, S., Réthoré, J., Hild, F. (2009) Digital image correlation and fracture: an advanced technique for estimating stress intensity factors of 2D and 3D cracks. *Journal of Physics D: Applied Physics*. **42**(21), 214004.

Ruybalid, A.P., Hoefnagels, J.P.M., van der Sluis, O., Geers, M.G.D. (2017) Full-field identification methods: comparison of FEM updating and integrated DIC. *Advancement of Optical Methods in Experimental Mechanics*. **3**, 289–297.

Scheepers, R., Newby, M., Doubell, P., Bezuidenhout, M.E.. (2010) Structural integrity and lifing of components with defects, an Eskom perspective. In *HIDA-5*. pp. 1–12.

Schreier, H., Orteu, J.J., Sutton, M.A. (2009) *Image correlation for shape, motion and deformation measurements: Basic concepts, theory and applications*. Springer US.

Shih, C.F., Moran, B., Nakamura, T. (1986) Energy release rate along a three-dimensional crack front in a thermally stressed body. *International Journal of Fracture*. **30**(2), 79–102.

Shih, C.F., Needleman, A. (1984) Fully plastic crack problems, Part 1: solutions by a penalty method. *Journal of Applied Mechanics*. **51**(1), 48.

Shivakumar, K.N., Raju, I.S. (1992) An equivalent domain integral method for three-dimensional mixed-mode fracture problems. *Engineering Fracture Mechanics*. **42**(6), 935–959.

Shoemake, K. (1994) *Euler angle conversion*. P. S. Heckbert, ed. Morgan Kaufmann.

Simha, N.K., Fischer, F.D., Shan, G.X., Chen, C.R., Kolednik, O. (2008) J-integral and crack driving force in elastic-plastic materials. *Journal of the Mechanics and Physics of Solids*. **56**(9), 2876–2895.

Sollero, P., Aliabadi, M. (1992) Boundary element analysis of crack problems for anisotropic composite laminates. In C. A. Brebbia, J. Dominguez, & F. Paris, eds. *Proc. Int. Conf. (2nd edn.), Boundary Elements in Engineering XIV*. Seville, pp. 299–314.

Srinivasa Reddy, B., Chatterji, B.N. (1996) An FFT-based technique for translation, rotation, and scale-invariant image registration. *IEEE Transactions on Image Processing*. **5**(8), 1266–1271.

Stern, M., Becker, E.B., Dunham, R.S. (1976) A contour integral computation of mixed-mode stress intensity factors. *International Journal of Fracture*. **12**(3), 359–368.

Stump, D.M., Zywicz, E. (1993) J-Integral computations in the incremental and deformation plasticity analysis of small-scale yielding. *Engineering Fracture Mechanics*. **45**(1), 61–77.

Sutton, M.A., Li, N., Joy, D.C., Reynolds, A.P., Li, X. (2007) Scanning electron microscopy for quantitative small and large deformation measurements Part I: SEM imaging at magnifications from 200 to 10,000. *Experimental Mechanics*. **47**(6), 775–787.

Sutton, M.A., Mingqi, C., Peters, W.H., Chao, Y.J., McNeill, S.R. (1986) Application of an optimized digital correlation method to planar deformation analysis. *Image and Vision Computing*. **4**(3), 143–150.

Sutton, M.A., Turner, J.L., Bruck, H.A., Chae, T.A. (1991) Full-field representation of discretely sampled surface deformation for displacement and strain analysis. *Experimental Mechanics*. **31**(2), 168–177.

Sutton, M.A., Turner, J.L., Chao, Y.J., Bruck, H.A., Chae, T.L. (1992) Experimental investigations of three-dimensional effects near a crack tip using computer vision. *International Journal of Fracture*. **53**(3), 201–228.

Sutton, M.A., Wolters, W.J., Peters, W.H., Ranson, W.F., McNeill, S.R. (1983) Determination of displacements using an improved digital correlation method. *Image and Vision Computing*. **1**, 133–139.

Tada, H., Paris, P.C., Irwin, G.R. (2000) *The Stress Analysis of Cracks Handbook, Third Edition*. 3rd ed. Three Park Avenue New York, NY 10016-5990: ASME.

Tagliaferri, F., Waller, J., Andò, E., Hall, S.A., Viggiani, G., Bésuelle, P., DeJong, J.T. (2011) Observing strain localisation processes in bio-cemented sand using x-ray imaging. *Granular Matter*. **13**(3), 247–250.

Trollip, H., Butler, A., Burton, J., Caetano, T., Godinho, C. (2014) Energy security in South Africa. *Mitigation Action Plans and Scenarios (MAPS)*. (17), 45.

Trtik, P., Marone, F., Stampanoni, M. (2009) Stripe and ring artifact removal with combined wavelet - fourier filtering. . **17**(10), 1844–1856.

Turner, D.Z. (2014) Peridynamics based digital image correlation algorithm suitable for cracks and other discountinuties. *Journal of Engineering Mechanics*. **141**(2), 1–10.

Walters, M.C., Paulino, G.H., Dodds, R.H. (2005) Interaction integral procedures for 3-D curved cracks including surface tractions. *Engineering Fracture Mechanics*. **72**(11), 1635–1663.

Wang, B., Pan, B. (2016) Subset-based local vs. finite element-based global digital image correlation: A comparison study. *Theoretical and Applied Mechanics Letters*. **6**(5), 200–208.

Wang, G., Garcia, D., Liu, Y., de Jeu, R., Johannes Dolman, A. (2012) A three-dimensional gap filling method for large geophysical datasets: Application to global satellite soil moisture observations. *Environmental Modelling and Software*. **30**, 139–142.

Wang, S.S., Yau, J.F., Corten, H.T. (1980) A mixed-mode crack analysis of rectilinear anisotropic solids using conservation laws of elasticity. *International Journal of Fracture*. **16**, 247–259.

Wang, W., Mottershead, J.E., Sebastian, C.M., Patterson, E.A. (2011) Shape features and finite element model updating from full-field strain data. *International Journal of Solids and Structures*. **48**(11–12), 1644–1657.

Wang, X., Ma, S.P. (2014) Mesh-based digital image correlation method using non-uniform elements for measuring displacement fields with high gradient. *Experimental Mechanics*. **54**(9), 1545–1554.

Wells, A.A. (1955) *The conditions for fast fracture in aluminum alloys with particular reference to Comet failures*.

Weng, S., Xia, Y., Xu, Y.L., Zhu, H.P. (2011) Substructure based approach to finite element model updating. *Computers & Structures*. **89**(9–10), 772–782.

Werlberger, M., Trobin, W., Pock, T., Wedel, A., Cremers, D., Bischof, H. (2009) Anisotropic Huber-L1 Optical Flow. In *BMVC*. pp. 201–211.

Westergaard, H.M. (1939) Bearing pressures and cracks. *Journal of Applied Mechanics*. **61**, A49–A53.

Williams, M.L. (1957) On the stress distribution at the base of a stationary crack. *Journal of Applied Mechanics*. **24**(3), 109–114.

Winkler, H. (2007) Energy policies for sustainable development in South Africa. *Energy for Sustainable Development*. **11**(1), 26–34.

Wittevrongel, L., Lava, P., Lomov, S. V., Debruyne, D. (2015) A self adaptive global digital image correlation algorithm. *Experimental Mechanics*. **55**(2), 361–378.

Xiao, Q.Z., Karihaloo, B.L. (2007) Implementation of hybrid crack element on a general finite element mesh and in combination with XFEM. *Computer Methods in Applied Mechanics and Engineering*. **196**(13–16), 1864–1873.

Yaofeng, S., Pang, J.H.L. (2007) Study of optimal subset size in digital image correlation of speckle pattern images. *Optics and Lasers in Engineering*. **45**, 967–974.

Yates, J.R., Zanganeh, M., Tai, Y.H. (2010) Quantifying crack tip displacement fields with DIC. *Engineering Fracture Mechanics*. **77**(11), 2063–2076.

Yau, J.F.F., Wang, S.S., Corten, H.T. (1980) A Mixed-Mode Crack Analysis of Isotropic Solids Using Conservation Laws of Elasticity. *Journal of Applied Mechanics*. **47**(2), 335.

Yoneyama, S. (2016) Basic principle of digital image correlation for in-plane displacement and strain measurement. *Advanced Composite Materials*. **25**(2), 105–123.

Yoneyama, S. (2011) Smoothing measured displacements and computing strains utilising finite element method. *Strain*. **47**(2), 258–266.

Yoneyama, S., Arikawa, S. (2012) Identification of boundary condition from measured displacements for linear elastic deformation fields. *Procedia IUTAM*. **4**, 215–226.

Yoneyama, S., Arikawa, S., Kurosu, Y. (2016) Evaluating thermal stresses and strains from measured displacements using an experimental-numerical hybrid method. In *Conference Proceedings of the Society for Experimental Mechanics Series*. Springer International Publishing, pp. 103–110.

Yoneyama, S., Arikawa, S., Kusayanagi, S., Hazumi, K. (2014) Evaluating J-integral from displacement fields measured by digital image correlation. *Strain*. **50**(2), 147–160.

Yoneyama, S., Morimoto, Y., Takashi, M. (2006) Automatic evaluation of mixed-mode stress intensity factors utilizing digital image correlation. *Strain*. **42**(1), 21–29.

Yoneyama, S., Ogawa, T., Kobayashi, Y. (2007) Evaluating mixed-mode stress intensity factors from full-field displacement fields obtained by optical methods. *Engineering Fracture Mechanics*. **74**(9), 1399–1412.

Zhao, J.Q., Zeng, P., Lei, L.P., Ma, Y. (2012) Initial guess by improved population-based intelligent algorithms for large inter-frame deformation measurement using digital image correlation. *Optics and Lasers in Engineering*. **50**(3), 473–490.

Zhou, P., Goodson, K.E. (2001) Subpixel displacement and deformation gradient measurement using digital image/speckle correlation (DISC). *Optical Engineering*. **40**(8), 1613–1620.

Appendix: Formulation of the surface-volume integral ($J_{s\text{-}vol}$) from the volume integral

In this section, the surface-volume integral is re-derived using the procedure used to derive the volume integral from Equation (2.37) as outlined by Shih et al. (Shih et al., 1986). This is achieved by applying a Q-function $\tilde{Q}$ that is constrained to be equal to $q(s)$ everywhere within the volume. Note that, as in the main text, the superscripted tilde signifies $Q = q$, and surfaces and volumes are indicated on Figure 5.1. The weighted average of the path integral $\tilde{J}_{\Delta s}$ can be expressed as a surface integral over the inner tube S_0 as,

$$\tilde{J}_{\Delta s}(\mathrm{s}) = \frac{1}{A_c}\int_{\Delta s}\int_{\Gamma_\varepsilon}\left(W n_1 - \sigma_{ij}\frac{\partial u_i}{\partial x_1}n_j\right) q \mathrm{d}\Gamma \mathrm{d}s$$
$$\tilde{J}_{\Delta s}(\mathrm{s}) = \frac{1}{A_c}\int_{S_0}\left(W n_1 - \sigma_{ij}\frac{\partial u_i}{\partial x_1}n_j\right)\tilde{Q}\,dA, \tag{A.1}$$

The surfaces enclosing of the outer volume (V_1) can be grouped as: $S_{V1} = S_1 + S_{a1} + S_{b1} + S_c - S_0$. Rearranging gives $S_0 = (S_1 + S_{a1} + S_{b1}) - S_{V1}$, and allows the right-hand-side of Equation A.1 to be expanded to:

$$\tilde{J}_{\Delta s}(\mathrm{s}) = \frac{1}{A_c}\int_{(S_1+S_{a1}+S_{b1}+S_c)}\left(W n_1 - \sigma_{ij}\frac{\partial u_i}{\partial x_1}n_j\right)\tilde{Q}\,dA$$
$$-\frac{1}{A_c}\int_{S_{V1}}\left(W n_k - \sigma_{ij}\frac{\partial u_i}{\partial x_1}n_j\right)\tilde{Q}\,dA, \tag{A.2}$$

The surface integrals S_{a1}, S_{b1} and S_c are zero because $\tilde{Q}$ is zero on S_{a1} and S_{b1} and assuming that tractions on the crack faces are zero (Figure 5.1). Usually Q is zero on the outer surface S_1, but $\tilde{Q}$ is not, so the surface integral over S_1 remains. Then applying the divergence theorem to the last term in Equation A.2 gives:

$$\tilde{J}_{\Delta s}(\mathrm{s}) = \frac{1}{A_c}\int_{S_1}\left(Wn_1 - \sigma_{ij}\frac{\partial u_i}{\partial x_1}n_j\right)\tilde{Q}dA + \frac{1}{A_c}\int_{V_1}\left(\sigma_{ij}\frac{\partial u_i}{\partial x_1} - W\delta_{1j}\right)\frac{\partial \tilde{Q}}{\partial x_j}dV - \frac{1}{A_c}\int_{S_{V1}}\frac{\partial}{\partial x_j}\left(\sigma_{ij}\frac{\partial u_i}{\partial x_1} - W\delta_{1j}\right)\tilde{Q}dA, \tag{A.3}$$

For straight cracks in stress equilibrium, $\frac{\partial}{\partial x_j}\left(\sigma_{ij}\frac{\partial u_i}{\partial x_1} - W\delta_{1j}\right) = 0$ (Rice, 1968), and only $j = 3$ remains in the last term because $\partial\tilde{Q}/\partial x_j = 0$ for $j = 1, 2$. Therefore:

$$\tilde{J}_{\Delta s}(\mathrm{s}) = \frac{1}{A_c}\int_{S_1}\left(Wn_1 - \sigma_{ij}\frac{\partial u_i}{\partial x_1}n_j\right)\tilde{Q}dA + \frac{1}{A_c}\int_{V_1}\left(\sigma_{ij}\frac{\partial u_i}{\partial x_1}n_j\right)\frac{\partial \tilde{Q}}{\partial x_3}dV, \tag{A.4}$$

Noting that $\tilde{Q} = q$ everywhere in V_1, Equation A.4 is then the same as Equation (5.7). This shows that J_{s-vol} can also be derived using the volume integral approach, within the framework of the classical J path-area and volume integrals using the assumptions of planar traction free faces, volumes free of singularities and crack front straightness on Δs.